Doctorate in Physical Sciences

Universidad de Cartagena
Fundada en 1827

Final Thesis Report

Phase stability of carbon, oxygen and carbon dioxide under extreme P-T conditions, beyond the harmonic approximation

Beatriz Helena Cogollo Olivo

Advisor
Javier Antonio Montoya Martínez, Ph. D.

Co-Advisor
Sandro Scandolo, Ph. D.

University of Cartagena

2020

Phase stability of carbon, oxygen and carbon dioxide under extreme P-T conditions, beyond the harmonic approximation

Final Thesis Report submitted for the degree of Doctor in Physical Sciences

Beatriz Helena Cogollo Olivo

Advisor

Javier Antonio Montoya Martínez, Ph. D.

Co-Advisor

Sandro Scandolo, Ph. D.

University of Cartagena

Doctorate in Physical Sciences

Cartagena de Indias

Colombia

January, 2020

Cartagena de Indias, 20 de enero de 2020

Señores miembros
COMITÉ CURRICULAR
Doctorado en Ciencias Físicas - SUE Caribe

Distinguidos miembros del Comité,

De conformidad con el Reglamento General, Reglamento Estudiantil del SUE-Caribe y lineamientos del programa, hago entrega del presente documento de propuesta de tesis doctoral titulada ***Phase stability of carbon, oxygen and carbon dioxide under extreme P-T conditions, beyond the harmonic approximation***, de la cual adjunto un (1) original, una (1) copia impresa y una (1) copia en formato electrónico CD, para ser evaluada y sustentada conforme a lo establecido.

Cordialmente,

<div style="text-align:center">

_____

Beatriz Helena Cogollo Olivo
Estudiante
Programa de Doctorado en Ciencias Físicas
SUE - Caribe

</div>

Visto Bueno:

<div style="text-align:center">

_____

Javier Antonio Montoya Martínez, Ph. D.
Docente
Facultad de Ciencias Exactas y Naturales
Universidad de Cartagena

</div>

Visto Bueno:

<div style="text-align:center">

_____

Javier Antonio Montoya Martínez, Ph. D.
Coordinador Institucional
Doctorado en Ciencias Físicas - SUE Caribe
Universidad de Cartagena

</div>

DOCTORADO EN CIENCIAS FÍSICAS

ACTA DE EVALUACIÓN DEL INFORME FINAL DE TESIS

FECHA	DD	MM	AA		FORMATO PDCF No.	01
	28	05	2019		Actualizado:	Mayo 2016

Título del Informe Final de Tesis

Phase stability of carbon, oxygen and mixtures under extreme P-T conditions, beyond the harmonic approximation

Nombre del (de la) Estudiante	Identificación
Beatriz Helena Cogollo Olivo	1.047.382.037

Grupo de Investigación

Modelado Computacional de sistemas físicos y estadísticos

Línea de Investigación

Física de materiales bajo condiciones extremas

Nombre del Director	Identificación
Javier Montoya Martínez	94.527.774

Nombre del Co-Director	Identificación
Sandro Scandolo	

1.0	Resultado de las Evaluaciones			
Evaluación	**Aprobada**	**Insuficiente**	**No aprobada**	
Documento Escrito	✓			
Sustentación Oral	✓	Una nota de Insuficiente o No aprobado en la prueba oral puede generar una repetición de la prueba, si se recomienda.		
Recomendación: (opcional)	Aprobada			

2.0	Firmas de los Jurados, Directores de Tesis, Director Regional o su Delegado	
Nombre del Jurado 1	CAETANO RODRIGUES MIRANDA	Vo. Bo. Firma
Nombre del Jurado 2	Jorge Mario Osorio Guillén	Vo. Bo. Firma
Nombre del Jurado 3	RICARDO VEGA MONROY	Vo. Bo. Firma
Director	Javier A. Montoya M.	Vo. Bo. Firma
Co-Director	SANDRO SCANDOLO	Vo. Bo. Firma

Director del Programa o Delegado	Rafael Sarmiento M.	Vo. Bo. Firma

3.0	Distinción (Si la hay)		
La máxima distinción (Laureada) sólo se otorgará a Tesis de valor excepcional.		**Meritoria**	**Laureada**
		✓	

Argumentación de la Distinción

· THE SET OF WORKS GIVE VERY INTERESTING AND ORIGINAL CONTRIBUTIONS FOR HIGH PRESSURE PHYSICS

· The new phase diagram for O_2 and CO_2 are important contributions to the solid state and planetary sciences.

Evaluación	Aprobado	Insuficiente	No aprobado
Documento Escrito	✓		
Sustentación Oral			

Firmas adicionales si hay distinción:

Nombre del Jurado 1	CAETANO RODRIGUES MIRANDA	Firma
	Nombre Manuscrito	
Identificación	FM 892258	

Nombre del Jurado 2	Jorge Mario Osorio Galin	Firma
	Nombre Manuscrito	
Identificación	98551676	

Nombre del Jurado 3	RICARDO VEGA MONROY	Firma
	Nombre Manuscrito	
Identificación	72158788	

DOCTORADO EN CIENCIAS FÍSICAS
EVALUACIÓN DOCUMENTAL DEL INFORME FINAL DE TESIS

(PARTE I)

FECHA	DD	MM	AA		FORMATO PDCF No.	01
	28	05	2019		Actualizado:	Mayo 2016

Título del Informe Final de Tesis	
Phase stability of carbon, oxygen and mixtures under extreme P-T conditions, beyond the harmonic approximation	
Nombre del (de la) Estudiante	**Identificación**
Beatriz Helena Cogollo Olivo	1.047.382.037
Grupo de Investigación	
Modelado Computacional de sistemas físicos y estadísticos	
Línea de Investigación	
Física de materiales bajo condiciones extremas	
Nombre del Director	**Identificación**
Javier Montoya Martínez	94.527.774
Nombre del Co-Director	**Identificación**
Sandro Escandolo	

Etapa I. Evaluación del documento escrito

Favor llenar los espacios de color naranja con una calificación que vaya de **0 a 10**, donde 10 equivale a un cumplimiento 100% satisfactorio del criterio de evaluación valorado.

En cada casilla que describe un criterio de evaluación, es recomendado reemplazar el texto guía (en color gris) por las correspondientes justificaciones que considere pertinentes para respaldar la valoración dada.

1.0	Título	
¿El título está acorde con las expectativas planteadas en el estudio?		8
2.0	**Introducción**	
¿Describe un problema delimitado y concreto? ¿La justificación es clara desde el punto de vista académico y científico? ¿El problema se encuentra contextualizado con la literatura existente?		7
3.0	**Fundamentación Teórica**	
¿Se evidencia una revisión exhaustiva de la literatura relevante al problema de estudio? ¿La presentación de las fuentes primarias y secundarias está bien organizada? ¿Describe de forma clara métodos, técnicas, hallazgos, etc., que han sido reportados y que son relevantes para su problema de investigación?		10
4.0	**Metodología**	
¿El diseño de investigación es coherente con el problema planteado? ¿Presenta claridad, pertinencia, consistencia, validez y confiabilidad? ¿Describe de forma adecuada los sistemas de estudio, diseño, métodos y procedimientos empleados, análisis estadístico, etc.?		10

5.0	Análisis e interpretación de los resultados	
¿Son claros y consistentes los resultados con todos los objetivos de la propuesta de tesis que fue aprobada para el/la estudiante? ¿Contiene el trabajo aportes a la ciencia, a la tecnología y a otras disciplinas del saber? ¿Los resultados son presentados de forma clara y precisa?		10
6.0	**Discusión**	
¿Se discutieron todos los resultados obtenidos? ¿Los resultados son interpretados de forma original? ¿Los resultados son confrontados con literatura actual y pertinente? ¿Hay discusión autocrítica con relación a los resultados esperados?		10
7.0	**Conclusiones**	
¿Están acordes las conclusiones con todos los objetivos del proyecto de tesis (ver anexo) que fue aprobada para el/la estudiante? ¿Reflejan con suficiencia las conclusiones los resultados obtenidos? ¿Las perspectivas futuras y las recomendaciones hechas por el/la estudiante son apropiadas de acuerdo a los resultados obtenidos?		8
8.0	**Calidad de la escritura del Informe Final de Tesis**	
¿El documento está escrito de forma clara y precisa? ¿La selección de terminología, redacción, gramática, puntuación y ortografía en general, es el adecuado para una tesis doctoral?		10

9.0	Anotaciones Específicas y Calificación	
Fallas de redacción, omisiones, exposición de conceptos, etc.		**Páginas o Sección**
Adicione celdas a su conveniencia		

Comentarios generales y recomendaciones

TO ENRICH EVEN MORE THE VERY NICE RESULTS IN THE THESIS, A THE
INTRODUCTION AND THE CONCLUSION PARTS COULD BE MORE DEVELOPED
BY BRINGING ATTENTION FOR THE RELEVANT FINDINGS IN THE THESIS

¿Se recomienda proceder con la sustentación oral del Informe Final? (Si/No)		SI
Nombre de quien evalúa	CAETANO RODRIGUES MIRANDA	*Caetano R. Miranda*
Identificación	FM892258	**Firma**

DOCTORADO EN CIENCIAS FÍSICAS
EVALUACIÓN DOCUMENTAL DEL INFORME FINAL DE TESIS

(PARTE I)

FECHA	DD	MM	AA		FORMATO PDCF No.	01
	28	05	2019		Actualizado:	Mayo 2016

Título del Informe Final de Tesis	
Phase stability of carbon, oxygen and mixtures under extreme P-T conditions, beyond the harmonic approximation	

Nombre del (de la) Estudiante	Identificación
Beatriz Helena Cogollo Olivo	1.047.382.037

Grupo de Investigación
Modelado Computacional de sistemas físicos y estadísticos

Línea de Investigación
Física de materiales bajo condiciones extremas

Nombre del Director	Identificación
Javier Montoya Martínez	94.527.774

Nombre del Co-Director	Identificación
Sandro Escandolo	

Etapa I. Evaluación del documento escrito

Favor llenar los espacios de color naranja con una calificación que vaya de **0 a 10**, donde 10 equivale a un cumplimiento 100% satisfactorio del criterio de evaluación valorado.

En cada casilla que describe un criterio de evaluación, es recomendado reemplazar el texto guía (en color gris) por las correspondientes justificaciones que considere pertinentes para respaldar la valoración dada.

1.0	Título	
El título está en concordancia con el estudio realizado en esta tesis de doctorado.		10

2.0	Introducción	
La introducción de la monografía expone en forma clara y concisa la importancia de estudiar carbón, oxígeno y el dióxido de carbón bajo condiciones extremas de presión y temperatura. Debido a la dificultad experimental para el estudio de estos sistemas aparentemente simples, el estudio teórico por medio de cálculos de primeros principios es completamente necesario para dilucidar los diagramas de fase a condiciones extremas.		10

3.0	Fundamentación Teórica	
Los capítulos 1-3 describen de forma muy resumida los fundamentos teóricos y metodología usadas en la tesis. El capítulo 1 debería tener referencias más actualizadas y una corta discusión sobre el efecto de diferentes funcionales en el cálculo de propiedades del estado base, en muchos sistemas cristalinos el uso de LDA, diferentes parametrizaciones de GGA y metaGGA, y los funcionales híbridos pueden llevar a		8

predecir valores muy diferentes en las presiones de transición de muchos sistemas simples tales como Si, Ge, Sn.

El capítulo 2 sobre los métodos de estructura electrónica es muy corto pero en una monografía de esta naturaleza puede llegar a ser suficiente para ilustrar la metodología. Una breve comparación de PAW con otros métodos all-electron hubiera sido deseable, sobre todo porque en las condiciones extremas de presión que se realizaron los cálculos de la tesis es mejor comparar y validar los resultados con otros códigos.

El capítulo 3 introduce el cálculo de propiedades vibracionales y termodinámicas de cristales de forma apropiada. Sin embargo, la última subsección (3.5) describe en su mayor parte el método SSCHA, y este no fué usado en los resultados presentados en la tesis.

Finalmente en mi concepto falto un capítulo de ecuaciones de estado para sólidos, este serviría de justificación porque se uso BM de tercer orden en toda la tesis y no otras EOS tal como la universal de Vinet. También falto una discusión porque estas EOS son validas en el rango de presión de Tpa.

4.0	**Metodología**	
El diseño de los cálculos y la forma de realizar todos los chequeos de convergencia de los principales parámetros variaciones del método de estructura electrónica utilizado son confiables y permiten concluir que los cálculos fueron hechos de forma coherente y sistemática (Apéndices A-C). Como he comentado en el punto anterior, faltó una comparación de los resultados obtenidos con el funcional PBE con otros funcionales tales como PZ, PW91, PBESol y algunos híbridos. Esto es necesario para validar los resultados. También faltó una mejor justificación y comparación entre diferentes EOS que sean validas en el rango de presión de los Tpa.		8
5.0	**Análisis e interpretación de los resultados**	
Los resultados obtenidos son de gran valor para la comunidad científica de la física del estado sólido, ciencias de los materiales, ciencias planetarias y química. Los resultados son muy bien analizados y discutidos, como concencuencia llevaron a la publicación de un excelente artículo en una de las revistas mas prestigiosas del estado sólido (Physical Review B) para el caso de oxígeno. Para el caso del carbón y el dióxido de carbón es un poco descepcionante que estos buenos resultados no hayan sido aun publicados y poder hacer parte de la lista de publicaciones de la tesis. Para estos dos sistemas que no han sido publicados puede ampliarse el análisis de los resultados usando otros funcionales y EOS y quizás poder usar la metodología SSCHA para incluir efectos anarmónicos que vayan mas allá de la QHA.		9
6.0	**Discusión**	
Los capítulos 4-6 presentan una discución detallada de los resultados obtenidos de la tesis. La obtención de los diagramas de fase de estos tres sistemas y su comparación y discusión con los ya publicados se hace con una buena calidad intelectual. Sin embargo como mencioné en puntos anteriores, realizar comparaciones entre diferentes funcionales, EOS y otros métodos de estructura electrónica es aconcejable, tal vez obligatorio, para validar los resultados obtenidos y poder afirmar los principales hallazgos de la tesis.		8

7.0	Conclusiones	
Las conclusiones están escritas de forma certera y correcta, reflejando una introyección del conocimiento aquirido en la elaboración de la tesis. Estas también muestan que se entiende las limitaciones de este estudio y proponen como conseguir en el futuro la inclusión de efectos anarmónicos por nuevas metodologías tales como SSCHA.		10
8.0	Calidad de la escritura del Informe Final de Tesis	
La tesis está escrita con gran esmero y brilla por su claridad. Aunque esta presenta una falla reiterativa en todo el texto: la falta de puntuación en las ecuaciones, están hacen parte integral del texto y deben llevar coma, punto y coma, punto como dictan las reglas de ortografía.		9
9.0	Anotaciones Específicas y Calificación	

Fallas de redacción, omisiones, exposición de conceptos, etc.	Páginas o Sección
Ecuaciones sin puntuación.	Secciones 1-6
Ec. 1.3 escibirla en unidades atómicas y aclarar en pie de página.	pg 3
Adicione celdas a su conveniencia	
Comentarios generales y recomendaciones	

¿Se recomienda proceder con la sustentación oral del Informe Final? (Si/No)	Si

Nombre de quien evalúa	Jorge Mario Osorio Guillén	Jorge M. Osorio Guillén
Identificación	CC 98552686	Firma

DOCTORADO EN CIENCIAS FÍSICAS

EVALUACIÓN DOCUMENTAL DEL INFORME FINAL DE TESIS

(PARTE I)

FECHA	DD	MM	AA		FORMATO PDCF No.	01
	28	05	2019		Actualizado:	Mayo 2016

Título del Informe Final de Tesis

Phase stability of carbon, oxygen and mixtures under extreme P-T conditions, beyond the harmonic approximation

Nombre del (de la) Estudiante	Identificación
Beatriz Helena Cogollo Olivo	1.047.382.037

Grupo de Investigación
Modelado Computacional de sistemas físicos y estadísticos

Línea de Investigación
Física de materiales bajo condiciones extremas

Nombre del Director	Identificación
Javier Montoya Martínez	94.527.774
Nombre del Co-Director	**Identificación**
Sandro Escandolo	

Etapa I. Evaluación del documento escrito

Favor llenar los espacios de color naranja con una calificación que vaya de **0 a 10**, donde 10 equivale a un cumplimiento 100% satisfactorio del criterio de evaluación valorado.

En cada casilla que describe un criterio de evaluación, es recomendado reemplazar el texto guía (en color gris) por las correspondientes justificaciones que considere pertinentes para respaldar la valoración dada.

1.0	Título	
El título está acorde con el estudio		10
2.0	**Introducción**	
Describe un problema concreto y se encuentra contextualizado con la literatura existente		10
3.0	**Fundamentación Teórica**	
Se evidencia una revisión extensa de la literatura relevante y describe de forma clara hallazgos que han sido reportados		10
4.0	**Metodología**	
La investigación es coherente con el problema planteado		9.0
5.0	**Análisis e interpretación de los resultados**	
Los resultados contienen aportes a la ciencia		9.0

6.0	Discusión	
Los resultados son confrontados con trabajos encontrados en la literatura		9.0
7.0	Conclusiones	
Las conclusiones están acorde con los objetivos del proyecto de tesis y reflejan los resultados obtenidos		9.0
8.0	Calidad de la escritura del Informe Final de Tesis	
El documento está escrito de forma clara y precisa, aunque debe mejorarse en la presentación del documento en formato de tesis doctoral		8.0
9.0	Anotaciones Específicas y Calificación	
Fallas de redacción, omisiones, exposición de conceptos, etc.		Páginas o Sección
Adicione celdas a su conveniencia		
Comentarios generales y recomendaciones		
Se anexa documento con correcciones		

¿Se recomienda proceder con la sustentación oral del Informe Final? (Si/No)			Si
Nombre de quien evalúa	Ricardo Vega Monroy		
Identificación	72158788		Firma

DOCTORADO EN CIENCIAS FÍSICAS
EVALUACIÓN SUSTENTACIÓN DEL INFORME FINAL DE TESIS

(PARTE II)

FECHA	DD	MM	AA		FORMATO PDCF No.	01
	28	05	2019		Actualizado:	Mayo 2016

Título del Informe Final de Tesis	
Phase stability of carbon, oxygen and mixtures under extreme P-T conditions, beyond the harmonic approximation	
Nombre del (de la) Estudiante	**Identificación**
Beatriz Helena Cogollo Olivo	1.047.382.037
Grupo de Investigación	
Modelado Computacional de sistemas físicos y estadísticos	
Línea de Investigación	
Física de materiales bajo condiciones extremas	
Nombre del Director	**Identificación**
Javier Montoya Martínez	94.527.774
Nombre del Co-Director	**Identificación**
Sandro Escandolo	

Etapa II. Sustentación del Informe Final de Tesis

Favor llenar los espacios de color naranja con una calificación que vaya de **0 a 10**, donde 10 equivale a cumplimiento satisfactorio del criterio de evaluación valorado. Una o más calificaciones por debajo de 5 pueden utilizarse como justificación para recomendar repetir la sustentación.

En la última casilla (Comentarios y Recomendaciones), es recomendado incluir las correspondientes justificaciones que considere pertinentes para respaldar la valoración dada.

1.0	Buena organización y coherencia entre lo expuesto y el documento escrito del Trabajo Final de Tesis	10
2.0	Claridad en la exposición del Trabajo Final de Tesis.	10
3.0	Demostración de conocimiento de los principios fundamentales involucrados, los métodos y las herramientas utilizados en el desarrollo del Trabajo Final	8
4.0	Manejo apropiado del lenguaje del tema en la línea o área de Investigación	10
5.0	Capacidad de síntesis	8
6.0	Sustentación y coherencia de las respuestas a las preguntas hechas por los asistentes y el jurado en el marco de la exposición	7
7.0	El/La estudiante domina los principios por los cuales los resultados obtenidos respaldan las hipótesis planteadas al inicio de la investigación.	8

8.0	La exposición se mantuvo dentro de los límites de tiempo establecidos	10
9.0	El/La estudiante proporcionó valor agregado a su presentación, es decir, no se limitó a leer las diapositivas presentadas.	10
Comentarios y Recomendaciones		

Nombre de quien evalúa	Jorge Mario Osorio Guillén	
		Jorge M Osorio Guillén
Identificación	98552686	**Firma**

DOCTORADO EN CIENCIAS FÍSICAS

EVALUACIÓN SUSTENTACIÓN DEL INFORME FINAL DE TESIS

(PARTE II)

FECHA	DD	MM	AA		FORMATO PDCF No.	01
	28	05	2019		Actualizado:	Mayo 2016

Título del Informe Final de Tesis	
Phase stability of carbon, oxygen and mixtures under extreme P-T conditions, beyond the harmonic approximation	
Nombre del (de la) Estudiante	**Identificación**
Beatriz Helena Cogollo Olivo	1.047.382.037
Grupo de Investigación	
Modelado Computacional de sistemas físicos y estadísticos	
Línea de Investigación	
Física de materiales bajo condiciones extremas	
Nombre del Director	**Identificación**
Javier Montoya Martínez	94.527.774
Nombre del Co-Director	**Identificación**
Sandro Escandolo	

Etapa II. Sustentación del Informe Final de Tesis

Favor llenar los espacios de color naranja con una calificación que vaya de **0 a 10**, donde 10 equivale a cumplimiento satisfactorio del criterio de evaluación valorado. Una o más calificaciones por debajo de 5 pueden utilizarse como justificación para recomendar repetir la sustentación.

En la última casilla (Comentarios y Recomendaciones), es recomendado incluir las correspondientes justificaciones que considere pertinentes para respaldar la valoración dada.

1.0	Buena organización y coherencia entre lo expuesto y el documento escrito del Trabajo Final de Tesis	10
2.0	Claridad en la exposición del Trabajo Final de Tesis.	10
3.0	Demostración de conocimiento de los principios fundamentales involucrados, los métodos y las herramientas utilizados en el desarrollo del Trabajo Final	9.0
4.0	Manejo apropiado del lenguaje del tema en la línea o área de Investigación	10
5.0	Capacidad de síntesis	10
6.0	Sustentación y coherencia de las respuestas a las preguntas hechas por los asistentes y el jurado en el marco de la exposición	9.0
7.0	El/La estudiante domina los principios por los cuales los resultados obtenidos respaldan las hipótesis planteadas al inicio de la investigación.	9.0

8.0	La exposición se mantuvo dentro de los límites de tiempo establecidos	10
9.0	El/La estudiante proporcionó valor agregado a su presentación, es decir, no se limitó a leer las diapositivas presentadas.	9.0

Comentarios y Recomendaciones

Nombre de quien evalúa	RICARDO VEGA MONROY	
Identificación	72158788	**Firma**

DOCTORADO EN CIENCIAS FÍSICAS

EVALUACIÓN SUSTENTACIÓN DEL INFORME FINAL DE TESIS

(PARTE II)

FECHA	DD	MM	AA		FORMATO PDCF No.	01
	28	05	2019		Actualizado:	Mayo 2016

Título del Informe Final de Tesis	
Phase stability of carbon, oxygen and mixtures under extreme P-T conditions, beyond the harmonic approximation	
Nombre del (de la) Estudiante	**Identificación**
Beatriz Helena Cogollo Olivo	1.047.382.037
Grupo de Investigación	
Modelado Computacional de sistemas físicos y estadísticos	
Línea de Investigación	
Física de materiales bajo condiciones extremas	
Nombre del Director	**Identificación**
Javier Montoya Martínez	94.527.774
Nombre del Co-Director	**Identificación**
Sandro Escandolo	

Etapa II. Sustentación del Informe Final de Tesis

Favor llenar los espacios de color naranja con una calificación que vaya de **0 a 10**, donde 10 equivale a cumplimiento satisfactorio del criterio de evaluación valorado. Una o más calificaciones por debajo de 5 pueden utilizarse como justificación para recomendar repetir la sustentación.

En la última casilla (Comentarios y Recomendaciones), es recomendado incluir las correspondientes justificaciones que considere pertinentes para respaldar la valoración dada.

1.0	Buena organización y coherencia entre lo expuesto y el documento escrito del Trabajo Final de Tesis	10
2.0	Claridad en la exposición del Trabajo Final de Tesis.	10
3.0	Demostración de conocimiento de los principios fundamentales involucrados, los métodos y las herramientas utilizados en el desarrollo del Trabajo Final	9
4.0	Manejo apropiado del lenguaje del tema en la línea o área de Investigación	9
5.0	Capacidad de síntesis	10
6.0	Sustentación y coherencia de las respuestas a las preguntas hechas por los asistentes y el jurado en el marco de la exposición	9
7.0	El/La estudiante domina los principios por los cuales los resultados obtenidos respaldan las hipótesis planteadas al inicio de la investigación.	9

8.0	La exposición se mantuvo dentro de los límites de tiempo establecidos	10
9.0	El/La estudiante proporcionó valor agregado a su presentación, es decir, no se limitó a leer las diapositivas presentadas.	10

Comentarios y Recomendaciones

IT MAY CONSIDER MODIFY THE TITLE TO INCLUDE CO_2 AND EXPAND THE INTRODUTION AND CONCLUSIONS UNDER THE RESULTS (VERY INTERESTING ONES) PEASPECT

THIS WAS A VERY HIGH LEVEL WORK ON HIGH-PRESSURE PHYSICS

Nombre de quien evalúa	CAETANO RODRIGUES MIRANDA	Caetano R. Miranda
Identificación	FM 892258	**Firma**

Contents

Introduction

Daily, we can observe how pressure and temperature have a profound effect on matter. For instance, at ambient pressure water transforms into vapor when heated to 100 °C, and becomes ice when cooled to temperatures below 0 °C. Nonetheless, these transformations can also be achieved starting from the liquid state by reducing or increasing pressure to reach the vapor o solid state, respectively. We can study the phase transitions by minimizing the Gibbs free energy:

$$G = U - ST + pV \tag{0.1}$$

Where U holds for the internal energy, S for the entropy, and V for the volume of the piece of matter under study. According to this expression, solid phases are favored at low temperatures and/or at high pressures, while at opposite conditions gas phases are favored. Liquids are favored at intermediate regimes.

Oxygen is a highly reactive nonmetal and an oxidizing agent that easily forms mixtures with most elements and several other compounds. By mass-fraction, oxygen is the third-most abundant element in the universe, after hydrogen and helium. At ambient conditions, oxygen is a colorless and odorless gas with the molecular formula O_2, where two oxygen atoms are chemically bound to each other with a covalent double bond. At atmospheric pressure and low temperature (below 54.36 K), solid oxygen is formed. Solid oxygen is particularly interesting because it is the only simple diatomic molecule to carry a magnetic moment, and it is considered a "spin-controlled" crystal that displays antiferromagnetic order in the low-temperature phases. At high pressure, solid oxygen transforms from an insulating to a metallic state; and at very low temperatures, it even changes into a superconducting state.

Referred to as the "king of the elements", carbon is a nonmetallic and tetravalent element, that is also the fourth most abundant element in the universe by mass. Because of the four electrons available to form covalent bonds, the atoms of carbon can bond

together in diverse ways, resulting in various allotropes of this element, being the best-known graphite and diamond. This element has attracted attention because of the system of carbon allotropes spans a range of extremes, i.e., graphite is one of the softest materials known, it is opaque and a good conductor of electricity, while diamond is the hardest naturally occurring substance, it is highly transparent and is an excellent electrical insulator.

At elevated temperatures, carbon reacts with oxygen to form oxocarbons or carbon oxides. The simplest and most common oxocarbons are carbon monoxide (CO) and carbon dioxide (CO_2). Carbon dioxide consists of a carbon atom covalently double bonded to two oxygen atoms. CO_2 is characterized by strong double bonds (C=O distance of 1.16 $\mathring{A}$) and rather weak intermolecular interactions, which has made it a very stable system that exhibits several molecular phases before its polymerization. Also at high pressures, another form of solid carbon dioxide is observed: an amorphous glass-like solid named carbonia, that can be produced by supercooling heated CO_2 at pressures above 40 GPa. Although this discovery confirmed that carbon dioxide could exist in a glass state similar to other members of its elemental family, like silicon (silica glass) and germanium dioxide, carbonia glass is not stable at normal pressures and reverts to gas when pressure is released.

Given their importance for life as we know it, carbon and oxygen have been extensively studied at pressures and temperatures found on the surface of the Earth. Nevertheless, despite their simplicity, they exhibit remarkable properties. Their abundance in the universe justifies the attention of the scientific community and explains the constant study of these two elements under extreme conditions. In order to study materials at extreme conditions, i.e., those similar at the interior of planets, experimentalists have designed apparatuses that apply force to a small area where the sample is confined. The diamond anvil cell (DAC) is the most commonly used device and state of the art DACs are able to reach pressures up to 600 GPa, but experiments at these extreme pressures are very challenging. Laser shock-wave experiments are able to reach the terapascal regime for a limited short time. However, along with very high pressures, temperatures of several thousand Kelvin are also achieved, altering the sample's state and making challenging the study of solids at extreme conditions, from the experimental point of view. The technical difficulty and high economical cost of high pressure experiments make theoretical approaches specially necessary. Fortunately, theoretical

approaches allow us to study materials under extreme conditions, since pressure can be monitored by employing the stress tensor of the system using the Hellmann-Feynman theorem from the ground-state energy calculation, or by calculating the total energy of the system at different volumes and then fitting to an equation of state.

In the present thesis report, we present a first-principles analysis of the electronic and vibrational properties of carbon, oxygen and carbon dioxide under high pressure, based on density functional theory. This document consists of two major parts: Part I summarizes the framework used for performing the calculations, and Part II is devoted to the study of carbon, oxygen and carbon dioxide at planetary conditions.

PART I

Theoretical Background

1 Density Functional Theory

Condensed phases of matter, such as solids, liquids, or amorphous, can be described, in a oversimplified way, as an arrangement of atoms that interact with each other. In principle, for non-relativistic systems, it only takes to solve the Schrödinger equation to obtain the properties of a microscopic system. Given the nature of the problem, it is mandatory to use quantum mechanics for an accurate description of the system. Moreover, even if the system is conformed by a few particles, the interaction between these particles creates quantum correlations that make the wave function of the system a complicated object. This is known as the many-body problem. As a result, the expectation of an exact solution of the Schrödinger equation becomes an impractical, or even impossible, task to accomplish. To address these challenges, several approximations at different levels of theory have been proposed for solving this problem.

1.1 The Adiabatic Born-Oppenheimer Approximation

In principle, all the properties of a quantum mechanical system consisting of N electrons and P nuclei of charge and mass Z_I and M_I, respectively, that interact among themselves under the influence of electrostatic forces and in absence of external potentials, can be derived by solving the time-independent Schrödinger equation:

$$\widehat{H}|\Psi_A\rangle = E_A|\Psi_A\rangle, \tag{1.1}$$

where Ψ_A is an eigenstate or wave function with quantum number A and E_A is an eigenvalue corresponding to the energy of the system. Its eigenfunction is given by:

$$\langle \mathbf{r}|\Psi_A\rangle = \Psi_A\left(\mathbf{r}_1, \ldots, \mathbf{r}_N, \mathbf{R}_1, \ldots, \mathbf{R}_P\right) = \Psi_A\left(\mathbf{r}, \mathbf{R}\right), \tag{1.2}$$

where $\mathbf{r} \equiv \mathbf{r}_1 \ldots \mathbf{r}_N$ and $\mathbf{R} \equiv \mathbf{R}_1 \ldots \mathbf{r}_P$ correspond to the set of the N electronic and the P nuclear coordinates, respectively. The Hamiltonian for this non-relativistic system is[1]:

$$
\begin{aligned}
\widehat{H} = &-\sum_{I=1}^{P} \frac{\hbar^2}{2M_I} \nabla_I^2 - \sum_{i=1}^{N} \frac{\hbar^2}{2m_e} \nabla_i^2 + \frac{e^2}{2} \sum_{I=1}^{P} \sum_{J \neq I}^{P} \frac{Z_I Z_J}{|\mathbf{R}_I - \mathbf{R}_J|} + \frac{e^2}{2} \sum_{i=1}^{N} \sum_{j \neq i}^{N} \frac{1}{|\mathbf{r}_i - \mathbf{r}_j|} \\
&- e^2 \sum_{I=1}^{P} \sum_{i=1}^{N} \frac{Z_I}{|\mathbf{R}_I - \mathbf{r}_i|} \\
= &\widehat{T}_I + \widehat{T}_e + \widehat{V}_{I,I} + \widehat{V}_{e,e} + \widehat{V}_{I,e},
\end{aligned}
\tag{1.3}
$$

where the first and second terms of the equation are the nuclear and electronic kinetic energy, $\widehat{T}_I$ and $\widehat{T}_e$, and the last three terms, $\widehat{V}_{I,I}$, $\widehat{V}_{e,e}$, and $\widehat{V}_{I,e}$, account for the nuclei-nuclei, electron-electron, and nuclei-electron Coulomb interactions, respectively.

Thus, it can be noticed that we have to deal with a $3(N+P)$ degrees of freedom problem. Moreover, the Coulomb interaction is the result of pair-wise terms that make impossible to separate the many-body Hamiltonian of equation 1.3 into single-particle ones. In this manner, an analytic solution for macroscopic systems is impossible $(N, M \sim 10^{23})$, therefore the use of approximations is mandatory to tackle this problem. Given the difference between the electron and nuclei masses $(M_I \sim 10^3 m_e)$, it is possible to assume, within the classical scheme, electrons will move much faster than the nuclei, hence every time the nuclei moves, the electrons will adjust their position with respect to the nuclei almost instantaneously. This allows us to treat electrons and nuclei as separate quantum mechanical systems and is the core idea behind the Born-Oppenheimer Approximation [1]. Thus, we can assume that the equation 1.1 can be solved with a factorized wave function that separates the electronic and the nuclear components as follows:

$$
\psi(\mathbf{R}, \mathbf{r}, t) = \sum_{\alpha} \Theta_\alpha(\mathbf{R}, t) \Phi_\alpha(\mathbf{R}, \mathbf{r}).
\tag{1.4}
$$

The evolution of the nuclear motion is described by the $\Theta_\alpha(\mathbf{R}, t)$ wave functions, and

---

[1]From now on, we will use atomic units: $\hbar = e = m_e = 1$. Thus, equation 1.3 becomes: $\widehat{H} = \frac{1}{2} \sum_I^P \frac{\mathbf{P}_I^2}{M_I} + \frac{1}{2} \sum_i^N \mathbf{p}_i^2 + \frac{1}{2} \sum_{I \neq J}^P \frac{Z_I Z_J}{|\mathbf{R}_I - \mathbf{R}_J|} + \frac{1}{2} \sum_{i \neq j}^N \frac{1}{|\mathbf{r}_i - \mathbf{r}_j|} - \sum_I^P \sum_i^N \frac{Z_I}{|\mathbf{R}_I - \mathbf{r}_i|}$

the electronic eigenstates are $\Phi_\alpha(\mathbf{R}, \mathbf{r})$, which depend on the nuclear position only parametrically. Consequently, the total Hamiltonian is separable into nuclear and electronic parts:

$$
\begin{aligned}
\widehat{H} &= \widehat{H}_I + \widehat{H}_e \\
&= \left(\widehat{T}_I + \widehat{V}_{I,I}\right) + \left(\widehat{T}_e + \widehat{U}_{e,e} + \widehat{V}_{I,e}\right),
\end{aligned}
\tag{1.5}
$$

thus, the electronic problem for a set of electronic positions $\mathbf{r}$ that depend on a particular nuclear configuration $\mathbf{R}$ can be solved by means of the time-independent Schrödinger equation:

$$
\widehat{H}_e \Phi_\alpha(\mathbf{R}, \mathbf{r}) = E_\alpha(\mathbf{R}) \Phi_\alpha(\mathbf{R}, \mathbf{r}).
\tag{1.6}
$$

The solution of equation 1.6 is a remarkable approximation for understanding and predicting properties of matter by analyzing their electronic structure and lattice vibrations, such as structural stability, heat capacity and sound velocity. It is important to emphasize that most of the time the analysis are focused on the ground electronic states, given the fact that these states are less complex to deal with than the electronic excited states. In what follows we will not emphasize the study of excited states, because our work does not cover phenomena like electronic transport, optical properties, and photo-dissociation, among others.

1.2   The Hartree and Hartree-Fock Approximations

In the quantum many-body theory finding the ground state of an inhomogeneous system conformed by N particles, i.e. electrons, is one of the most relevant problems. From the electronic Hamiltonian defined in equation 1.5, we can obtain the ground state energy as follows:

$$
E_e = \langle\Phi|\widehat{H}_e|\Phi\rangle = \langle\Phi|\widehat{T}_e + \widehat{U}_{e,e} + \widehat{V}_{I,e}|\Phi\rangle = \langle\Phi|\widehat{T}_e|\Phi\rangle + \langle\Phi|\widehat{V}_{e,e}|\Phi\rangle + \langle\Phi|\widehat{V}_{I,e}|\Phi\rangle, \tag{1.7}
$$

where $|\Phi\rangle$ states as the N-electron ground state wave function, $\widehat{T}_e$ is the electronic kinetic energy, $\widehat{U}_{e,e}$ is the electron-electron interaction, and $\widehat{V}_{I,e}$ corresponds to the electron-nucleus interaction[2]. These terms can be written as:

$$T_e = \langle\Phi|\widehat{T}_e|\Phi\rangle = \frac{1}{2}\sum_{i=1}^{N}\langle\Phi|\nabla_i^2|\Phi\rangle = \frac{1}{2}\int\left[\nabla_i^2\rho_1\left(\mathbf{r},\mathbf{r}'\right)\right]_{\mathbf{r}=\mathbf{r}'}\mathrm{d}\mathbf{r}; \tag{1.8}$$

$$U_{e,e} = \langle\Phi|\widehat{U}_{e,e}|\Phi\rangle = \frac{1}{2}\sum_{i=1}^{N}\sum_{j\neq i}^{N}\langle\Phi|\frac{1}{|\mathbf{r}_i-\mathbf{r}_j|}|\Phi\rangle = \frac{1}{2}\iint\frac{\rho\left(\mathbf{r}\right)\rho\left(\mathbf{r}'\right)}{|\mathbf{r}-\mathbf{r}'|}\mathrm{d}\mathbf{r}\mathrm{d}\mathbf{r}'; \tag{1.9}$$

$$V_{ext} = \langle\Phi|\widehat{V}_{ext}|\Phi\rangle = \sum_{i=1}^{N}\langle\Phi|v_{ext}\left(\mathbf{r}_i\right)|\Phi\rangle = \int v_{ext}\left(\mathbf{r}_i\right)\rho\left(\mathbf{r}\right)\mathrm{d}\mathbf{r}. \tag{1.10}$$

In the electron-electron interaction yields the two-body interaction. A first attempt to deal with this problem, is to consider this interaction as a classical electrostatic interaction. This implies that the electrons are now treated as non correlated particles. Introducing the two-body correlation $g\left(\mathbf{r},\mathbf{r}'\right)$ as:

$$\rho_2\left(\mathbf{r},\mathbf{r}'\right) = \rho\left(\mathbf{r}\right)\rho\left(\mathbf{r}'\right)g\left(\mathbf{r},\mathbf{r}'\right), \tag{1.11}$$

thus, for a classical electrostatic interaction the two-body correlation is not taken into account at all, therefore $g\left(\mathbf{r},\mathbf{r}'\right) = 1$. This is known as the Hartree Approximation. This approximation allows us to rewrite the electron-electron interaction defined in equation 1.9:

$$U_{e,e} = \frac{1}{2}\iint\frac{\rho\left(\mathbf{r}\right)\rho\left(\mathbf{r}'\right)}{|\mathbf{r}-\mathbf{r}'|}\mathrm{d}\mathbf{r}\mathrm{d}\mathbf{r}' = \frac{1}{2}\iint\frac{\rho_2\left(\mathbf{r},\mathbf{r}'\right)}{|\mathbf{r}-\mathbf{r}'|}\mathrm{d}\mathbf{r}\mathrm{d}\mathbf{r}'. \tag{1.12}$$

This approximation ignores many characteristics of the intrinsic nature of electrons, for instance, the effect of the repulsion force produced by two electrons or the fact that electrons are indistinguishable spin-$1/2$ fermions. Therefore, it is mandatory to build a more realistic model of the electron-electron interaction.

---

[2]From now on, $\widehat{V}_{I,e}$ will be written as $\widehat{V}_{ext}$, which is a generalized form of the electron-nucleus interaction.

Repulsion force can be easily included by adding a term that incorporates exchange and correlation effects:

$$U_{e,e} = \frac{1}{2} \iint \frac{\rho_2\left(\mathbf{r}, \mathbf{r}'\right)}{|\mathbf{r} - \mathbf{r}'|} \mathrm{d}\mathbf{r}\mathrm{d}\mathbf{r}' + \frac{1}{2} \iint \frac{\rho_2\left(\mathbf{r}, \mathbf{r}'\right)}{|\mathbf{r} - \mathbf{r}'|} \left[g\left(\mathbf{r}, \mathbf{r}'\right) - 1\right] \mathrm{d}\mathbf{r}\mathrm{d}\mathbf{r}'. \qquad (1.13)$$

On the other hand, we have to redefine the wave-function in such a way that it is anti-symmetric in order to obey Pauli's Exclusion Principle. This can be done by proposing an anti-symmetrical many-body wave function in the form of a Slater determinant. This approach is the Hartree-Fock approximation:

$$\Phi_\alpha^{HF}\left(\mathbf{r}\right) = \frac{1}{\sqrt{N!}} \begin{pmatrix} \varphi_{\alpha_1}\left(\mathbf{r}_1\right) & \varphi_{\alpha_1}\left(\mathbf{r}_2\right) & \cdots & \varphi_{\alpha_1}\left(\mathbf{r}_N\right) \\ \varphi_{\alpha_2}\left(\mathbf{r}_1\right) & \varphi_{\alpha_2}\left(\mathbf{r}_2\right) & \cdots & \varphi_{\alpha_2}\left(\mathbf{r}_N\right) \\ \vdots & \vdots & \ddots & \vdots \\ \varphi_{\alpha_N}\left(\mathbf{r}_1\right) & \varphi_{\alpha_N}\left(\mathbf{r}_2\right) & \cdots & \varphi_{\alpha_N}\left(\mathbf{r}_N\right) \end{pmatrix}, \qquad (1.14)$$

where $\varphi_{\alpha_i}\left(\mathbf{r}_j\right)$ is the jth one-electron wave-function at the α_i^{th} state. This is the result of Hartree's assumption that the many-electron wave function can be expressed as a product of one-electron orbitals. Although the determinant in equation 1.14 satisfies Pauli's Exclusion Principle, there is still the lack of the correlation term that arises from the interaction between electrons. However, it is important to highlight that despite the fact that neglecting the electron-electron interaction is indeed a very crude approach, solving a single-body problem is much more easier than a many-body one. This is the reason why several mean field theories have been proposed for dealing the many-body electron-electron pair-potential into a single-body operator that behaves as an external potential, like the electron-nuclei interaction.

1.3   The Hohenberg-Kohn Theorems

Two main approaches were developed for understanding the interacting electron gas. The first one treated the electrons as non-interacting particles that exhibit collective excitations [2]. The other one, known as the Thomas-Fermi method [3, 4], defines

the atom as an ensemble of an negatively charged cloud, that is made of uniformly distributed electrons, around a nuclei that is characterized by its spatial coordinates and momentum, i.e. a six-dimensional phase space, in which the total energy of the system could be represented as a functional of the electronic density $n_\alpha(\mathbf{r})$.

In the early beginnings of Density Functional Theory (DFT), Hohenberg and Kohn [5] proved that there exits an universal functional of the density $F[n_\alpha(\mathbf{r})]$ that allow us to calculate the ground-state energy $E_{\alpha=0}[n_{\alpha=0}(\mathbf{r})]$ associated with a certain external potential $V_{ext}(\mathbf{r})$. The core of DFT lies on the two theorems proposed by Hohenberg and Kohn [5, 6]:

THEOREM 1:   *For any system of interacting particles in an external potential* $V_{\text{ext}}(\mathbf{r})$, *the potential* $V_{\text{ext}}(\mathbf{r})$ *is determined uniquely, except for a constant, by the ground state particle density* $n_{\alpha=0}(\mathbf{r})$.

PROOF:

Let's suppose two different external potentials $V_{ext}^1(\mathbf{r})$ and $V_{ext}^2(\mathbf{r})$ which differ by more than a constant. Each potential leads to a different Hamiltonian, namely $\widehat{H}^1$ and $\widehat{H}^2$, which have different ground state wave functions $\psi_{\alpha=0}^1$ and $\psi_{\alpha=0}^2$, which are hypothesized to have the same ground state density $n_{\alpha=0}(\mathbf{r})$. Since $\psi_{\alpha=0}^2$ is not the ground state of $\widehat{H}^1$, we have:

$$E_{\alpha=0}^1 = \langle \psi_{\alpha=0}^1 | \widehat{H}^1 | \psi_{\alpha=0}^1 \rangle < \langle \psi_{\alpha=0}^2 | \widehat{H}^1 | \psi_{\alpha=0}^2 \rangle.$$

Rewriting $\langle \psi_{\alpha=0}^2 | \widehat{H}^1 | \psi_{\alpha=0}^2 \rangle$:

$$\langle \psi_{\alpha=0}^2 | \widehat{H}^1 | \psi_{\alpha=0}^2 \rangle = \langle \psi_{\alpha=0}^2 | \widehat{H}^2 | \psi_{\alpha=0}^2 \rangle + \langle \psi_{\alpha=0}^2 | \widehat{H}^1 - \widehat{H}^2 | \psi_{\alpha=0}^2 \rangle$$
$$= E_{\alpha=0}^2 + \int n_{\alpha=0}(\mathbf{r}) \left[V_{ext}^1(\mathbf{r}) - V_{ext}^2(\mathbf{r}) \right] d\mathbf{r}.$$

Replacing into the first expression:

$$E_{\alpha=0}^1 < E_{\alpha=0}^2 + \int n_{\alpha=0}(\mathbf{r}) \left[V_{ext}^1(\mathbf{r}) - V_{ext}^2(\mathbf{r}) \right] d\mathbf{r}.$$

Repeating the same procedure for $E_{\alpha=0}^2$ we obtain:

$$E_{\alpha=0}^2 < E_{\alpha=0}^1 + \int n_{\alpha=0}(\mathbf{r}) \left[V_{ext}^2(\mathbf{r}) - V_{ext}^1(\mathbf{r}) \right] d\mathbf{r}.$$

Adding the two inequalities we finally get:

$$E_{\alpha=0}^1 + E_{\alpha=0}^2 < E_{\alpha=0}^1 + E_{\alpha=0}^2.$$

Since this result does not make any sense, it can be concluded that is not possible that two different potentials can lead to the same ground state density. Additionally, since the Hamiltonian is fully determined, all the many-body wave functions for the ground and excited states are also determined. Thus, if only the ground state density $n_{\alpha=0}(\mathbf{r})$ is given, it is possible to determine all the properties of the system.

THEOREM 2:   *An universal functional for the energy* $\mathrm{E}_\alpha\left[\mathrm{n}_\alpha\left(\mathbf{r}\right)\right]$ *in terms of the density* $\mathrm{n}_\alpha\left(\mathbf{r}\right)$ *can be defined, valid for any external potential* $\mathrm{V}_{\mathrm{ext}}\left(\mathbf{r}\right)$. *For any particular* $\mathrm{V}_{\mathrm{ext}}\left(\mathbf{r}\right)$, *the exact ground state* $(\alpha = 0)$ *energy of the system is the global minimum value of this functional and the density* $\mathrm{n}_\alpha\left(\mathbf{r}\right)$ *that minimizes the functional is the exact ground state* $\mathrm{n}_\alpha\left(\mathbf{r}\right)$.

PROOF:

If $\mathrm{n}_\alpha\left(\mathbf{r}\right)$ is specified all the properties of the system can be uniquely determined, therefore the total energy functional can be expressed as:

$$E_\alpha^{HK}\left[n_\alpha\left(\mathbf{r}\right)\right] = T_e\left[n_\alpha\left(\mathbf{r}\right)\right] + U_{e,e}\left[n_\alpha\left(\mathbf{r}\right)\right] + \int n_\alpha\left(\mathbf{r}\right)V_{ext}\left(\mathbf{r}\right)d\mathbf{r}$$

$$= F^{HK}\left[n_\alpha\left(\mathbf{r}\right)\right] + \int n_\alpha\left(\mathbf{r}\right)V_{ext}\left(\mathbf{r}\right)d\mathbf{r}.$$

Let's consider a system with ground state density $\mathrm{n}_\alpha^1\left(\mathbf{r}\right)$, which corresponds to the potential $\mathrm{V}_{\mathrm{ext}}^1\left(\mathbf{r}\right)$. The Hohenberg-Kohn functional $\left(F^{HK}\left[n_\alpha\left(\mathbf{r}\right)\right]\right)$ is equal to the expectation value of the Hamiltonian in the unique ground state that has wave function ψ_α^1.

$$E_\alpha^1 = \langle\psi_\alpha^1|\widehat{H}^1|\psi_\alpha^1\rangle.$$

Now, if we consider a different density $\mathrm{n}_\alpha^2\left(\mathbf{r}\right)$, corresponding to a different wave function ψ_α^2, we obtain;

$$E_\alpha^2 = \langle\psi_\alpha^2|\widehat{H}^1|\psi_\alpha^2\rangle > \langle\psi_\alpha^1|\widehat{H}^1|\psi_\alpha^1\rangle = E_\alpha^1.$$

Therefore, for any density $\mathrm{n}_\alpha\left(\mathbf{r}\right)$ different from the ground state density $\mathrm{n}_{\alpha=0}\left(\mathbf{r}\right)$, the energy evaluated by $F^{HK}\left[n_\alpha\left(\mathbf{r}\right)\right]$ is greater.

Thus, the universal functional $F^{HK}[n_\alpha(\mathbf{r})]$ does not depend explicitly on the external potential, but on the electronic density of the system. Moreover, this functional is sufficient to determine the exact solution of the full many-body Schrödinger equation, and consequently its ground state energy and density.

1.4   The Kohn-Sham Equations

In order to implement DFT, Kohn and Sham [7] proposed a practical approach based on separating the different energy contributions: the many-body problem is replaced with an auxiliary system that is easier to solve. This new system, contrary to the interacting electronic system, is a non-interacting one that would have the exactly same ground state density. This implies, that the Hamiltonian of the non-interacting electronic system is now separable:

$$H_e(\mathbf{r}) = \sum_{i=1}^{N}\left[-\frac{\hbar^2}{2m}\nabla_{\mathbf{r}_i}^2 + V^{KS}(\mathbf{r}_i)\right] = \sum_{i=1}^{N} H^{KS}(\mathbf{r}_i). \qquad (1.15)$$

Here $V^{KS}(\mathbf{r}_i)$ is the reference potential in which the ground state density of $H^e(\mathbf{r})$ equals $n_\alpha(\mathbf{r})$, and the Hohenberg-Kohn's theorem ensures the equivalence between the ground state energy and the energy of the non-interacting system. The total Kohn-Sham state $|\psi_\alpha^{KS}\rangle$ of the non-interacting electrons is exactly described by an anti-symmetrized wave function of the Slater determinant type, made of one-electron orbitals. The Kohn-Sham one-electron states of the one-electron states $|\phi_{\alpha_i}\rangle$ satisfy:

$$H^{KS}|\phi_{\alpha_i}\rangle = \epsilon_{\alpha_i}|\phi_{\alpha_i}\rangle. \qquad (1.16)$$

Moreover, the density can be written in terms of the single-particle wave functions:

$$n_\alpha(\mathbf{r}) = \sum_{i=1}^{N}|\phi_{\alpha_i}(\mathbf{r})|^2. \qquad (1.17)$$

From the second theorem of Hohenberg-Kohn, the electronic energy functional can

be written as:

$$E^e[n_\alpha] = T_e[n_\alpha] + E_{e,e}[n_\alpha] + E_{ext}[n_\alpha], \tag{1.18}$$

where $E_{ext}[n_\alpha]$ corresponds to the electron-nuclei interaction energy:

$$E_{ext}[n_\alpha] = \int d\mathbf{r}\, n_\alpha(\mathbf{r})\, V_{ext}(\mathbf{r}). \tag{1.19}$$

However the first two terms of equation 1.18 cannot be expressed in a straightforward form as the third one. Then, it is necessary to determine the non-interacting kinetic energy $T_e^{KS}[n_\alpha]$:

$$\begin{aligned}
T_e^{KS}[n_\alpha] &= \langle \psi_\alpha^{KS}|T_e|\psi_\alpha^{KS}\rangle \\
&= -\frac{1}{2}\sum_{i=1}^{N}\langle \phi_{\alpha_i}|\nabla^2|\phi_{\alpha_i}\rangle = -\frac{1}{2}\sum_{i=1}^{N}\int d\mathbf{r}\,\phi_{\alpha_i}^*(\mathbf{r})\,\nabla^2\phi_{\alpha_i}(\mathbf{r}).
\end{aligned} \tag{1.20}$$

It is important to point out that the density dependence of $T_e^{KS}[n_\alpha]$ is implicit and comes from the density dependence of the single-electron wave functions ϕ_{α_i}. Nevertheless, the expression derived in equation 1.20 is not the exact kinetic energy of the interacting system. The error arises due to the lack of the correlation contribution to the kinetic energy and it comes from the fact that the true many-body wave function is not a Slater determinant. A similar procedure is followed to determine $E_{e,e}^{KS}[n_\alpha]$:

$$\begin{aligned}
E_{e,e}^{KS}[n_\alpha] &= \langle \psi_\alpha^{KS}|E_{e,e}|\psi_\alpha^{KS}\rangle \\
&= E_H[n_\alpha] + E_X[n_\alpha],
\end{aligned} \tag{1.21}$$

where:

$$E_H[n_\alpha] = \frac{1}{2}\iint d\mathbf{r}d\mathbf{r}'\frac{n_{\alpha_i}(\mathbf{r})\,n_{\alpha_i}(\mathbf{r}')}{|\mathbf{r}-\mathbf{r}'|}, \tag{1.22}$$

is the Hartree energy and corresponds to the self-interaction of the electronic density, and:

$$E_X[n_\alpha] = -\frac{1}{2}\sum_{i,j}\iint d\mathbf{r}d\mathbf{r}' \frac{\phi_{\alpha_i}^*(\mathbf{r})\,\phi_{\alpha_i}(\mathbf{r}')\,\phi_{\alpha_j}^*(\mathbf{r})\,\phi_{\alpha_j}(\mathbf{r}')}{|\mathbf{r}-\mathbf{r}'|}, \tag{1.23}$$

is the electronic exchange energy which accounts for the antisymmetric nature of the wave function. As it happened for $T_e^{KS}[n_\alpha]$, $E_{e,e}^{KS}[n_\alpha]$ lacks of the correlation contribution to the electron-electron energy. Taking this correlation terms into account, we can rewrite the total energy functional from equation 1.18 as:

$$E^e[n_\alpha] = T_e^{KS}[n_\alpha] + E_H[n_\alpha] + E_X[n_\alpha] + E_{ext}[n_\alpha] + T_C[n_\alpha] + E_{e,e,C}[n_\alpha]. \tag{1.24}$$

Given the nature of the problem, the only way to obtain the exact correlation contribution is by solving the many-body Schrödinger equation, therefore mean field theories such DFT the correlation terms are approximated to some degree. Additionally, given the difficulty of evaluate $E_X[n_\alpha]$ in comparison with $T_e^{KS}[n_\alpha]$, $E_H[n_\alpha]$, and $E_{ext}[n_\alpha]$, it is a common approach to approximate the exchange energy as well. Thus, grouping the terms that are approximate, we obtain the exchange and correlation term $E_{xc}[n_\alpha]$, leading to the final form of the total energy functional:

$$E^e[n_\alpha] = T_e^{KS}[n_\alpha] + E_H[n_\alpha] + E_{ext}[n_\alpha] + E_{xc}[n_\alpha]. \tag{1.25}$$

If we know the functional $E_{xc}[n_\alpha]$, then the exact ground state energy and density of the many-body problem could be found by solving the Kohn-Sham equations for a non-interacting system.

1.5   LDA and GGA Exchange-Correlation Functionals

Many E_{xc} functional have been proposed in the past years, however the most famous approximation is the Local Density Approximation (LDA). LDA was first formally introduced by Kohn and Sham [7], although the idea behind this approximation was already used by Thomas, Fermi and Dirac in their theory. The approach of LDA assumes the exchange-correlation energy contribution $E_{xc}^{LDA}[n]$ as a functional of the ground state energy. The inhomogeneous electronic system is considered as a locally homogeneous electron gas in which the exchange-correlation hole can be calculated at every point $\mathbf{r}$ with electronic density $[n_{\alpha}]$ accurately, and its energy can be written in terms of the average energy of the homogeneous electron gas $\epsilon_{xc}^{HEG}[n(\mathbf{r})]$ [8], where the energy remains constant throughout space[3]:

$$E_{xc}^{LDA}[n] = \int d\mathbf{r}\, n(\mathbf{r})\, \epsilon_{xc}^{HEG}[n(\mathbf{r})]. \tag{1.26}$$

In practice, $\epsilon_{xc}^{HEG}[n(\mathbf{r})]$ is parametrized as $\epsilon_{xc}^{HEG}[n(\mathbf{r})] \equiv \epsilon_{xc}^{LDA}[n(\mathbf{r})] = \epsilon_{x}^{LDA}[n(\mathbf{r})] + \epsilon_{c}^{LDA}[n(\mathbf{r})]$, where the calculation of the correlation term depends on the nature of the density of the system, therefore several parametrizations of this term have been carried out [9, 10, 11, 12, 13, 14, 15]. On the other hand, exchange term is computed as:

$$\epsilon_{x}^{LDA}[n] = -\frac{3}{4}\left(\frac{3}{\pi}\right) n^{1/3}. \tag{1.27}$$

Despite its simplicity, LDA has proven to behave better than expected and is still used today. However, major issues such as its failure for dealing systems which inhomogeneities are high or the overestimation of binding energies, and consequently the underestimation of the bond lengths, have motivated the develop of semilocal approximations that try to take into account the inhomogeneities in the electronic density. This is done within the Generalized Gradient Approximation (GGA) scheme, where non-local terms are included in order to introduce a correction with the gradient of the density:

---

[3]For simplicity, we drop the $\alpha = 0$ indices.

$$E_{xc}^{GGA}[n] = \int d\mathbf{r} \, n(\mathbf{r}) \, \epsilon_{xc}[n(\mathbf{r}), |\nabla n(\mathbf{r})|]. \tag{1.28}$$

Over the years several gradient expansions have been proposed [16, 17, 18] and they have marked an improvement over LDA in different aspects such as binding energies, atomic energies, bond lenghts, and angles. For this work, our calculations were performed using the PBE (PBE) [18] parametrization of the E_{xc}:

$$E_{xc}^{PBE}[n] = E_x^{PBE}[n] + E_c^{PBE}[n]. \tag{1.29}$$

The exchange energy $E_x^{PBE}[n]$ in the PBE functional has the form:

$$E_x^{PBE}[n] = \int d\mathbf{r} \, [n] \, \epsilon_x^{LDA}[n(\mathbf{r})] \, F_x(s), \tag{1.30}$$

where $\epsilon_x^{LDA}[n(\mathbf{r})]$ is the same used in LDA (equation 1.27). $F_x(s)$ introduces the gradient correction to the density:

$$F_x(s) = 1 + \kappa - \frac{\kappa}{1 + \mu s^2/\kappa}, \tag{1.31}$$

with $s = \frac{|\nabla n|}{6n^{3/4}}$ and $\kappa \leq 0.804$. On the other hand, the correlation term $E_c^{PBE}[n]$ has the form:

$$E_c^{PBE}[n] = \int d\mathbf{r} \, n(\mathbf{r}) \left(\epsilon_c^{LDA}[n(\mathbf{r})] + H[n(\mathbf{r}), \zeta, t] \right), \tag{1.32}$$

where $\epsilon_c^{LDA}[n(\mathbf{r})]$ is the correlation contribution to the energy from LDA. $H[n(\mathbf{r}), \zeta, t]$ is built as:

$$H[n(\mathbf{r}), \zeta, t] = \gamma \phi^3 \ln \left[1 + \frac{\beta}{\gamma} t^2 \left(\frac{1 + At^2}{1 + At^2 + A^2 t^4} \right) \right]. \tag{1.33}$$

Here, $\phi = \left[(1 + \zeta)^{2/3} - (1 - \zeta)^{2/3} \right]/2$ is a spin-scaling factor with magnetization density ζ. The density gradient parameter is defined as $t = |\nabla n|/2\phi k_s n$, where k_s is the Thomas-Fermi screening wave number. $\gamma = [1 - \ln(2)]/\pi^2$ and the function A has

the following form:

$$A = \frac{\beta}{\gamma} \left[e^{-\epsilon_c^{LDA}[n]/\left(\gamma\phi^3\right)} - 1 \right].$$

(1.34)

Finally, the parameter μ introduced in the equation 1.31 is related to β via:

$$\mu = \frac{\pi^2}{3}\beta.$$

(1.35)

2   Electronic Structure

Condensed phases in general are macroscopic objects that are made up of a immense number of atoms, of the order of Avogadro's number ($\sim 6 \times 10^{23}$). In a microscopic scale, crystalline solids can be effectively treated as infinite by means of a basis constituted by a few atoms that is replicated periodically uninterruptedly along one, two, or three directions in space. Bloch's theorem is used to take advantage of the periodicity of the system, making the analysis and its implementation, much easier.

The methodological efforts also include different types of representation of the non-valence electrons, in an attempt to describe the electron wave functions in an accurate, yet computationally favorable way. This is achieved with pseudopotentials and other related techniques, such as the projector augmented wave method.

2.1   Bloch's Theorem and Plane-Wave Basis Sets

In a perfect crystal, the ions are arranged in a regular, periodic array, that is characterized by a Bravais lattice, whose position vectors $\mathbf{R}$ are of the form:

$$\mathbf{R} = n_1 \mathbf{a}_1 + n_2 \mathbf{a}_2 + n_3 \mathbf{a}_3, \tag{2.1}$$

where n_i and $\mathbf{a}_i$ are integers and the primitive lattice vectors (not all in the same plane), respectively. For a deeper understanding of periodic structures, it is necessary introduce the reciprocal lattice, which can be constructed from the three primitive vectors:

$$\mathbf{b}_1 = 2\pi \frac{\mathbf{a}_2 \times \mathbf{a}_3}{\mathbf{a}_1 \cdot (\mathbf{a}_2 \times \mathbf{a}_3)}, \quad \mathbf{b}_2 = 2\pi \frac{\mathbf{a}_1 \times \mathbf{a}_1}{\mathbf{a}_1 \cdot (\mathbf{a}_2 \times \mathbf{a}_3)}, \quad \mathbf{b}_3 = 2\pi \frac{\mathbf{a}_1 \times \mathbf{a}_2}{\mathbf{a}_1 \cdot (\mathbf{a}_2 \times \mathbf{a}_3)}. \tag{2.2}$$

The primitive vectors of the reciprocal lattice must satisfy $\mathbf{b}_i \cdot \mathbf{a}_j = 2\pi\delta_{ij}$, where $\delta_{ij} = 0, \quad i \neq j$ and $\delta_{ij} = 1, \quad i = j$. Now, any vector $\mathbf{k}$ can be written as a linear combination of the $\mathbf{b}_i$:

$$\mathbf{G} = m_1\mathbf{b}_1 + m_2\mathbf{b}_2 + m_3\mathbf{b}_3. \tag{2.3}$$

Due to the periodic structure of a crystal lattice the Hamiltonian is periodic, thus for any $\mathbf{R}$:

$$H^e(\mathbf{r}) = H^e(\mathbf{r} + \mathbf{R}). \tag{2.4}$$

Which also holds for any effective single-electron Hamiltonian and potential, and keeping the same notation are $H^{KS}(\mathbf{r})$ and $V^{KS}(\mathbf{r})$, respectively. Bloch's theorem [19] states that the single-electron solutions must be of the following form:

$$\phi_{n\mathbf{k}}(\mathbf{r}) = e^{i\mathbf{k}\cdot\mathbf{r}}u_{n\mathbf{k}}(\mathbf{r})$$
$$\phi_{n\mathbf{k}}(\mathbf{r} + \mathbf{R}) = e^{i\mathbf{k}\cdot\mathbf{R}}\phi_{n\mathbf{k}}(\mathbf{r}), \tag{2.5}$$

where $u_{n\mathbf{k}}(\mathbf{r})$ has the periodicity of the lattice, n is a band index, and $\mathbf{k}$ is the wave vector of the electron. Several methods have been proposed to solve the Kohn-Sham equations in periodic systems, such as pseudopotentials and the projector augmented wave method (PAW), which will be explained in the following sections.

2.2   Pseudopotentials

We consider *valence electrons*[4] to be those outside of a closed shell configuration. The s and p electrons are usually considered valence electrons, since they are responsible for bonding. This is why, in some cases, it is more convenient to treat valence electrons and core electrons separately, being these *core electrons* those that are tightly bound to the nuclei and are not involved in chemical bonding. Therefore, one can neglect the

---

[4]Although all electrons are the same, this language abuse is used to indicate single-particle electronic states, rather than electrons themselves.

consequences of core electrons in the valence electrons' wave functions by treating the first ones as frozen orbitals. The effective core potential, or pseudopotential, represents the nucleus with its core electrons and it reduces significantly the number of degrees of freedom of the electron gas, because the number of electrons that are treated explicitly is smaller, therefore the amount of computational resources that are need decreases as well.

Once the wave functions inside the core region can be neglected, these can be replaced with a smooth, nodeless function $\check{\psi}_i(\mathbf{r})$ that outside the cutoff radius R_c, coincides with the all-electron wave function $\psi_i(\mathbf{r})$. Thus, the pseudo-wave function $\tilde{\psi}_i(\mathbf{r})$ is constructed as follows and it is shown in figure 2.1.

$$\tilde{\psi}_i(\mathbf{r}) = \begin{cases} \check{\psi}_i(\mathbf{r}) & \text{, for } |\mathbf{r}| < R_c \\ \psi_i(\mathbf{r}) & \text{, for } |\mathbf{r}| \leq R_c. \end{cases} \tag{2.6}$$
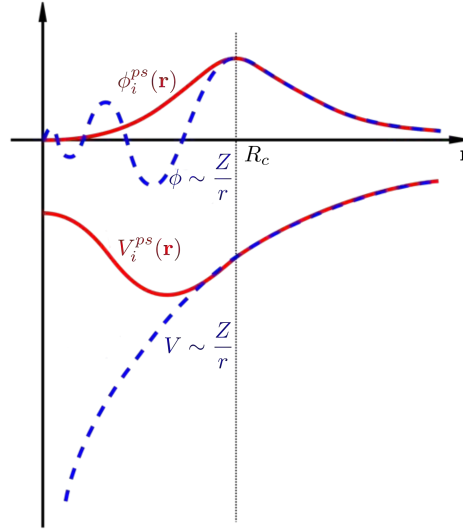

Figure 2.1: Schematic illustration of all-electron (blue, dashed lines) and a pseudoelectron (red, solid lines) potentials and their corresponding wave functions. The radius at which all-electron and pseudoelectron values match is the cutoff core radius R_c (black, dotted line).

The pseudopotential approximation has established itself as an accurate method for studying structural properties in solids, despite the inevitable (sometimes large) deviations from the experimental values, which are caused by the density functional method used and not the by use of the pseudopotential approximation [20]. However,

when core-valence correlation or-overlap effects, among others, become relevant it is then necessary to reevaluate the use of pseudopotentials. For instance, in the theoretical study of materials under high-pressure it is mandatory to have certainty that the valence densities of the neighbouring atoms do not penetrate significantly into the core region of the atom carrying a pseudopotential. In cases like that, single-point all-electron calculations at the optimized pseudopotential geometry are advisable.

2.3   Projector Augmented Wave Method

The implementation of the Projector Augmented Wave (PAW) method [21] overcomes deficiencies of the pseudopotential method for dealing with d and f orbitals. Near the ion core, the wave function oscillates rapidly (see figure 2.1, blue dotted line) and this implies that a very fine mesh is required to describe the wave functions accurately- The PAW approach deals with these oscillatory wave functions by transforming them into smooth wave functions and providing a way to compute the all-electron properties from them.

Let's consider an atom a enclosed within some atom-specific augmentation region $|\mathbf{r}-\mathbf{R}| < r_c^a$, where r_c^a is the cutoff radius of that region. The all-electron wave function[5] is related to a pseudo-wave function as:

$$|\psi_i\rangle = \hat{\mathcal{T}}|\tilde{\psi}_i\rangle. \tag{2.7}$$

It is important to remember that after a certain distance from the core, the true wave function is already smooth, therefore, $\hat{\mathcal{T}}$ should modify it in the region near the nuclei:

$$\hat{\mathcal{T}} = 1 + \sum_a \hat{\mathcal{T}}^a, \tag{2.8}$$

---

[5]The all-electron wave function corresponds to the Kohn-Sham single particle wave function and it should not be confused with the many-body wave function.

thus, the effect of $\hat{\mathcal{T}}^a$ is limited to the augmentation region.

In the augmentation region, and around each atom a, it is convenient to expand the pseudo-wave function into pseudo-partial waves:

$$
\begin{aligned}
|\phi_n^a\rangle &= \left(1 + \hat{\mathcal{T}}^a\right)|\tilde{\phi}_n^a\rangle \\
&= |\tilde{\phi}_n^a\rangle + \hat{\mathcal{T}}^a|\tilde{\phi}_n^a\rangle \implies \hat{\mathcal{T}}^a|\tilde{\phi}_n^a\rangle = |\phi_n^a\rangle - |\tilde{\phi}_n^a\rangle.
\end{aligned}
\tag{2.9}
$$

Outside the augmentation region $\hat{\mathcal{T}}^a$ should be doing nothing, implying that $\phi_n^a(\mathbf{r}) = \tilde{\phi}_n^a(\mathbf{r})$. Inside the augmentation region the partial waves form a complete set, therefore we can expand the pseudo-wave functions as:

$$
|\tilde{\psi}_i\rangle = \sum_n c_n |\tilde{\phi}_n^a\rangle.
\tag{2.10}
$$

Given the linear nature of the $\hat{\mathcal{T}}^a$ operator, the coefficients c_n can then be written as an inner product with a set of projector functions $|\tilde{p}_n^a\rangle$:

$$
c_n = \langle \tilde{p}_n^a | \tilde{\psi}_i\rangle.
\tag{2.11}
$$

The projector must be localized within its own augmentation region. Additionally, since the augmentation spheres do not overlap, we expect to one center expansion of the smooth wave function $|\tilde{\psi}_i^a\rangle = \sum_n |\tilde{\phi}_n^a\rangle\langle\tilde{p}_n^a|\tilde{\psi}_i\rangle$ to reduce to $|\tilde{\psi}_i\rangle$ itself inside the augmentation sphere. Therefore, the smooth projector function must satisfy the following condition inside the augmentation sphere:

$$
\sum_n |\tilde{\phi}_n^a\rangle\langle\tilde{p}_n^a| = 1.
\tag{2.12}
$$

This also implies that the projector functions should be orthonormal to the smooth partial waves inside the augmentation sphere:

$$
\langle \tilde{p}_{n_1}^a | \tilde{\phi}_{n_2}^a\rangle = \delta_{n_1,n_2}, \, for |\mathbf{r} - \mathbf{R}| < r_c^a.
\tag{2.13}
$$

Using the completeness relation (equation 2.12) and equation 2.9, into $\hat{\mathcal{T}}^a$ we have

that:

$$\hat{\mathcal{T}}^a = \sum_n \hat{\mathcal{T}}^a |\tilde{\phi}_n^a\rangle\langle\tilde{p}_n^a| = \sum_n \left(|\phi_n^a\rangle - |\tilde{\phi}_n^a\rangle\right)\langle\tilde{p}_n^a|. \tag{2.14}$$

Taking into account that outside the augmentation region $\hat{\mathcal{T}} = 1$ and $\phi_n^a\left(\mathbf{r}\right) - \tilde{\phi}_n^a\left(\mathbf{r}\right) = 0$, we can rewrite equation 2.8 as:

$$\hat{\mathcal{T}} = 1 + \sum_a \sum_n \left(|\phi_n^a\rangle - |\tilde{\phi}_n^a\rangle\right)\langle\tilde{p}_n^a|. \tag{2.15}$$

Replacing $\hat{\mathcal{T}}$ into equation 2.7 we can then obtain the complete wave function in the PAW formalism:

$$\begin{aligned}
|\psi_i\rangle &= \left[1 + \sum_a \sum_n \left(|\phi_n^a\rangle - |\tilde{\phi}_n^a\rangle\right)\langle\tilde{p}_n^a|\right]|\tilde{\psi}_i\rangle \\
&= |\tilde{\psi}_i\rangle + \sum_a \sum_n \langle\tilde{p}_n^a|\tilde{\psi}_i\rangle\left(|\phi_n^a\rangle - |\tilde{\phi}_n^a\rangle\right).
\end{aligned} \tag{2.16}$$

2.4   Computational Method

Our electronic structure calculations were carried out using the software suite `Quantum ESPRESSO` [22, 23]. The self-consistent calculation for the electronic energy is described in the following flowchart:

The initial wave function guess is built by the superposition of the individual atom's valence electron wavefunctions. This density allows us to construct the V^{KS} potential, and consequently solve the Kohn-Sham eigenvalue equation (1.16). The new eigenfunctions provide a new electronic density to start over a new cycle. The calculation stops when a convergence value (defined by the user at the beginning of the calculation) is reached for the total energy.

In order to obtain the exact Kohn-Sham state an infinite number of plane waves are
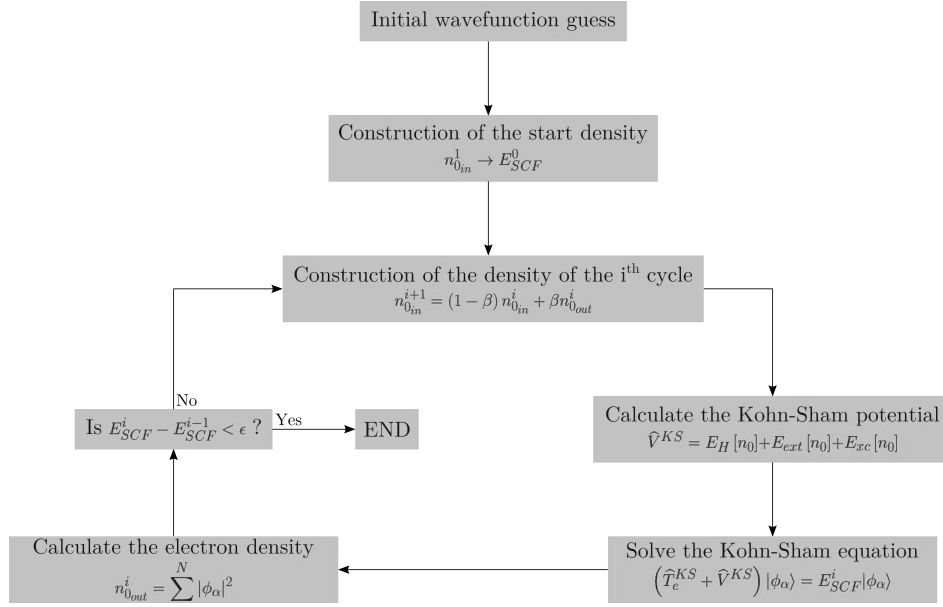
Figure 2.2: Reduced flowchart of the self-consistent sequence for solving the Kohn-Sham equation. $|\Delta E|$ is the difference between two consecutive self-consistent cycles and ϵ is the chosen threshold.

need. As this is, in practical terms, impossible, one must fix an energy cutoff for the plane waves: $E_{cutoff} \geq 1/2|\mathbf{k} + \mathbf{G}|$. This value determines the number of $\mathbf{G}$ vectors in the expansion that satisfy the desired accuracy of the electronic energy. Additionally, the number of $\mathbf{k}$ vectors in the first Brillouin zone for an ideal crystal is also infinite. Instead, a Monkhorst-Pack grid [24] is chosen and optimized. Both, E_{cutoff} and $\mathbf{k}$ points grid, depends on both the system to analyze and the pseudopotentials used. Finally, for a better and faster convergence in metallic systems, a smeared function is introduced for calculating the ground state density. This was done by introducing a low electronic temperature using the Fermi-Dirac smearing function.

3   The Nuclear Problem

The adiabatic Born-Oppenheimer approximation makes a distinction between the motion of the electrons and the nuclei, thus, leaving us with two equations to solve. So far, we have shown the way of solving the first equation, corresponding to the electronic part. Although many properties of solids are directly related to the electronic degrees of freedom, many others, such as superconductivity and thermal conductivity, originate from the nuclear motion. The nuclear Schrödinger equation (1.5) holds the information about the ionic motion, and it is solved for the electronic ground state ($\alpha = 0$).

3.1   The Harmonic Approximation

In a crystal structure, its equilibrium lattice sites correspond to the positions of the ions at the local minimum of the Born-Oppenheimer energy surface. From now on, the nuclear positions are not fixed parameters any longer, therefore, we can now define the position of an ion s that has a displacement u from its equilibrium position as:

$$\mathbf{R}_s = \mathbf{R}_s^0 + \mathbf{u}_s. \tag{3.1}$$

In order to know about the nuclear motion, and the physical properties related with it, we can calculate the contribution of atomic vibrations to the free energy of the system trough the harmonic approximation (HA). The goal in this approximation is to find the normal modes of a crystal by calculating the energies (or frequencies) of the non-interacting phonons as a function of their wave vectors $\mathbf{q}$. This approximation relies on the following two assumptions [25]:

- The displacements of the atoms are small and around their equilibrium positions.

- The interatomic potential $U(\mathbf{R})$ can be expanded in a Taylor series and we keep only its quadratic term.

In fact, according to the second condition we have:

$$U(\mathbf{R}) = U(\mathbf{R^0}) + \sum_{msl} \left.\frac{\partial U}{\partial u_{ms}^l}\right|_{\mathbf{R^0}} u_{ms}^l + \frac{1}{2}\sum_{msl}\sum_{m's'l'} \left.\frac{\partial^2 U}{\partial u_{ms}^l \partial u_{m's'}^{l'}}\right|_{\mathbf{R^0}} u_{ms}^l u_{m's'}^{l'}$$
$$+ \frac{1}{6}\sum_{msl}\sum_{m's'l'}\sum_{m''s''l''} \left.\frac{\partial^3 U}{\partial u_{ms}^l \partial u_{m's'}^{l'} \partial u_{m''s''}^{l''}}\right|_{\mathbf{R^0}} u_{ms}^l u_{m's'}^{l'} u_{m''s''}^{l''} + (\dots),$$

(3.2)

where m runs up to the the number of $\mathbf{q}$-points[6] in the first Brilloiun zone $N_{\mathbf{q}}$; s up to the maximum number of atoms per unit cell; and l runs for the Cartesian coordinates x, y, and z.

In equation 3.2, $U(\mathbf{R^0})$ is a constant with no relevance for the dynamical problem. The partial derivative of the second terms produces a force and, by definition, must be zero at equilibrium. Finally, if we truncate the expansion up to the quadratic term, the nuclear Hamiltonian of any atom corresponds to a simple three-dimensional harmonic oscillator:

$$H_I(\mathbf{R}) \approx U(\mathbf{R^0}) + \sum_{msl} \frac{\left(P_{ms}^l\right)^2}{2m_s} + \frac{1}{2}\sum_{msl}\sum_{m's'l'} \Phi_{msm's'}^{ll'} u_{ms}^l u_{m's'}^{l'},$$

(3.3)

where:

$$\Phi_{msm's'}^{ll'} \equiv \left.\frac{\partial^2 U}{\partial u_{ms}^l \partial u_{m's'}^{l'}}\right|_{\mathbf{R^0}}.$$

(3.4)

And it corresponds to the interatomic force constants. The Fourier transformed force constants are defined as:

$$\Phi_{ss'}^{ll'}(\mathbf{q}, \mathbf{q'}) = \frac{1}{N_{\mathbf{q}}}\sum_{mm'} \Phi_{msm's'}^{ll'} e^{-i(\mathbf{q}\cdot\mathbf{R}_{ms} + \mathbf{q'}\cdot\mathbf{R}_{m's'})}$$
$$= \Phi_{ss'}^{ll'}(\mathbf{q}) = \Phi_{ss'}^{ll'}(\mathbf{q}, -\mathbf{q}) = \sum_m \Phi_{msm's'}^{ll'} e^{-i(\mathbf{q}\cdot\mathbf{R}_{ms})}.$$

(3.5)

Similarly, let's define the Fourier transforms of the nuclear displacement and mo-

---

[6]The number of $\mathbf{q}$-points are not necessarily the same number of $\mathbf{k}$ points $N_{\mathbf{k}}$ used for the electronic structure calculation.

mentum operators:

$$u_s^l(\mathbf{q}) = \frac{1}{\sqrt{N_\mathbf{q}}} \sum_n e^{i\mathbf{q}\cdot\mathbf{T}_m} u_{ms}^l; \tag{3.6}$$

$$P_s^l(\mathbf{q}) = \frac{1}{\sqrt{N_\mathbf{q}}} \sum_n e^{-i\mathbf{q}\cdot\mathbf{T}_m} P_{ms}^l. \tag{3.7}$$

By assuming the following transformation to the bosonic ladder operators,

$$u_s(\mathbf{q}) = \sum_\mu \frac{1}{\sqrt{2m_s\omega_\mu(\mathbf{q})}} \epsilon_{s\mu}^l(\mathbf{q}) \left(b_{\mu\mathbf{q}} + b_{\mu-\mathbf{q}}^\dagger\right); \tag{3.8}$$

$$P_s(\mathbf{q}) = -i \sum_\mu \sqrt{\frac{m_s\omega_\mu(\mathbf{q})}{2}} \epsilon_{s\mu}^l(\mathbf{q}) \left(b_{\mu\mathbf{q}} - b_{\mu-\mathbf{q}}^\dagger\right), \tag{3.9}$$

where $\epsilon_{s\mu}(\mathbf{q})$ and $\omega_\mu(\mathbf{q})$ are the polarization vector (of atom s in the unit cell) and the vibrational mode μ with momentum $\mathbf{q}$, respectively. Additionally, the following commutation relation are satisfied:

$$\left[b_{\mu\mathbf{q}}, b_{\mu'\mathbf{q}'}^\dagger\right] = \delta_{\mu\mu'}\delta_{\mathbf{q}\mathbf{q}'}, \quad [b_{\mu\mathbf{q}}, b_{\mu'\mathbf{q}'}] = 0, \quad \left[b_{\mu\mathbf{q}}^\dagger, b_{\mu'\mathbf{q}'}^\dagger\right] = 0. \tag{3.10}$$

The nuclear Hamiltonian can be diagonalized and written, in the second quantization, as a sum of independent harmonic oscillators [19]:

$$H_I = U_0 + \sum_\mu \sum_\mathbf{q}^{1^{st}BZ} \omega_\mu(\mathbf{q}) \left(b_{\mu\mathbf{q}}^\dagger b_{\mu\mathbf{q}} + \frac{1}{2}\right), \tag{3.11}$$

where the eigenvalues are defined as:

$$\Omega_\mu(\mathbf{q}) = U_0 + \omega_\mu(\mathbf{q}) \left(n_{\mu\mathbf{q}} + \frac{1}{2}\right). \tag{3.12}$$

Here, U_0 is the ground state electronic energy of the system at equilibrium and it already includes the contribution due to the ion-ion interaction. The vibrational modes $\omega_\mu(\mathbf{q})$ are the phonon frequencies that allow us to determine the phonon spectrum,

which is the phonon frequency vs. momentum dispersion relation. Finally, the polarization vectors (eigenvectors) and phonon frequencies (eigenvalues) can be obtained by diagonalizing the dynamical matrix $D_{ss'}^{ll'} = \Phi_{ss'}^{ll'}(\mathbf{q}) / \sqrt{m_s m_{s'}}$:

$$\omega_\mu^2(\mathbf{q})\, \epsilon_{s\mu}^l(\mathbf{q}) = \sum_{s'} \sum_{l'} D_{ss'}^{ll'}(\mathbf{q})\, \epsilon_{s'\mu}^{l'}(\mathbf{q}). \tag{3.13}$$

With the advent of methods for solving the Schrödinger equation based on density functional theory (DFT), several *ab initio* methods for studying harmonic phonon properties of solids have been proposed, such as the frozen phonon approach [26, 27], supercell small displacement method [28, 29] and density functional perturbation theory (DFPT) [30]. Because of these developments, *ab initio* calculations of harmonic phonon dispersion curves and phonon mode Grüneisen parameters have become routine. Therefore, effects related to the lattice dynamics, such as lattice specific heat, Debye-Waller factors, thermal diffuse scattering, among others, that are correctly described within the harmonic approximation, can be (relatively easily) estimated due to the optimized computational codes that are available nowadays.

3.2   Linear Response Theory for Phonons

Once the nuclear problem is formulated, it is necessary to solve the derivatives of U that appear in equation 3.4 for obtaining the dynamical matrices. An *ab initio* calculation of these derivatives is a burdensome task. Fortunately, through the Hellmann-Feynman theorem [31, 32] the first derivative of the energy can be calculated in a much easier manner:

$$\frac{\partial U}{\partial u_{ms}^l} = \langle \psi_0^e | \frac{\partial H^e}{\partial u_{ms}^l} | \psi_0^e \rangle = \frac{\partial V_{I,I}}{\partial u_{ms}^l} + \int \mathrm{d}\mathbf{x}\, n(\mathbf{x})\, \frac{\partial V_{ext}(\mathbf{x})}{\partial u_{ms}^l}. \tag{3.14}$$

Similarly, the dynamical matrices can be obtained from equation 3.14 as:

$$\Phi^{ll'}_{msm's'} = \left.\frac{\partial^2 U}{\partial u^l_{ms}\partial u^{l'}_{m's'}}\right|_{\mathbf{R^0}}$$

$$= \int d\mathbf{x} n\left(\mathbf{x}\right)\left.\frac{\partial n\left(\mathbf{x}\right)}{\partial u^l_{ms}}\right|_{\mathbf{R^0}}\left.\frac{\partial V_{ext}\left(\mathbf{x}\right)}{\partial u^l_{ms}}\right|_{\mathbf{R^0}} + \int d\mathbf{x} n\left(\mathbf{x}\right)\left.\frac{\partial^2 V_{ext}\left(\mathbf{x}\right)}{\partial u^l_{ms}\partial u^{l'}_{m's'}}\right|_{\mathbf{R^0}} \qquad (3.15)$$

$$+ \left.\frac{\partial^2 V_{I,I}\left(\mathbf{x}\right)}{\partial u^l_{ms}\partial u^{l'}_{m's'}}\right|_{\mathbf{R^0}}.$$

Equation 3.15 shows how the electronic properties can be used for calculating phonons. However, it requires to know the electronic density $n\left(\mathbf{x}\right)$ and its derivative with respect to the nuclear positions $\frac{\partial n(\mathbf{x})}{\partial u^l_{ms}}$. The latter can be calculated from linear response theory: the density response function $\chi\left(\mathbf{x}, \mathbf{x}'\right)$ relates the change in the electronic density due to any external potential[7] V_{ext}:

$$\Delta n\left(\mathbf{x}\right) = \int d\mathbf{x}' \chi\left(\mathbf{x}, \mathbf{x}'\right)\Delta V_{ext}\left(\mathbf{x}'\right). \qquad (3.16)$$

If we assume that the electron-ion potential changes linearly with respect to the nuclear displacements, we can expand any function f that depends on this parameter as $f\left(\mathbf{x}\right) = f^0\left(\mathbf{x}\right) + \Delta f\left(\mathbf{x}\right)$, where the first term corresponds to the value of f evaluated at the equilibrium positions of the ions, and:

$$\Delta f\left(\mathbf{x}\right) = \sum_{msl}\left.\frac{\partial f\left(\mathbf{x}\right)}{\partial u^l_{ms}}\right|_{\mathbf{R^0}} u^l_{ms}, \qquad (3.17)$$

thus, the derivative of the density can be expressed as:

$$\frac{\partial n\left(\mathbf{x}\right)}{\partial u^l_{ms}} = \int d\mathbf{x} \chi\left(\mathbf{x}, \mathbf{x}'\right)\frac{\partial V_{ext}\left(\mathbf{x}'\right)}{\partial u^{l'}_{m's'}}. \qquad (3.18)$$

Now, it is straightforward to rewrite the dynamical matrix in terms of the electronic density response function:

---

[7]For lattice vibrations, the external potential is the change due to the displacements of the ions from their equilibrium positions that modify the electron-ion interaction.

$$\left.\frac{\partial^2 U}{\partial u_{ms}^l \partial u_{m's'}^{l'}}\right|_{\mathbf{R^0}} = \int \mathrm{d}\mathbf{x}\mathrm{d}\mathbf{x}' \left.\frac{\partial V_{ext}(\mathbf{x})}{\partial u_{ms}^l}\right|_{\mathbf{R^0}} \chi(\mathbf{x}, \mathbf{x}') \left.\frac{\partial V_{ext}(\mathbf{x}')}{\partial u_{m's'}^{l'}}\right|_{\mathbf{R^0}}$$
$$+ \int \mathrm{d}\mathbf{x}\, n(\mathbf{x}) \left.\frac{\partial^2 V_{ext}(\mathbf{x})}{\partial u_{ms}^l \partial u_{m's'}^{l'}}\right|_{\mathbf{R^0}} + \left.\frac{\partial^2 V_{I,I}(\mathbf{x})}{\partial u_{ms}^l \partial u_{m's'}^{l'}}\right|_{\mathbf{R^0}}. \tag{3.19}$$

The density response is calculated as:

$$\chi(\mathbf{x}, \mathbf{x}') = \lim_{\eta \to 0^+} \sum_\alpha \frac{\langle \psi_0^e | n(\mathbf{x}) | \psi_\alpha^e \rangle \langle \psi_\alpha^e | n(\mathbf{x}') | \psi_0^e \rangle}{(E_0^e - E_\alpha^e) + i\eta} + \frac{\langle \psi_{e,0} | n(\mathbf{x}') | \psi_\alpha^e \rangle \langle \psi_\alpha^e | n(\mathbf{x}) | \psi_{e,0} \rangle}{(E_0^e - E_\alpha^e) - i\eta} \tag{3.20}$$

Although this method has proven to be successful when applied to several systems [33, 34, 35, 36], it has some limitations as well, being very critical the extremely high demand of computation resources for calculating *ab initio* the response function for real systems. This flaw was overcame by means of the perturbation theory.

3.3 Density Functional Perturbation Theory

As the name suggests, this approach takes advantage of the first order perturbation theory for calculating, from the displacements of the ions from their equilibrium positions, the variation of the Kohn-Sham orbitals. This allows us to obtain the induced electron density and finally get the force constant matrix.

We begin by making a first order expansion in the following quantities:

$$H^{KS} \to H^{KS} + \Delta H^{KS};$$
$$\epsilon_{n\mathbf{k}} \to \epsilon_{n\mathbf{k}} + \Delta\epsilon_{n\mathbf{k}};$$
$$|\phi_{n\mathbf{k}}\rangle \to |\phi_{n\mathbf{k}}\rangle + \Delta|\phi_{n\mathbf{k}}\rangle; \tag{3.21}$$
$$n(\mathbf{x}) \to n(\mathbf{x}) + \Delta n(\mathbf{x}).$$

With them, we obtain an eigenvalue problem at linear level:

$$
\begin{aligned}
\left(H^{KS} - \epsilon_{n\mathbf{k}}\right)|\Delta\psi_{n\mathbf{k}}\rangle &= H^{KS}|\Delta\psi_{n\mathbf{k}}\rangle + \Delta H^{KS}|\Delta\psi_{n\mathbf{k}}\rangle - \epsilon_{n\mathbf{k}}|\Delta\psi_{n\mathbf{k}}\rangle - \Delta\epsilon_{n\mathbf{k}}|\Delta\psi_{n\mathbf{k}}\rangle \\
&\quad + H^{KS}|\psi_{n\mathbf{k}}\rangle - H^{KS}|\psi_{n\mathbf{k}}\rangle + \epsilon_{n\mathbf{k}}|\psi_{n\mathbf{k}}\rangle - \epsilon_{n\mathbf{k}}|\psi_{n\mathbf{k}}\rangle \\
&\quad + \Delta H^{KS}|\psi_{n\mathbf{k}}\rangle - \Delta H^{KS}|\psi_{n\mathbf{k}}\rangle + \Delta\epsilon_{n\mathbf{k}}|\psi_{n\mathbf{k}}\rangle - \Delta\epsilon_{n\mathbf{k}}|\psi_{n\mathbf{k}}\rangle \\
&= H^{KS}|\psi_{n\mathbf{k}} + \Delta\psi_{n\mathbf{k}}\rangle + \Delta H^{KS}|\psi_{n\mathbf{k}} + \Delta\psi_{n\mathbf{k}}\rangle \\
&\quad - \left(H^{KS} + \Delta H^{KS}\right)|\psi_{n\mathbf{k}}\rangle - \epsilon_{n\mathbf{k}}|\psi_{n\mathbf{k}} + \Delta\psi_{n\mathbf{k}}\rangle \\
&\quad - \Delta\epsilon_{n\mathbf{k}}|\psi_{n\mathbf{k}} + \Delta\psi_{n\mathbf{k}}\rangle + \left(\epsilon_{n\mathbf{k}} + \Delta\epsilon_{n\mathbf{k}}\right)|\psi_{n\mathbf{k}}\rangle \\
&= H^{KS}|\psi_{n\mathbf{k}}\rangle + \Delta H^{KS}|\psi_{n\mathbf{k}}\rangle - H^{KS}|\psi_{n\mathbf{k}}\rangle - \epsilon_{n\mathbf{k}}|\psi_{n\mathbf{k}}\rangle \\
&\quad - \Delta\epsilon_{n\mathbf{k}}|\psi_{n\mathbf{k}}\rangle + \epsilon_{n\mathbf{k}}|\psi_{n\mathbf{k}}\rangle \\
&= \left(\Delta H^{KS} - \Delta\epsilon_{n\mathbf{k}}\right)|\psi_{n\mathbf{k}}\rangle.
\end{aligned}
$$

$$(3.22)$$

This expression is know as the Sternheimer equation [37] and is the perturbed version of equation 1.16.

The electronic density is calculated by filling the electronic states of energy ϵ following the zero temperature Fermi-Dirac distribution $2\left[\theta\left(\epsilon_F - \epsilon\right)\right]$:

$$
n\left(\mathbf{x}\right) = \sum_n \sum_{\mathbf{k}}^{1^{st}BZ} 2\theta\left(\epsilon_F - \epsilon_{n\mathbf{k}}\right)|\phi_{n\mathbf{k}}\left(\mathbf{x}\right)|^2, \tag{3.23}
$$

where ϵ_F is the Fermi energy of the system, which indicates the energy of the highest occupied electronic state, and the factor 2 is included to account for spin-degeneracy. The change in the electronic density is obtained by a simple derivation of equation 3.23:

$$
\Delta n\left(\mathbf{x}\right) = 2\Re \sum_n \sum_{\mathbf{k}}^{1^{st}BZ} 2\left[\theta\left(\epsilon_F - \epsilon_{n\mathbf{k}}\right)\right]\phi_{n\mathbf{k}}^*\left(\mathbf{x}\right)\Delta\phi_{n\mathbf{k}}\left(\mathbf{x}\right). \tag{3.24}
$$

Finally, we get the change in the Hamiltonian ΔH^{KS} using the functional derivative of the electron-electron interaction potential with respect to the density:

$$
\Delta H^{KS}\left(\mathbf{x}\right) = \Delta V_{ext}\left(\mathbf{x}\right) + \int d\mathbf{x}\,K\left(\mathbf{X}, \mathbf{x}'\right)\Delta n\left(\mathbf{x}'\right), \tag{3.25}
$$

where $K\left(\mathbf{X}, \mathbf{x}'\right)$ is the kernel of the integral and is defined as:

$$K\left(\mathbf{x}, \mathbf{x}'\right) = \frac{\delta V_H\left(\mathbf{x}\right)}{\delta n\left(\mathbf{x}'\right)} + \frac{\delta V_{xc}\left(\mathbf{x}\right)}{\delta n\left(\mathbf{x}'\right)} = \frac{1}{\left|\mathbf{x} - \mathbf{x}'\right|} + f_{xc}\left(\mathbf{x}, \mathbf{x}'\right). \qquad (3.26)$$

Equations 3.22, 3.24, and 3.25, form a set of self-consistent equations for the perturbed system and follows a similar procedure as the one described in figure 2.2.

Our dynamical matrices were calculated using the *ph.x* code of the `PHonon` package of `Quantum ESPRESSO` [22, 23]. Since DFPT calculations require a large amount of computational resources, the first Brillouin zone in a $\mathbf{q}$-point mesh and the phonons are calculated only at those points. The force constant matrix is obtained by using a discrete Fourier transform as implemented in the *q2r.x* code of the same package. Finally, we obtain the phonon spectra by performing a Fourier interpolation in the reciprocal space. This is done by making use of the *matdyn.x* code that is also available in the `PHonon` package.

3.4   The Quasi-Harmonic Approximation

Although widely used, the harmonic approximation (HA) has some severe flaws that make this model imprecise for the description of several thermal properties. For instance, since the vibrational frequencies do not depend on interatomic distances, the vibrational contribution to the internal energy does not depend on volume, therefore, the equilibrium volume of a crystal does not depend on temperature. Apart from this, the harmonic approximation predicts an infinite thermal conductivity, vibrons or phonons with an infinite lifetime, and the temperature independence of the vibrational spectra [38].

As a way to correct some of the biggest errors in the harmonic approximation, the quasi-harmonic approximation (QHA) was proposed [39, 38]. QHA deals with some of the most relevant inaccuracies of the HA without requiring any explicit calculation of anharmonic interaction coefficients, and has been used with density functional theory (DFT) and density functional perturbation theory (DFPT) in several applications that

are relevant for planetary sciences. In the QHA, the anharmonicity is considered as a weak effect, and, by taking into account only the thermal expansion, the atomic force constants and the phonon frequencies are renormalized [25].

The Helmholtz free energy of the crystal is determined via the regular harmonic expression, but constraining it to some global parameter upon which vibrational frequencies may depend:

$$F(X, T) = U_0(X) + F_0(\mathbf{q}|X) + F_{thermal}(\mathbf{q}, T|X), \qquad (3.27)$$

where X is the global constrain, which is usually the volume[8] V. Thus if $X = V$, the lattice vibrations remain harmonic but with volume-dependent frequencies. On the other hand, $U_0(X)$ is the electronic energy at zero temperature, and $F_0(\mathbf{q}|X)$ is the zero-temperature energy of the crystal as a function of V:

$$F_0(\mathbf{q}|V) \equiv F_0(\mathbf{q}) = \frac{1}{2}\frac{1}{N_{\mathbf{q}}}\sum_{\mu}\sum_{\mathbf{q}}^{1^{st}BZ}\omega_{\mu}(\mathbf{q}). \qquad (3.28)$$

And the thermal free energy is given by:

$$F_{thermal}(\mathbf{q}, T|V) \equiv F_{thermal}(\mathbf{q}, T) = -\frac{1}{N_{\mathbf{q}}}k_B T \ln(Z_{thermal})$$

$$= -\frac{1}{N_{\mathbf{q}}}k_B T \ln\left(\prod_{\mathbf{q}}\sum_{n(\mathbf{q})}\sum_{\mu}^{1^{st}BZ}e^{-n\omega_{\mu}(\mathbf{q})/k_B T}\right)$$

$$= -\frac{1}{N_{\mathbf{q}}}k_B T \ln\left[\prod_{\mathbf{q}}\sum_{\mu}^{1^{st}BZ}\left(1 - e^{-\omega_{\mu}(\mathbf{q})/k_B T}\right)^{-1}\right]$$

$$= \frac{1}{N_{\mathbf{q}}}k_B T \sum_{\mathbf{q}}^{1^{st}BZ}\ln\sum_{\mu}\left(1 - e^{-\omega_{\mu}(\mathbf{q})/k_B T}\right).$$

$$(3.29)$$

The equation of state can be obtained when equation (3.29) is differentiated with

---

[8]Thus, the free energy of the crystal does not depend any longer on the coordinates of the atoms, but only on its volume.

respect to volume:

$$P = -\left.\frac{\partial F}{\partial V}\right|_T = -\frac{\partial U_0}{\partial V} + \frac{1}{V} \sum_{\mathbf{q}}^{1^{st}BZ} \ln \sum_{\mu} \omega_\mu(\mathbf{q}) \gamma_\mu(\mathbf{q}) \left(\frac{1}{2} + \frac{1}{e^{\omega_\mu(\mathbf{q})/k_B T} - 1}\right), \quad (3.30)$$

where $\gamma_\mu(\mathbf{q})$ are the Grüneisen mode parameters and are defined as:

$$\gamma_{\_}\mu(\mathbf{q}) = -\frac{V}{\omega_\mu(\mathbf{q})} \frac{\partial \omega_\mu(\mathbf{q})}{\partial V}. \quad (3.31)$$

Nevertheless, perhaps due to the simplicity of both harmonic and quasi-harmonic approximations, that also make them easy to implement in computational codes, these two approaches fail when they try to explain properties and phenomena that are related to thermodynamic, kinetic and dynamic properties of strongly anharmonic lattices. One case in which these situations occur is when the atomic displacements around their equilibrium positions are much larger than the range in which the harmonic potential is valid. Similar behavior has been observed when systems are close to a dynamical instability, light atoms are present, or when the temperature is close to the melting point of the solid. In these instability scenarios, i.e., materials close to a temperature or pressure-induced phase transition, it is mandatory the inclusion of anharmonic corrections to the free energy for describing accurately the thermodynamic properties of the system of study.

3.5 Anharmonic Corrections to the Helmholtz Energy

The definition of harmonic and anharmonic varies from one treatment to another. In this context, the word *harmonic* means that the modal are independent of both V and T; on the other hand the *quasi-harmonic approximation* assumes that the modal frequencies are independent of T but dependent on V, as $(\partial \ln \omega_\mu(\mathbf{q})/\partial \ln T)_V$ is zero. Therefore, it can be asserted that there is some anharmonicity in the quasi-harmonic

approximation because the bond oscillations are no longer strictly sinusoidal. Thus, *anharmonicity* can be defined as contributions in T terms to the free energy beyond those arising from the quasi-harmonic thermal energy.

Several attempts have been proposed to include anharmonicities, being *ab initio* molecular dynamics (AIMD) [40] one of the most commonly used. However, since AIMD is based on Newtonian mechanics, quantum nuclear effects are not well characterized. Therefore, AIMD is limited to temperatures above the Debye temperature. A way to overcome this limitation is to use quantum baths [41, 42], but this solution has the disadvantage that it is only valid for harmonic potentials [43, 44]. Nevertheless, this problem can be overcome by using path-integral molecular dynamics (PIMD) [45], but it requires massive computational resources, making its implementation very restricted.

Recently, a new method [46] has been developed to deal with anharmonic effects beyond perturbation theory: the stochastic self-consistent harmonic approximation (SS-CHA). In this method, the free energy is minimized with respect to a trial density matrix described by an arbitrary harmonic Hamiltonian. The minimization is done with respect to all the free parameters in the trial harmonic Hamiltonian, like phonon frequencies and eigenvectors, and by following a stochastic procedure, the gradient of the free energy is calculated. This approach is valid to treat anharmonicities at any temperature in the nonperturbative regime and can be used to calculate thermodynamic and dynamical properties, among others, being less computationally expensive than PIMD.

3.5.1 The Stochastic Self-Consistent Harmonic Approximation

Given the nuclear Hamiltonian $H = T_I + U$, its partition function is $Z_H = \text{tr}\left[e^{-\beta H}\right]$ and the Helmholtz free energy is:

$$F_H = -\frac{1}{\beta}\ln\left(Z_H\right) = \text{tr}\left(\rho_H H\right) + \frac{1}{\beta}\text{tr}\left[\rho_H \ln\left(\rho_H\right)\right], \tag{3.32}$$

where $\rho_H = e^{-\beta H}/\mathrm{tr}\left(e^{-\beta H}\right)$ corresponds to the density matrix and $1/\beta = k_B T$. The trial Hamiltonian is defined as $\mathcal{H} = T_I + \mathcal{U}$ and we can build a trial density matrix $\rho_{\mathcal{H}}$ from it. Analogously, we can write its corresponding free energy as:

$$F_{\mathcal{H}} = \mathrm{tr}\left(\rho_{\mathcal{H}}\mathcal{H}\right) + \frac{1}{\beta}\mathrm{tr}\left[\rho_{\mathcal{H}}\ln\left(\rho_{\mathcal{H}}\right)\right]. \tag{3.33}$$

By computing the free energy with the actual anharmonic Hamiltonian H, but using the trial density matrix $\rho_{\mathcal{H}}$ we obtain:

$$\mathcal{F}_H\left(\mathcal{H}\right) = \mathrm{tr}\left(\rho_{\mathcal{H}}H\right) + \frac{1}{\beta}\mathrm{tr}\left[\rho_{\mathcal{H}}\ln\left(\rho_{\mathcal{H}}\right)\right], \tag{3.34}$$

which satisfies the Gibbs-Bogoliubov inequality:

$$F_H \leq \mathcal{F}_H\left(\mathcal{H}\right). \tag{3.35}$$

Adding and subtracting $\mathrm{tr}\left(\rho_{\mathcal{H}}\mathcal{H}\right)$ in equation 3.34:

$$\begin{aligned}
\mathcal{F}_H\left(\mathcal{H}\right) &= \mathrm{tr}\left(\rho_{\mathcal{H}}H\right) + \frac{1}{\beta}\mathrm{tr}\left[\rho_{\mathcal{H}}\ln\left(\rho_{\mathcal{H}}\right)\right] + \mathrm{tr}\left(\rho_{\mathcal{H}}\mathcal{H}\right) - \mathrm{tr}\left(\rho_{\mathcal{H}}\mathcal{H}\right) \\
&= \mathrm{tr}\left(\rho_{\mathcal{H}}\mathcal{H}\right) + \frac{1}{\beta}\mathrm{tr}\left[\rho_{\mathcal{H}}\ln\left(\rho_{\mathcal{H}}\right)\right] + \mathrm{tr}\left(\rho_{\mathcal{H}}H - \rho_{\mathcal{H}}\mathcal{H}\right) \\
&= \mathcal{F}_H\left(\mathcal{H}\right) + \mathrm{tr}\left[\rho_{\mathcal{H}}\left(H - \mathcal{H}\right)\right] \\
&= \mathcal{F}_H\left(\mathcal{H}\right) + \mathrm{tr}\left[\rho_{\mathcal{H}}\left(U - \mathcal{U}\right)\right].
\end{aligned} \tag{3.36}$$

This is the function that has to be minimized with respect to the trial Hamiltonian $\mathcal{H}$ The trial potential $\mathcal{U}$ is restricted to a harmonic one, so $\mathcal{H}$ takes the form:

$$\mathcal{H} = \sum_{ms}\sum_{l}\frac{\left(P_{ms}^{l}\right)^2}{2m_{ms}} + \frac{1}{2}\sum_{mm'}\sum_{ss'}\sum_{ll'}\tilde{u}_{ms}^{l}\tilde{\Phi}_{mm'ss'}^{ll'}\tilde{u}_{m's'}^{l'}, \tag{3.37}$$

where $\tilde{\Phi}_{mm'ss'}^{ll'}$ is the trial force constant matrix and the atomic displacements $\tilde{\mathbf{u}}_{m's'}$ are referred to the average nuclear positions $\tilde{\mathbf{R}}^0$.

$\mathcal{F}_H(\mathcal{H})$ has to be minimized with respect to Φ and this implies the implicit minimization with respect to phonon frequencies $\omega_{\mu\mathcal{H}}$ and polarization vectors $\epsilon^m_{s\mu\mathcal{H}}$ from the diagonalization of the force constant matrices. Furthermore, it also has to be minimized with respect to $\tilde{\mathbf{R}}^0$, which are not necessarily the $\mathbf{R}^0$ positions of the minimum of the energy landscape.

The expression for $\mathcal{F}_H(\mathcal{H})$ and its gradients are the following

$$\mathcal{F}_H(\mathcal{H}) = F_{\mathcal{H}} + \int d\mathbf{R} \left[U(\mathbf{R}) - \mathcal{U}(\mathbf{R}) \right] \rho_{\mathcal{H}}(\mathbf{R}); \tag{3.38}$$

$$\nabla_{\tilde{\mathbf{R}}^0} \mathcal{F}_H(\mathcal{H}) = - \int d\mathbf{R} \left[\mathbf{f}(\mathbf{R}) - \mathbf{f}_{\mathcal{H}}(\mathbf{R}) \right] \rho_{\mathcal{H}}(\mathbf{R}); \tag{3.39}$$

$$
\begin{aligned}
\nabla_{\tilde{\Phi}} \mathcal{F}_H(\mathcal{H}) = - \sum_{mm'ss'll'\mu} \sqrt{\frac{m_{s'}}{m_s}} \left[\epsilon^{lm}_{s\mu\mathcal{H}} \nabla_{\tilde{\Phi}} \ln(a_{\mu\mathcal{H}}) + \nabla_{\tilde{\Phi}} \epsilon^{lm}_{s\mu\mathcal{H}} \right] \epsilon^{l'm'}_{s'\mu\mathcal{H}} \\
\times \int d\mathbf{R} \left[f^{lm}_s(\mathbf{R}) - f^{lm}_{s\mathcal{H}}(\mathbf{R}) \right] \left(R^{l'm'}_{s'} - R^{l'm'0}_{s'} \right) \rho_{\mathcal{H}}(\mathbf{R}),
\end{aligned}
\tag{3.40}
$$

with:

$$a_{\mu\mathcal{H}} = \sqrt{\coth(\beta\omega_{\mu\mathcal{H}}/2)(2\omega_{\mu\mathcal{H}})}, \tag{3.41}$$

which is known as the normal length of the mode μ, and $R \equiv \{R_I \dots R_M\}$ corresponds to the nuclear configuration. $\rho_{\mathcal{H}}(\mathbf{R})$ holds for the probability to find the system described by $\mathcal{H}$ in that configuration $\mathbf{R}$. Finally $\mathbf{f}(\mathbf{R})$ is the vector formed by all the atomic forces for the nuclear configuration $\mathbf{R}$ and $\mathbf{f}_{\mathcal{H}}(\mathbf{R})$ are the forces defined by $\mathcal{H}$. The only non-analytic terms in equations 3.38, 3.39, and 3.40, are the integrals and, of course, the actual forces $\mathbf{f}(\mathbf{R})$.

Since integrals are non-analytic terms, evaluating them becomes a challenging, time-consuming task. Within SSCHA, these integrals are evaluated stochastically by converting them in a finite sum using the relationship:

$$\int d\mathbf{R} \mathcal{O}\left(\mathbf{R}\right) \rho\left(\mathbf{R}\right) \simeq \frac{1}{N_c} \sum_{I=1}^{N_c} \mathcal{O}\left(\mathbf{R}_I\right) \equiv \langle \mathcal{O} \rangle. \tag{3.42}$$

The set of $\mathbf{R}_I$ configurations is created according to the distribution $\rho\left(\mathbf{R}\right)$. $\mathcal{O}h$ is any operator and N_c is the number of configurations we have created. In the limit $N_c \to \infty$, we can recover the exact value of the integral.

The Conjugated-Gradient (CG) method is used for the minimization and it is carried out in a subspace of the parameters that preserve crystal symmetries: a symmetrized
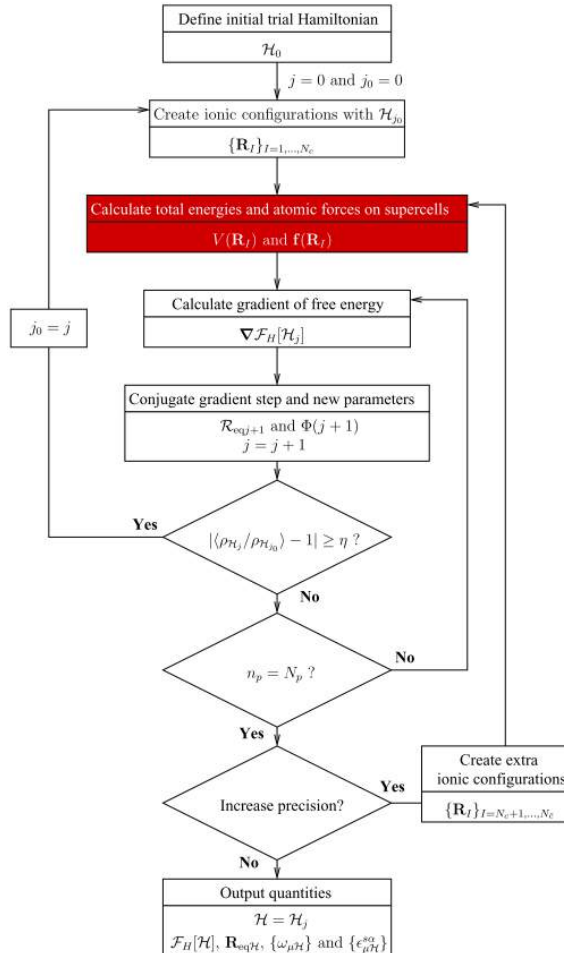
Figure 3.1: Flowchart of the SSCHA procedure. The step marked in red corresponds to the *ab initio* calculation of the total energies and forces on the supercells, representing (almost) all the computer time of the SSCHA implementation. Taken from Ref. [46].

vector basis is used to define $\tilde{\Phi}$ and $\tilde{\mathbf{R}}_0$, and this allows us to obtain a different number of independent coefficients N_p to minimize, that will depend on the system. The minimization process is described in figure 3.1.

The initial trial Hamiltonian $\mathcal{H}_0$ is usually the harmonic Hamiltonian obtained in the phonon calculation using DFPT[9]. With this Hamiltonian, along with the $\rho_{\mathcal{H}_0}(\mathbf{R})$, the N_c configurations are created. For each configuration the energy and the forces are calculated using supercells. These quantities allow us to evaluate the integrals in 3.38, 3.39, and 3.40, and perform a conjugates-gradient step, that will update $\tilde{\mathbf{R}}_0$ and $\tilde{\Phi}$ leading us to a new $\mathcal{H}_j$. Since each CG step is computationally demanding, create a new configuration from every new $\rho_{\mathcal{H}_j}$ would make the SSCHA minimization process very inefficient. As a mechanism for improve the method, a re-weighting importance sampling technique is used that allows rewriting equation 3.42 as:

$$\int \mathrm{d}\mathbf{R}\,\mathcal{O}(\mathbf{R})\,\rho(\mathbf{R}) \simeq \frac{1}{N_c}\sum_{I=1}^{N_c} \mathcal{O}(\mathbf{R}_I)\,\frac{\rho_{\mathcal{H}_j}}{\rho_{\mathcal{H}_{j_0}}}. \tag{3.43}$$

Here, j_0 is the latest iteration at which configurations were created. The configurations created with $\mathcal{H}_{j_0}$ can be reused as long as the deviation of $\langle \frac{\rho_{\mathcal{H}_j}}{\rho_{\mathcal{H}_{j_0}}} \rangle$ from unity is not larger than a fixed parameter η, and, in case this happens, new configurations will be created with $\mathcal{H}_j$. The minimization process ends when the chosen convergence criterion is achieved.

---

[9]It is important to address that the harmonic Hamiltonian cannot be used if the system is unstable in the harmonic approximation.

4   Electronic Structure Calculations at Extreme Pressure

Density functional theory is one of the most popular electronic structure methods and it has an inherent advantage since the convergence to the exact solution is systematic. Electronic structure calculations aim to numerically solve the Schrödinger equation for a system with only the basic description provided. However, it is well known that because of its nature it is impossible to solve such an equation unless one makes few approximations. To obtain the approximate eigenstates, approximations are made on various levels. The treatment of electron-electron interactions is the principle source of difficulty: the physical and chemical properties of a system depend principally on the interaction of the electrons with each other and with the atomic cores. These interactions cannot easily be separated out or treated without approximation.

4.1   PAW vs. all-electron

Due to the extensive acceptance of density functional theory, there are a large amount of dedicated codes that are available for the scientific community for calculating physical properties of crystals and molecules. Thus, it is only natural to expect that they exhibit some level of differences between them in terms of implementation of the DFT formalism by the developers. This technical discrepancy was a major issue a decade ago given the lack of a consensus on the results obtained with older DFT implementations. Fortunately, this situation seems to be overcame with the release of the latest versions of packages and suites, in which the most commonly used DFT codes and methods have proven to predict essentially the same results, regardless the code used [47].

This new scenario has shed some peace of mind on the selection of the DFT computer code for performing the calculations. However, there is still the concern regard-

ing the numerical solution scheme for solving the Kohn-Sham equations. All-electron approaches are traditionally considered as the gold-standard for DFT calculations, because the ionic potential is implemented without any pseudization of the core electrons. Therefore, this approach implies, of course, a higher computational cost, when compared to other methods such as pseudopotentials. Nevertheless, since both all-electron and pseudopotential methods have their own intrinsic advantages, it is highly desirable to achieve high precision for both methods [48].

Since there is not an absolute reference against which to compare different methods for performing DFT calculations, Lejaeghere *et al.* [47] performed DFT computations for five distinct sets of material properties, divided into energetic (ΔE_{coh})[10] and elastic quantities (V_0, B_0, B_1, C_{ij})[11], on 71 elemental crystals. However, they realized that is not convenient to compare this properties directly because different units are involved. Therefore, they presented a criterion (the Δ gauge) for pairwise code comparison in an unequivocal way. For each element i, of the 71 elements that they studied, they defined the Δ_i quantity as the root-mean-square difference between the $E^i(V)$ profile from the equation of state of two different methods (a and b) over a $\pm 6\%$ interval around the equilibrium volume V_0^i:

$$\Delta^i(a,b) = \sqrt{\frac{\int_{0.94V_0^i}^{1.06V_0^i} \left(E_b^i(V) - E_a^i(V)\right)^2 dV}{0.12V_0^i}}. \tag{4.1}$$

Thus, the Δ_i value contains the information regarding the deviation between equilibrium volumes, bulk moduli, and any other EOS-derived observables in a single number.

Now, if we want to determine how accurate are the pseudopotential methods when compared with all-electron approaches, we can then calculate the Δ value to obtain information regarding the error bar associated with the pseudization scheme for the different elements of the periodic table. A small error is then related with a small value of Δ, so at this point, it is necessary to establish which values of Δ can be considered as "small".

From a more recent study performed again by Lejaeghere *et al.* [48] they compared

---

[10]Cohesive energy.
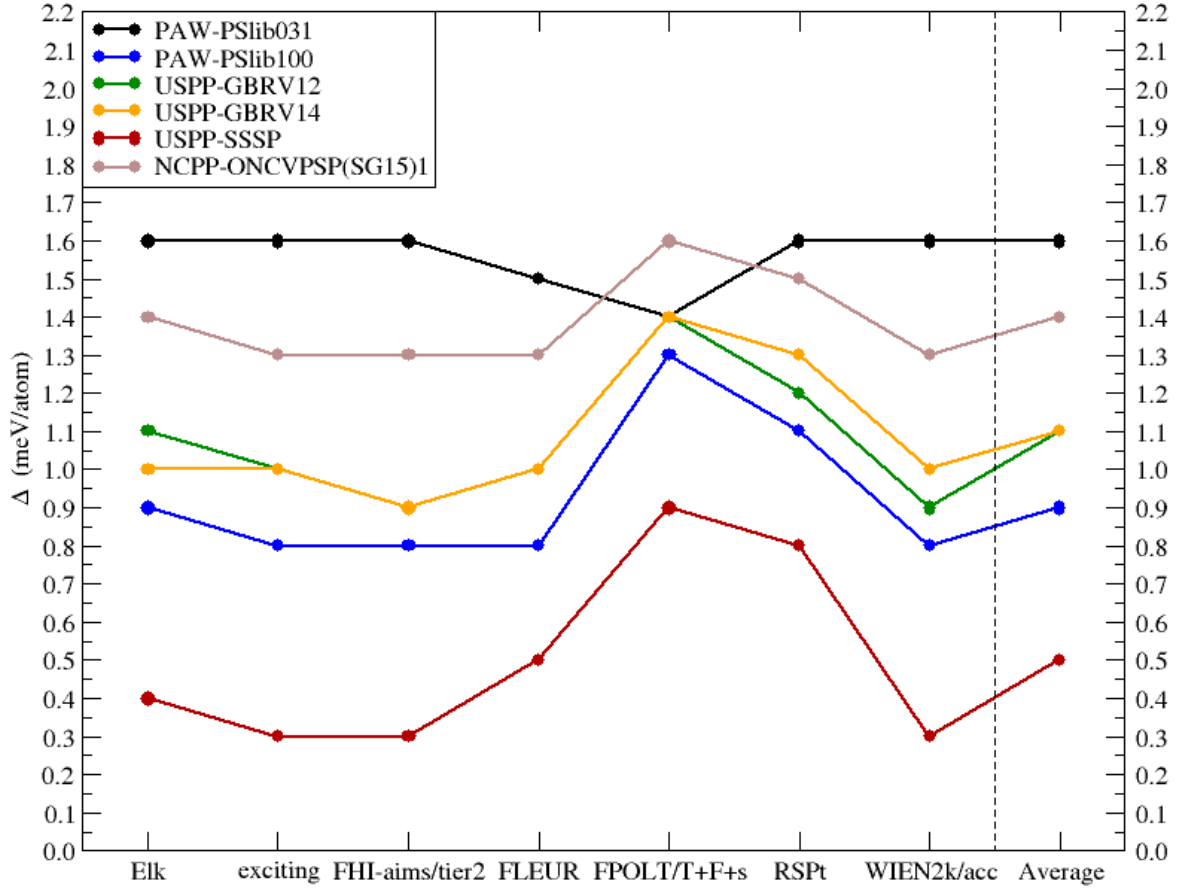[11]Volume, bulk modulus, derivative of the bulk modules, and other elastic constants, respectively.

Figure 4.1: Δ values between all-electron codes and different potential sets of Quantum ESPRESSO, namely PAW, ultrasoft (USPP), and norm-conserving (NCPP) pseudopotential methods. The tags of the different all-electron codes stand for code/specification. Adapted from [48].

high-quality experimental data against high-precision measurements of EOS from all-electron calculations, and the differences between codes in terms of commonly reported EOS parameters. They concluded that a Δ value of 1 or even 2 meV per atom is sufficient to state that the EOS is indistinguishable for all purposes.

In this work, we used the Quantum ESPRESSO suite [22, 23] for calculating the physical properties of carbon, oxygen, and carbon dioxide. The values of Δ between different all-electron codes, namely Elk, exciting, FHI-aims, FLEUR, FPOLT, RSPt, and WIEN2k, and the potential sets that are available in Quantum ESPRESSO (PAW, ultrasoft, and norm–conserving pseudopotential methods), are displayed in Fig. 4.1.

Finally, a recent study [49] tested up to eight pseudopotentials for the PBE functional

with the PWscf and PHonon codes of the Quantum ESPRESSO suite. All the libraries include the three main pseudization approaches: norm-conserving (NC), ultrasoft (US), and projector-augmented wave (PAW). For the case of PAW, they include the following libraries: pslibrary.0.3.1 [50], pslibrary.1.0.0 [51], and the library proposed by Topsakal and Wentzcovitch for the rare-earth elements [52]. They compared the equation of state calculated with the pseudopotential simulations with reference all-electron results. This all-electron calculations used as reference were performed with the WIEN2k code.

The information regarding different pseudotentials that are available in Quantum ESPRESSO, specifically for carbon and oxygen, are in table 4.1.

Table 4.1: Pseudopotential testing protocol applied to carbon and oxygen. The valence number (Z) of the pseudotential and the Δ factor (in meV/atom) with respect to the reference all-electron results are displayed.

Carbon				Oxygen		
Pseudopotential	Z	Δ		Pseudopotential	Z	Δ
SG15	4	2.365		SG15	6	0.391
Goedecker	4	0.137		Goedecker	6	0.991
GBRV-1.2	4	0.279		GBRV-1.2	6	2.425
031US	4	1.620		031US	6	1.633
031PAW	4	0.443		031PAW	6	1.116
100US	4	0.787		100US	6	5.124
100PAW	4	0.424		100PAW	6	4.877

In this work, we used PAW pseudopotentials from the pslibrary.0.3.1 for both carbon and oxygen. Detailed information regarding their performance is described in the following subsections.

4.1.1   Equation of state

The Birch-Murnaghann fit of the energy as a function of volume for carbon and oxygen made with the pslibrary.0.3.1 of the PAW pseudopotential with the reference all-electron results, is shown in Fig. 4.2.

(a)   (b)
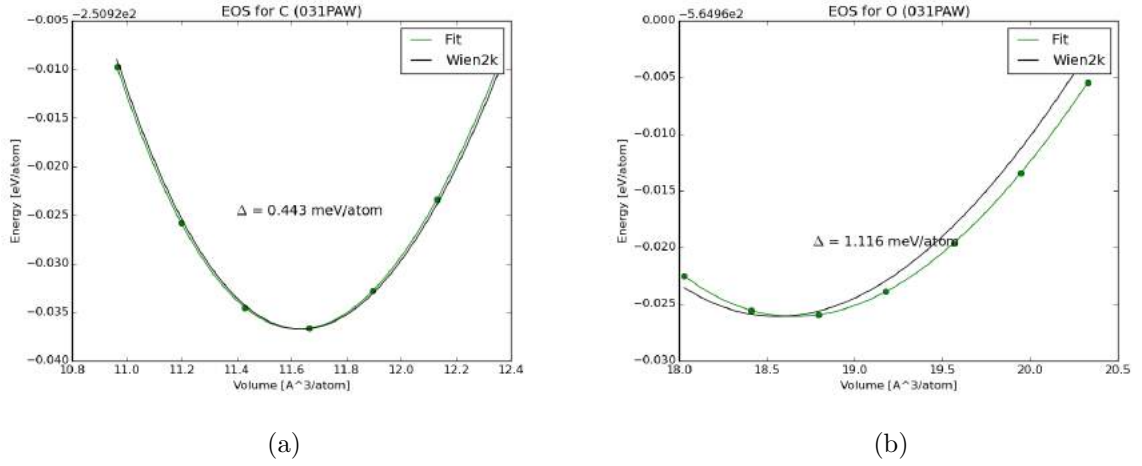
Figure 4.2: Comparison of the Birch-Murnaghan fit of the pseudopotential EOS (green line) with the reference all-electron results (black line) for (a) carbon and (b) oxygen. Taken from: `https://www.materialscloud.org` as stated in Ref. [49].

4.1.2   Phonon frequencies

The information related to the different phonon frequencies are condensed into a single parameter $\delta\omega$ [49], that represents the relative average deviation (in percentage) among all the phonon frequencies ω calculated at $\mathbf{q} = \frac{1}{2}, \frac{1}{2}, \frac{1}{2}$ for each wavefunction cutoff E_c.
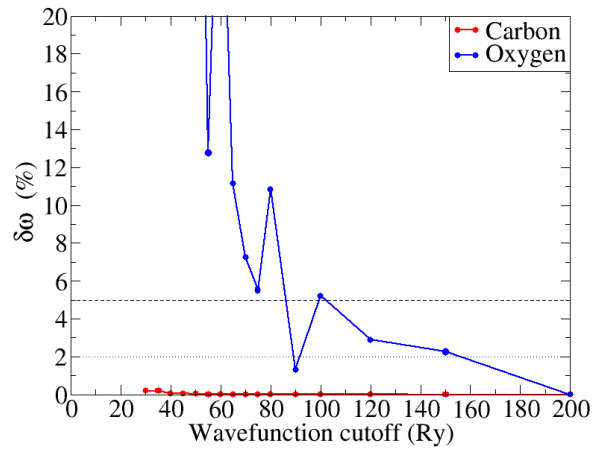
Figure 4.3: Relative average deviation of phonon frequencies with respect to the reference all-electron results for carbon (red) and oxygen (blue). Taken from: `https://www.materialscloud.org` as stated in Ref. [49].

4.1.3   Stress tensor

The convergence of the stress is not evaluated by checking the convergence of the pressure itself, but as monitoring its conversion into an equivalent volume. Thus, the parameter δV_{press} [49] is defined as the relative volume deviation (in percentage) due to the residual pressure of a calculation performed at the cutoff E_c.
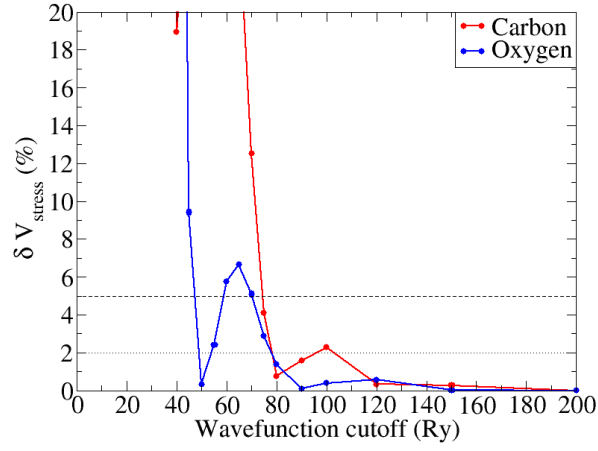
Figure 4.4: Relative volume deviation with respect to the reference all-electron results for carbon (red) and oxygen (blue). Taken from: `https://www.materialscloud.org` as stated in Ref. [49].

4.1.4   Cohesive energy

The quantity δE_{coh} (in meV/atom) [49] is defined as the absolute difference between the cohesive energy at a given cutoff E_c an the one at the reference wavefunction cutoff E_c^{ref}.
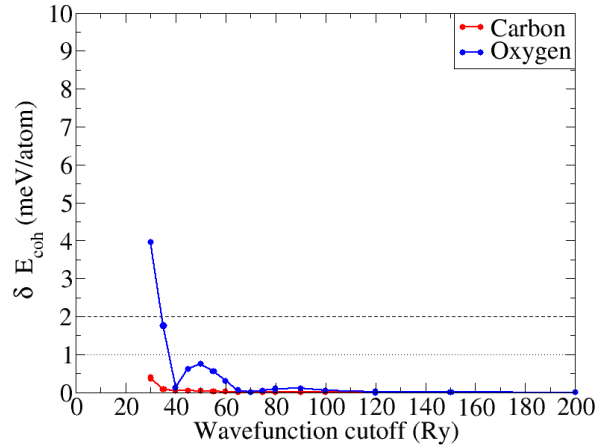
Figure 4.5: Absolute difference of the cohesive energy with respect to the reference all-electron results for carbon (red) and oxygen (blue). Taken from: `https://www.materialscloud.org` as stated in Ref. [49].

4.2   Exchange-Correlation Functional

The Kohn-Sham density functional theory is the most used method for the theoretical modeling of solids, surfaces, and molecules at the quantum level, and its accuracy depends on the chose approximation of the exchange-correlation functional (E_{xc}): since the exact form of this functional is still unknown, there are a large number of available functionals for solid-state physics [53, 54, 55, 56, 57] and quantum chemistry [53, 58, 59, 60, 61]. Multiple developments have made the functionals more sophisticated and accurate, and the majority of these functionals belong to one of the rungs of Jacob's ladder [62, 63].

For practical reasons, pseudopotentials are the method of choice for modelling materials and it has been shown that pseudopotentials can reproduce quite well the results obtained with an all-electron approach, with a substantially smaller computational cost [48, 49], however as we go up the rungs of the Jacob's ladder the functional form gets more complex and more expensive to compute. Therefore, it is necessary to chose the rung appropriate to the required accuracy and computational resources available for the calculations.
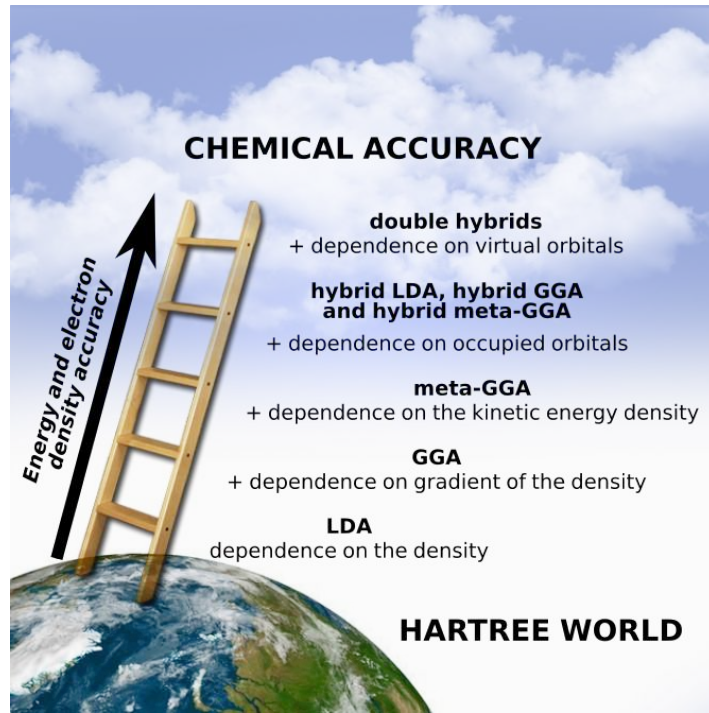
Figure 4.6: Jacob's ladder of density functional approximations.

A recent study [64] tested a large number of exchange-correlation functional that span the first four rungs of Jacob's ladder. They computed several solid-state properties (lattice constant, bulk modulus, and cohesive energy) in strongly bound solids and weakly bound solids, separately. One of their most important observations in that work was that for the solids bound by strong interactions it does not seem to be really necessary to go beyond the GGA approximation since several of these functionals are overall as accurate as the more expensive meta-GGA (MGGA) and hybrid functionals.

In the study of materials at high-pressure it has been stated that the transition pressure between solid phases depends on the choice of the exchange-correlation functional. Nevertheless, PBE still is a good enough approximation, based on the agreement of the experimentally observed EOS [65, 66] and DFT calculations, although there remains a *small* error in the transition pressure where it is shifted to lower pressures by less than 10%, when the vibrational contribution to the free energy is included [67]. Moreover, when PBE is compared with the BLYP paramerization for GGA, similar total energies and stress anisotropy are obtained [66].

The choice of PBE for our work is motivated by the performed benchmarks [64] and

multiple high-pressure works that shows a good agreement between PBE and theoretical and experimental equation of state [67, 66, 68, 69].
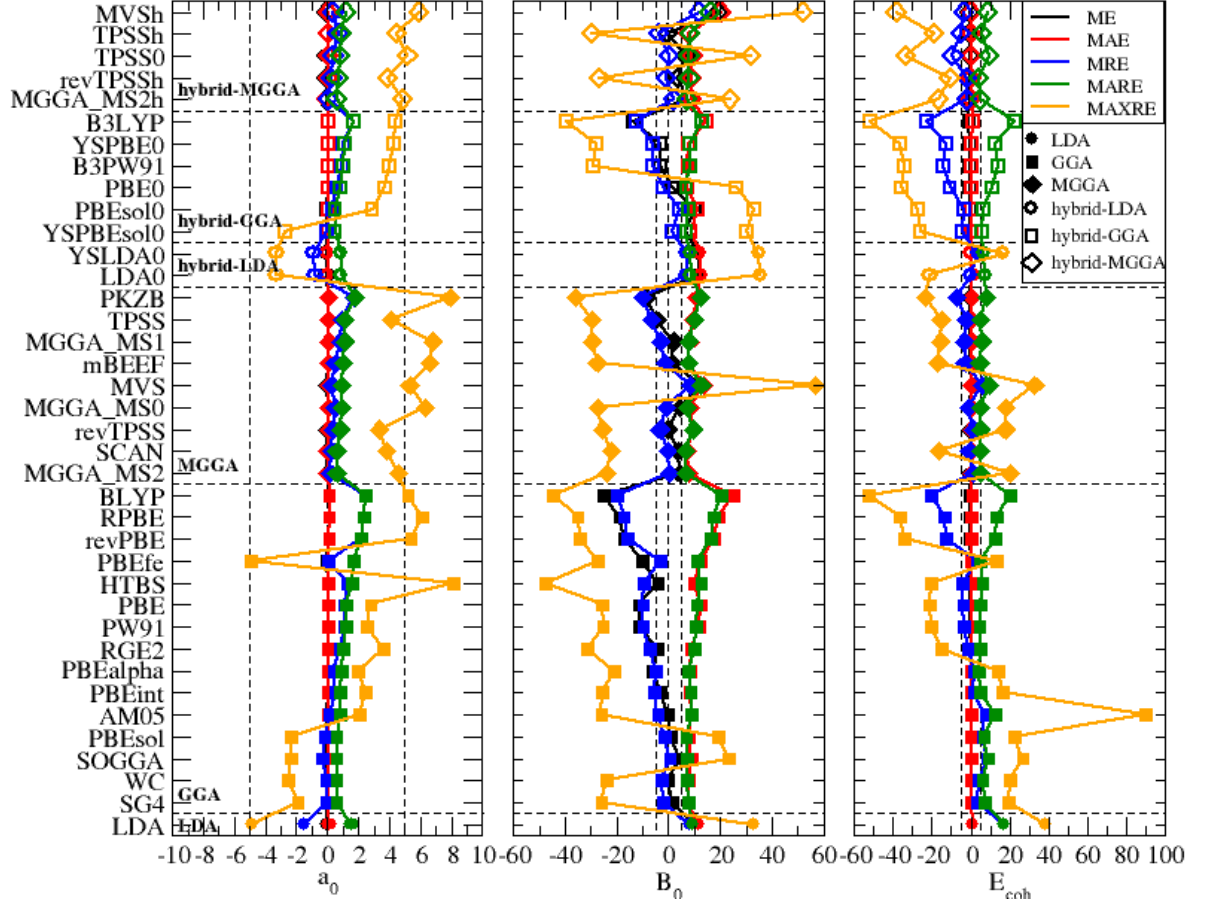
Figure 4.7: The mean error in (ME, black), mean absolute error (MAE, red), mean relative error (MRE, blue), mean absolute relative error (MARE, green), and maximum relative error (MAXRE, orange) on the testing set of the strongly bound solids reported in Ref. [64] for the (a) lattice constant a_0, (b) bulk modulus B_0, and (c) cohesive energy E_{coh}, when computed with LDA (full circles), GGA (full squares), MGGA (full diamonds), hybrid-LDA (open circles), hybrid-GGA (open squares), and hybrid-MGGA (open diamonds) functionals. The units of the ME and MAE are $\mathring{A}$, GPa, and eV/atom for a_0, B_0, and E_{coh}, respectively, and % for the MRE, MARE, and MAXRE. Adapted from Ref. [64].

4.3   Equations of State

A large number of equations in the literature are suitable for expressing the isothermal pressure-volume relationship. Since the bulk module (B_0), its first derivative (B_0), and the deformation of the volume with respect to the reference volume (V/V_0) can be measured precisely in the laboratory, they are available to define the isothermal equation of state (EoS). Thus, any isothermal EoS with only three arbitrary constants can be defined completely.

Though the isothermal equation of state is strictly applicable only at absolute zero, it is often used to describe the EoS of geophysical materials at room temperature or to duplicate the experimental data of materials taken at the room temperature isotherm. The justification of this rests on the similarity of the bulk modulus values of oxides and silicates at room temperature and at absolute zero, i.e., for minerals with a high Debye temperature [70]: for hard solid of geophysics and planetary sciences, room temperature is well below de the Debye temperature, and B_0 changes little between 0 K and 273 K. However, this statement cannot be made for soft solids like alkali metals.

The most widely used isothermal equation of state in solid geophysics is known as the third order Birch-Murnaghan EoS [71], given by:

$$P(V) = \frac{3B_0}{2}\left[\left(\frac{V_0}{V}\right)^{\frac{7}{3}} - \left(\frac{V_0}{V}\right)^{\frac{5}{3}}\right]\left\{1 + \frac{3}{4}(B_0' - 4)\left[\left(\frac{V_0}{V}\right)^{\frac{2}{3}} - 1\right]\right\} \qquad (4.2)$$

$$E(V) = E_0 + \frac{9V_0 B_0}{16}\left\{\left[\left(\frac{V_0}{V}\right)^{\frac{2}{3}} - 1\right]B_0' + \left[\left(\frac{V_0}{V}\right)^{\frac{2}{3}} - \right]^2\left[6 - 4\left(\frac{V_0}{V}\right)^{\frac{2}{3}}\right]\right\} \qquad (4.3)$$

The long use and wide application of the Birch-Murnaghan EoS has engendered for it a certain authority in the literature. However, its validity in the limit of the extreme compression has been questioned. A recent study [72] discussed the Shanker [73], Tait

[74, 75], Vinet [76], and Birch-Murnaghan [71] equation of states to check their validity a very large pressures. All these EOSs where compared with experimental data and also tested for the basic criteria which must be satisfied by an EOS for its validity and applicability as suggested by Stacy [77, 78, 79]:

1. In the limit $\to \infty, V/V_0 \to 0$.

2. With the increase in pressure isothermal bulk modulus must increase continuously and in the limit of infinity pressure $B \to \infty$.

3. B_0' must decrease progressively with the increase in pressure such that B_0' remains greater than 5/3 in the limit of infinite pressure.

Finally, in their work, Kholiya *et al.* [72] conclude that Tait, Vinet, and Birch-Murnaghan EOSs give the results compatible with the experimental findings but Tait
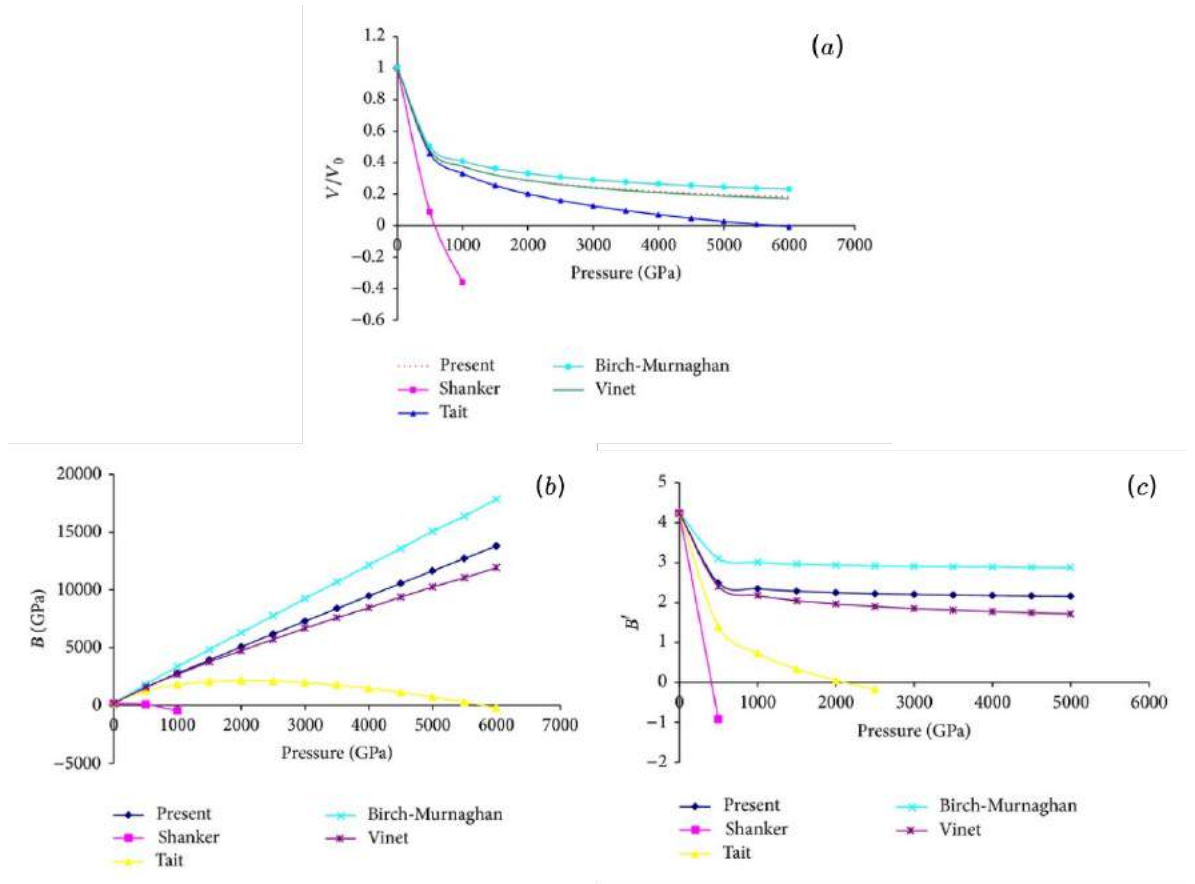
Figure 4.8: (a) Compression behavior V/V_0, (b) bulk modulus B_0, and (c) first order pressure derivative of bulk modulus B_0' at ultrahigh pressure using different EoSs. Taken from [72].

and Vinet EOSs fail to satisfy the basic criteria of an equation of state.

In general, for most applications of the equations of state there is little justification for choosing one EoS over another strictly on the basis of fundamentals. The choice is made on basis of convenience and tradition [70].

Part II

Carbon, Oxygen and Mixtures Under Extreme Conditions

5 Diamond and Post-Diamond Carbon Phases

In this section we perform density functional perturbation theory for diamond and post-diamond phases up to 3.50 TPa. Our goal is to reproduce the reported phase boundaries and to estimate the melting line varying the temperature up to 10000K and using corrections beyond the harmonic approximation.

5.1 Introduction

Given its importance to the sustainability of life on our planet, carbon is one of the most extensively studied materials. It has an extraordinary flexibility thanks to its oxidation range that goes from -4 to $+4$ allowing it to bond to itself and more than 80 elements. The two well-known stable phases of solid carbon are graphite and diamond, where the first is the most stable form at ambient conditions and the latter is stable at higher pressures, up to roughly 1 TPa. However, carbon exhibits a rich variety of solid structures [80, 81] like graphene [82], nanotubes [83], fullerenes [84], and the controversial carbynes [85, 86].

In the context of planetary sciences, it is expected that in the interior of super-Earths diamond transforms into other solid phases. This hypothesis has motivated theoretical studies that have proposed several post-diamond phases. The first one is found at around ~ 0.9 TPa: a body-centered cubic phase composed by eight atoms in the unit cell (BC8) [87, 88, 89, 90, 91], which is followed by a simple cubic (SC) phase above $\sim$ 2.5 TPa [90, 91]. These phase transformations affect the electric conductivity of carbon at high pressures. The BC8 phase maintains the sp^3 bonding from the diamond phase, but with some of its bond angles distorted, implying that the BC8 phase exhibit a reduced band gap, in comparison to diamond, and eventually becoming a weak metal

within the DFT formalism. Moreover, the six-coordinated SC phase is a metallic one, in which the covalent bond present in the two previous phases does not exist any longer.

Furthermore, in the multi-terapascal regime more phases have been proposed theoretically [90], with the following sequence: simple hexagonal (sh) → face-centered cubic (fcc) → double hexagonal closed packed (DHCP) → body-centered cubic (bcc), with transition pressures 6.4, 21, 270, and 650 TPa, respectively. These phases have been included in proposed phase diagrams [92, 89, 90, 91, 93], since there is no experimental evidence of the stability of the mentioned phases. Knowing the properties of carbon under extreme conditions of pressure and temperature is essential not only to comprehend the models of astrophysical bodies such as solar [94, 95, 96, 97] and extra-solar [98, 99] planets with carbon-rich interiors, white dwarf stars [100, 101, 102] and their interiors [103, 104], but also to understand the physics and chemistry of mono-atomic materials in general.

Given the enormous pressures that are required for the experimental study of the solid-liquid interface, the estimation of the melting curve from experimental data is challenging [105, 106]. Nevertheless, due to recent technical developments in dynamic shock-wave (ramp) compression it might be possible to achieve temperature and pressure conditions in the laboratory that are within the solid portion of selected phase diagrams [107, 108, 109], implying that reliable data from experiments may soon be able to study the properties of this element at planetary conditions. As a result, several attempts to determine the melting line of carbon at very high pressures have been
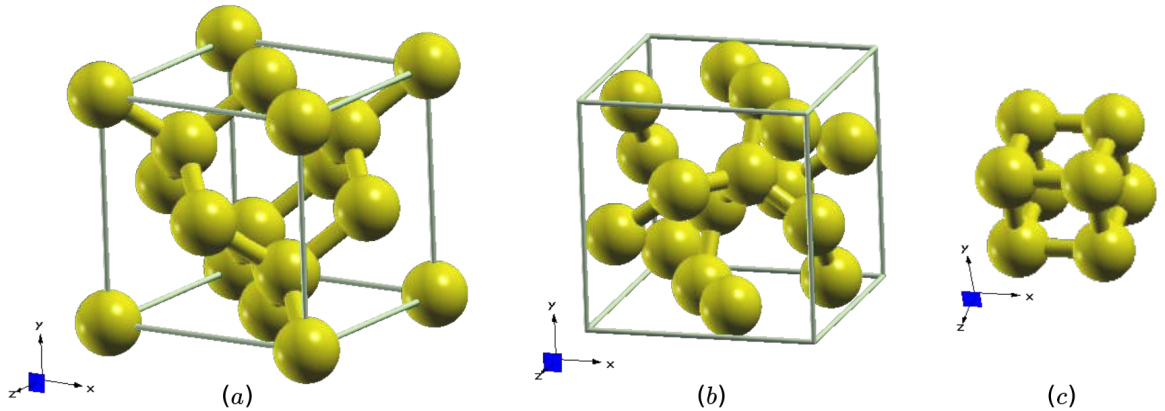

Figure 5.1: Studied high-pressure carbon phases: (a) Diamond at 0.5 TPa, (b) BC8 at 2.0 TPa, and (c) SC at 3.0 TPa.

made theoretically trying to include small anharmonic contributions [87, 92, 89, 91, 93]. However, the results are susceptible to the selected methodology for computing the free energy. Therefore, there is not a consensus on the theoretical work existing so far, that should be refined using more sophisticated, accurate methods until experimental information becomes available.

5.2   Computational Details

Carbon was examined in the pressure range from 0.25 to 3.50 TPa, which includes diamond, BC8, and SC. We performed variable-cell optimization calculation at steps of 0.25 TPa to obtain the structural parameters for all the phases using Density Functional Theory (DFT) as implemented in the Quantum ESPRESSO [22, 23] suite using projector augmented waves pseudopotential [21] with six electrons per atom. Generalized gradient approximation (GGA) of the exchange-correlation functional approximation of DFT of the Perdew-Burke-Ernzerhof (PBE) [18] form was used. The kinetic energy cutoff was set to 200 Ry[12], and $\mathbf{k}$-points grids of $8 \times 8 \times 8$, $4 \times 4 \times 4$, and $32 \times 32 \times 32$, were used for diamond, BC8, and SC, respectively, for integrating the Brillouin zone with the Monkhorst-Pack method [24]. These parameters ensure an energy convergence better than 1 meV/atom.

At $T = 0$K, harmonic dynamical matrices were obtained within Density Functional Perturbation Theory (DFPT) in the linear response regime [30] with a $\mathbf{q}$-points grid of $2 \times 2 \times 2$ for diamond and BC8, and $6 \times 6 \times 6$ for SC. Finite temperature contributions to the Helmholtz free energy were computed by means of QHA [39, 38] from 0 to 10000 K. We fitted the Helmholtz free energy and the volume of each phase at different temperatures to a 3rd order Birch-Murnaghan equation of state with a variance (χ^2) of order 10^{-6} or better, for all fits. Finally, the Gibbs free energy was calculated as:

$$G(P,T) \;\; = \;\; F[V(P,T),T] + PV(P,T). \tag{5.1}$$

_____

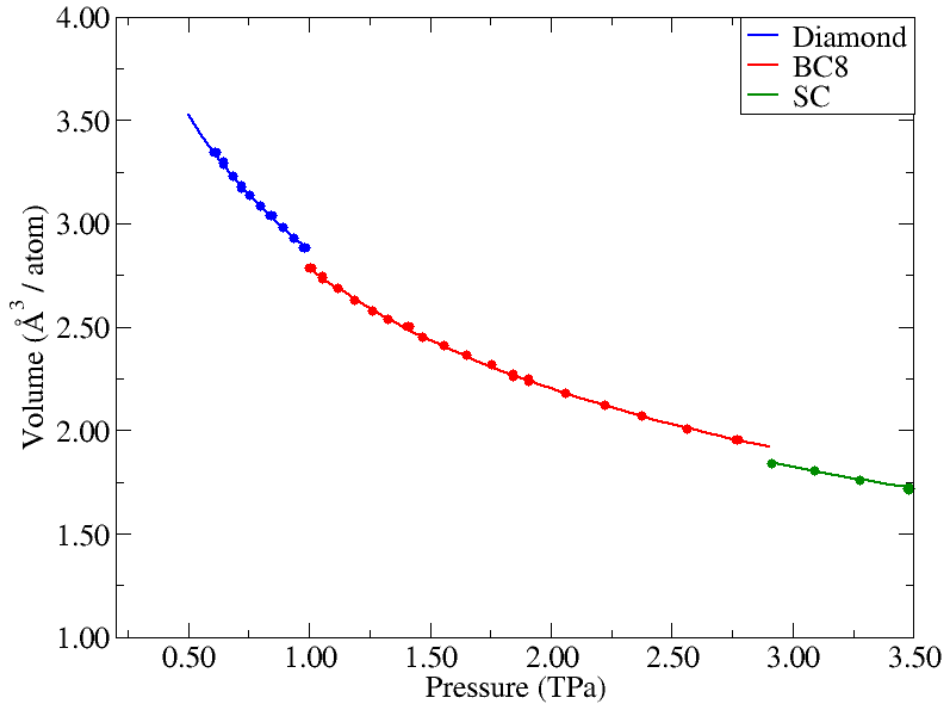[12]Data regarding convergence calculations can be found in the Appendix A

Figure 5.2: Pressure-volume relation of diamond (blue solid line), BC8 (red solid lines), and SC (solid green line), obtained from the 3$^{\text{rd}}$ order Birch-Murnaghan equation of state at room temperature. For each phase, calculated values from Ref. [90] are displayed in circles.

5.3   Phase transition boundaries

We begin our analysis by comparing the volume obtained from our equation of state with the data collected by Martinez-Canales *et al.* [90]. In their work, they used accurate pseudopotentials with small core radii and with all six electrons included explicitly. Thus, their proposed equation of state of carbon at high pressure is a good reference for evaluating our data. In Fig. 5.2 we show the volumes of the different phases as a function of pressure, indicating a good agreement between both equations of state.

Carbon has been studied widely, and the boundaries between phases have been calculated in several theoretical works, Refs. [87, 92, 89, 91, 93], some of which included small anharmonic corrections that refined the phase diagram of carbon at extreme conditions of pressure and temperature. We started by performing a comparison between our calculations from the quasi-harmonic approximation and proposed phase bound-

aries. The phase boundaries obtained using the finite temperature contribution to the free energy calculated using QHA are in excellent agreement with those including anharmonic effects as seen in Fig. 5.3. These results indicate that the quasi-harmonic approximation might be sufficient for calculating thermodynamical properties for diamond and post-diamond phases.

5.4   Melting Line for High-Pressure Carbon

In the temperature range used for our thermal calculations, we expect that at the highest values carbon becomes fluid for all phases. Initially we can estimate the possible solid-to-liquid transition region based on the Lindemann criteria. For each set of solid-phase simulations, we computed the ratio of the root-mean-squared displacement of the atoms to the nearest-neighbor distance. The melting lines assuming different critical
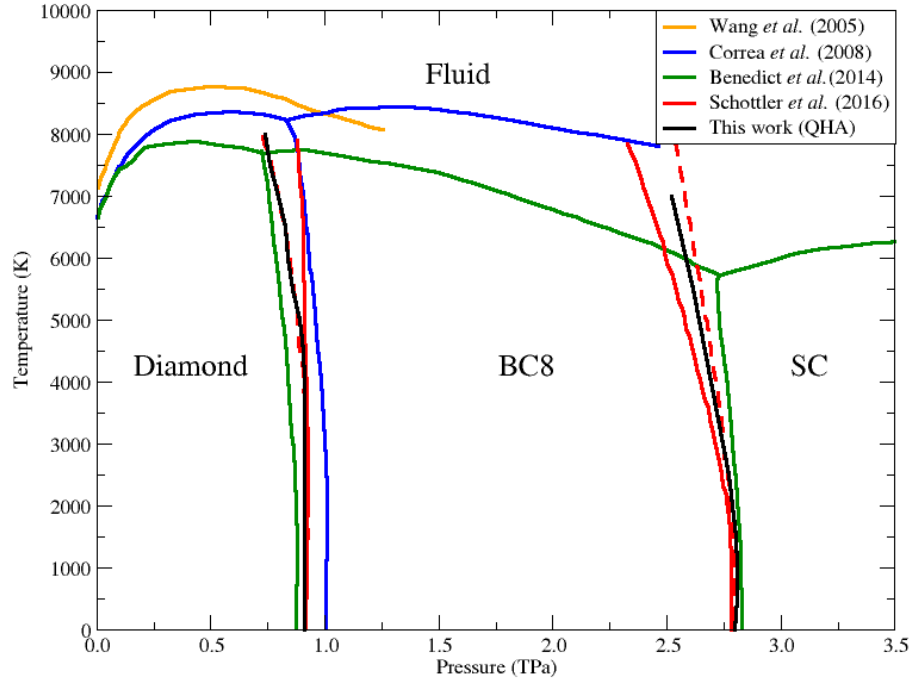
Figure 5.3: Proposed phase diagram for carbon at extreme conditions of pressure and temperature. Our calculated phase boundaries (black solid lines) are compared with previous theoretical calculations. The small anharmoic corrections performed by Schöttler *et al.* [93] are displayed in red dashed lines.
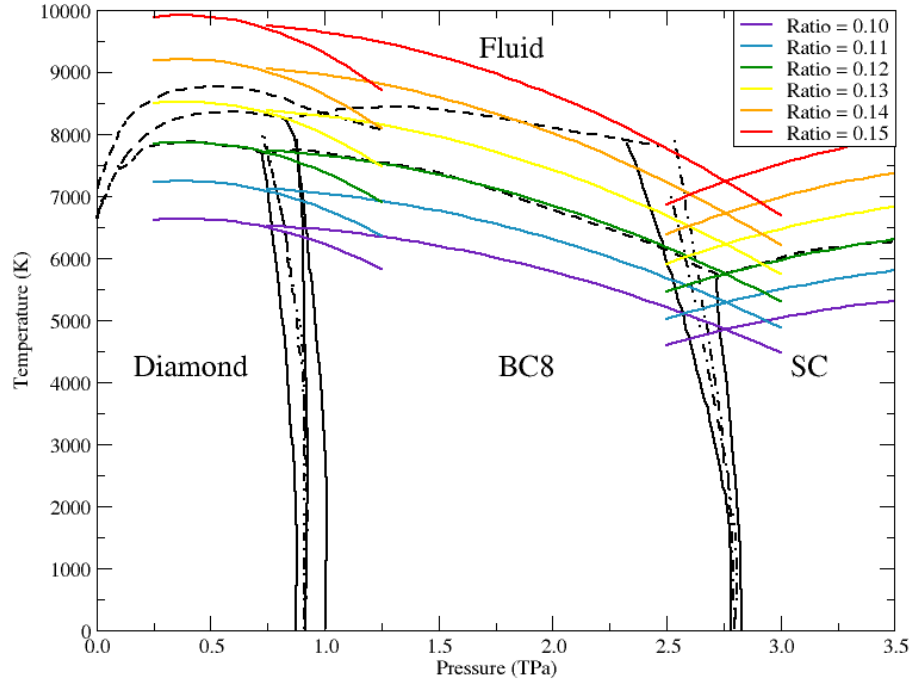
Figure 5.4: Estimated melting lines for phases of carbon in the terapascal regime for different critical Lindemann ratios.

Lindemann ratios are displayed in Fig. 5.4.

Although the Lindemann ratio of a solid phase is a quantity that for any given material normally reaches values between 0.10 and 0.15 at melting, in Fig. 5.4 we can observe that for carbon at this range of critical values the expected melting temperatures can span several thousand Kelvin. Thus, the right critical value of the Lindemann ratio for describing the transition to liquid in this chemical element, at high pressures, should be set close to 0.12. This critical value is supported by a comparison against recent results by Bendict *et al.* [91] for the melting line. Moreover, we can corroborate this by considering that, in the vicinity of melting, the entropy change for carbon's solid → liquid transition is estimated between 20 and 30 J · mol / K [92, 110]. Using that criteria, we were able to find a melting line using a threshold of 20 J · mol / K, as shown in Fig. 5.5. These results, point to the selection of 0.12 for the Lindemann ratio as a reasonable critical value to closely estimate melting curves, which, used with caution, could potentially be useful for post-SC phases of carbon as well.

Although we managed to reproduce the shape for the melting line using two different
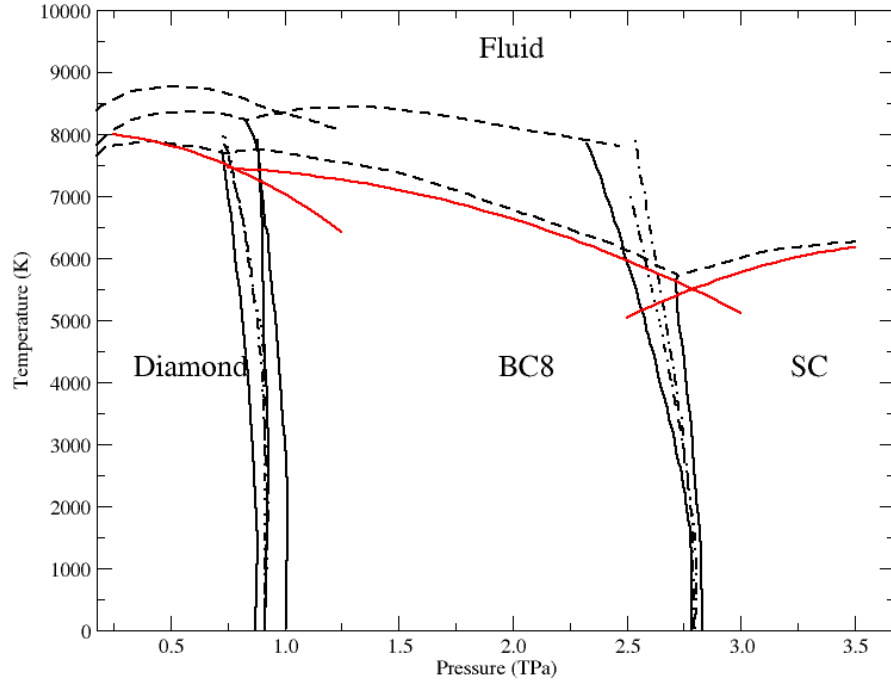
Figure 5.5: Estimated melting line for diamond and post-diamond phases using the difference of entropy as a criteria.

criteria, it is important to stress that only anharmonic effects could properly describe the melting line, since in the vicinity of the region of the solid-to-fluid transition non-harmonic behavior is crucial. However, due to technical challenges, we were unable to include as part of this report all the calculations that are required to incorporate anharmonic contributions using the stochastic self-consistent harmonic approximation, described earlier.

5.5   Conclusions

Using the quasi-harmonic approximation, the proposed solid-to-solid transition boundaries between diamond and subsequent phases that involve small non-harmonic corrections can be reproduced. Lindemann ratios in solids provide a reasonable approximation for finding the presence of melting transitions, at least qualitatively. Melting temper-

atures obtained with this method can be placed in a sufficiently restricted region of the P-T phase diagram by tuning the ratio's critical value that is used as a threshold, through comparison with alternative methods. Here, a Lindemann ratio around 0.12 is suggested as the best critical value to determine melting in carbon. Finally, in future studies, it is important to include non-harmonic effects into the Gibbs free energy in order to estimate the melting line more precisely, since QHA is not accurate enough for studying solid phases close to their transition into fluid. However, as shown here, QHA provides a reasonably good starting point.

6 Post-ζ Phases of Solid Oxygen

In this chapter we perform an exhaustive analysis of the electronic and the vibrational properties of the non-molecular phases of solid oxygen in the 1 to 10 TPa pressure range and within the quasi-harmonic approximation (QHA). These phases were proposed theoretically by Sun *et al.* [111], but they only reported the enthalpy-pressure relation. Our goal is to elucidate the impact of the finite temperature effects in the relative stability of those phases.

6.1 Introduction

Owing to the magnetic character of the O_2 molecule, the element oxygen exhibits a richer phase diagram than other low-Z diatomic molecules such as H_2, N_2, CO or F_2. Six phases of solid oxygen have been observed experimentally so far: half of them (α, β, and γ) exist under equilibrium vapor pressure, and the other three (δ, ϵ, and ζ) are obtained in the high-pressure regime. As pressure increases, oxygen shows a wide range of physical properties that go from insulating [112] to metallic [113], including also anti-ferromagnetic [114, 115, 116, 117] and superconducting [118, 119] phases. At the highest pressure reached for this element in the laboratory, about 130 GPa under diamond-anvil cell compression, it remains molecular[119]. In the ϵ-O_2 phase, which is stable between 8 and 96 GPa at ambient temperature[113], the oxygen molecules associate into clusters composed of four molecules, but they fully retain their molecular character as confirmed by vibrational spectroscopy and X-ray diffraction[120, 121].

All other group-VI elements develop non-molecular and eventually monoatomic structures at much lower pressure. Sulfur transforms into a chain-like polymeric phase at about 15 GPa and eventually becomes monoatomic, with a rhombohedral β-Po structure at 153 GPa[122]. Phases with a β-Po structure are also reported for Se at 60 GPa [123], for Te at 11 GPa [124], and for Po at ambient pressure [125]. Moreover,
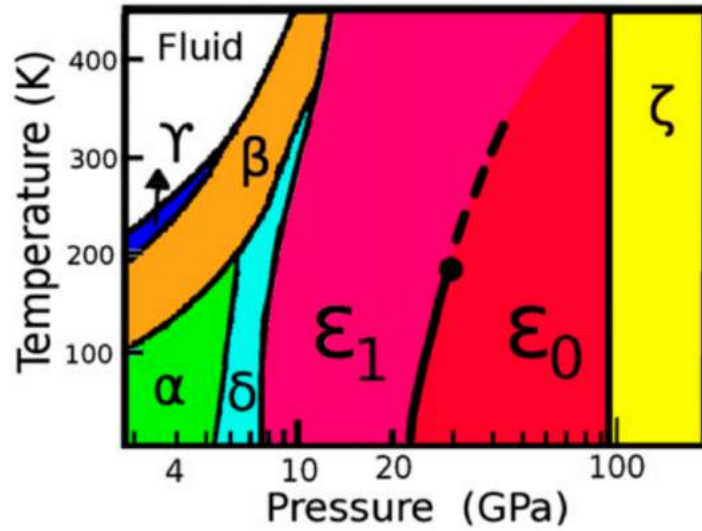
Figure 6.1: Phase diagram of solid oxygen. Taken from Ref. [112]
.

both selenium and tellurium exhibit a body-centered cubic (bcc) structure as a post β-Po phase [123, 126, 127]. For oxygen, however, an earlier theoretical study has shown that the monoatomic β-Po structure is less stable than molecular phases at multi-megabar pressures [128]. The reluctance of oxygen to give up its molecular character has been attributed in a recent study by Sun *et al.* to the strong electron lone-pair repulsion in the non-molecular phases. This resembles, we notice, the reluctance of the electron-richer halogen elements to lose their molecular character. For instance, Fluorine is molecular up to the highest pressures experimentally achieved so far in this element [129], while Cl_2, Br_2, and I_2 dissociate around 157, 115, and 43 GPa respectively [130, 131, 132, 133, 134, 135, 136, 137, 138].

In the same work, Sun *et al.*[111] show that oxygen remains molecular up to 1.9 TPa before transforming into a semiconducting square-spiral-like polymeric structure with symmetry $I4_1/acd$ and oxygen in two-fold coordination. This phase is then reported to transform at 3.0 TPa into a phase with $Cmcm$ symmetry, consisting of zigzag chains that pack atoms more efficiently than the square-spiral chains. Finally, when pressure reaches 9.3 TPa, the in-plane zigzag chains merge into a layered structure with $Fmmm$ symmetry and four equidistant nearest neighbors for each oxygen atom[111].

Temperature can have profound effects on the stability of molecular phases, both in their liquid and solid forms. Shock-compression experiments indicate that at about
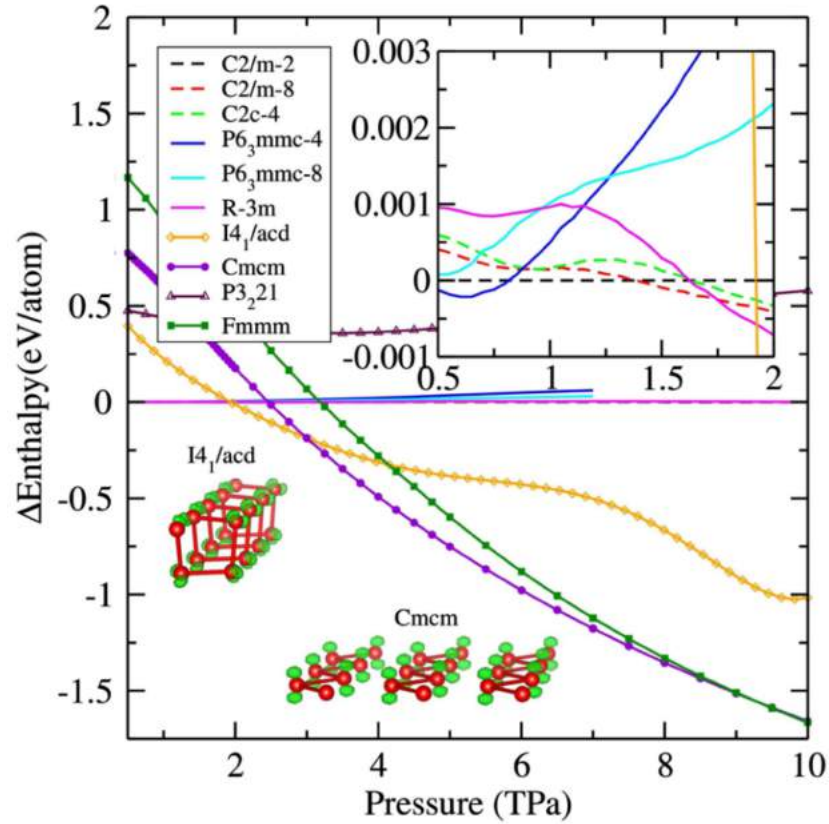
Figure 6.2: Enthalpy-pressure for proposed post-ζ phases for solid oxygen. Taken from Ref. [111]
.

100 GPa the oxygen molecule dissociates in the fluid when the temperature exceeds 4000 K [139]; whereas theoretical studies based on *ab initio* molecular dynamics place molecular dissociation above 80 GPa at temperatures that exceed 5000 K [140]. Unfortunately, nothing is known about the temperature effects on the phase diagram of *solid* oxygen at extreme pressures. A crude extrapolation of the oxygen melting line, based on theoretical and experimental data [141, 142], yields a melting temperature of about 26000 K at 1.9 TPa. Although this extrapolation is based on data below 100 GPa and is, therefore, to be taken with caution, this provides a hint that solid oxygen phases could indeed be the stable forms of this element in some planetary interiors. Hence, the understanding of the effects of temperature on the solid portion of oxygen's phase diagram at multi–megabar pressures is not only relevant from a fundamental perspective, but also for its potential relevance to planetary studies. Moreover, recent technical developments in dynamic shock-wave (ramp) compression have made it possible to achieve temperature and pressure conditions in the laboratory that are within

the solid portion of selected phase diagrams [107, 108, 109], suggesting that experiments may soon be able to study the properties of this element at planetary conditions.

The ground state calculations performed by Sun *et al.* [111] show that the transitions from molecular to polymeric and finally to 4-fold coordinated have dramatic effects on the vibrational properties of solid oxygen. Finite-temperature contributions to the free energy should, therefore, differ substantially between different phases and the phase transitions at high temperature may, as a consequence, differ quantitatively and qualitatively from the ones calculated at zero temperature. In this work, by performing density functional theory (DFT) together with quasi-harmonic approximation (QHA) calculations for the determination of vibrational free energies, we extend the current theoretical knowledge on the ultra-high-pressure region of the phase diagram of solid oxygen to temperatures up to 8000 K. We find that temperature has a remarkable effect on the phase diagram of this element indeed, resulting in the disappearance of two previously reported non-molecular forms at sufficiently high temperature.

6.2   Computational Details

Out of the several crystalline structures considered in the earlier theoretical work by Sun *et al.*[111], we select here the ones that were found to be stable in the range of pressure 1-10 TPa: a molecular structure with symmetry $R\bar{3}m$, and three non-molecular structures with symmetry $I4_1/acd$, $Cmcm$, and $Fmmm$, respectively. Enthalpy differences among the different molecular structures considered in Ref. [111] ($P6_3/mmc$, $C2/m$, $C2/c$, and $R\bar{3}m$) are small compared to enthalpy differences between molecular and non-molecular structures, so we expect transition pressures between molecular and non-molecular phases to be to largely independent of the specific molecular structure considered.

The structural properties were calculated using DFT as implemented in Quantum ESPRESSO [22, 23]. The electron-ion interactions were treated using a projector augmented wave [21] pseudopotential with six valence electrons. The valence electron wavefunctions are expanded in a plane-wave basis set with a kinetic energy cutoff of
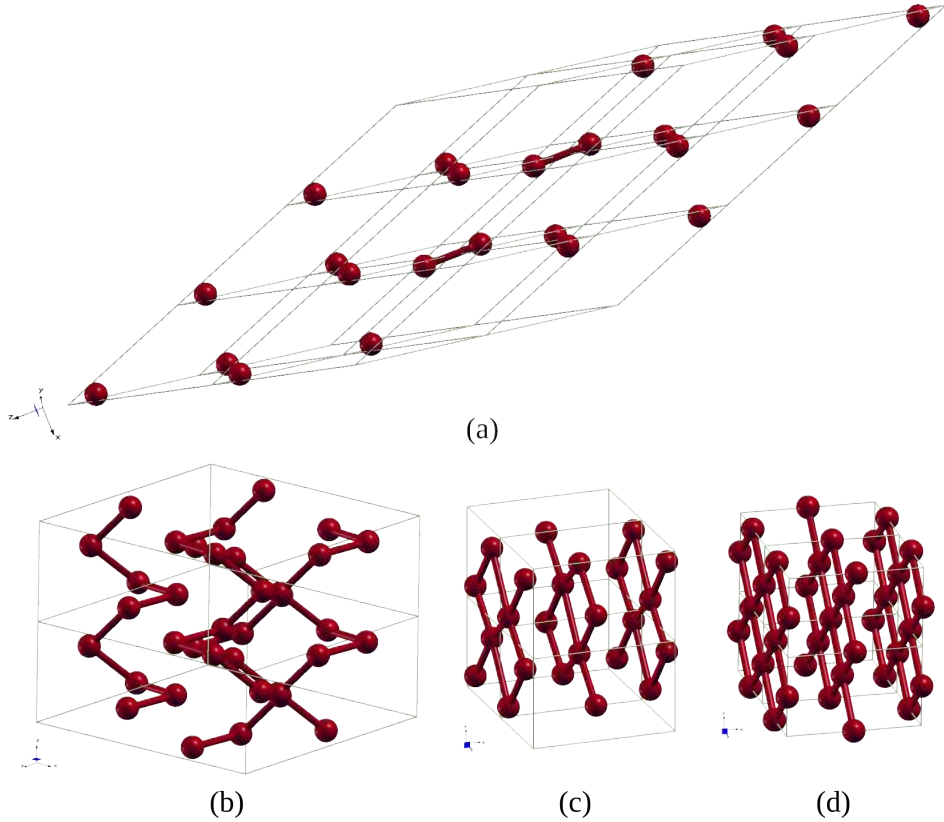
Figure 6.3: Some of the proposed post-ζ phases of solid oxygen: (a) $R\bar{3}m$ at 1.5 TPa, (b) $I4_1/acd$ at 2.0 TPa, (c) $Cmcm$ at 3.5 TPa, and (d) $Fmmm$ at 8.0 TPa.

400 Ry[13]. The exchange-correlation functional was approximated by the generalized gradient approximation (GGA) of the Perdew-Burke-Ernzerhof form [18]. Brillouin zone integrations were carried out using k-point grids generated with the Monkhorst–Pack method [24]. The size of these grids are $18 \times 18 \times 18$, $4 \times 4 \times 12$, $8 \times 16 \times 16$ and $8 \times 16 \times 16$ for the primitive cells of the four phases of oxygen considered in this study; these choices provided a total-energy-difference convergence of 2 meV per atom or better. The structural parameters for all the structures were obtained by performing variable cell optimization at various values of pressure. Note that the energies and electronic structures of the four structures have been already studied by Sun $et\ al.$ [111]; they showed that at $T = 0$ K, all the phases are metallic at the terapascal regime, except for $I4_1/acd$ which is a wide-gap semiconductor. For the metallic phases, the calculations were done using the Fermi-Dirac smearing technique with a width of 43 meV, in order to take into account the electronic entropy at 500 K. This width was

---

[13]Data regarding convergence calculations are in the Appendix B

kept fixed while calculating the vibrational properties at all temperatures, as justified by the lack of sensitivity of our free energy results with respect to this parameter.

The vibrational properties at $T = 0$ K were calculated using density functional perturbation theory (DFPT) in the linear response regime [30]. The q-point grids used to obtain the dynamical matrices were as follows: $4 \times 4 \times 4$ for $R\bar{3}m$, $2 \times 2 \times 6$ for $I4_1/acd$, $2 \times 4 \times 4$ for $Cmcm$, and $2 \times 4 \times 4$ for $Fmmm$.

Finite-temperature contributions to the Helmholtz free energy were obtained using the QHA [39, 38]. As we are interested in determining the pressure-temperature (P–T) phase diagram, we have calculated the Gibbs free energy as set in equation 5.1. The value of the P is obtained by fitting Eq. 5.1 to a 3rd order Birch-Murnaghan equation of state for each of the phases at different temperatures and their corresponding parameters are specified in the Appendix B. All fits had a variance (χ^2) of order 10^{-5} or better.

6.3   Proposed Phase Diagram for Ultra-High Pressure Phases of Solid Oxygen

We begin our analysis by considering the case $T = 0$ K, with and without the zero-point energy contributions. In the low-pressure region of this study we find that the contribution of the ZPE is marginal, moving the transition pressures 0.08 TPa and 0.02 TPa higher than those reported without ZPE when going from $R\bar{3}m$ to $I4_1/acd$ and from $I4_1/acd$ to $Cmcm$ respectively (see Fig.6.4). In the high-pressure region, our enthalpy-pressure relations show that the transition from $Cmcm$ to $Fmmm$ at 0 K is located near 8.6 TPa if ZPE is not included; this is 0.7 TPa lower than the transition pressure found by Sun *et al.* with the same approximations [111]. Our equations of state were fitted on a broader set of volumes than Sun *et al.*, usually fifteen or more volumes per structure. We believe that this could be one of the reasons for the discrepancy. Moreover, when the ZPE contribution is included, it has a noticeable effect, shifting the transition pressure from 8.6 TPa to 7.5 TPa.
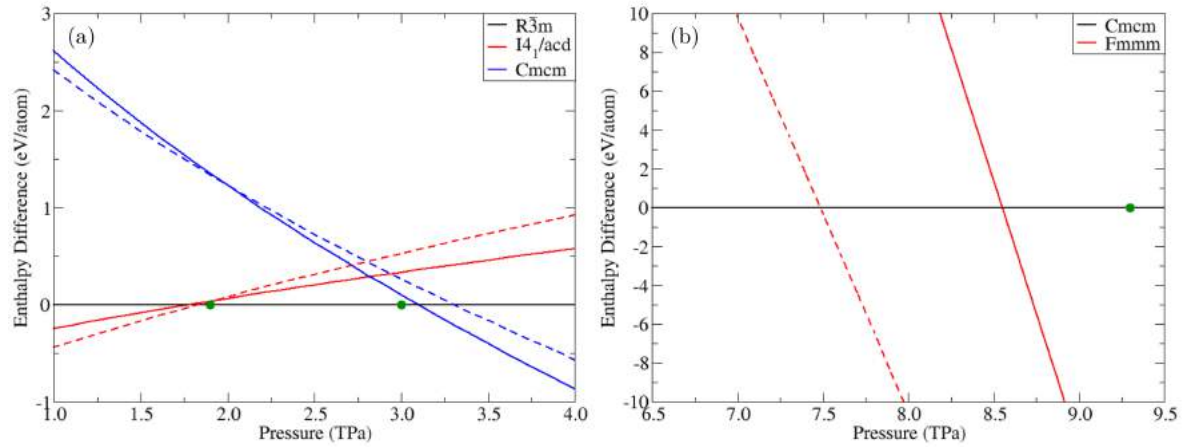
Figure 6.4: Enthalpy-pressure relations without (solid lines) and with (dashed) with ZPE for post-ζ phases of solid oxygen in (a) the low-pressure region which includes $R\bar{3}m$ (reference, black), $I4_1/acd$ (red), and $Cmcm$ (blue), and in (b) the high-pressure region where $Cmcm$ (reference, black) and $Fmmm$ (red) are represented. Transition-pressure reported by Sun et $al.$ are in green dots.

We now consider the effects of finite temperature on the Gibbs free energies and transition pressures. Our calculations are based on the QHA and may suffer from the incomplete consideration of anharmonicities, in particular when the system approaches the melting temperature, therefore, our analysis is restricted here to temperatures below 8000 K.

The finite temperature contribution to the free energy has dramatic consequences on the relative stability of the crystalline phases (Fig.6.5). For instance, the pressure location for the $R\bar{3}m$ to $I4_1/acd$ phase boundary is shifted towards higher pressures by approximately 1 TPa when the temperature is raised from 0 to 5000 K, indicating that the molecular $R\bar{3}m$ phase enlarges its region of stability with respect to the polymeric $I4_1/acd$, as temperature increases. However, the finite temperature contribution hardly changes the transition boundary between the phases $I4_1/acd$ and $Cmcm$, as we observed an increment of just 0.05 TPa at 5000 K with respect to the transition pressure calculated at 0 K. We observe that the region that encompassed the $I4_1/acd$ phase narrows down as temperature increases until, at 2.9 TPa and 5200 K, there is a triple point above which this phase disappears completely. Thus, the picture of $I4_1/acd$ as an insulating solid phase lying between two metallic ones ($R\bar{3}m$ and $Cmcm$) is only valid at relatively low temperatures. Unlike the previous two cases, the shift seen in the case of the $Cmcm$-to-$Fmmm$ transition is towards lower pressures and is much more pronounced, leading to a second triple point at 3.2 TPa and 7800 K, where the $R\bar{3}m$,
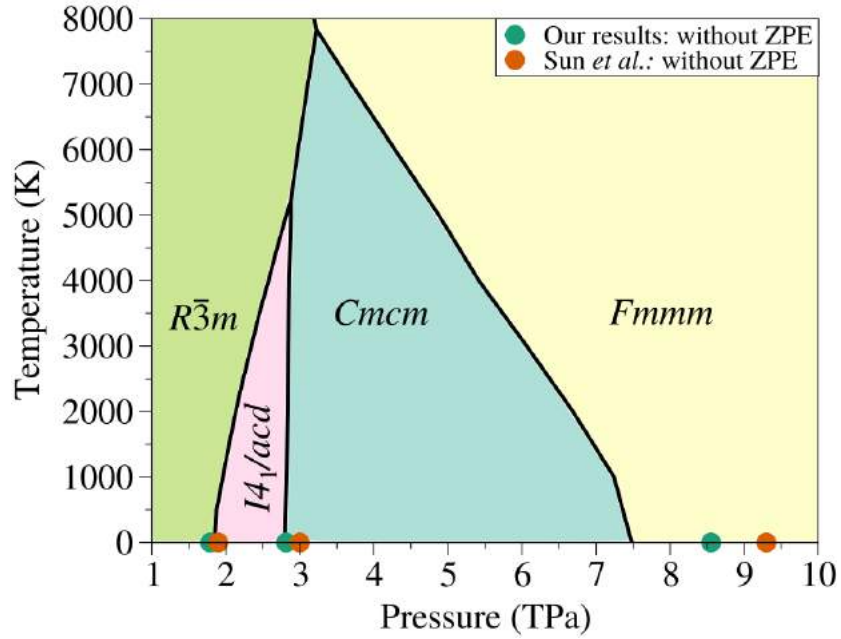
Figure 6.5: Proposed finite temperature phase diagram for solid oxygen at extreme conditions of pressure and temperature. The transition pressures P_{T}, at zero temperature without taking into account the zero-point energy (ZPE), reported by Sun *et al.* [111] and calculated in the present study, are marked as orange and green circles, respectively. The phase boundaries at finite temperature, corresponding to calculations including ZPE and using an electronic temperature of 500 K, are shown by solid black lines.

$Cmcm$, and $Fmmm$ phases meet. This indicates that above 8000 K Oxygen transforms directly from a molecular to a four-fold coordinated form.

So far our analysis has been restricted to a single molecular structure ($R\bar{3}m$) as a representative of the stable solid molecular oxygen form before polymerization. In order to test the validity of our assumption that $R\bar{3}m$ can be considered as representative of the stable molecular structure, we repeated the calculations with a different molecular structure, of symmetry $C2/m$. This structure was found to possess the second lowest enthalpy after $R\bar{3}m$, among the structures considered by Sun *et al.* [111]. We find that the transition line between $C2/m$ and the other structures is indistinguishable from the transition line of $R\bar{3}m$ (see Fig. 6.6, suggesting that not only enthalpy, but also entropy is very similar among different molecular forms.

As already mentioned, an extrapolation of the measured melting line of Oxygen to TPa pressures yields a melting temperature exceeding 25000 K at 2 TPa. An indepen-
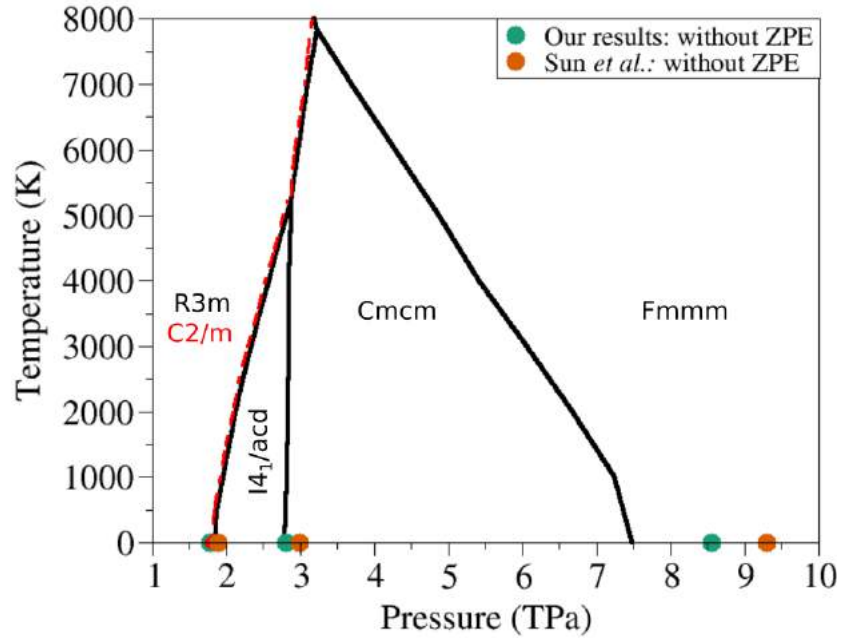
Figure 6.6: Proposed phase diagram for solid oxygen at extreme conditions of pressure and temperature. The phase boundaries between molecular phases $R\bar{3}m$ and $C2/m$ and the non-molecular phases $I4_1/acd$ and $Cmcm$, are shown in black solid line and red dashed line, respectively.
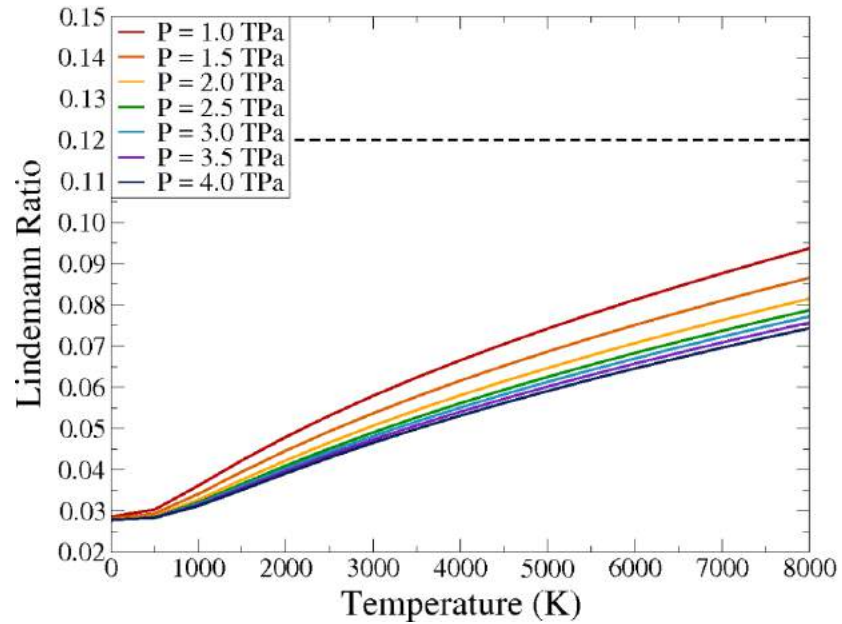

Figure 6.7: Lindemann ratio of the molecular phase $R\bar{3}m$ as a function of temperature at different pressures. The dashed line indicates the value in which the system is expected to become liquid.

dent estimate of the melting temperature can be obtained by calculating the Lindemann ratio of the solid phases, a quantity that normally reaches values between 0.1 and 0.15 at melting. We calculated the Lindemann ratio for the $R\bar{3}m$ molecular structure and for the $Fmmm$ structure within the QHA approximation. In the case of the molecular structure we assumed that melting takes place between a molecular solid and a molecular liquid and evaluated the Lindemann ratio based on the mean-square displacement of the center of mass of the molecules. We found that calculated values of L_R are always below 0.095, for both phases, in the temperature range from 0 K to 8000 K, as seen in Fig. 6.7. Our calculations therefore rule out the presence of a liquid in the pressure and temperature region considered in this work.

We were also able to confirm that strongly localized lone pairs persist into the polymeric phases with an OX_2E_2 bent shape, as already noted by Sun *et al.* [111]. This, together with an electron counting argument, can explain the reluctance of oxygen to take higher coordinated structures. The formation in $I4_1/acd$ of one additional covalent bond and the lone pair repulsion between chains, contribute to making it stiffer and less flexible than the molecular $R\bar{3}m$ phase. At temperatures below 4000 K the contribution to the entropy of the high frequency vibron in Fig.6.8a is limited by quantum effects. The remaining modes show a frequency increase across the transition, which implies a decrease of the vibrational entropy. This is consistent with the positive slope of the transition line at finite temperature (see Fig.6.5). Similarly, the $I4_1/acd$ and $Cmcm$ phases are characterized by having two covalent bonds per oxygen and very similar lone pair repulsion between chains. Therefore, one does not expect important changes
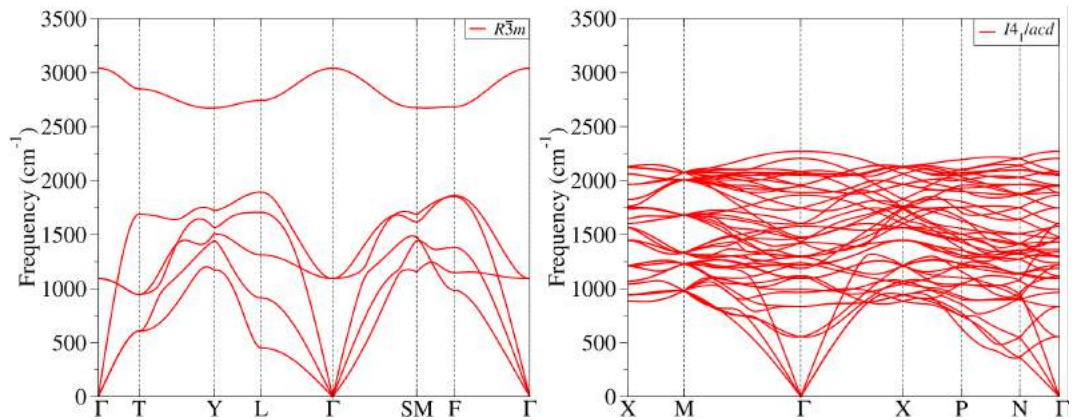

Figure 6.8: Phonon dispersions of oxygen in (a) $R\bar{3}m$ with the vibron mode in dashed line and (b) $I4_1/acd$ phases at 2.0 TPa.

in terms of bonding and stiffness, which justifies why we observe an almost vertical transition line between these two polymeric forms in the P-T phase diagram (Fig. 6.5).

6.4   The $Cmcm$-to-$Fmmm$ phase transition

As pressure increases above 4 TPa and keeps approaching the vicinity of the $Cmcm \rightarrow Fmmm$ transition, the bent shape of the lone pairs in $Cmcm$ starts to allow for a non-symmetrical four-fold coordination, which brings the formation of two additional weak covalent bonds per each oxygen prior to the final transition towards the fully symmetric $Fmmm$ configuration; this is shown in Fig 6.9(a) by the charge density profiles. This process causes a gradual merging of the so-called zigzag chains into a layered structure. For instance, at $T = 0$ K and 7.0 TPa, the four shortest links for each oxygen consist of two sets of bonds with lengths 1.04 Å and 1.18 Å, respectively. Instead, when $Cmcm$ transforms into $Fmmm$ above 7.5 TPa not only the coordination of the oxygen atoms becomes symmetrical, with an equal length of 1.10 Å, but also we can see now that the lone pairs adopt the OX_4E_2 square planar shape, as a consequence of the higher symmetry of this phase as Fig. 6.9(b) shows.
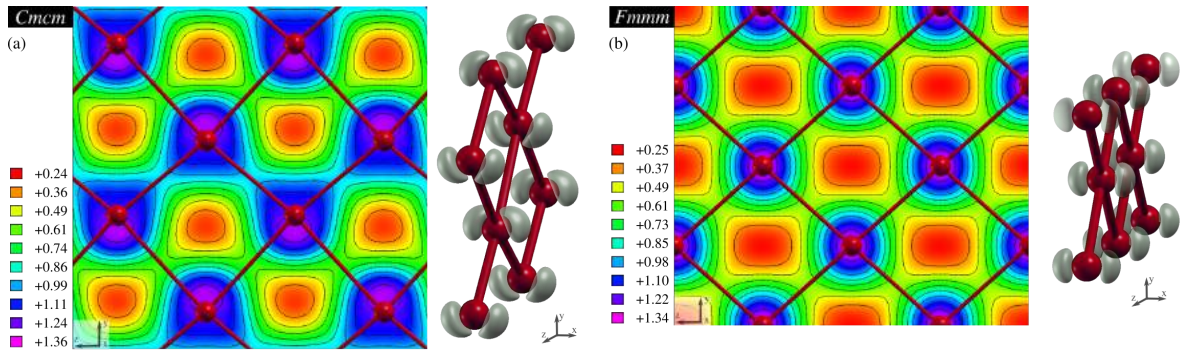
Figure 6.9: Electronic charge densities along the [100] direction and electron lone pairs of (a) $Cmcm$ and (b) $Fmmm$ at 7.5 TPa. The color scales indicate the values of the charge density in $e/Bohr^3$. On the left panel, the isosurface of red and orange regions are electron poor; while blue and violet regions are electron rich. Additionally, isosurface contours are shown by solid black lines. On the right panel, the lone pairs are represented by transparent gray colors; the corresponding isosurface value is $+1.25$ $e/Bohr^3$. The oxygen atoms are represented by red spheres and the $Cmcm$ zigzag chains are shown in red and pink.
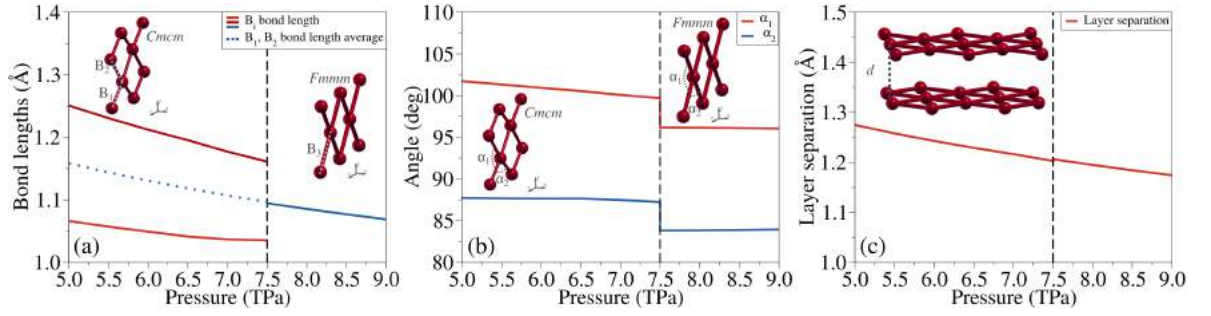
Figure 6.10: Pressure dependence of (a) bond lengths for $Cmcm$ (B_1 and B_2, red and pink solid lines, respectively) and $Fmmm$ (B_3, blue solid line), (b) internal angles (α_1 and α_2, red and blue solid lines, respectively) of $Cmcm$ and $Fmmm$, and (c) the layer separation d (red solid line) for $Cmcm$ and $Fmmm$ are shown. The vertical black dashed line corresponds to the calculated transition pressure between these two phases. The average of B_1 and B_2 are also shown by a dotted blue line in (a).

From a space-group point of view, $Cmcm$ is a subgroup of $Fmmm$ so that the transition can be classified in principle as a second-order phase transition. Coupling of the strain with the internal degrees of freedom, however, introduces a slight discontinuity in the structural parameters (see Fig. 6.10), similarly to the case of the stishovite(rutile) to the CaCl$_2$-type phase transition in SiO$_2$ [143]. Further evidence for the quasi-second-order nature of the transition comes from the phonon dispersions of the two phases.

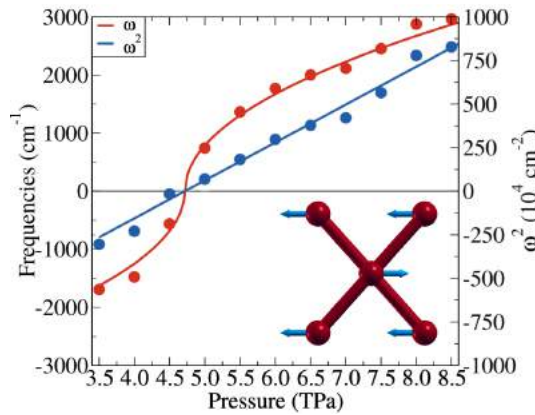Figure 6.11: Evolution of a $Fmmm$ phonon mode at the zone boundary as a function of pressure. The normal mode is along the [100] direction, and its frequencies (ω) are plotted in red. A linear relation between the squared phonon frequencies (ω^2) and pressure (blue) is observed and indicates that the phonon softening occurs near 4.7 TPa. The normal mode is represented as blue arrows on the atoms of the $Fmmm$ structure.
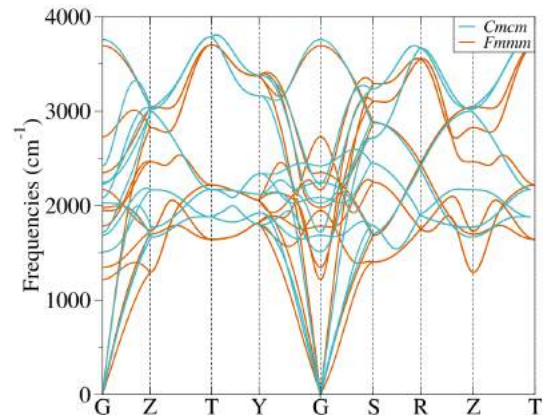

Figure 6.12: Phonon dispersions of oxygen in (a) $Cmcm$ (in cyan) and (b) $Fmmm$ (in orange) phases at 8.0 TPa. Note that the supercell size has been used in both the cases.
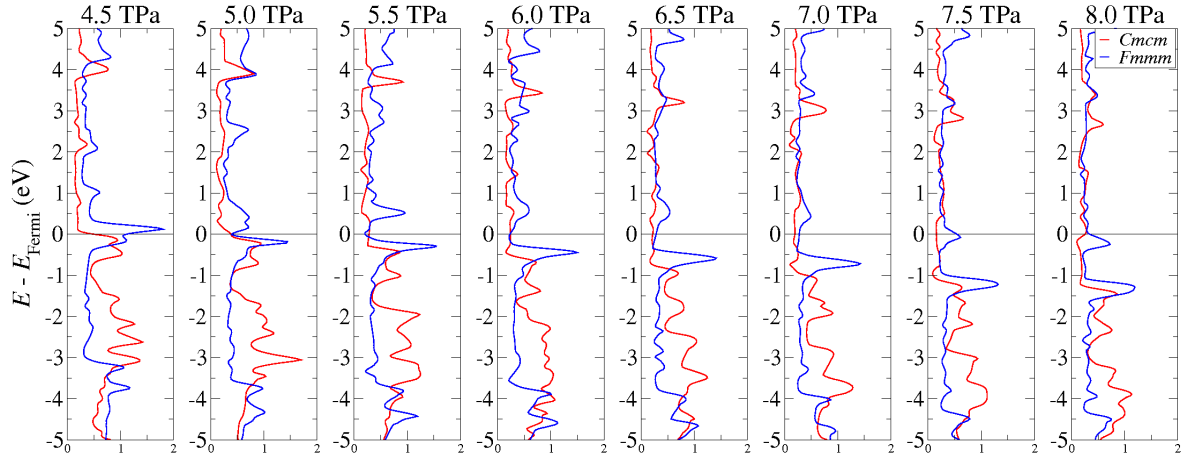
73

Figure 6.13: Electronic DOS of oxygen in (a) $Cmcm$ (in red) and (b) $Fmmm$ (in blue) phases as a function of pressure.

In Fig. 6.11 we show the pressure-dependence of the frequency of the phonon mode at the Brillouin Zone vector of the $Fmmm$ phase corresponding to the reciprocal lattice vector of the $Cmcm$ phase. The mode becomes unstable when pressure is decreased below 4.7 TPa, indicating a lattice instability of the $Fmmm$ phase towards $Cmcm$, as also confirmed by the pattern of the unstable mode, shown in the inset of Fig. 6.11. A characteristic feature of second-order phase transitions is the higher entropy of the high-symmetry phase with respect to the low-symmetry phase. This is consistent with the pronounced left-turning of the $Cmcm$ to $Fmmm$ phase transition line at finite temperatures in Fig. 6.5, and it is confirmed by the phonon dispersions of the two phases calculated at the transition pressure of 8.0 TPa (Fig. 6.12). Contrary to the naive expectation that frequencies become stiffer in the high-pressure ($Fmmm$) phase with respect to the low-pressure ($Cmcm$) phase, the phonon dispersion of the $Cmcm$ phase has modes that are marginally higher in energy than those of the $Fmmm$ phase. This is consistent with the lower entropy of the $Cmcm$ phase with respect to the $Fmmm$ phase.

To gain further insight into the driving force of the quasi-second-order transition, we show in Fig. 6.13 the electronic density of states (DOS) of the two phases in the vicinity of the pressure where $Fmmm$ becomes unstable. Interestingly, the DOS of the $Fmmm$ phase shows a pronounced peak that crosses the Fermi level between 4.5 and 5.0 TPa, the same pressure of the phonon instability reported in Fig. 6.11. The distortion leading to the $Cmcm$ structure causes a lowering of the DOS at the Fermi level. We, there-

fore, argue that the $Cmcm$ to $Fmmm$ transition is driven by an electronic instability qualitatively similar to a commensurate charge-density-wave transition. A similar phenomenology has been observed in other chalcogen elements, where it has been shown to be connected with the emergence of a superconducting state in the undistorted state ($Fmmm$ in this case) close to the transition pressure to the distorted phase [122].

6.5 Conclusions

Our theoretically predicted phase diagram of Oxygen at extreme pressures and temperatures extends earlier calculation at high pressure and zero temperature and shows that temperature has a profound effect on the phase diagram. At finite temperatures, the molecular phase expands its stability range to pressures exceeding 3 TPa at the highest temperatures considered in this work (8000 K). On the contrary, the range of stability of the first non-molecular phase, $I4_1/acd$, shrinks with temperature and the phase is no longer thermodynamically stable above 5000 K. Interesting physics underlies the transition between the $Cmcm$ and the $Fmmm$ non-molecular phases. Our calculations indicate a quasi-second-order transition between the two phases and show that the transition is driven by an electronic instability causing a softening of the corresponding phonon mode. We argue that this may imply a superconducting state which is beyond the scope of this work but which certainly deserves further attention. The range of pressures and temperatures examined in this work are now within reach of ramp-compression experiments which we hope will soon shed additional light on the intriguing aspects of the pressure-induced demise of molecular oxygen as reported in this and other recent theoretical studies.

7   Molecular and Non-Molecular Carbon Dioxide

In this chapter we show the results of our *ab initio* analysis of the vibrational properties of some of the phases of carbon dioxide (CO_2), including molecular and non-molecular ones, up to 70 GPa and 2000 K. Our goal is to provide useful information that leads to diminish the uncertainty in the currently accepted phase diagram, where the phase boundaries are still a matter of discussion.

7.1   Introduction

Widely studied during the past years, carbon dioxide (CO_2) is a fascinating system that exhibits up to seven solid phases despite its simple molecular form (see Fig. 7.1), that is, a linear structure made of two covalent bonds between each oxygen and the carbon atom, with a bond length of 1.16 Å under ambient conditions [144]. At room temperature the CO_2 gas transforms into a liquid at 7.5 MPa, and at 0.5 GPa it solidifies into the face-centered cubic phase I ($Pa\bar{3}$) [145, 146]. Remaining at room temperature, but going above 10 GPa, phase I transforms to the orthorhombic phase III ($Cmca$), with a minimal volume change associated to the $Pa\bar{3} \rightarrow Cmca$ transition [147]. A recent theoretical study has provided insight on the mechanism of the polymorphic $Pa\bar{3}$-to-$Cmca$ transition, showing this transition as a concerted distortion process in which the CO_2 molecules rearrange by distorting the CO_2-I lattice anisotropically [148]. By heating phase III above 16 GPa and $\sim$ 500 K [149, 150], phase II can be obtained. However, CO_2-II can be recovered at ambient temperature suggesting that the CO_2 III-to-II transition is not only irreversible, but also that CO_2-III is a metastable phase that can only be obtained by compressing the phase I at low temperatures [149, 151]. Initially presented as a pseudo-six-fold phase, it was thought that phase II was an intermediate state between the molecular and the extended solid form of CO_2 [152].
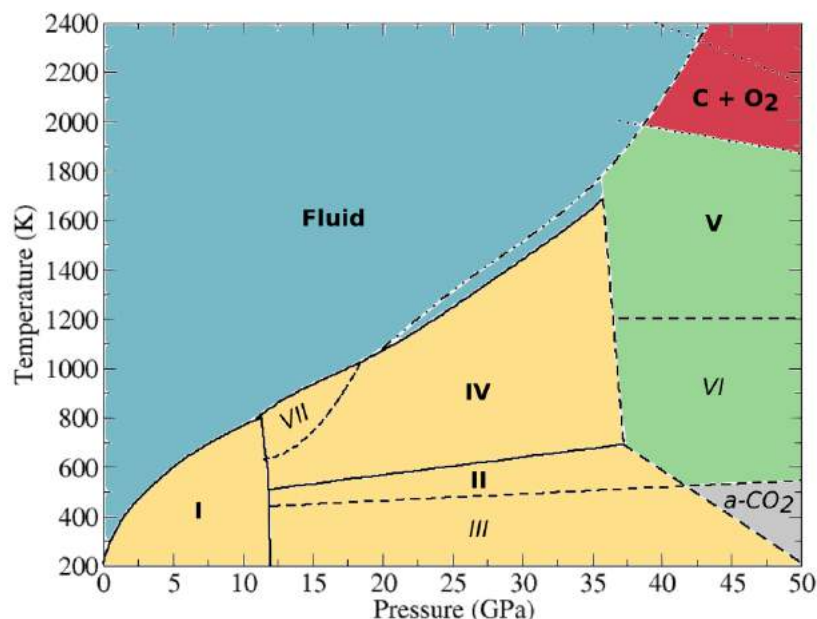
Figure 7.1: High-pressure CO_2 phase diagram adapted from Ref. [158]. Yellow, green, blue, red, and gray areas correspond to the molecular, non-molecular, fluid, dissociated, and amorphous forms of CO_2. Solid lines correspond to thermodynamic phase boundaries, while dashed lines are kinetic boundaries. The dot-dashed line represents the fluid curve, and the dotted lines indicate the regions where carbon dioxide decomposed into carbon and oxygen. The selected names in italic stated the metastable phases.

However, experimental results disproved the existence of an intermediate bonding state and identified the structure of phase II as $P4_2/mnm$ [153]. When CO_2-II is heated in the $500 - 720$ K range, depending on the pressure [149, 151], phase II transforms into CO_2-IV. As occurred with phase II, phase IV was designated as intermediate bonding state [154]. However, it was shown experimentally that CO_2-IV is still composed of linear molecules and its crystalline structure is the rhombohedral $R\bar{3}c$ [155]. Interestingly, an intermediate phase between CO_2-I and CO_2-IV was observed by heating CO_2-I and going up to 20 GPa at 950 K, this was identified as a molecular high-temperature stable $Cmca$ phase [156]. Given the fact that this phase (CO_2-VII) and CO_2-III have the same space group, it was thought that these two phases were indeed identical. However, differences between their Raman spectra suggested that they were different [156]. Nevertheless, a recent theoretical study based on crystal structure prediction *via* evolutionary algorithms has shown that CO_2-III relaxes into CO_2-VII. Therefore they propose that these two phases are in fact the same [157].

The non-molecular CO_2-V phase was first synthesized by laser heating CO_2-III above

40 GPa and 1800 K [159], and its crystalline structure was determined to be a partially collapsed cristobalite structure, with space group $I\bar{4}2d$ [160, 161]. Employing an isothermal compression of CO_2-II at temperatures between 530 and 650 K, and going above 50 GPa, another non-molecular form of carbon dioxide (CO_2-VI) was synthesized [154] and it is interpreted as a layered tetrahedral phase [162]. In addition to the molecular and polymeric phases, an amorphous form of carbon dioxide (a-CO_2) was observed after compressing CO_2-III in the pressure range 40 – 48 GPa at room temperature [151]. Moreover, at pressures between 30 and 80 GPa, and temperatures above 1700 K, CO_2-V dissociates into elemental carbon (diamond) and oxygen (ϵ-O_2) [163, 164]. The currently accepted phase diagram that includes all the mentioned forms of solid CO_2 along with the region where it becomes into a fluid is shown in Fig. 7.1.

Thus, theoretical and experimental studies have proven that CO_2 owns a very complex phase diagram made of molecular, non-molecular, and amorphous forms, as shown in Fig. 7.1. Nevertheless, the phase boundaries are still a matter of discussion given the presence of several kinetic boundaries, that may differ to each other depending on the $P-T$ path followed. Particular attention has been directed towards the molecular-to-non-molecular boundary, where in the past decade the proposed kinetic barriers have been essentially different. Santoro $et\ al.$ [165] transformed CO_2-II and CO_2-III into CO_2-V and using Raman spectroscopy proposed a phase diagram where the CO_2 transformation to a non-molecular form started around 21 GPa at $T=0K$ at room temperature, and the boundary between the molecular and the non-molecular structures exhibits a positive slope. Nonetheless, a later study by Santoro and Gorelli [166] proposed a new kinetic border with negative slope from infrared spectroscopy measurements based on the formation of amorphous carbonia from the molecular CO_2. Therefore, given the difficulty to experimentally determine the thermodynamic phase boundary between the molecular and non-molecular forms, due to the large metastability exhibited by CO_2 in the high-pressure regime, in the present work we present a theoretical phase boundary between the molecular phases II, III, and IV, and the non-molecular phase V.
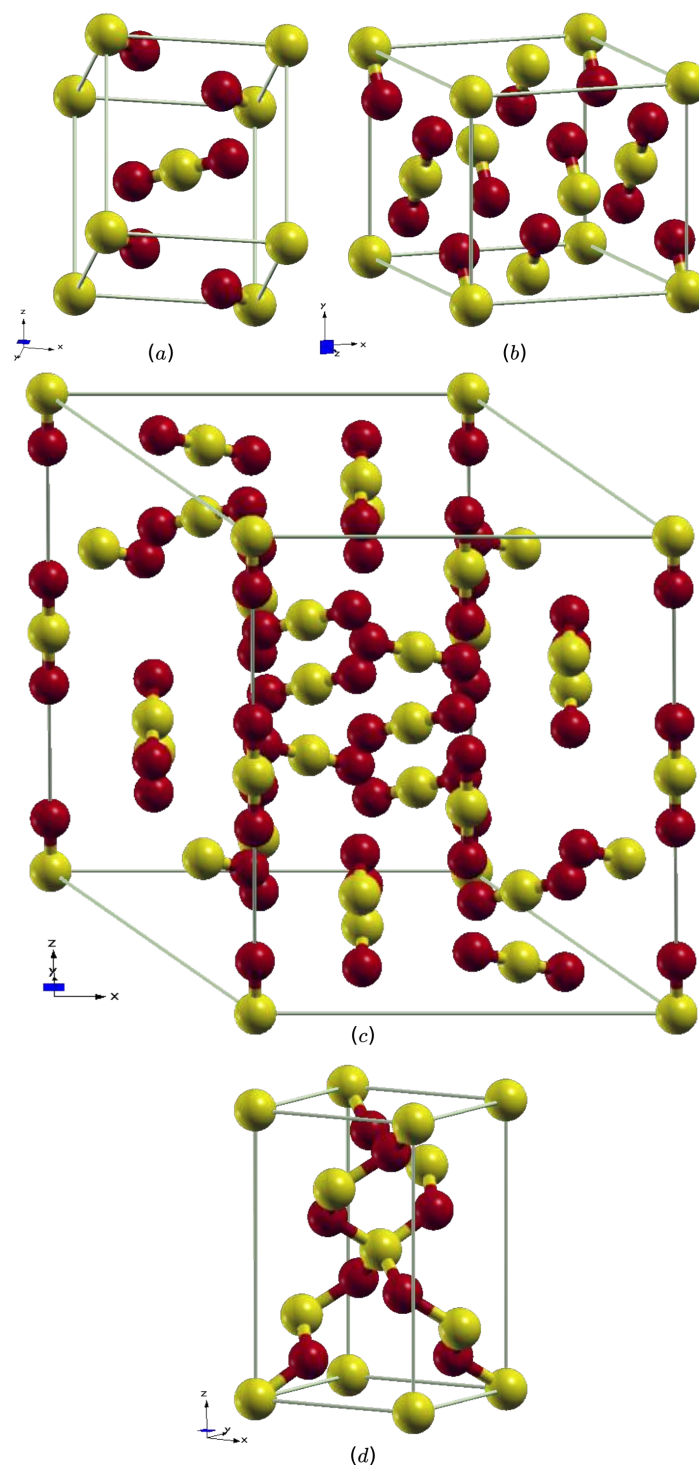
Figure 7.2: Studied phases of carbon dioxide: (a) CO_2-II ($P4_2/mnm$), (b) CO_2-III ($Cmcm$), (c) CO_2-IV ($R\bar{3}c$) at 18 GPa, and (d) CO_2-V ($I\bar{4}2d$) at 26 GPa. Carbon atoms are represented as yellow spheres, while oxygen atoms corresponds to the red ones.

7.2   Computational Details

Ab initio electronic structure calculations were carried out using density functional theory (DFT) and the projector augmented wave (PAW) method, as implemented in the Quantum ESPRESSO suite [22, 23] with a kinetic energy cutoff of 200 Ry for the plane-wave basis set[14]. Generalized gradient approximation (GGA) for the exchange-correlation energy was implemented using the Perdew-Burke-Ernzerhof functional [18]. The Monkhorst-Pack method [24] was used to generate the k-points grids for sampling the Brillouin zone. Selected grids for the primitive cells of the phases $P4_2/mnm$, $Cmca$, $R\bar{3}c$, and $I\bar{4}2d$, namely CO_2-II, CO_2-III, CO_2-IV, and CO_2-V, respectively were chosen to ensure an energy convergence better than 1 meV per formula unit (f.u.) of CO_2. Variable-cell optimization calculations were performed to obtain the structural parameters for all phases within a range from 10 to 70 (GPa) at steps of 4 GPa.

Density functional perturbation theory (DFPT) within the linear response scheme [30] was used to calculate the vibrational properties of the three different CO_2 phases at zero temperature. By means of the quasi-harmonic approximation (QHA) [39, 38] the finite-temperature contributions to the Helmholtz free energy were computed. For the construction of the pressure-temperature (P-T) phase diagram, we first obtained for each phase the value of P, and subsequently V, by fitting the Helmholtz free energy at different temperatures to a 3rd order Birch-Murnaghan equation of state. The variance (χ^2) of all fits were of order 10^{-5} or better. Finally, the Gibbs free energy was calculated as set in equation 5.1.

7.3   Phase Boundaries and Phase Diagram of solid CO_2

We start making a comparison of the volumes reported from predicted and experimental structures for phases CO_2-II, CO_2-III, CO_2-IV, and CO_2-V, with our relaxed

---

[14]Data regarding convergence calculations are in the Appendix C
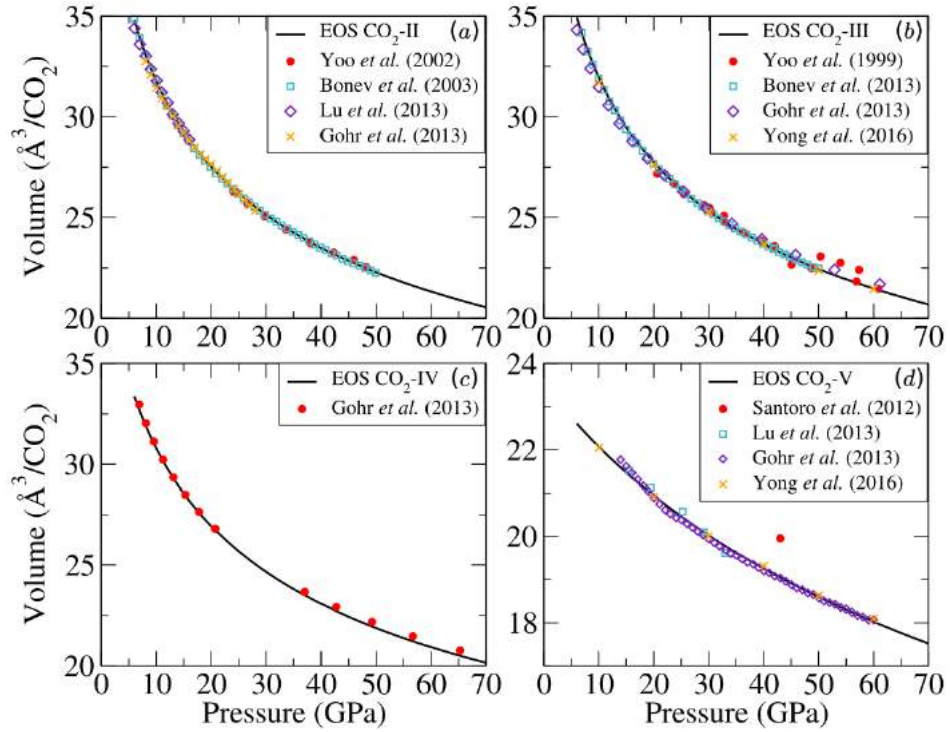
Figure 7.3: Pressure-volume relation of phases (a) II, (b) III, (c) IV, and (d) V of CO_2 obtained from the 3rd order Birch-Murnaghan equation of state at room temperature are shown in black solid lines. For each case, reported values from experimental (red circles) and theoretical (blue squares, purple diamonds and yellow crosses) studies for the different phases are displayed as well.

structures. The variation of volume as a function of the pressure of the molecular and non-molecular phases at room temperature was computed using the 3rd order Birch-Murnaghan equation of state is reported in Fig. 7.3. Calculated unit cell volumes are in excellent agreement with values reported in theoretical and experimental studies.

7.3.1　Molecular to non-molecular phase transitions

Finite temperature contributions to the Gibbs free energy were calculated based on QHA. The phase boundaries between each of the molecular phases of CO_2 phases II, III and IV, and the non-molecular phase V, are shown in Fig. 7.4. The phase transition between the molecular phases and phase V, were in the range between 20 and 35 GPa, and 0 to 1600K. Around 25.5 GPa and for temperatures below $\sim$ 600K, the CO_2-II
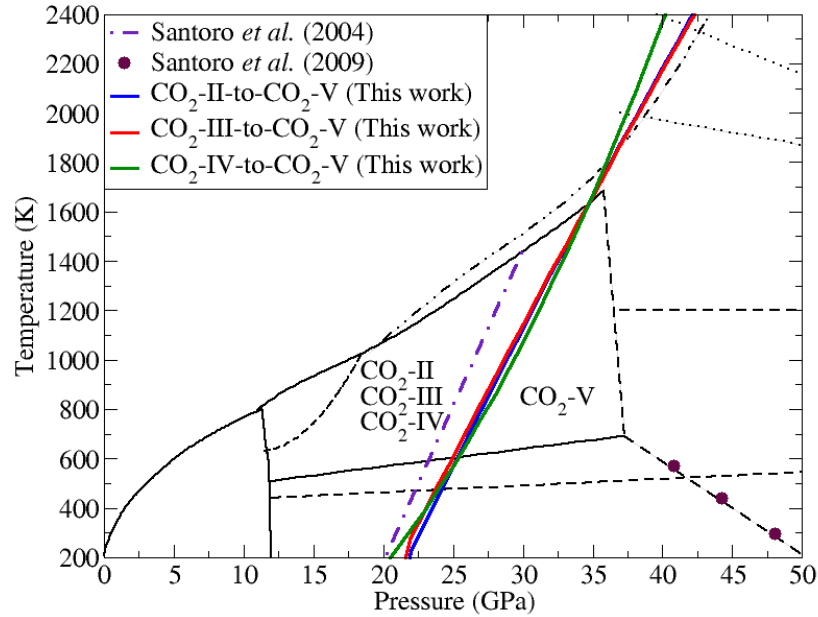
Figure 7.4: Phase boundaries between molecular phases CO_2-II (blue), CO_2-III (red), and CO_2-IV (green), and the non-molecular phase CO_2-V. Proposed boundaries in previous works are also included: Ref. [165] (violet dashed line) and Ref. [166] (indigo circles).

(blue solid line in Fig. 7.4) is the most stable phase given, while CO_2-IV becomes more stable at higher temperatures (green solid line in Fig. 7.4). This is in agreement with the reported thermodynamic phase boundary between phase III and IV (black solid line in Fig. 7.4), however, our calculations suggest that CO_2-III is a metastable phase at all temperatures (red solid line in Fig. 7.4) in the solid portion of the phase diagram where the transition from molecular phases to the non-molecular CO_2-V was studied.

In a first attempt to determine the boundary between the molecular and the non-molecular phases, Santoro $et\ al.$ [165] proposed the beginning of the phase V around 21 GPa at room temperature as a middle point in the region between 12 and 30, where CO_2-V is expected to be metastable when is decompressed into CO_2-I (violet dashed line in Fig. 7.4). It is important to emphasize that phase V was not yet established in 2004, when this work was published, therefore the transition pressure that they proposed at room temperature around 21 GPa did not have any other justification than an educated guess. Before the crystalline structure of CO_2-V was unequivocally determined, theoretical studies suggested that above ~ 20 GPa this phase becomes stable [167, 168]. These theoretical works predicted transition pressures from CO_2-

II and CO_2-III to the non-molecular forms based on enthalpy relations in the range between 18 and 21 GPa [167, 168, 169]. Our data suggests 21.5 and 20.8 GPa for the transition into CO_2-V from CO_2-II and CO_2-III, respectively, which are in agreement with previous theoretical works. Nonetheless, in a latter work, Santoro and Gorelli [166] dramatically redefined the previous kinetic border based on infrared spectroscopy measurements (indigo dots in Fig. 7.4), leading to a new boundary with negative slope. They suggested that the non-molecular forms of CO_2 are expected to be after the kinetic boundary and the phase boundary between molecular and non-molecular forms should not intersect the non-molecular P-T region delimited by the kinetic line. The proposed boundary not only does not intersect the non-molecular region, but it also respects the region assigned to the non-molecular, crystalline phase V. However, phase V is denser than the molecular phases and also lower in entropy, then, according to the Claperyon equation: $dP/dT = \Delta S/\Delta V$, where ΔS and ΔV are the variation of entropy and volume, respectively between two phases that coexist at thermodynamic equilibrium, it is expected that the slope of the phase boundary is positive, as shown in table 7.1. Additionally, our calculations shows a triple point between phases IV and V, and the liquid phase at 35 GPa and 1600 K.

Table 7.1: Thermodynamic properties of carbon dioxide from the molecular phases $P4_2/mnm$ (CO_2-II) and $R\bar{3}c$ (CO_2-IV) to the non-molecular phase $I\bar{4}2d$ (CO_2-V). ΔS_{CO_2-V} and ΔS_{CO_2-V} are the volume and the entropy difference, respectively, between the molecular phase and phase V. Subscript T states for *transition*.

| | P_T | T_T | V | ΔV_{CO_2-V} | S | ΔS_{CO_2-V} | dT/dP |
	GPa	K	a.u.^{3}/atom		J·mol/K		K/GPa
$P4_2/mnm$	21.95	200	4.0610	0.9538	-5.7145	-5.6997	0.0159
	22.57	300	4.0513	0.9508	-7.0807	-7.0598	0.0243
	23.50	400	4.0296	0.9394	-10.7455	-10.7160	0.0334
	24.41	500	4.0094	0.9284	-15.3715	-15.3345	0.0389
	25.33	600	3.9896	0.9172	-20.3605	-20.3167	0.0427
$R\bar{3}c$	25.06	600	3.3852	0.3090	-20.3900	-20.3462	0.1265
	25.39	800	3.3714	0.2999	-20.7385	-20.6944	0.1302
	26.45	1000	3.3520	0.2941	-21.2663	-21.2211	0.1355
	31.27	1200	3.3436	0.2922	-22.0603	-22.0127	0.1460
	33.10	1400	3.3285	0.2904	-22.5765	-22.5265	0.1572
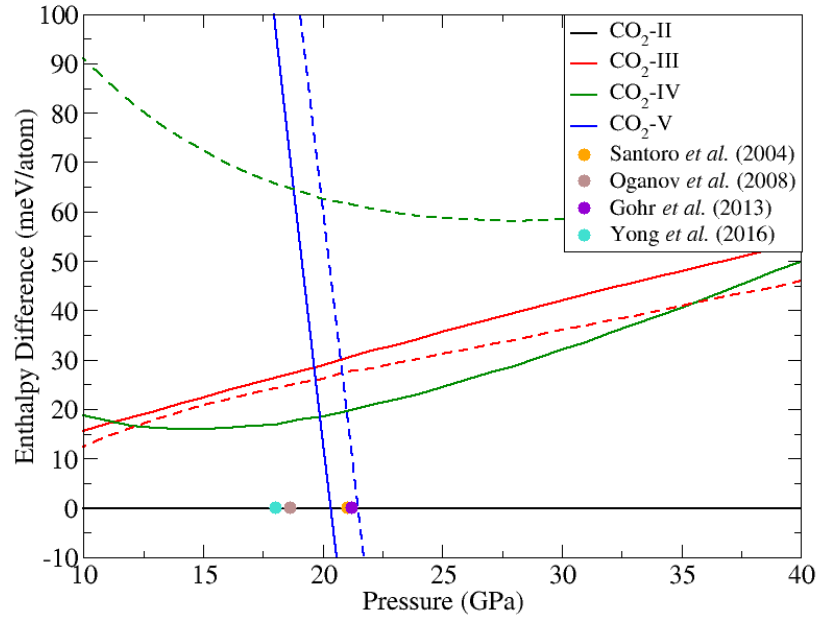
Figure 7.5: Enthalpy-pressure relations without (solid lines) and with (dashed) ZPE for studied phases of carbon dioxide: $P42/mnm$ (reference, black), $Cmcm$ (red), $R\bar{3}c$ (green), and $Cmcm$ (blue). Transition-pressure reported by Santoro $et\ al.$ [165], Oganov $et\ al.$ [167], Gohr $et\ al.$ [168], and Yong $et\ al.$ [169], are in orange, brown, violet, and cyan dots, respectively.

7.3.2   Boundaries between molecular phases

In the region below 35 GPa and up to 1600K, the molecular phases I, II, III, and IV, co-exist. In the present section we focused in the pressure range from 15 to 35 GPa. According to the enthalpy-pressure relations shown in Fig. 7.5, with and without the zero-point energy contribution, at T = 0 K, CO_2-II is the most stable phase until the transition to CO_2-V. This indicates that the orthorhombic phase $Cmca$ obtained after the compression of phase I is metastable, as it was already reported [149, 170]. The kinetic barrier between CO_2-II and CO_2-III is overcome when the system is heated, where phase III becomes thermodynamically stable at finite temperature (blue solid line in Fig. 7.6).

After the inclusion of phase IV to delimit its stability region, CO_2-II's is reduced in temperature. The calculated phase boundary between phases II and IV (green solid

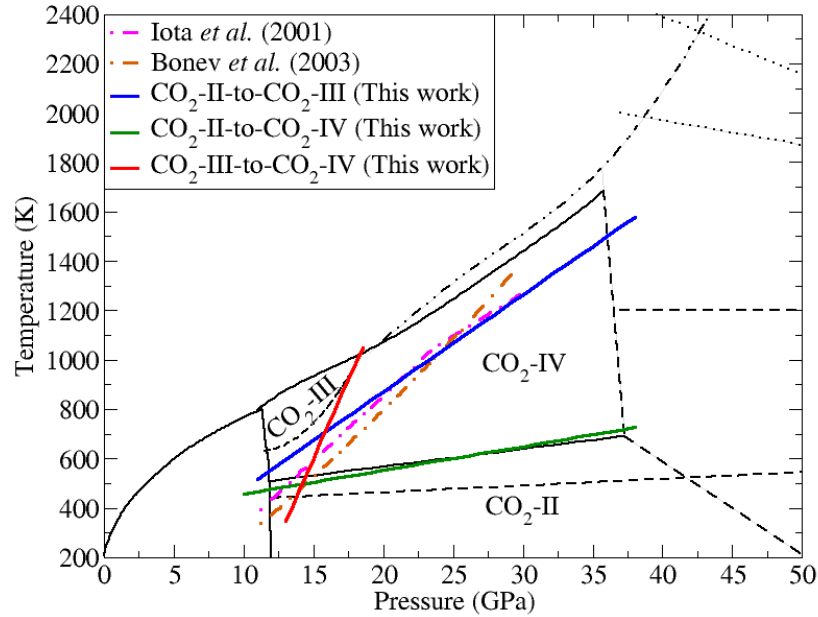Figure 7.6: Phase boundaries between (a) CO_2-II and CO_2-III (blue), (b) CO_2-II and CO_2-IV (green), and (c) CO_2-III and CO_2-IV (red). Suggested boundaries reported by Iota *et al.* [149] (experimental) and Bonev [170] (theoretical), are shown in magenta and orange dot-dashed lines, respectively.

line in Fig. 7.6) is in agreement with its known thermodynamic transition line [155]. Additionally, the region of stability of phase III narrows down to a much smaller one limited up to 18 GPa (blue solid line in Fig. 7.6). Our findings are in agreement with previous studies that suggested $Cmcm$ phase as a temperature stabilized phase [170]. However, the work of Bonev *et al.* does not include CO_2-IV since its structure was still a matter of debate at the time of their publication, therefore their results propose a wide region for CO_2-III. Interestingly, the refined region for CO_2-III obtained in our calculations is actually in the P–T vicinity of the so-called phase VII. There has been controversy around weather phases III and VII are or not likely identical. A recent theoretical work has shown that they are in fact the same, but our data shows that the phase III is limited only to the region where phase VII was observed.
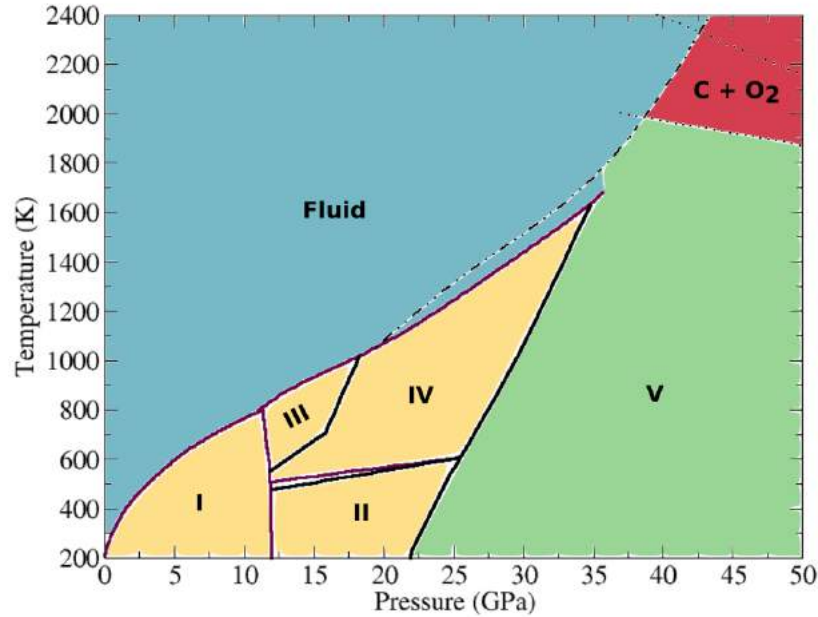
Figure 7.7: Proposed finite temperature phase diagram for carbon dioxide at high pressure. The phase boundaries at finite temperature, corresponding to calculations including ZPE and using an electronic temperature of 500 K, are shown by solid black lines, while previously reported thermodynamic boundaries are set in gray. Yellow, green, blue and red areas correspond to the molecular, non-molecular, fluid, and dissociated forms of CO_2.

7.4   Conclusions

In summary, we have presented theoretical calculations that redefined the transition boundary from molecular to non-molecular phases of carbon dioxide. The proposed line now has a positive slope starting at 21.5 GPa at T = 0, reaching a triple point between phase IV, V, and the liquid phase at 35 GPa and 1600 K, indicating that non-molecular phases have a wider region of stability. Moreover, it was shown that phase II is the most stable molecular phase at low temperatures, instead of phase III. Additionally, we were able to confirm the thermodynamic boundary line between CO_2-II and CO_2-IV. Interestingly, since our results show that CO_2-III is stabilized at high temperature, its stability region was narrowed down to the P – T vicinity were phase VII was reported, implying not only that phase III and phase VII are indeed the same, but that the portion of the phase diagram corresponding to phase III is in fact beloging to CO_2-II. It is necessary to study theoretically other metastable phases that were not taken into account in this study, namely CO_2-VI and the amorphous phase, to evaluate

their impact in the phase diagram.

Closing remarks

The primary goal of this thesis report was to provide an accurate description from the theoretical point of view of carbon, oxygen, and one of their mixtures, namely carbon dioxide. In all cases, we focused on the high-pressure region of their phase diagram, where there are open questions and controversy around them. With this in mind, we have presented a vibrational analysis of several phases for each system. Our calculations were performed within the density functional theory framework, and the inclusion of the thermal contribution to the Gibbs free energy was done using the quasi-harmonic approximation.

Since we have already concluded at the end of every chapter that dealt with a different system, here we will give some remarks about some relevant findings that emerged under pressure. In "*Persistence and Eventual Demise of Oxygen Molecules at Terapascal Pressures*", Sun *et al.* performed computational searches for structures of solid oxygen under high pressure in the multi-TPa region. They found how oxygen remained molecular almost up to 2 TPa, and as long as pressure increases, its electronic properties exhibit a complex evolution, swapping between insulation, semiconducting, and metallic. It is above 9 TPa when oxygen finally forms a four-fold coordinated phase of space group $Fmmm$. Nevertheless, that work stated that temperature might have a significant effect on the transition from molecular to polymeric oxygen phases, and that was our starting point for the work on oxygen. Our finite temperature calculations, based on the quasi-harmonic approximation, and therefore also on phonon frequencies, gave us the first behavior that drew our attention: phonon frequencies are expected to increase with pressure. This is due to when the interatomic distances are reduced, the forces on the atoms get stronger. However, in the case of phase $Fmmm$ of solid oxygen, this was not the case: its phonon softening reduces when pressure is applied, which has a profound effect on the phase boundary between $Cmcm$ and $Fmmm$, where a negative slope is exhibited. Moreover, at finite temperatures, the molecular phase expands its stability range to pressures exceeding 3 TPa at the highest temperatures considered in this work (8000 K). On the contrary, the range of stability of the first non-molecular phase, $I4_1/acd$, shrinks with temperature and the phase is no longer

thermodynamically stable above 5000 K, and the same behavior is observed for $Cmcm$ above 7800 K.

On the other hand, the work on carbon dioxide has been strongly influenced by two experimental papers that span the $P-T$ where should lies the boundary between the molecular and the non-molecular phases of CO_2. Santoro *et al.*, in the work "*In situ high $P-T$ Raman spectroscopy and laser heating of carbon dioxide*", proposed a phase diagram where the boundary between molecular and non-molecular phases at room temperature is located at 20 GPa, roughly half-way between the lowest pressure of quenching and the pressure of synthesis for phase V. Later, in "*Constraints on the phase diagram of nonmolecular CO_2 imposed by infrared spectroscopy*", Santoro and Gorelli stated that the *kinetic* boundary between CO_2-III and the a-CO_2 non-molecular structure, i.e., the $P-T$ region where the transformation occurs upon compression, has a negative slope, while basic thermodynamic considerations suggest that the slope of the true phase boundary should be positive. These two works set a pressure range of approximately 30 GPa in which the molecular/non-molecular boundary at zero temperature should be located. Via *ab-initio* techniques, we were able to provide theoretical insight into the long-term discussion around the boundary between molecular and non-molecular phases of carbon dioxide. Our results suggest that the boundary between the molecular phases and the non-molecular phase V has a positive slope. Moreover, we found a triple point between phase IV, V, and the liquid phase at 35 GPa and 1600 K, indicating that CO_2-V has a broader region of stability than previously reported. Also, it was shown that phase II is the most stable molecular phase at low temperatures, extending its region of stability to every $P-T$ condition where phase III has been reported experimentally. Nevertheless, our results also show that CO_2-III is instead stabilized at high temperature and its stability region coincides with the $P-T$ conditions where phase VII has been reported experimentally, implying that phase III and phase VII are indeed the same.

On the technical side, we were able to reproduce the phase boundaries transition between phases of carbon can be reproduced with a minimum amount of computational cost by using the quasi-harmonic approximation. Although QHA is enough to replicate these transitions that include small anharmonic corrections, for the study of the melting line the quasi-harmonic approximation is not accurate enough, and it is necessary to add the anharmonic correction to the free energy in order to estimate the solid-to-fluid

transition accurately.

Appendices

A   Carbon

A.1   Convergence calculations

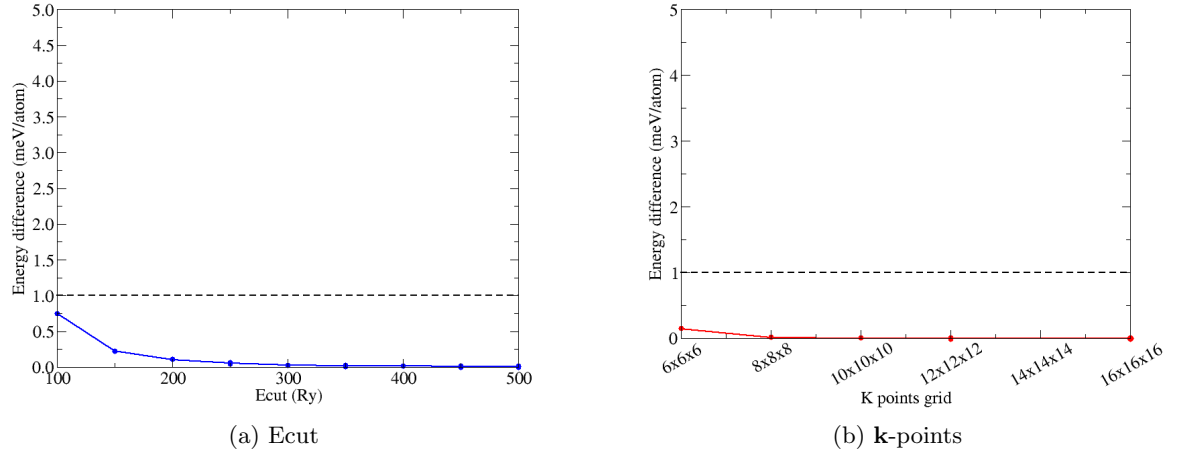### A.1.1   Electronic structure parameters

Diamond

(a) Ecut

(b) **k**-points

Figure A.1: Electronic energy convergence as a function of (a) Kinetic energy cutoff and (b) **k**-points grid for Diamond at 1.25 TPa
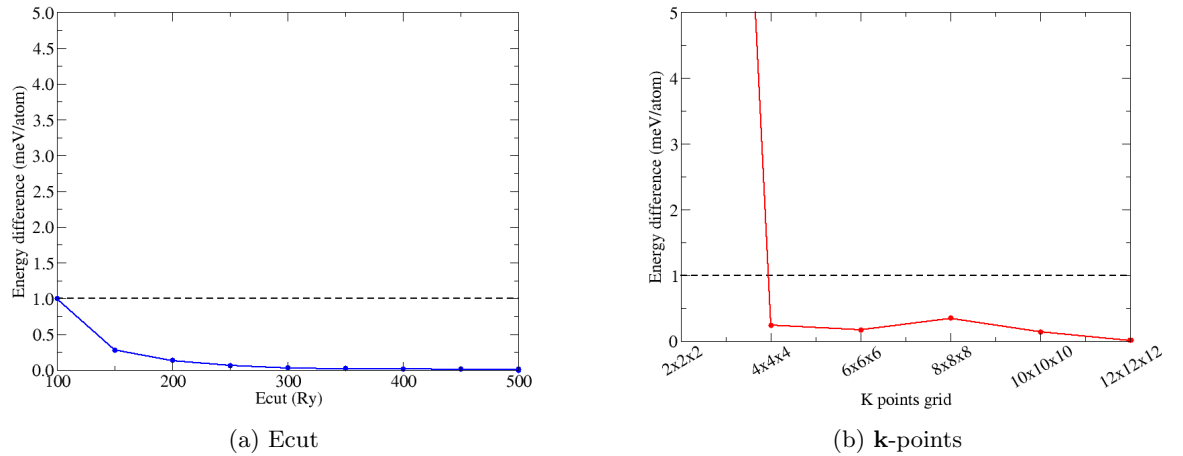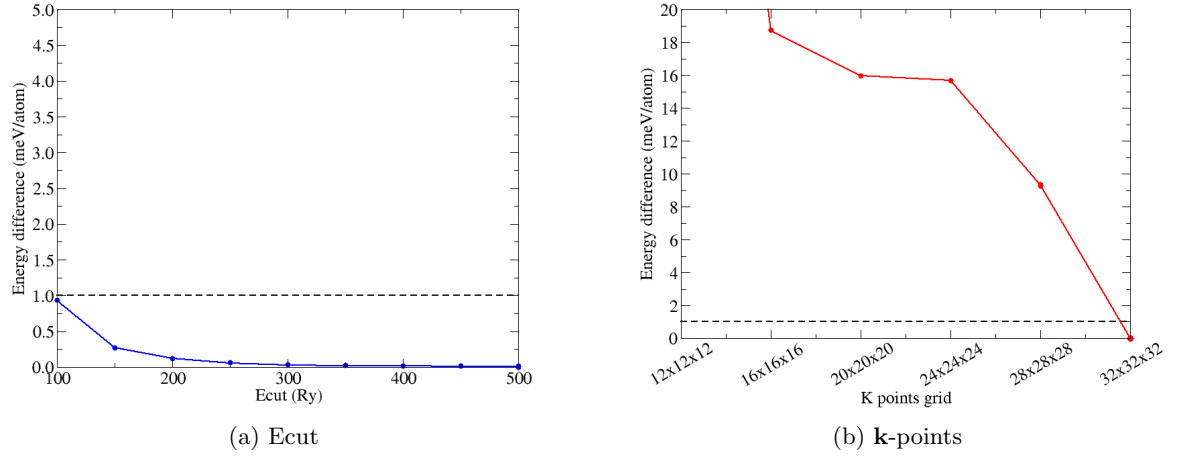
BC8

(a) Ecut

(b) **k**-points

Figure A.2: Electronic energy convergence as a function of (a) Kinetic energy cutoff and (b) **k**-points grid for BC8 at 3.00 TPa

Simple Cubic

(a) Ecut

(b) **k**-points

Figure A.3: Electronic energy convergence as a function of (a) Kinetic energy cutoff and (b) **k**-points grid for SC at 3.50 TPa

A.1.2   q-points grid

Diamond
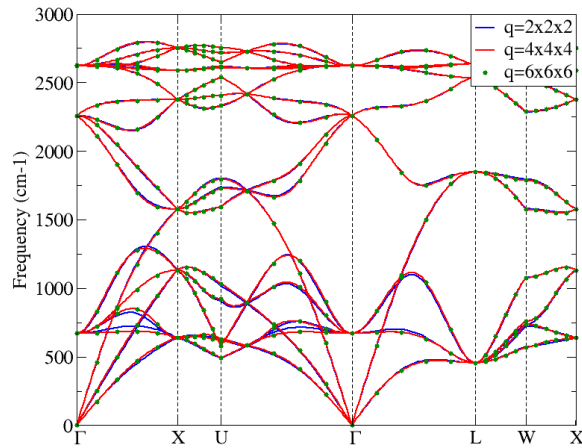
Figure A.4: Phonon dispersion for Diamond at 1.25 TPa with **q**-points grid of $2 \times 2 \times 2$ (blue solid line), $4 \times 4 \times 4$ (red solid line), and $6 \times 6 \times 6$ (green dots).
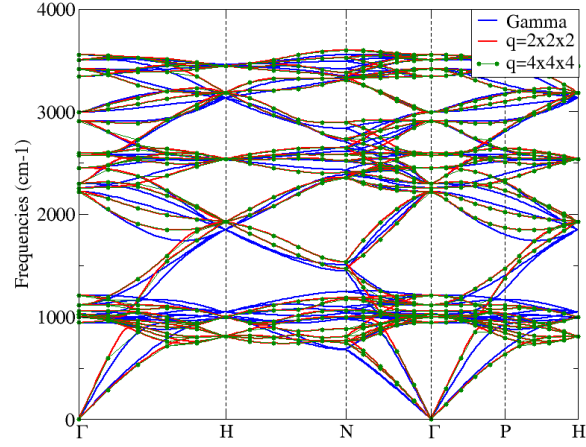
BC8

Figure A.5: Phonon dispersion for BC8 at 3.00 TPa with **q**-points grid at Gamma point (blue solid line), $2 \times 2 \times 2$ (red solid line), and $4 \times 4 \times 4$ (green dots).
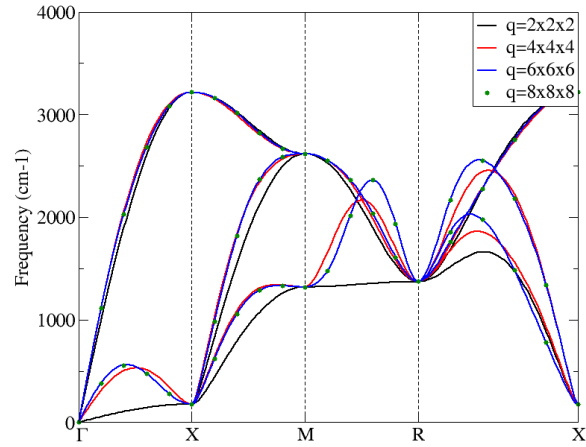
Simple Cubic

Figure A.6: Phonon dispersion for SC at 3.50 TPa with **q**-points grid for $2 \times 2 \times 2$ (black solid line), $4 \times 4 \times 4$ (red solid line), $6 \times 6 \times 6$ (blue solid line) and $8 \times 8 \times 8$ (green dots).

A.1.3   Zero-point energy

Table A.1: Zero-point energy convergence for (a) Diamond at 1.25 TPa, (b) BC8 at 3.00 TPa, and (c) SC at 3.00 TPa. All the energy values of $F_0(\mathbf{q})$ are in Ry.

q-points grid	$F_0(\mathbf{q})$
$2 \times 2 \times 2$	0.19866
$4 \times 4 \times 4$	0.19960
$6 \times 6 \times 6$	0.19976

(a) Diamond

q-points grid	$F_0(\mathbf{q})$
Γ	0.46470
$2 \times 2 \times 6$	0.46914
$4 \times 4 \times 4$	0.46942

(b) BC8

q-points grid	$F_0(\mathbf{q})$
$4 \times 4 \times 4$	0.02622
$6 \times 6 \times 6$	0.02512
$8 \times 8 \times 8$	0.02513

(c) SC

A.2   Structural parameters

Diamond

Table A.2: Lattice parameters and atomic positions of Diamond. Symmetry group: 227. Wyckoff letter: a.

P (TPa)	Lattice parameters (a.u.; °)	
0.25	a = b = c = 6.06111	$\alpha = \beta = \gamma = 90.0000$
0.50	a = b = c = 5.74014	$\alpha = \beta = \gamma = 90.0000$
0.75	a = b = c = 5.52638	$\alpha = \beta = \gamma = 90.0000$
1.00	a = b = c = 5.36583	$\alpha = \beta = \gamma = 90.0000$
1.25	a = b = c = 5.23734	$\alpha = \beta = \gamma = 90.0000$

BC8

Table A.3: Lattice parameters and atomic positions of BC8. Symmetry group: 206. Wyckoff letter: c.

P (TPa)	Lattice parameters (a.u.; °)		Atomic coordinates
0.75	a = b = c = 6.88929	$\alpha = \beta = \gamma = 90.0000$	x = 0.10219
1.00	a = b = c = 6.69059	$\alpha = \beta = \gamma = 90.0000$	x = 0.10309
1.25	a = b = c = 6.53183	$\alpha = \beta = \gamma = 90.0000$	x = 0.10379
1.50	a = b = c = 6.39974	$\alpha = \beta = \gamma = 90.0000$	x = 0.10435
1.75	a = b = c = 6.28674	$\alpha = \beta = \gamma = 90.0000$	x = 0.10481
2.00	a = b = c = 6.18815	$\alpha = \beta = \gamma = 90.0000$	x = 0.10519
2.25	a = b = c = 6.10070	$\alpha = \beta = \gamma = 90.0000$	x = 0.10552
2.50	a = b = c = 6.02218	$\alpha = \beta = \gamma = 90.0000$	x = 0.10581
2.75	a = b = c = 5.95099	$\alpha = \beta = \gamma = 90.0000$	x = 0.10606
3.00	a = b = c = 5.88591	$\alpha = \beta = \gamma = 90.0000$	x = 0.10629

Simple Cubic

Table A.4: Lattice parameters and atomic positions of SC. Symmetry group: 221. Wyckoff letter: a.

P	Lattice parameters	
(TPa)	(a.u.; °)	
2.50	a = b = c = 2.35816	$\alpha = \beta = \gamma = 90.0000$
2.75	a = b = c = 2.33055	$\alpha = \beta = \gamma = 90.0000$
3.00	a = b = c = 2.30531	$\alpha = \beta = \gamma = 90.0000$
3.25	a = b = c = 2.28208	$\alpha = \beta = \gamma = 90.0000$
3.50	a = b = c = 2.26052	$\alpha = \beta = \gamma = 90.0000$

A.3   EOS parameters

Diamond

Table A.5: 3rd order Birch-Murnaghan EOS parameters for diamond from 0.25 to 1.00 TPa.

T	V_0	B_0	B_0'	E_0	T	V_0	B_0	B_0'	E_0
0	3.31978	6496.630	2.474	-18.411	5500	3.29013	8450.370	2.084	-18.549
500	3.31720	6629.190	2.444	-18.415	6000	3.28728	8677.410	2.043	-18.570
1000	3.31937	6515.890	2.470	-18.411	6500	3.28447	8908.230	2.002	-18.591
1500	3.31428	6794.330	2.409	-18.422	7000	3.28167	9143.540	1.960	-18.614
2000	3.31121	6978.780	2.370	-18.432	7500	3.27894	9382.100	1.919	-18.637
2500	3.30810	7173.290	2.330	-18.445	8000	3.27624	9624.050	1.877	-18.661
3000	3.30503	7374.180	2.290	-18.459	8500	3.27355	9871.340	1.836	-18.685
3500	3.30197	7580.630	2.249	-18.474	9000	3.27094	10119.900	1.794	-18.710
4000	3.29896	7791.500	2.208	-18.491	9500	3.26834	10373.900	1.752	-18.735
4500	3.29598	8007.060	2.167	-18.509	10000	3.26576	10632.200	1.710	-18.761
5000	3.29302	8227.320	2.126	-18.529					

BC8

Table A.6: 3rd order Birch-Murnaghan EOS parameters for BC8 from 0.75 to 3.00 TPa.

T	V_0	B_0	B_0'	E_0	T	V_0	B_0	B_0'	E_0
0	3.22716	7985.040	2.375	-18.336	5500	3.26768	7487.740	2.342	-18.492
500	3.22756	7978.570	2.374	-18.337	6000	3.27174	7448.200	2.338	-18.515
1000	3.23045	7928.690	2.373	-18.342	6500	3.27577	7410.130	2.334	-18.539
1500	3.23441	7868.790	2.371	-18.351	7000	3.27979	7373.060	2.330	-18.563
2000	3.23858	7812.280	2.368	-18.363	7500	3.28377	7337.400	2.325	-18.589
2500	3.24278	7759.300	2.365	-18.377	8000	3.28773	7302.820	2.321	-18.614
3000	3.24699	7709.040	2.361	-18.393	8500	3.29167	7269.280	2.317	-18.641
3500	3.25118	7661.140	2.358	-18.410	9000	3.29558	7236.970	2.312	-18.668
4000	3.25534	7615.260	2.354	-18.429	9500	3.29947	7205.450	2.308	-18.695
4500	3.25948	7571.200	2.350	-18.449	10000	3.30333	7175.270	2.304	-18.723
5000	3.26359	7528.730	2.346	-18.470					

Simple Cubic

Table A.7: 3rd order Birch-Murnaghan EOS parameters for simple cubic from 2.50 to 3.50 TPa.

T	V_0	B_0	B_0'	E_0	T	V_0	B_0	B_0'	E_0
0	3.43918	3870.790	2.529	-18.321	5500	5.31068	170.680	2.431	-18.947
500	3.45802	3694.410	2.533	-18.329	6000	5.31269	174.077	2.421	-18.977
1000	3.49195	3458.090	2.521	-18.354	6500	5.30796	179.242	2.411	-19.008
1500	3.60039	2750.320	2.511	-18.414	7000	5.31219	182.443	2.400	-19.041
2000	3.79760	1842.670	2.500	-18.506	7500	5.31325	186.441	2.390	-19.073
2500	3.95756	1362.620	2.490	-18.576	8000	5.31215	190.575	2.381	-19.106
3000	4.30814	728.691	2.480	-18.683	8500	5.31326	195.074	2.370	-19.141
3500	5.00453	242.563	2.470	-18.810	9000	5.31329	199.596	2.360	-19.176
4000	5.26226	170.735	2.460	-18.859	9500	5.37081	188.868	2.351	-19.216
4500	5.29161	167.548	2.451	-18.889	10000	5.68703	129.361	2.340	-19.280
5000	5.30537	168.122	2.441	-18.918					

B   Solid Oxygen

B.1   Convergence calculations
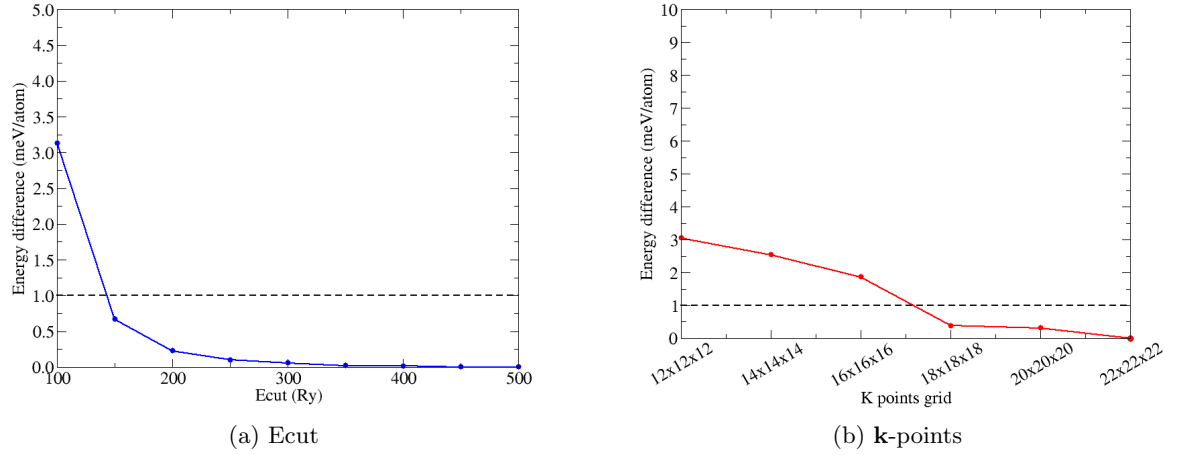
B.1.1   Electronic structure parameters

R$\bar{3}$m

(a) Ecut   (b) **k**-points

Figure B.1: Electronic energy convergence as a function of (a) Kinetic energy cutoff and (b) **k**-points grid for $R\bar{\mathbf{3}}m$ at 4.0 TPa

I4$_1$/acd

(a) Ecut   (b) **k**-points
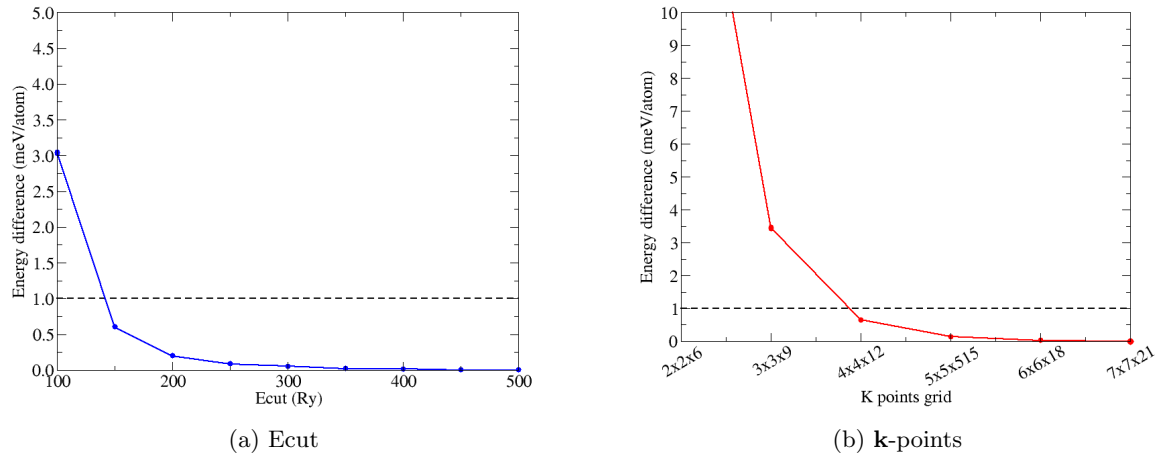
Figure B.2: Electronic energy convergence as a function of (a) Kinetic energy cutoff and (b) **k**-points grid for $I4_{\mathbf{1}}/acd$ at 4.0 TPa

Cmcm

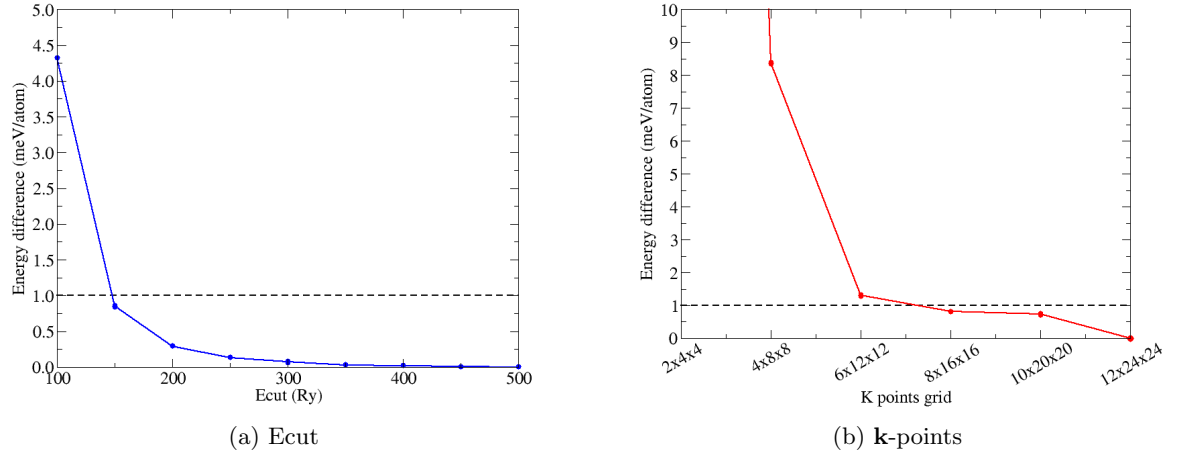(a) Ecut   (b) **k**-points

Figure B.3: Electronic energy convergence as a function of (a) Kinetic energy cutoff and (b) **k**-points grid for *Cmcm* at 10.0 TPa

Fmmm

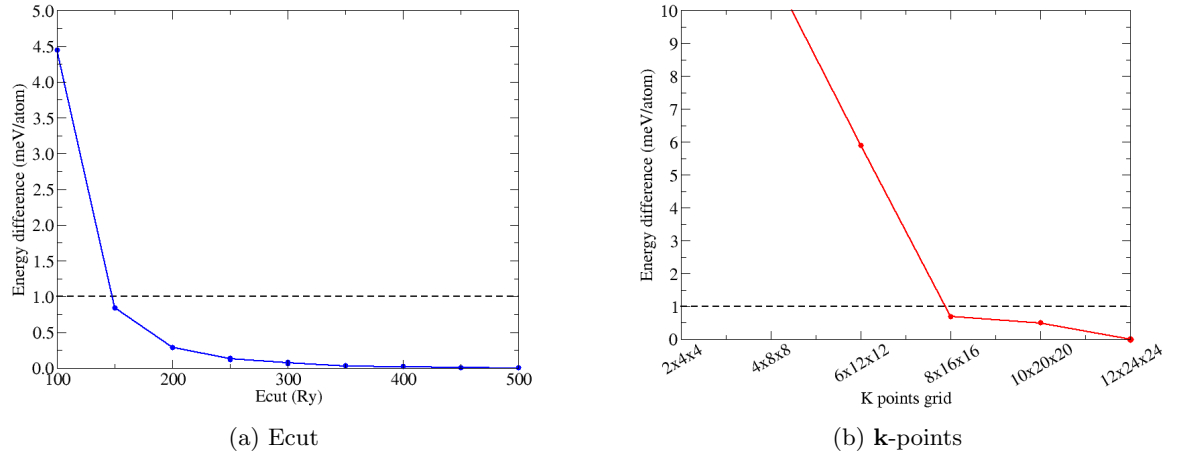(a) Ecut   (b) **k**-points

Figure B.4: Electronic energy convergence as a function of (a) Kinetic energy cutoff and (b) **k**-points grid for *Fmmm* at 10.0 TPa
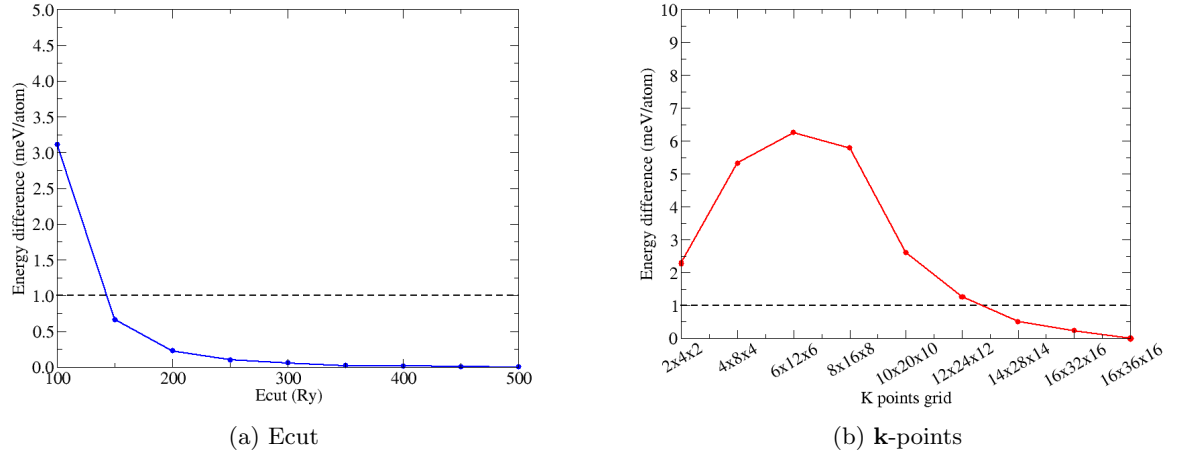
C2/m

(a) Ecut

(b) **k**-points

Figure B.5: Electronic energy convergence as a function of (a) Kinetic energy cutoff and (b) **k**-points grid for $C2/m$ at 4.0 TPa
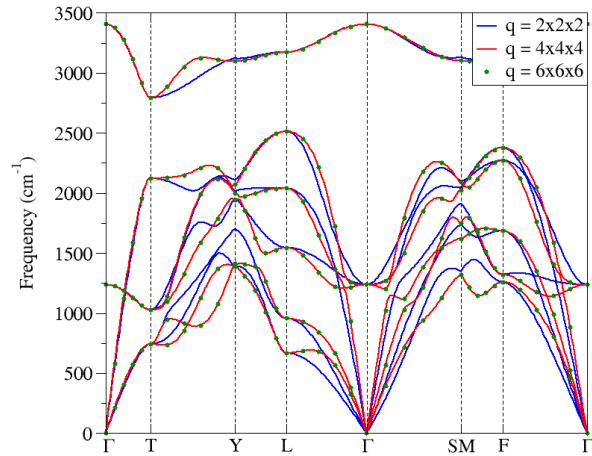
B.1.2   q-points grid

R$\bar{\textbf{3}}$m

Figure B.6: Phonon dispersion for $R\bar{\textbf{3}}m$ at 4.0 TPa with **q**-points grid of $2 \times 2 \times 2$ (blue solid line), $4 \times 4 \times 4$ (red solid line), and $6 \times 6 \times 6$ (green dots).

I4$_1$/acd

Figure B.7: Phonon dispersion for $I4_1/acd$ at 4.0 TPa with **q**-points grid of $1 \times 1 \times 3$ (blue solid line), $2 \times 2 \times 6$ (red solid line), and $3 \times 3 \times 9$ (green dots).

Cmcm

Figure B.8: Phonon dispersion for $Cmcm$ at 10.0 TPa with **q**-points grid of $1 \times 2 \times 2$ (blue solid line), $2 \times 4 \times 4$ (red solid line), and $3 \times 6 \times 6$ (green dots).

Fmmm
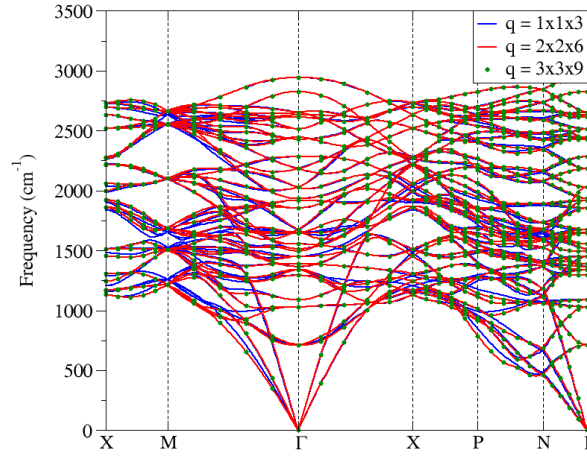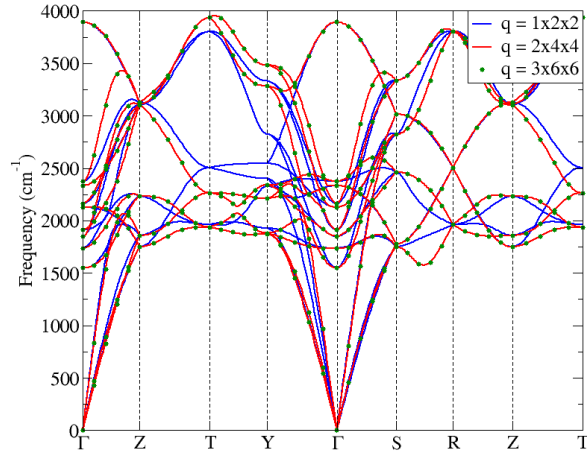

Figure B.9: Phonon dispersion for $Cmcm$ at 10.0 TPa with **q**-points grid of $1 \times 2 \times 2$ (blue solid line), $2 \times 4 \times 4$ (red solid line), and $3 \times 6 \times 6$ (green dots).

C2/m

Figure B.10: Phonon dispersion for $I4_1/acd$ at 4.0 TPa with **q**-points grid of $1 \times 2 \times 2$ (blue solid line), $2 \times 4 \times 4$ (red solid line), and $3 \times 6 \times 6$ (green dots).
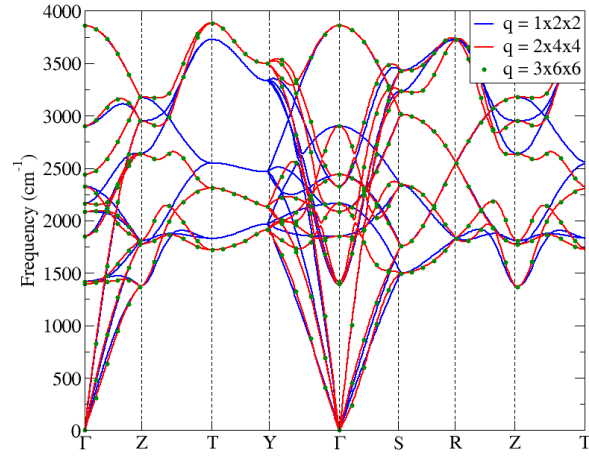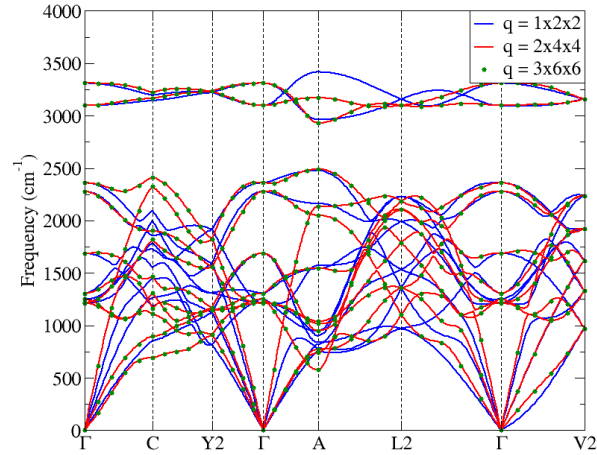
B.1.3   Zero-point energy

Table B.1: Zero-point energy convergence for (a) $R\bar{3}m$, (b) $I4_1/acd$, and (e) $C2m$ at 4.0 TPa, and (c) $Cmcm$ and (d) $Fmmm$ at 10.0 TPa. All the energy values of $F_0(\mathbf{q})$ are in Ry.

q-points grid	$F_0(\mathbf{q})$
$2 \times 2 \times 2$	0.04642
$4 \times 4 \times 4$	0.04732
$6 \times 6 \times 6$	0.04746

(a) $R\bar{3}m$

q-points grid	$F_0(\mathbf{q})$
$1 \times 1 \times 3$	0.40546
$2 \times 2 \times 6$	0.40815
$3 \times 3 \times 9$	0.40843

(b) $I4_1/acd$

q-points grid	$F_0(\mathbf{q})$
$1 \times 2 \times 2$	0.12951
$2 \times 4 \times 4$	0.13177
$3 \times 6 \times 6$	0.13198

(c) $Cmcm$

q-points grid	$F_0(\mathbf{q})$
$1 \times 2 \times 2$	0.12622
$2 \times 4 \times 4$	0.12694
$3 \times 6 \times 6$	0.12698

(d) $Fmmm$

q-points grid	$F_0(\mathbf{q})$
$1 \times 2 \times 2$	0.09481
$2 \times 4 \times 4$	0.96108
$3 \times 6 \times 6$	0.96282

(e) $C2/m$

B.2   Structural parameters

R$\bar{3}$m

Table B.2: Lattice parameters and atomic positions of $R\bar{3}m$. Symmetry group: 166 (rhombohedral axes). Wyckoff letter: c.

P (TPa)	Lattice parameters (a.u.; °)		Atomic coordinates
1.0	a = b = c = 5.08172	$\alpha = \beta = \gamma = 36.9128$	x = 0.92796
1.5	a = b = c = 4.87032	$\alpha = \beta = \gamma = 36.7013$	x = 0.92687
2.0	a = b = c = 4.72002	$\alpha = \beta = \gamma = 36.5349$	x = 0.92613
2.5	a = b = c = 4.60462	$\alpha = \beta = \gamma = 36.3724$	x = 0.92546
3.0	a = b = c = 4.51307	$\alpha = \beta = \gamma = 36.1962$	x = 0.92490
3.5	a = b = c = 4.43808	$\alpha = \beta = \gamma = 36.0057$	x = 0.92433
4.0	a = b = c = 4.37151	$\alpha = \beta = \gamma = 35.8670$	x = 0.92391

I4$_1$/acd

Table B.3: Lattice parameters and atomic positions of $I4_1/acd$. Symmetry group: 142. Wyckoff letter: f.

P (TPa)	Lattice parameters (a.u.; °)			Atomic coordinates
1.0	a = b = 9.46471	c/a = 0.39408	$\alpha = \beta = \gamma = 90.0000$	x = 0.13759
1.5	a = b = 9.07545	c/a = 0.38978	$\alpha = \beta = \gamma = 90.0000$	x = 0.13647
2.0	a = b = 8.79188	c/a = 0.38747	$\alpha = \beta = \gamma = 90.0000$	x = 0.13573
2.5	a = b = 8.56900	c/a = 0.38603	$\alpha = \beta = \gamma = 90.0000$	x = 0.13515
3.0	a = b = 8.38513	c/a = 0.38510	$\alpha = \beta = \gamma = 90.0000$	x = 0.13468
3.5	a = b = 8.22894	c/a = 0.38444	$\alpha = \beta = \gamma = 90.0000$	x = 0.13427
4.0	a = b = 8.09282	c/a = 0.38403	$\alpha = \beta = \gamma = 90.0000$	x = 0.13390

Cmcm

Table B.4: Lattice parameters and atomic positions of *Cmcm*. Symmetry group: 63. Wyckoff letter: c.

P (TPa)	Lattice parameters (a.u.; °)				Atomic coordinates
1.0	a = 5.93751	b/a = 0.65637	c/a = 0.60385	$\alpha = \beta = \gamma = 90.0000$	y = 0.18769
1.5	a = 5.65141	b/a = 0.64451	c/a = 0.61934	$\alpha = \beta = \gamma = 90.0000$	y = 0.19291
2.0	a = 5.44830	b/a = 0.63897	c/a = 0.62859	$\alpha = \beta = \gamma = 90.0000$	y = 0.19627
2.5	a = 5.29200	b/a = 0.63539	c/a = 0.63530	$\alpha = \beta = \gamma = 90.0000$	y = 0.19915
3.0	a = 5.16426	b/a = 0.63410	c/a = 0.63983	$\alpha = \beta = \gamma = 90.0000$	y = 0.20105
3.5	a = 5.05778	b/a = 0.63371	c/a = 0.64279	$\alpha = \beta = \gamma = 90.0000$	y = 0.20276
4.0	a = 4.96659	b/a = 0.63226	c/a = 0.64612	$\alpha = \beta = \gamma = 90.0000$	y = 0.20497
4.5	a = 4.88802	b/a = 0.63207	c/a = 0.64752	$\alpha = \beta = \gamma = 90.0000$	y = 0.20702
5.0	a = 4.81792	b/a = 0.63195	c/a = 0.64881	$\alpha = \beta = \gamma = 90.0000$	y = 0.20882
5.5	a = 4.75418	b/a = 0.63189	c/a = 0.65015	$\alpha = \beta = \gamma = 90.0000$	y = 0.21074
6.0	a = 4.69714	b/a = 0.63175	c/a = 0.65109	$\alpha = \beta = \gamma = 90.0000$	y = 0.21264
6.5	a = 4.64512	b/a = 0.63184	c/a = 0.65171	$\alpha = \beta = \gamma = 90.0000$	y = 0.21427
7.0	a = 4.59704	b/a = 0.63062	c/a = 0.65342	$\alpha = \beta = \gamma = 90.0000$	y = 0.21698
7.5	a = 4.55193	b/a = 0.63073	c/a = 0.65425	$\alpha = \beta = \gamma = 90.0000$	y = 0.21824
8.0	a = 4.51006	b/a = 0.62944	c/a = 0.65617	$\alpha = \beta = \gamma = 90.0000$	y = 0.22084
8.5	a = 4.47076	b/a = 0.62911	c/a = 0.65721	$\alpha = \beta = \gamma = 90.0000$	y = 0.22270
9.0	a = 4.43705	b/a = 0.63164	c/a = 0.65742	$\alpha = \beta = \gamma = 90.0000$	y = 0.22396
9.5	a = 4.40139	b/a = 0.62201	c/a = 0.66433	$\alpha = \beta = \gamma = 90.0000$	y = 0.23131
10.0	a = 4.36998	b/a = 0.61097	c/a = 0.67616	$\alpha = \beta = \gamma = 90.0000$	y = 0.25000

Fmmm

Table B.5: Lattice parameters and atomic positions of *Fmmm*. Symmetry group: 69. Wyckoff letter: a.

P (TPa)	Lattice parameters (a.u.; °)			
5.0	a = 4.83536	b/a = 0.60122	c/a = 0.67047	$\alpha = \beta = \gamma = 90.0000$
5.5	a = 4.76913	b/a = 0.60222	c/a = 0.67202	$\alpha = \beta = \gamma = 90.0000$
6.0	a = 4.70959	b/a = 0.60330	c/a = 0.67301	$\alpha = \beta = \gamma = 90.0000$
6.5	a = 4.65565	b/a = 0.60433	c/a = 0.67368	$\alpha = \beta = \gamma = 90.0000$
7.0	a = 4.60580	b/a = 0.60522	c/a = 0.67445	$\alpha = \beta = \gamma = 90.0000$
7.5	a = 4.55918	b/a = 0.60612	c/a = 0.67529	$\alpha = \beta = \gamma = 90.0000$
8.0	a = 4.51572	b/a = 0.60703	c/a = 0.67601	$\alpha = \beta = \gamma = 90.0000$
8.5	a = 4.47550	b/a = 0.60789	c/a = 0.67650	$\alpha = \beta = \gamma = 90.0000$
9.0	a = 4.43807	b/a = 0.60876	c/a = 0.67672	$\alpha = \beta = \gamma = 90.0000$
9.5	a = 4.40251	b/a = 0.60959	c/a = 0.67708	$\alpha = \beta = \gamma = 90.0000$
10.0	a = 4.37002	b/a = 0.61098	c/a = 0.67614	$\alpha = \beta = \gamma = 90.0000$

C2/m

Table B.6: Lattice parameters and atomic positions of *C2/m*. Symmetry group: 12 (unique axis b). Wyckoff letter: i.

P (TPa)	Lattice parameters (a.u.; °)	Atomic coordinates
1.0	a = 5.57599 b/a = 0.57689 c/a = 0.91105 $\alpha = \gamma = 90.0000$ $\beta = 111.4403$	x = 0.07199 z = 0.21620
1.5	a = 5.31650 b/a = 0.57637 c/a = 0.91564 $\alpha = \gamma = 90.0000$ $\beta = 111.2768$	x = 0.07294 z = 0.21943
2.0	a = 5.12857 b/a = 0.57686 c/a = 0.92004 $\alpha = \gamma = 90.0000$ $\beta = 111.2442$	x = 0.07391 z = 0.22171
2.5	a = 4.97892 b/a = 0.57748 c/a = 0.92471 $\alpha = \gamma = 90.0000$ $\beta = 111.1611$	x = 0.07465 z = 0.22374
3.0	a = 4.85559 b/a = 0.57794 c/a = 0.92925 $\alpha = \gamma = 90.0000$ $\beta = 111.0723$	x = 0.07526 z = 0.22550
3.5	a = 4.75713 b/a = 0.57654 c/a = 0.93236 $\alpha = \gamma = 90.0000$ $\beta = 110.9304$	x = 0.07561 z = 0.22708
4.0	a = 4.67585 b/a = 0.57432 c/a = 0.93399 $\alpha = \gamma = 90.0000$ $\beta = 110.7216$	x = 0.07561 z = 0.22842

B.3   EOS parameters

R$\bar{3}$m

Table B.7: 3rd order Birch-Murnaghan EOS parameters for $R\bar{3}m$ from 1.0 to 4.0 TPa.

T	V_0	B_0	B_0'	E_0	T	V_0	B_0	B_0'	E_0
0	4.01212	113.831	3.924	-41.403	4500	4.97984	15.170	3.964	-41.829
500	4.03278	108.393	3.926	-41.393	5000	5.15071	11.141	3.968	-41.821
1000	4.09250	94.310	3.930	-41.391	5500	5.20817	10.123	3.968	-41.834
1500	4.17115	78.827	3.934	-41.406	6000	5.21827	10.022	3.968	-41.859
2000	4.26442	64.046	3.939	-41.443	6500	5.22393	10.000	3.968	-41.887
2500	4.37301	50.611	3.944	-41.506	7000	5.22838	10.000	3.968	-41.915
3000	4.49838	38.876	3.949	-41.613	7500	5.23278	10.000	3.968	-41.943
3500	4.64536	28.826	3.955	-41.733	8000	5.23717	10.000	3.967	-41.974
4000	4.81970	20.485	3.960	-41.816					

I4$_1$/acd

Table B.8: 3rd order Birch-Murnaghan EOS parameters for $I4_1/acd$ from 1.0 to 4.0 TPa.

T	V_0	B_0	B_0'	E_0	T	V_0	B_0	B_0'	E_0
0	3.58415	331.530	3.884	-41.457	4500	5.17006	10.032	3.971	-41.756
500	3.57125	344.476	3.882	-41.455	5000	5.17617	10.015	3.970	-41.781
1000	3.58833	329.709	3.884	-41.465	5500	5.18218	10.000	3.970	-41.807
1500	3.65080	278.257	3.892	-41.488	6000	5.18732	10.000	3.970	-41.833
2000	3.76536	205.013	3.905	-41.523	6500	5.19246	10.000	3.970	-41.860
2500	3.95736	125.801	3.923	-41.570	7000	5.19671	10.015	3.969	-41.889
3000	4.29153	57.387	3.944	-41.628	7500	5.20176	10.016	3.969	-41.916
3500	4.71719	23.382	3.961	-41.684	8000	5.20707	10.011	3.968	-41.946
4000	5.07612	11.805	3.970	-41.728					

Cmcm

Table B.9: 3rd order Birch-Murnaghan EOS parameters for $Cmcm$ from 1.0 to 4.0 TPa.

T	V_0	B_0	B_0'	E_0	T	V_0	B_0	B_0'	E_0
4000	5.16084	10.000	3.970	-41.697	6500	5.18474	10.000	3.968	-41.849
4500	5.16568	10.000	3.969	-41.745	7000	5.18917	10.005	3.968	-41.878
5000	5.17049	10.000	3.969	-41.770	7500	5.19340	10.013	3.968	-41.906
5500	5.17527	10.000	3.969	-41.795	8000	5.19810	10.011	3.968	-41.937
6000	5.18003	10.000	3.968	-41.822					

Table B.10: 3rd order Birch-Murnaghan EOS parameters for *Cmcm* from 5.0 to 9.0 TPa.

T	V_0	B_0	B_0'	E_0	T	V_0	B_0	B_0'	E_0
0	6.57580	0.981	3.988	-41.593	4500	7.13688	0.477	3.991	-41.709
500	6.60674	0.940	3.988	-41.594	5000	7.33095	0.376	3.991	-41.732
1000	6.61869	0.926	3.989	-41.598	5500	7.49259	0.309	3.992	-41.756
1500	6.64109	0.900	3.989	-41.606	6000	7.54730	0.290	3.992	-41.779
2000	6.64740	0.895	3.989	-41.616	6500	7.58073	0.280	3.992	-41.802
2500	6.66182	0.881	3.989	-41.630	7000	7.74203	0.232	3.993	-41.828
3000	6.68037	0.861	3.989	-41.645	7500	7.78986	0.220	3.993	-41.853
3500	6.69944	0.842	3.989	-41.662	8000	7.82937	0.211	3.993	-41.878
4000	6.89566	0.650	3.990	-41.685					

Fmmm

Table B.11: 3rd order Birch-Murnaghan EOS parameters for *Fmmm* from 5.0 to 9.0 TPa.

T	V_0	B_0	B_0'	E_0	T	V_0	B_0	B_0'	E_0
0	6.14390	1.749	3.986	-41.518	4500	8.01438	0.163	3.994	-41.691
500	6.37615	1.248	3.988	-41.526	5000	8.05792	0.156	3.994	-41.716
1000	6.59767	0.917	3.989	-41.538	5500	8.17003	0.138	3.994	-41.743
1500	6.82594	0.676	3.990	-41.554	6000	8.25689	0.126	3.994	-41.770
2000	7.06531	0.497	3.991	-41.574	6500	8.30858	0.120	3.994	-41.798
2500	7.27376	0.384	3.992	-41.595	7000	8.33724	0.117	3.994	-41.826
3000	7.46975	0.303	3.992	-41.617	7500	8.45408	0.104	3.994	-41.856
3500	7.76323	0.215	3.993	-41.642	8000	8.48268	0.101	3.995	-41.886
4000	7.90483	0.184	3.993	-41.667					

C2/m

Table B.12: 3rd order Birch-Murnaghan EOS parameters for *C2/m* from 1.0 to 4.0 TPa.

T	V_0	B_0	B_0'	E_0	T	V_0	B_0	B_0'	E_0
0	3.96781	127.123	3.920	-41.411	4500	4.83189	20.186	3.959	-41.864
500	4.00406	116.343	3.923	-41.398	5000	5.02147	14.160	3.964	-41.850
1000	4.06016	101.967	3.927	-41.397	5500	5.17016	10.859	3.967	-41.841
1500	4.13197	86.455	3.931	-41.414	6000	5.21882	10.029	3.968	-41.858
2000	4.21484	71.769	3.936	-41.453	6500	5.22399	10.018	3.968	-41.886
2500	4.30122	59.409	3.940	-41.522	7000	5.22877	10.013	3.967	-41.914
3000	4.41393	46.659	3.945	-41.632	7500	5.23377	10.004	3.967	-41.942
3500	4.53406	36.358	3.950	-41.758	8000	5.23846	10.000	3.967	-41.972
4000	4.67201	27.544	3.955	-41.850					

C   Carbon dioxide

C.1   Convergence calculations

C.1.1   Electronic structure parameters

Phase II - P4$_2$/mnm

(a) Ecut

(b) **k**-points

Figure C.1: Electronic energy convergence as a function of (a) Kinetic energy cutoff and (b) **k**-points grid for CO_2-II at 70 GPa

Phase III - Cmca
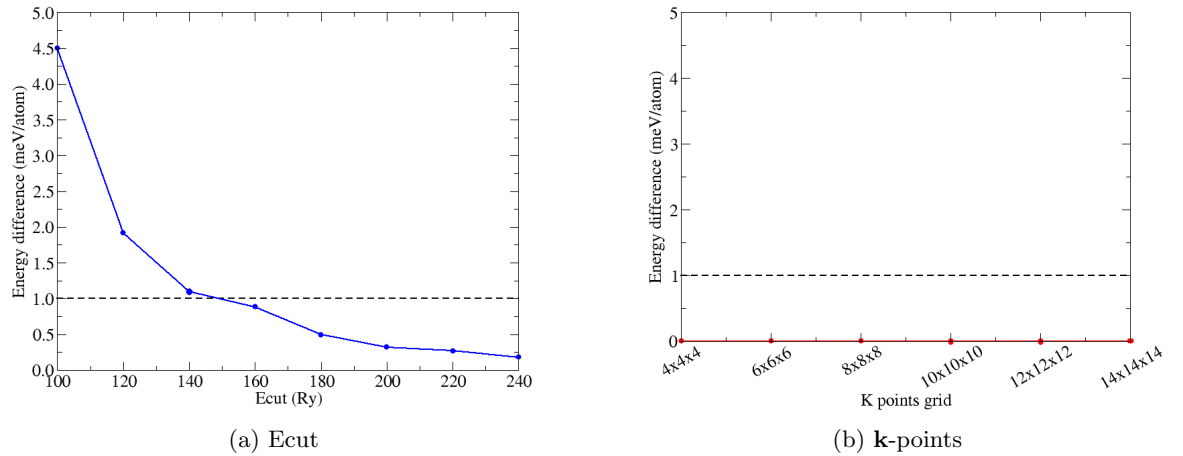
(a) Ecut

(b) **k**-points

Figure C.2: Electronic energy convergence as a function of (a) Kinetic energy cutoff and (b) **k**-points grid for CO_2-III at 70 GPa

Phase IV - R$\bar{3}$c
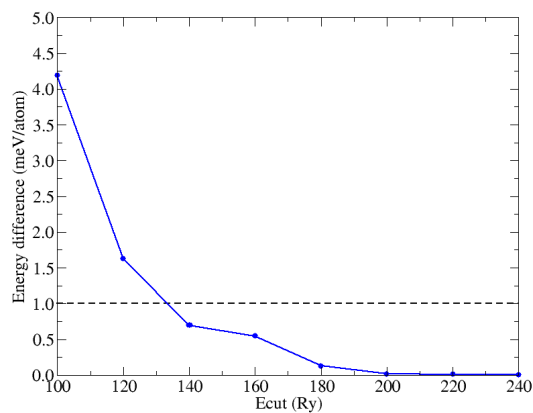
(a) Ecut
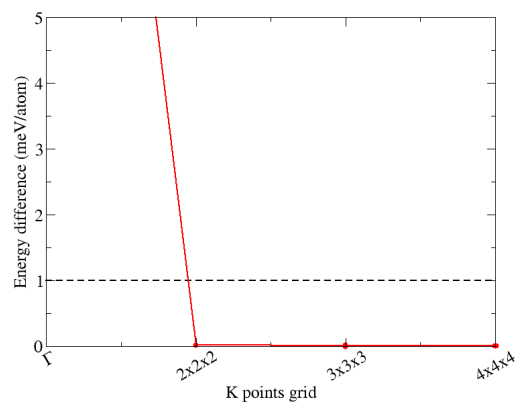
(b) **k**-points

Figure C.3: Electronic energy convergence as a function of (a) Kinetic energy cutoff and (b) **k**-points grid for CO_2-IV at 70 GPa

Phase V - I$\bar{4}$2d
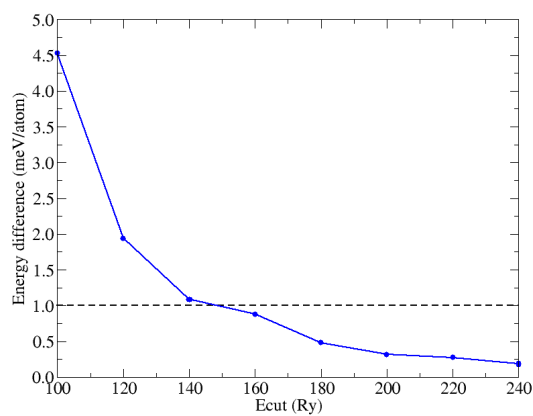
(a) Ecut
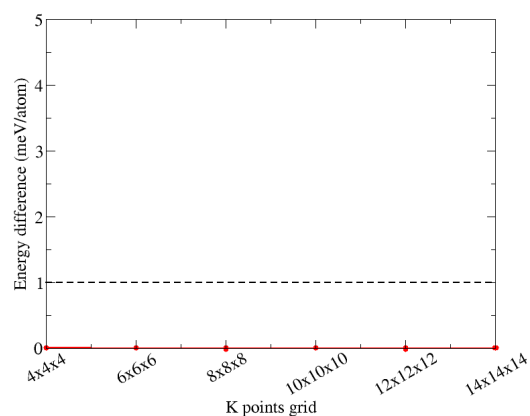
(b) **k**-points
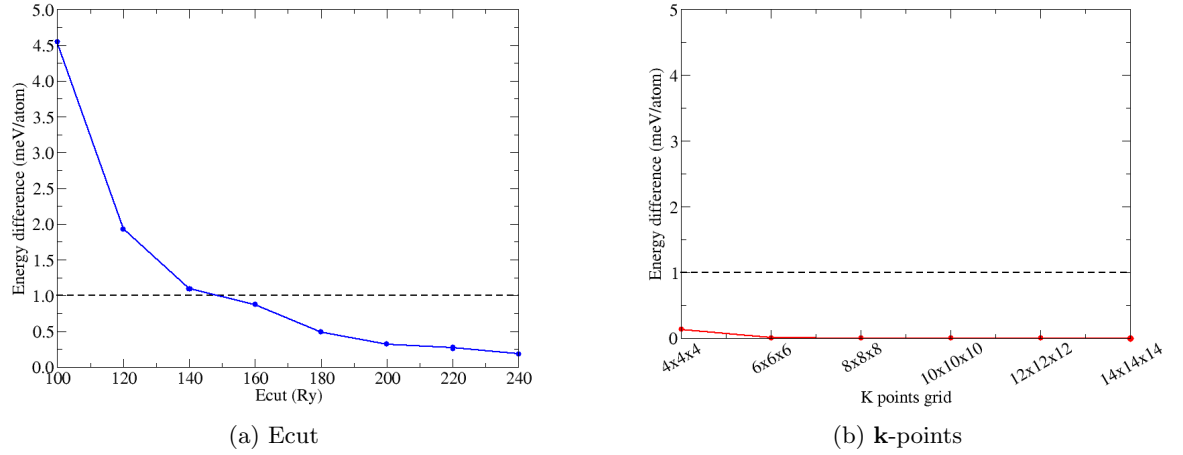
Figure C.4: Electronic energy convergence as a function of (a) Kinetic energy cutoff and (b) **k**-points grid for CO_2-V at 70 GPa

C.1.2   q-points grid

Phase II - P4$_2$/mnm
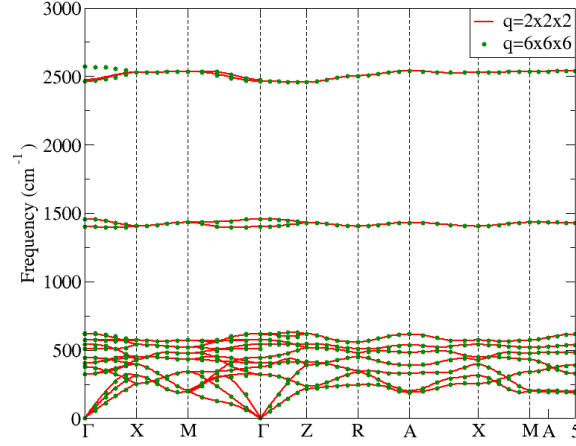
Figure C.5: Phonon dispersion for CO$_2$-II at 70 GPa with **q**-points grid of $2 \times 2 \times 2$ (red solid line) and $4 \times 4 \times 4$ (green dots).

Phase III - Cmca
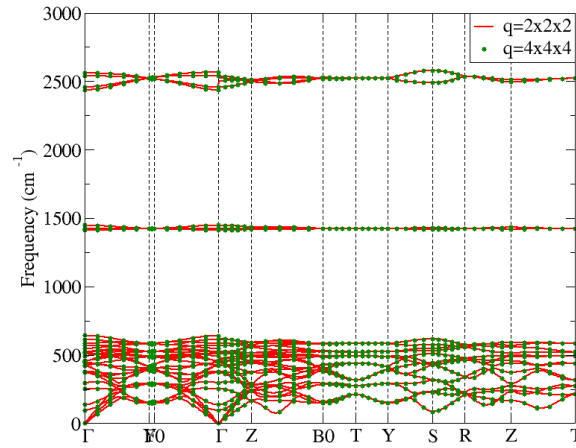
Figure C.6: Phonon dispersion for CO$_2$-III at 70 GPa with **q**-points grid of $2 \times 2 \times 2$ (red solid line) and $4 \times 4 \times 4$ (green dots).

Phase IV - R$\bar{3}$c
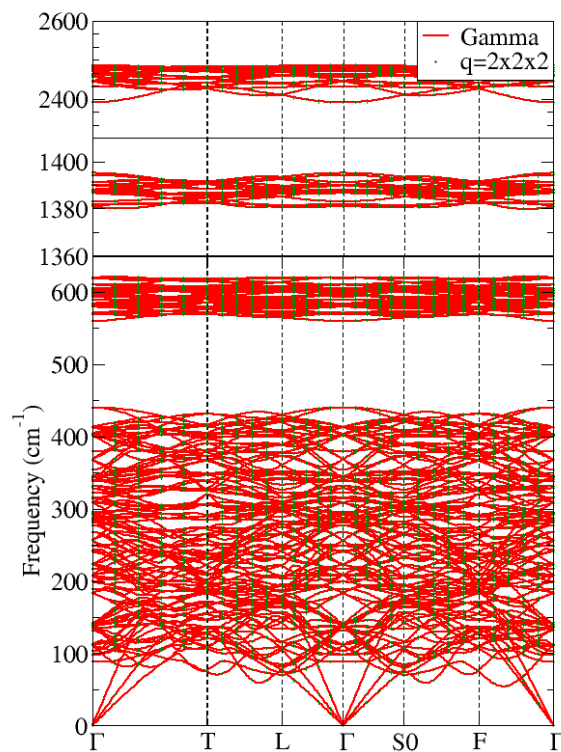
Figure C.7: Phonon dispersion for CO_2-IV at 42 GPa at Gamma point (red solid line) and with **q**-points grid of $2 \times 2 \times 2$ (green dots).

Phase V - I$\bar{4}$2d
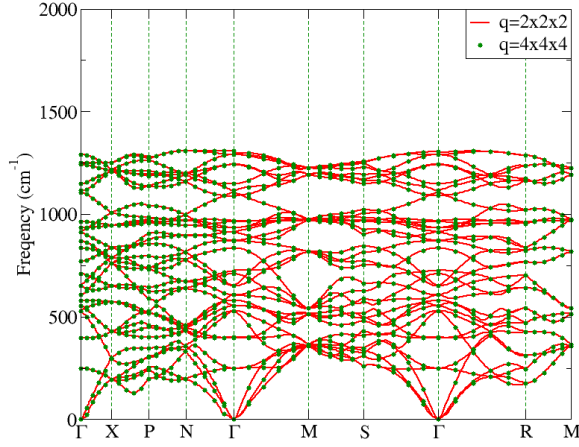
Figure C.8: Phonon dispersion for CO_2-V at 70 GPa with **q**-points grid of $2 \times 2 \times 2$ (red solid line) and $4 \times 4 \times 4$ (green dots).

C.1.3 Zero-point energy

Table C.1: Zero-point energy convergence for (a) $P4_2/mnm$, (b) $Cmca$, and (d) $I\bar{4}2d$ at 70 TPa, and (c) $R\bar{3}c$, at 42 GPa. All the energy values of $F_0(\mathbf{q})$ are in Ry.

q-points grid	$F_0(\mathbf{q})$
$2 \times 2 \times 2$	0.06167
$4 \times 4 \times 4$	0.06190
(a) $P4_2/mnm$	

q-points grid	$F_0(\mathbf{q})$
$2 \times 2 \times 2$	0.12346
$4 \times 4 \times 4$	0.12344
(b) $Cmca$	

q-points grid	$F_0(\mathbf{q})$
$Gamma$	0.67072
$2 \times 2 \times 2$	0.6982
(c) $R\bar{3}c$	

q-points grid	$F_0(\mathbf{q})$
$2 \times 2 \times 2$	0.13920
$4 \times 4 \times 4$	0.13949
(d) $I\bar{4}2d$	

C.2   Structural parameters

Phase II - P4$_2$/mnm

Table C.2: Lattice parameters and atomic positions of CO_2-II. Symmetry group: 136. Wyckoff letter for C: a. Wyckoff letter for O: f.

P (GPa)	Lattice parameters (a.u.; °)			Atomic coordinates
10	a = b = 7.21112	c/a = 1.14309	$\alpha = \beta = \gamma = 90.0$	y = 0.21581
14	a = b = 7.04109	c/a = 1.14684	$\alpha = \beta = \gamma = 90.0$	y = 0.22074
18	a = b = 6.91560	c/a = 1.14791	$\alpha = \beta = \gamma = 90.0$	y = 0.22449
22	a = b = 6.81652	c/a = 1.14766	$\alpha = \beta = \gamma = 90.0$	y = 0.22752
26	a = b = 6.73484	c/a = 1.14667	$\alpha = \beta = \gamma = 90.0$	y = 0.23005
30	a = b = 6.66556	c/a = 1.14520	$\alpha = \beta = \gamma = 90.0$	y = 0.23223
34	a = b = 6.60535	c/a = 1.14345	$\alpha = \beta = \gamma = 90.0$	y = 0.23414
38	a = b = 6.55228	c/a = 1.14152	$\alpha = \beta = \gamma = 90.0$	y = 0.23584
42	a = b = 6.50488	c/a = 1.13946	$\alpha = \beta = \gamma = 90.0$	y = 0.23736
46	a = b = 6.46211	c/a = 1.13731	$\alpha = \beta = \gamma = 90.0$	y = 0.23875
50	a = b = 6.42304	c/a = 1.13511	$\alpha = \beta = \gamma = 90.0$	y = 0.24003
54	a = b = 6.38726	c/a = 1.13288	$\alpha = \beta = \gamma = 90.0$	y = 0.24120
58	a = b = 6.35418	c/a = 1.13065	$\alpha = \beta = \gamma = 90.0$	y = 0.24229
62	a = b = 6.32344	c/a = 1.12839	$\alpha = \beta = \gamma = 90.0$	y = 0.24330
66	a = b = 6.29480	c/a = 1.12613	$\alpha = \beta = \gamma = 90.0$	y = 0.24425
70	a = b = 6.26795	c/a = 1.12389	$\alpha = \beta = \gamma = 90.0$	y = 0.24515

Phase III - Cmca

Table C.3: Lattice parameters and atomic positions of CO_2-III. Symmetry group: 64. Wyckoff letter for C: a. Wyckoff letter for O: f.

P (GPa)	Lattice parameters (a.u.; °)			Atomic coordinates
10	a = b = 9.05274	c/a = 1.26933	$\alpha = \beta = \gamma = 90.0$	y = 0.28696 z =0.38532
14	a = b = 8.80933	c/a = 1.28288	$\alpha = \beta = \gamma = 90.0$	y = 0.28262 z =0.38342
18	a = b = 8.61185	c/a = 1.29577	$\alpha = \beta = \gamma = 90.0$	y = 0.27917 z =0.38186
22	a = b = 8.46166	c/a = 1.30436	$\alpha = \beta = \gamma = 90.0$	y = 0.27632 z =0.38069
26	a = b = 8.32923	c/a = 1.31317	$\alpha = \beta = \gamma = 90.0$	y = 0.27386 z =0.37965
30	a = b = 8.21960	c/a = 1.31954	$\alpha = \beta = \gamma = 90.0$	y = 0.27172 z =0.37879
34	a = b = 8.12034	c/a = 1.32584	$\alpha = \beta = \gamma = 90.0$	y = 0.26978 z =0.37802
38	a = b = 8.03321	c/a = 1.33133	$\alpha = \beta = \gamma = 90.0$	y = 0.26804 z =0.37735
42	a = b = 7.95214	c/a = 1.33701	$\alpha = \beta = \gamma = 90.0$	y = 0.26645 z =0.37672
46	a = b = 7.88049	c/a = 1.34140	$\alpha = \beta = \gamma = 90.0$	y = 0.26498 z =0.37617
50	a = b = 7.81412	c/a = 1.34536	$\alpha = \beta = \gamma = 90.0$	y = 0.26361 z =0.37566
54	a = b = 7.75273	c/a = 1.34933	$\alpha = \beta = \gamma = 90.0$	y = 0.26232 z =0.37519
58	a = b = 7.69340	c/a = 1.35356	$\alpha = \beta = \gamma = 90.0$	y = 0.26110 z =0.37474
62	a = b = 7.64013	c/a = 1.35692	$\alpha = \beta = \gamma = 90.0$	y = 0.25996 z =0.37434
66	a = b = 7.58929	c/a = 1.36034	$\alpha = \beta = \gamma = 90.0$	y = 0.25888 z =0.37395
70	a = b = 7.54245	c/a = 1.36306	$\alpha = \beta = \gamma = 90.0$	y = 0.25785 z =0.37360

Phase IV - R$\bar{3}$c

Table C.4: Lattice parameters and atomic positions of CO_2-IV. Symmetry group: 167 (hexagonal axes). Wyckoff letter for C_1: b. Wyckoff letter for C_2: e. Wyckoff letter for O_1: c. Wyckoff letter for O_2: f.

P (GPa)	Lattice parameters (a.u.; °)	Atomic coordinates
10	a = b = 16.90884 c/a = 1.23255	C_2: x = 0.25003 – O_1: z = 0.10557
	$\alpha = \beta = \gamma = 90.0$	O_2: x = 0.13820 y = 0.31894 z = 0.20851
14	a = b = 16.53781 c/a = 1.23098	C_2: x = 0.24972 – O_1: z = 0.10793
	$\alpha = \beta = \gamma = 90.0$	O_2: x = 0.14130 y = 0.32013 z = 0.20789
18	a = b = 16.25574 c/a = 1.22968	C_2: x = 0.24950 – O_1: z = 0.10979
	$\alpha = \beta = \gamma = 90.0$	O_2: x = 0.14374 y = 0.32110 z = 0.20744
22	a = b = 16.02759 c/a = 1.22860	C_2: x = 0.24932 – O_1: z = 0.11133
	$\alpha = \beta = \gamma = 90.0$	O_2: x = 0.14577 y = 0.32192 z = 0.20710
26	a = b = 15.83540 c/a = 1.22769	C_2: x = 0.24917 – O_1: z = 0.11265
	$\alpha = \beta = \gamma = 90.0$	O_2: x = 0.14752 y = 0.32263 z = 0.20682
30	a = b = 15.66934 c/a = 1.22691	C_2: x = 0.24904 – O_1: z = 0.11380
	$\alpha = \beta = \gamma = 90.0$	O_2: x = 0.14906 y = 0.32327 z = 0.20659
32	a = b = 15.52294 c/a = 1.22624	C_2: x = 0.24892 – O_1: z = 0.11483
	$\alpha = \beta = \gamma = 90.0$	O_2: x = 0.15043 y = 0.32384 z = 0.20640
36	a = b = 15.39192 c/a = 1.22567	C_2: x = 0.24882 – O_1: z = 0.11577
	$\alpha = \beta = \gamma = 90.0$	O_2: x = 0.15168 y = 0.32436 z = 0.20622
42	a = b = 15.27328 c/a = 1.22518	C_2: x = 0.24871 – O_1: z = 0.11661
	$\alpha = \beta = \gamma = 90.0$	O_2: x = 0.15283 y = 0.32483 z = 0.20607

Phase V - I$\bar{4}$2d

Table C.5: Lattice parameters and atomic positions of CO_2-V. Symmetry group: 122. Wyckoff letter for C: a. Wyckoff letter for O: d.

P (GPa)	Lattice parameters (a.u.; °)			Atomic coordinates
10	a = b = 7.28496	c/a = 1.54138	$\alpha = \beta = \gamma = 90.0$	x = 0.17482
14	a = b = 7.21001	c/a = 1.55487	$\alpha = \beta = \gamma = 90.0$	x = 0.17860
18	a = b = 7.13976	c/a = 1.56837	$\alpha = \beta = \gamma = 90.0$	x = 0.18211
22	a = b = 7.07345	c/a = 1.58193	$\alpha = \beta = \gamma = 90.0$	x = 0.18539
26	a = b = 7.01054	c/a = 1.59560	$\alpha = \beta = \gamma = 90.0$	x = 0.18847
30	a = b = 6.95058	c/a = 1.60937	$\alpha = \beta = \gamma = 90.0$	x = 0.19139
34	a = b = 6.89323	c/a = 1.62328	$\alpha = \beta = \gamma = 90.0$	x = 0.19415
38	a = b = 6.83815	c/a = 1.63733	$\alpha = \beta = \gamma = 90.0$	x = 0.19678
42	a = b = 6.78509	c/a = 1.65154	$\alpha = \beta = \gamma = 90.0$	x = 0.19929
46	a = b = 6.73410	c/a = 1.66578	$\alpha = \beta = \gamma = 90.0$	x = 0.20169
50	a = b = 6.68481	c/a = 1.68009	$\alpha = \beta = \gamma = 90.0$	x = 0.20399
54	a = b = 6.63742	c/a = 1.69432	$\alpha = \beta = \gamma = 90.0$	x = 0.20618
58	a = b = 6.59178	c/a = 1.70846	$\alpha = \beta = \gamma = 90.0$	x = 0.20829
62	a = b = 6.54804	c/a = 1.72232	$\alpha = \beta = \gamma = 90.0$	x = 0.21029
66	a = b = 6.50592	c/a = 1.73595	$\alpha = \beta = \gamma = 90.0$	x = 0.21222
70	a = b = 6.46579	c/a = 1.74912	$\alpha = \beta = \gamma = 90.0$	x = 0.21405

C.3   EOS parameters

Phase II - P4$_2$/mnm

Table C.6: 3rd order Birch-Murnaghan EOS parameters for Phase II - P4$_2$/mnm from 10 to 50 GPa.

T	V_0	B_0	B_0'	E_0	T	V_0	B_0	B_0'	E_0
0	6.80953	125.032	3.760	-101.762	1300	7.18581	99.038	3.277	-101.876
100	6.82206	123.021	3.750	-101.763	1400	7.21894	97.040	3.247	-101.890
200	6.84637	121.023	3.709	-101.767	1500	7.25228	95.071	3.218	-101.904
300	6.87407	119.061	3.663	-101.772	1600	7.28638	93.048	3.191	-101.918
400	6.90334	117.022	3.617	-101.779	1700	7.32093	91.022	3.165	-101.933
500	6.93319	115.028	3.572	-101.787	1800	7.35554	89.059	3.140	-101.948
600	6.96365	113.013	3.529	-101.796	1900	7.39100	87.041	3.117	-101.964
700	6.99412	111.070	3.487	-101.805	2000	7.42684	85.046	3.094	-101.980
800	7.02520	109.078	3.448	-101.816	2100	7.46326	83.048	3.072	-101.996
900	7.05686	107.027	3.410	-101.827	2200	7.50029	81.047	3.051	-102.012
1000	7.08870	105.013	3.375	-101.838	2300	7.53790	79.053	3.031	-102.029
1100	7.12058	103.050	3.340	-101.850	2400	7.57642	77.032	3.011	-102.046
1200	7.15291	101.065	3.308	-101.863	2500	7.61567	75.011	2.993	-102.063

Phase III - Cmca

Table C.7: 3rd order Birch-Murnaghan EOS parameters for Phase III - Cmca from 10 to 50 GPa.

T	V_0	B_0	B_0'	E_0	T	V_0	B_0	B_0'	E_0
0	6.64095	181.136	3.683	-101.755	1300	7.28346	81.593	3.403	-101.879
100	6.65533	177.035	3.677	-101.756	1400	7.38371	71.795	3.391	-101.895
200	6.68902	169.066	3.655	-101.760	1500	7.50490	61.473	3.380	-101.912
300	6.72478	161.953	3.625	-101.766	1600	7.53569	61.409	3.335	-101.927
400	6.76268	154.899	3.595	-101.773	1700	7.53618	62.655	3.326	-101.940
500	6.80058	148.572	3.564	-101.781	1800	7.54890	65.466	3.250	-101.956
600	6.83607	143.637	3.527	-101.791	1900	7.55685	67.633	3.203	-101.972
700	6.88385	135.342	3.505	-101.801	2000	7.58195	68.859	3.143	-101.988
800	6.95221	122.389	3.503	-101.812	2100	7.60042	69.971	3.100	-102.005
900	6.99521	117.323	3.470	-101.824	2200	7.61796	71.158	3.060	-102.021
1000	7.05432	109.099	3.450	-101.837	2300	7.72957	63.108	3.047	-102.041
1100	7.12116	100.316	3.432	-101.850	2400	7.87491	53.707	3.040	-102.062
1200	7.19687	91.125	3.417	-101.864	2500	8.09517	41.715	3.041	-102.085

Phase IV - R$\bar{3}$c

Table C.8: 3rd order Birch-Murnaghan EOS parameters for Phase IV - R$\bar{3}$c from 10 to 50 GPa.

T	V_0	B_0	B_0'	E_0	T	V_0	B_0	B_0'	E_0
0	6.64095	181.136	3.683	-101.755	1300	7.28346	81.593	3.403	-101.879
100	6.65533	177.035	3.677	-101.756	1400	7.38371	71.795	3.391	-101.895
200	6.68902	169.066	3.655	-101.760	1500	7.50490	61.473	3.380	-101.912
300	6.72478	161.953	3.625	-101.766	1600	7.53569	61.409	3.335	-101.927
400	6.76268	154.899	3.595	-101.773	1700	7.53618	62.655	3.326	-101.940
500	6.80058	148.572	3.564	-101.781	1800	7.54890	65.466	3.250	-101.956
600	6.83607	143.637	3.527	-101.791	1900	7.55685	67.633	3.203	-101.972
700	6.88385	135.342	3.505	-101.801	2000	7.58195	68.859	3.143	-101.988
800	6.95221	122.389	3.503	-101.812	2100	7.60042	69.971	3.100	-102.005
900	6.99521	117.323	3.470	-101.824	2200	7.61796	71.158	3.060	-102.021
1000	7.05432	109.099	3.450	-101.837	2300	7.72957	63.108	3.047	-102.041
1100	7.12116	100.316	3.432	-101.850	2400	7.87491	53.707	3.040	-102.062
1200	7.19687	91.125	3.417	-101.864	2500	8.09517	41.715	3.041	-102.085

Phase V - I$\bar{4}$2d

Table C.9: 3rd order Birch-Murnaghan EOS parameters for Phase V - I$\bar{4}$2d from 10 to 50 GPa.

T	V_0	B_0	B_0'	E_0	T	V_0	B_0	B_0'	E_0
0	5.44055	1356.100	3.279	-101.654	1300	5.49148	1236.130	3.335	-101.711
100	5.44081	1355.180	3.280	-101.654	1400	5.49729	1222.790	3.342	-101.719
200	5.44195	1352.690	3.280	-101.655	1500	5.50318	1209.490	3.349	-101.728
300	5.44408	1347.930	3.280	-101.656	1600	5.50920	1196.020	3.356	-101.737
400	5.44713	1340.700	3.283	-101.658	1700	5.51531	1182.470	3.363	-101.747
500	5.45086	1331.700	3.287	-101.661	1800	5.52152	1168.760	3.370	-101.757
600	5.45508	1321.460	3.292	-101.665	1900	5.52785	1154.960	3.377	-101.767
700	5.45967	1310.390	3.298	-101.670	2000	5.53432	1140.750	3.385	-101.778
800	5.46451	1298.940	3.303	-101.675	2100	5.54082	1126.990	3.391	-101.789
900	5.46961	1286.800	3.309	-101.681	2200	5.54746	1112.920	3.398	-101.800
1000	5.47486	1274.480	3.316	-101.688	2300	5.55422	1098.670	3.406	-101.811
1100	5.48040	1260.790	3.325	-101.695	2400	5.56108	1084.390	3.413	-101.823
1200	5.48563	1250.520	3.325	-101.702	2500	5.56803	1070.210	3.420	-101.835

List of Publications

Part of the work presented here has been published in the following references:

1 *Phase diagram of oxygen at extreme pressure and temperature conditions: An* ab initio
   study

   Beatriz H. Cogollo-Olivo, Sandro Scandolo, Sananda Biswas and Javier A. Montoya

   Physical Review B 98, 094103 (2018)

2 Ab initio *determination of the phase diagram of* CO_2 *at high pressures and temperatures*

   Beatriz H. Cogollo-Olivo, Sandro Scandolo, Sananda Biswas and Javier A. Montoya

   arXiv: 1908.11352 [cond-mat.mtrl-sci] (2019)

   In press **Physical Review Letters** (2020)

Phase diagram of oxygen at extreme pressure and temperature conditions: An *ab initio* study

Beatriz H. Cogollo-Olivo

Universidad de Cartagena, Doctorado en Ciencias Físicas Cartagena de Indias, 130001, Colombia
and The Abdus Salam ICTP, Condensed Matter and Statistical Physics Section Trieste, Strada Costiera 11, 34151, Italy

Sananda Biswas

The Abdus Salam ICTP, Condensed Matter and Statistical Physics Section Trieste, Strada Costiera 11, 34151, Italy
and Institut für Theoretische Physik, Goethe-Universität Frankfurt, 60438 Frankfurt am Main, Germany

Sandro Scandolo

The Abdus Salam ICTP, Condensed Matter and Statistical Physics Section Trieste, Strada Costiera 11, 34151, Italy

Javier A. Montoya

Universidad de Cartagena, Instituto de Matemáticas Aplicadas Cartagena de Indias, 130001, Colombia

The phase diagram of solid oxygen at terapascal pressures and several thousand Kelvin has been studied with *ab initio* density functional theory within the quasiharmonic approximation for the vibrational free energy. Our work extends previous theoretical studies done at zero temperature and shows that temperature has a dramatic effect on the sequence of phases. At low temperature, the transition from onefold (molecular) to fourfold coordination takes place through two intermediate phases with twofold coordination and space groups $I4_1/acd$ and $Cmcm$. Above 8000 K we find that these two intermediate phases are no longer stable, and oxygen transforms directly from a molecular phase to a fourfold coordinated phase of space group $Fmmm$. We also find that the transition between $Cmcm$ and $Fmmm$ can be ascribed as a second-order transition driven by an electronic instability.

I. INTRODUCTION

Owing to the magnetic character of the O_2 molecule, the element oxygen exhibits a richer phase diagram than other low-Z diatomic molecules such as H_2, N_2, CO, or F_2. Six phases of solid oxygen have been observed experimentally so far: Half of them (α, β, and γ) exist under equilibrium vapor pressure, and the other three (δ, ϵ, and ζ) are obtained in the high-pressure regime. As pressure increases, oxygen shows a wide range of physical properties that go from insulating [1] to metallic [2], including also antiferromagnetic [3–6] and superconducting [7,8] phases. At the highest pressure reached for this element in the laboratory, about 130 GPa under diamond-anvil cell compression, it remains molecular [8]. In the ϵ-O_2 phase, which is stable between 8 and 96 GPa at ambient temperature [2], the oxygen molecules associate into clusters composed of four molecules, but they fully retain their molecular character as confirmed by vibrational spectroscopy and x-ray diffraction [9,10].

All other group-VI elements develop nonmolecular and eventually monoatomic structures at much lower pressure. Sulfur transforms into a chainlike polymeric phase at about 15 GPa and eventually becomes monoatomic, with a rhombohedral β-Po structure at 153 GPa [11]. Phases with a β-Po structure are also reported for Se at 60 GPa [12], for Te at 11 GPa [13], and for Po at ambient pressure [14]. Moreover, both selenium and tellurium exhibit a body-centered

cubic (bcc) structure as a post β-Po phase [12,15,16]. For oxygen, however, an earlier theoretical study has shown that the monoatomic β-Po structure is less stable than molecular phases at multimegabar pressures [17]. The reluctance of oxygen to give up its molecular character has been attributed in a recent study by Sun *et al.* to the strong electron lone-pair repulsion in the nonmolecular phases. This resembles, we notice, the reluctance of the electron-richer halogen elements to lose their molecular character. For instance, fluorine is molecular up to the highest pressures experimentally achieved so far in this element [18], while Cl_2, Br_2, and I_2 dissociate around 157, 115, and 43 GPa, respectively [19–27].

In the same work, Sun *et al.* [28] show that oxygen remains molecular up to 1.9 TPa before transforming into a semiconducting square-spiral-like polymeric structure with symmetry $I4_1/acd$ and oxygen in twofold coordination. This phase is then reported to transform at 3.0 TPa into a phase with $Cmcm$ symmetry, consisting of zigzag chains that pack atoms more efficiently than the square-spiral chains. Finally, when pressure reaches 9.3 TPa, the in-plane zigzag chains merge into a layered structure with $Fmmm$ symmetry and four equidistant nearest neighbors for each oxygen atom [28].

Temperature can have profound effects on the stability of molecular phases, both in their liquid and solid forms. Shock-compression experiments indicate that at about 100 GPa the oxygen molecule dissociates in the fluid when the temperature exceeds 4000 K [29], whereas theoretical studies based on

ab initio molecular dynamics place molecular dissociation above 80 GPa at temperatures that exceed 5000 K [30]. Unfortunately, nothing is known about the temperature effects on the phase diagram of *solid* oxygen at extreme pressures. A crude extrapolation of the oxygen melting line, based on theoretical and experimental data [31,32], yields a melting temperature of about 26 000 K at 1.9 TPa. Although this extrapolation is based on data below 100 GPa and is, therefore, to be taken with caution, this provides a hint that solid oxygen phases could indeed be the stable forms of this element in some planetary interiors. Hence, the understanding of the effects of temperature on the solid portion of oxygen's phase diagram at multimegabar pressures is not only relevant from a fundamental perspective, but also for its potential relevance to planetary studies. Moreover, recent technical developments in dynamic shock-wave (ramp) compression have made it possible to achieve temperature and pressure conditions in the laboratory that are within the solid portion of selected phase diagrams [33–35], suggesting that experiments may soon be able to study the properties of this element at planetary conditions.

The ground state calculations performed by Sun *et al.* [28] show that the transitions from molecular to polymeric and finally to fourfold coordinated have dramatic effects on the vibrational properties of solid oxygen. Finite-temperature contributions to the free energy should, therefore, differ substantially between different phases and the phase transitions at high temperature may, as a consequence, differ quantitatively and qualitatively from the ones calculated at zero temperature. In this work, by performing density functional theory (DFT) together with quasiharmonic approximation (QHA) calculations for the determination of vibrational free energies, we extend the current theoretical knowledge on the ultrahigh-pressure region of the phase diagram of solid oxygen to temperatures up to 8000 K. We find that temperature has a remarkable effect on the phase diagram of this element indeed, resulting in the disappearance of two previously reported nonmolecular forms at sufficiently high temperature.

II. METHODS

Out of the several crystalline structures considered in the earlier theoretical work by Sun *et al.* [28], we select here the ones that were found to be stable in the range of pressure 1–10 TPa: a molecular structure with symmetry $R\bar{3}m$ and three nonmolecular structures with symmetry $I4_1/acd$, $Cmcm$, and $Fmmm$, respectively. Enthalpy differences among the different molecular structures considered in Ref. [28] ($P6_3/mmc$, $C2/m$, $C2/c$, and $R\bar{3}m$) are small compared to enthalpy differences between molecular and nonmolecular structures, so we expect transition pressures between molecular and nonmolecular phases to be largely independent of the specific molecular structure considered. Here we consider the $R\bar{3}m$ phase as representative of the stable solid molecular oxygen form before polymerization and tested the validity of this assumption with a test calculation on a different molecular structure with symmetry $C2/m$.

The structural properties were calculated using DFT as implemented in QUANTUM ESPRESSO [36]. The electron-ion interactions were treated using a projector augmented

wave pseudopotential with six valence electrons. The valence electron wave functions are expanded in a plane-wave basis set with a kinetic energy cutoff of 400 Ry. The exchange-correlation functional was approximated by the generalized gradient approximation (GGA) of the Perdew-Burke-Ernzerhof form [37]. Brillouin zone integrations were carried out using k-point grids generated with the Monkhorst-Pack method [38]. The size of these grids are $18 \times 18 \times 18$, $4 \times 4 \times 12$, $8 \times 16 \times 16$, and $8 \times 16 \times 16$ for the primitive cells of the four phases of oxygen considered in this study; these choices provided a total-energy-difference convergence of 2 meV per atom or better. The structural parameters for all the structures were obtained by performing variable cell optimization at various values of pressure. Note that the energies and electronic structures of the four structures have been already studied by Sun *et al.* [28]; they showed that at $T = 0$ K, all the phases are metallic at the terapascal regime, except for $I4_1/acd$ which is a wide-gap semiconductor. Our calculations agree well with those results, as discussed in Sec. III. For the metallic phases, the calculations were done using the Fermi-Dirac smearing technique with a width of 43 meV, in order to take into account the electronic entropy at 500 K. This width was kept fixed while calculating the vibrational properties at all temperatures, as justified by the lack of sensitivity of our free energy results with respect to this parameter.

The vibrational properties at $T = 0$ K were calculated using density functional perturbation theory (DFPT) in the linear response regime [39]. The q-point grids used to obtain the dynamical matrices were as follows: $4 \times 4 \times 4$ for $R\bar{3}m$, $2 \times 2 \times 6$ for $I4_1/acd$, $2 \times 4 \times 4$ for $Cmcm$, and $2 \times 4 \times 4$ for $Fmmm$.

Finite-temperature contributions to the Helmholtz free energy were obtained using the QHA [40,41]:

$$F(V, T) = U_0(V) + \frac{1}{2} \sum_{\mathbf{qs}} \hbar\omega_{\mathbf{qs}}$$

$$+ k_\mathrm{B} T \sum_{\mathbf{qs}} \ln[1 - \exp(-\hbar\omega_{\mathbf{qs}}/k_\mathrm{B} T)], \quad (1)$$

where $\omega_{\mathbf{qs}}$ is the frequency of the mode $\mathbf{s}$ at point $\mathbf{q}$ in the Brillouin zone and a given volume V; $U_0(V)$ is the ground state electronic energy of the crystal at volume V, and the second and third terms on the right-hand-side of the above equation are the zero-point energy (ZPE) and the thermal vibrational contribution to the free energy, respectively, at volume V.

As we are interested in determining the pressure-temperature (P-T) phase diagram, we have calculated the Gibbs free energy as:

$$G(P, T) = F[V(P, T), T] + PV(P, T), \quad (2)$$

where the value of the P is obtained by fitting Eq. (1) to a third order Birch-Murnaghan equation of state for each of the phases at different temperatures and their corresponding parameters are specified in the Supplemental Material [42]. All fits had a variance (χ^2) of order 10^{-5} or better.

III. RESULTS AND DISCUSSION

We begin our analysis by considering the case $T = 0$ K, with and without the zero-point energy contributions. In the
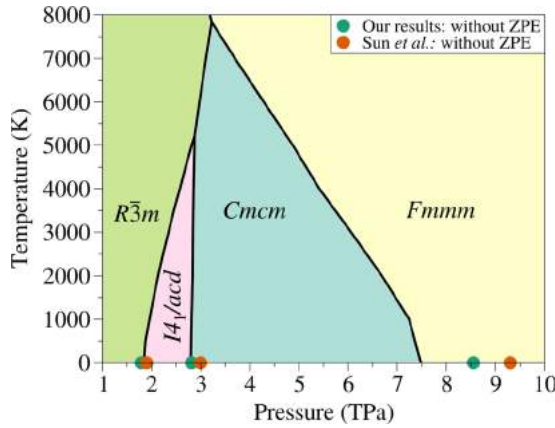
FIG. 1. Proposed finite temperature phase diagram for solid oxygen at extreme conditions of pressure and temperature. The transition pressures P_T, at zero temperature without taking into account the zero-point energy (ZPE), reported by Sun *et al.* [28] and calculated in the present study, are marked as orange and green circles, respectively. The phase boundaries at finite temperature, corresponding to calculations including ZPE and using an electronic temperature of 500 K, are shown by solid black lines.

low-pressure region of this study we find that the contribution of the ZPE is marginal, moving the transition pressures 0.08 TPa and 0.02 TPa higher than those reported without ZPE when going from $R\bar{3}m$ to $I4_1/acd$ and from $I4_1/acd$ to $Cmcm$, respectively (see Fig. 1). In the high-pressure region, our enthalpy-pressure relations show that the transition from $Cmcm$ to $Fmmm$ at 0 K is located near 8.6 TPa if ZPE is not included; this is 0.7 TPa lower than the transition pressure found by Sun *et al.* with the same approximations [28]. Our equations of state were fitted on a broader set of volumes than Sun *et al.*, usually fifteen or more volumes per structure. We believe that this could be one of the reasons for the discrepancy. Moreover, when the ZPE contribution is included, it has a noticeable effect, shifting the transition pressure from 8.6 TPa to 7.5 TPa.

We now consider the effects of finite temperature on the Gibbs free energies and transition pressures. Our calculations are based on the QHA and may suffer from the incomplete consideration of anharmonicities, in particular when the system approaches the melting temperature, therefore, our analysis is restricted here to temperatures below 8000 K.

The finite temperature contribution to the free energy has dramatic consequences on the relative stability of the crystalline phases (Fig. 1). For instance, the pressure location for the $R\bar{3}m$ to $I4_1/acd$ phase boundary is shifted towards higher pressures by approximately 1 TPa when the temperature is raised from 0 to 5000 K, indicating that the molecular $R\bar{3}m$ phase enlarges its region of stability with respect to the polymeric $I4_1/acd$, as temperature increases. However, the finite temperature contribution hardly changes the transition boundary between the phases $I4_1/acd$ and $Cmcm$, as we observed an increment of just 0.05 TPa at 5000 K with respect to the transition pressure calculated at 0 K. We observe that the region that encompassed the $I4_1/acd$ phase narrows down as temperature increases until, at 2.9 TPa and 5200 K, there is a triple point above which this phase disappears completely. Thus, the picture of $I4_1/acd$ as an insulating solid phase lying between two metallic ones ($R\bar{3}m$ and $Cmcm$) is only valid at relatively low temperatures. Unlike the previous two cases, the shift seen in the case of the $Cmcm$-to-$Fmmm$ transition is towards lower pressures and is much more pronounced, leading to a second triple point at 3.2 TPa and 7800 K, where the $R\bar{3}m$, $Cmcm$, and $Fmmm$ phases meet. This indicates that above 8000 K oxygen transforms directly from a molecular to a fourfold coordinated form.

So far our analysis has been restricted to a single molecular structure ($R\bar{3}m$). In order to test the validity of our assumption that $R\bar{3}m$ can be considered as representative of the stable molecular structure, we repeated the calculations with a different molecular structure, of symmetry $C2/m$. This structure was found to possess the second lowest enthalpy after $R\bar{3}m$, among the structures considered by Sun *et al.* [28]. We find that the transition line between $C2/m$ and the other structures is indistinguishable from the transition line of $R\bar{3}m$, suggesting that not only enthalpy but also entropy is very similar among different molecular forms.

As already mentioned, an extrapolation of the measured melting line of oxygen to TPa pressures yields a melting temperature exceeding 25 000 K at 2 TPa. An independent estimate of the melting temperature can be obtained by calculating the Lindemann ratio of the solid phases, a quantity that normally reaches values between 0.1 and 0.15 at melting. We calculated the Lindemann ratio for the $R\bar{3}m$ molecular structure and for the $Fmmm$ structure within the QHA approximation. In the case of the molecular structure we
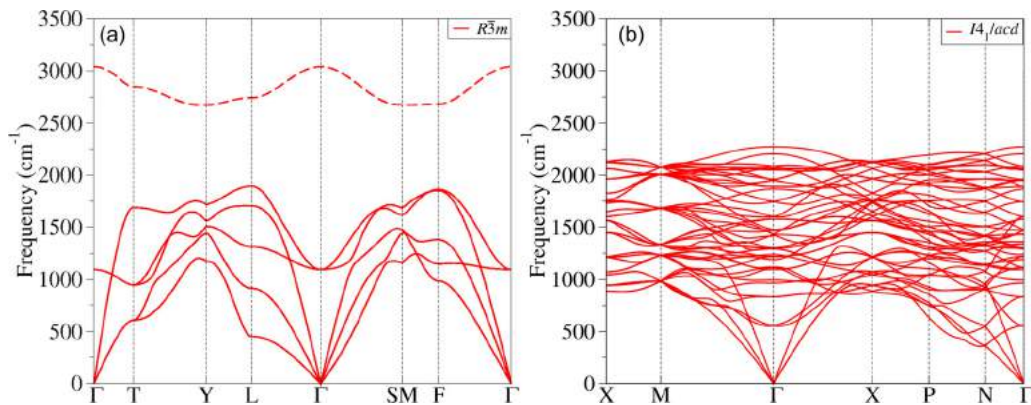

FIG. 2. Phonon dispersions of oxygen in (a) $R\bar{3}m$ with the vibron mode in dashed line and (b) $I4_1/acd$ phases at 2.0 TPa.
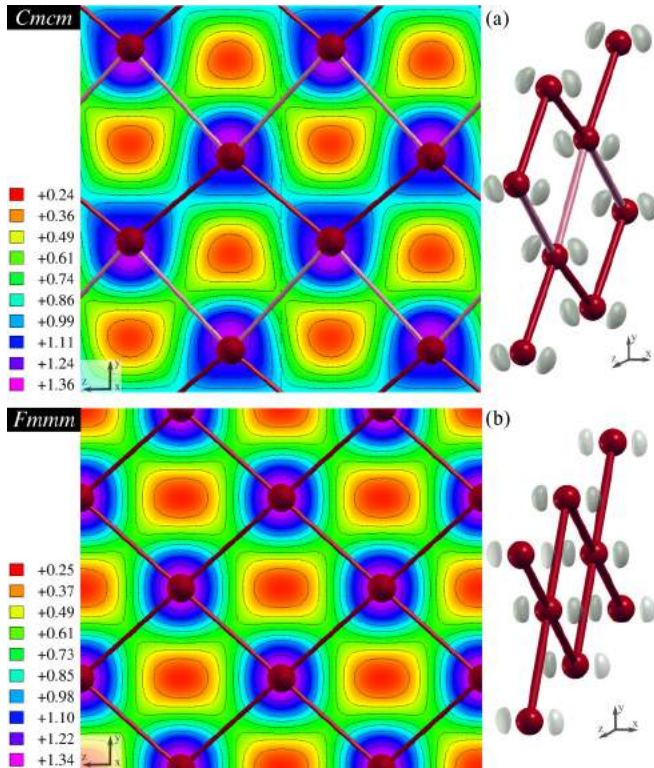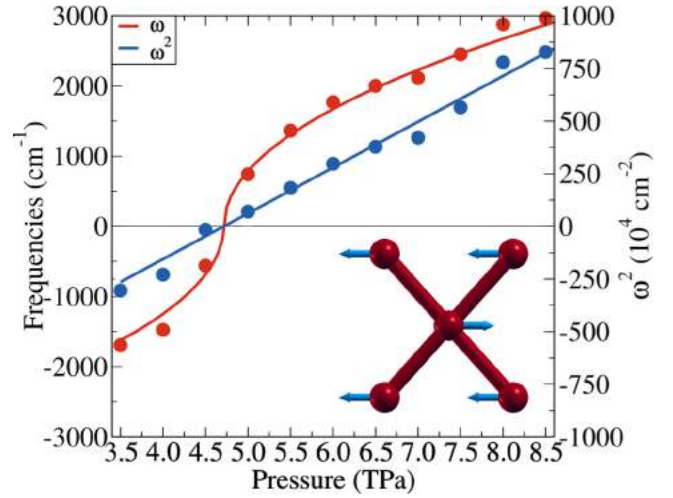
FIG. 5. Evolution of a *Fmmm* phonon mode at the zone boundary as a function of pressure. The normal mode is along the [100] direction, and its frequencies (ω) are plotted in red. A linear relation between the squared phonon frequencies (ω^2) and pressure (blue) is observed and indicates that the phonon softening occurs near 4.7 TPa. The normal mode is represented as blue arrows on the atoms of the *Fmmm* structure.

FIG. 3. Electronic charge densities along the [100] direction and electron lone pairs of (a) *Cmcm* and (b) *Fmmm* at 7.5 TPa. The color scales indicate the values of the charge density in e/Bohr^3. On the left panel, the isosurface of red and orange regions are electron poor, while blue and violet regions are electron rich. Additionally, isosurface contours are shown by solid black lines. On the right panel, the lone pairs are represented by transparent gray colors; the corresponding isosurface value is $+1.25\,e$/Bohr^3. The oxygen atoms are represented by red spheres and the *Cmcm* zigzag chains are shown in red and pink.

assumed that melting takes place between a molecular solid and a molecular liquid and evaluated the Lindemann ratio based on the mean-square displacement of the center of mass of the molecules. We found that calculated values of L_R are always below 0.095, for both phases, in the temperature range from 0 K to 8000 K. Our calculations therefore rule out the

presence of a liquid in the pressure and temperature region considered in this work.

We were also able to confirm that strongly localized lone pairs persist into the polymeric phases with an OX_2E_2 bent shape, as already noted by Sun *et al.* [28]. This, together with an electron counting argument, can explain the reluctance of oxygen to take higher coordinated structures. The formation in $I4_1/acd$ of one additional covalent bond and the lone pair repulsion between chains, contribute to making it stiffer and less flexible than the molecular $R\bar{3}m$ phase. At temperatures below 4000 K the contribution to the entropy of the high frequency vibron in Fig. 2(a) is limited by quantum effects. The remaining modes show a frequency increase across the transition, which implies a decrease of the vibrational entropy. This is consistent with the positive slope of the transition line at finite temperature (see Fig. 1). Similarly, the $I4_1/acd$ and *Cmcm* phases are characterized by having two covalent bonds per oxygen and very similar lone pair repulsion between
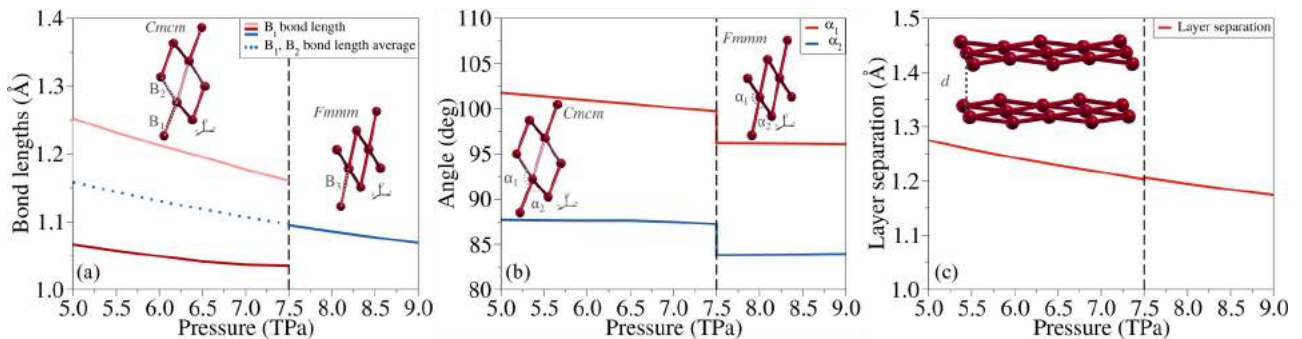
FIG. 4. Pressure dependence of (a) bond lengths for *Cmcm* (B$_1$ and B$_2$, red and pink solid lines, respectively) and *Fmmm* (B$_3$, blue solid line), (b) internal angles (α_1 and α_2, red and blue solid lines, respectively) of *Cmcm* and *Fmmm*, and (c) the layer separation d (red solid line) for *Cmcm* and *Fmmm* are shown. The vertical black dashed line corresponds to the calculated transition pressure between these two phases. The average of B$_1$ and B$_2$ are also shown by a dotted blue line in (a).
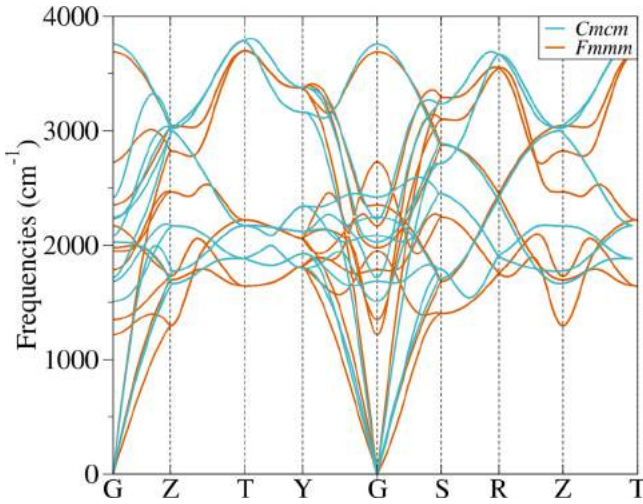
FIG. 6. Phonon dispersions of oxygen in *Cmcm* (in cyan) and *Fmmm* (in orange) phases at 8.0 TPa. Note that the supercell size has been used in both the cases.

chains. Therefore, one does not expect important changes in terms of bonding and stiffness, which justifies why we observe an almost vertical transition line between these two polymeric forms in the *P*-*T* phase diagram (Fig. 1).

As pressure increases above 4 TPa and keeps approaching the vicinity of the *Cmcm* → *Fmmm* transition, the bent shape of the lone pairs in *Cmcm* starts to allow for a nonsymmetrical fourfold coordination, which brings the formation of two additional weak covalent bonds per each oxygen prior to the final transition towards the fully symmetric *Fmmm* configuration; this is shown in Fig. 3(a) by the charge density profiles. This process causes a gradual merging of the so-called zigzag chains into a layered structure. For instance, at $T = 0$ K and 7.0 TPa, the four shortest links for each oxygen consist of two sets of bonds with lengths 1.04 Å and 1.18 Å, respectively. Instead, when *Cmcm* transforms into *Fmmm* above 7.5 TPa not only the coordination of the oxygen atoms becomes symmetrical, with an equal length of 1.10 Å, but also we can see now that the lone pairs adopt the OX_4E_2 square

planar shape, as a consequence of the higher symmetry of this phase as Fig. 3(b) shows.

From a space-group point of view, *Cmcm* is a subgroup of *Fmmm* so that the transition can be classified in principle as a second-order phase transition. Coupling of the strain with the internal degrees of freedom, however, introduces a slight discontinuity in the structural parameters (see Fig. 4), similarly to the case of the stishovite (rutile) to the $CaCl_2$-type phase transition in SiO_2 [43]. Further evidence for the quasi-second-order nature of the transition comes from the phonon dispersions of the two phases. In Fig. 5 we show the pressure dependence of the frequency of the phonon mode at the Brillouin zone vector of the *Fmmm* phase corresponding to the reciprocal lattice vector of the *Cmcm* phase. The mode becomes unstable when pressure is decreased below 4.7 TPa, indicating a lattice instability of the *Fmmm* phase towards *Cmcm*, as also confirmed by the pattern of the unstable mode, shown in the inset of Fig. 5. A characteristic feature of second-order phase transitions is the higher entropy of the high-symmetry phase with respect to the low-symmetry phase. This is consistent with the pronounced left turning of the *Cmcm* to *Fmmm* phase transition line at finite temperatures in Fig. 1, and it is confirmed by the phonon dispersions of the two phases calculated at the transition pressure of 8.0 TPa (Fig. 6). Contrary to the naive expectation that frequencies become stiffer in the high-pressure (*Fmmm*) phase with respect to the low-pressure (*Cmcm*) phase, the phonon dispersion of the *Cmcm* phase has modes that are marginally higher in energy than those of the *Fmmm* phase. This is consistent with the lower entropy of the *Cmcm* phase with respect to the *Fmmm* phase.

To gain further insight into the driving force of the quasi-second-order transition, we show in Fig. 7 the electronic density of states (DOS) of the two phases in the vicinity of the pressure where *Fmmm* becomes unstable. Interestingly, the DOS of the *Fmmm* phase shows a pronounced peak that crosses the Fermi level between 4.5 and 5 TPa, the same pressure of the phonon instability reported in Fig. 5. The distortion leading to the *Cmcm* structure causes a lowering of the DOS at the Fermi level. We, therefore, argue that the *Cmcm* to *Fmmm* transition is driven by an electronic
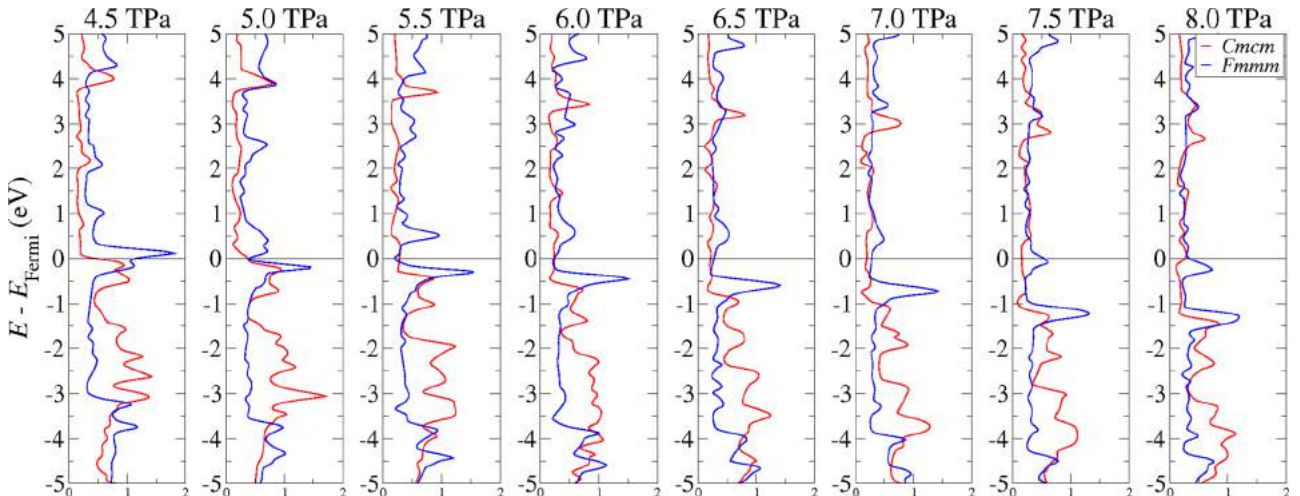

FIG. 7. Electronic DOS of oxygen in *Cmcm* (in red) and *Fmmm* (in blue) phases as a function of pressure.

instability qualitatively similar to a commensurate charge-density-wave transition. A similar phenomenology has been observed in other chalcogen elements, where it has been shown to be connected with the emergence of a superconducting state in the undistorted state (*Fmmm* in this case) close to the transition pressure to the distorted phase [11].

IV. CONCLUSIONS

Our theoretically predicted phase diagram of oxygen at extreme pressures and temperatures extends earlier calculation at high pressure and zero temperature and shows that temperature has a profound effect on the phase diagram. At finite temperatures, the molecular phase expands its stability range to pressures exceeding 3 TPa at the highest temperatures considered in this work (8000 K). On the contrary, the range of stability of the first nonmolecular phase, $I4_1/acd$, shrinks with temperature and the phase is no longer thermodynamically stable above 5000 K. Interesting physics underlies the transition between the *Cmcm* and the *Fmmm* nonmolecular

phases. Our calculations indicate a quasi-second-order transition between the two phases and show that the transition is driven by an electronic instability causing a softening of the corresponding phonon mode. We argue that this may imply a superconducting state which is beyond the scope of this work but which certainly deserves further attention. The range of pressures and temperatures examined in this work are now within reach of ramp-compression experiments which we hope will soon shed additional light on the intriguing aspects of the pressure-induced demise of molecular oxygen as reported in this and other recent theoretical studies.

[1] Y. Crespo, M. Fabrizio, S. Scandolo, and E. Tosatti, Proc. Natl. Acad. Sci. USA **111**, 10427 (2014).

[2] Y. Akahama, H. Kawamura, D. Häusermann, M. Hanfland, and O. Shimomura, Phys. Rev. Lett. **74**, 4690 (1995).

[3] M. Nicol, K. R. Hirsch, and W. B. Holzapfel, Chem. Phys. Lett. **68**, 49 (1979).

[4] D. Schiferl, D. T. Cromer, L. A. Schwalbe, and R. L. Mills, Acta Crystallogr. Sect. B **39**, 153 (1983).

[5] F. A. Gorelli, M. Santoro, L. Ulivi, and M. Hanfland, Phys. Rev. B **65**, 172106 (2002).

[6] I. N. Goncharenko, O. L. Makarova, and L. Ulivi, Phys. Rev. Lett. **93**, 055502 (2004).

[7] Y. Ma, A. R. Oganov, and C. W. Glass, Phys. Rev. B **76**, 064101 (2007).

[8] G. Weck, S. Desgreniers, P. Loubeyre, and M. Mezouar, Phys. Rev. Lett. **102**, 255503 (2009).

[9] L. F. Lundegaard, G. Weck, M. I. McMahon, S. Desgreniers, and P. Loubeyre, Nature (London) **443**, 201 (2006).

[10] H. Fujihisa, Y. Akahama, H. Kawamura, Y. Ohishi, O. Shimomura, H. Yamawaki, M. Sakashita, Y. Gotoh, S. Takeya, and K. Honda, Phys. Rev. Lett. **97**, 085503 (2006).

[11] O. Degtyareva, E. Gregoryanz, H. K. Mao, and R. J. Hemley, High Pressure Research **25**, 17 (2005).

[12] Y. Akahama, M. Kobayashi, and H. Kawamura, Phys. Rev. B **47**, 20 (1993).

[13] J. C. Jamieson and D. B. McWhan, J. Chem. Phys. **43**, 1149 (1965).

[14] R. J. DeSando and R. C. Lange, J. Inorg. Nucl. Chem. **28**, 1837 (1966).

[15] F. El Haj Hassan, A. Hijazi, M. Zoaeter, and F. Bahsoun, Physica B: Condensed Matter **363**, 82 (2005).

[16] M. Otani and N. Suzuki, Phys. Rev. B **63**, 104516 (2001).

[17] T. Oda, K. Sugimori, H. Nagao, I. Hamada, S. Kagayama, M. Geshi, H. Nagara, K. Kusakabe, and N. Suzuki, J. Phys.: Condens. Matter **19**, 365211 (2007).

[18] Q. Lv, X. Jin, T. Cui, Q. Zhuang, Y. Li, Y. Wang, K. Bao, and X. Meng, Chin. Phys. B **26**, 076103 (2017).

[19] P. Li, G. Gao, and Y. Ma, J. Chem. Phys. **137**, 064502 (2012).

[20] T. Kenichi, S. Kyoko, F. Hiroshi, and O. Mitsuko, Nature (London) **423**, 971 (2003).

[21] T. Kume, T. Hiraoka, Y. Ohya, S. Sasaki, and H. Shimizu, Phys. Rev. Lett. **94**, 065506 (2005).

[22] D. Duan, Y. Liu, Y. Ma, Z. Liu, T. Cui, B. Liu, and G. Zou, Phys. Rev. B **76**, 104113 (2007).

[23] A. Fujii, Y. Hase, K. Ohishi, Y. Fujihisa, H. Hamaya, and N. Onodera, Solid State Commun. **59**, 85 (1986).

[24] Y. Fujii, K. Hase, N. Hamaya, Y. Ohishi, A. Onodera, O. Shimomura, and K. Takemura, Phys. Rev. Lett. **58**, 796 (1987).

[25] R. Reichlin, A. K. McMahan, M. Ross, S. Martin, J. Hu, R. J. Hemley, H. K. Mao, and Y. Wu, Phys. Rev. B **49**, 3725 (1994).

[26] Y. Fujii, K. Hase, Y. Ohishi, H. Fujihisa, N. Hamaya, K. Takemura, O. Shimomura, T. Kikegawa, Y. Amemiya, and T. Matsushita, Phys. Rev. Lett. **63**, 536 (1989).

[27] H. Fujihisa, Y. Fujii, K. Takemura, and O. Shimomura, J. Phys. Chem. Solids **56**, 1439 (1995).

[28] J. Sun, M. Martinez-Canales, D. D. Klug, C. J. Pickard, and R. J. Needs, Phys. Rev. Lett. **108**, 045503 (2012).

[29] M. Bastea, A. C. Mitchell, and W. J. Nellis, Phys. Rev. Lett. **86**, 3108 (2001).

[30] B. Militzer, F. Gygi, and G. Galli, Phys. Rev. Lett. **91**, 265503 (2003).

[31] G. Weck, P. Loubeyre, J. H. Eggert, M. Mezouar, and M. Hanfland, Phys. Rev. B **76**, 054121 (2007).

[32] A. F. Goncharov, N. Subramanian, T. R. Ravindran, M. Somayazulu, V. B. Prakapenka, and R. J. Hemley, J. Chem. Phys. **135**, 84512 (2011).

[33] J. R. Rygg, J. H. Eggert, A. E. Lazicki, F. Coppari, J. A. Hawreliak, D. G. Hicks, R. F. Smith, C. M. Sorce, T. M. Uphaus, B. Yaakobi, and G. W. Collins, Rev. Sci. Instrum. **83** (2012).

[34] R. F. Smith, J. H. Eggert, R. Jeanloz, T. S. Duffy, D. G. Braun, J. R. Patterson, R. E. Rudd, J. Biener, A. E. Lazicki, A. V. Hamza, J. Wang, T. Braun, L. X. Benedict, P. M. Celliers, and G. W. Collins, Nature (London) **511**, 330 (2014).

[35] J. Wang, F. Coppari, R. F. Smith, J. H. Eggert, A. E. Lazicki, D. E. Fratanduono, J. R. Rygg, T. R. Boehly, G. W. Collins, and T. S. Duffy, Phys. Rev. B **94**, 104102 (2016).

[36] P. Giannozzi, S. Baroni, N. Bonini, M. Calandra, R. Car, C. Cavazzoni, D. Ceresoli, G. L. Chiarotti, M. Cococcioni, I. Dabo, A. Dal Corso, S. De Gironcoli, S. Fabris, G. Fratesi, R. Gebauer, U. Gerstmann, C. Gougoussis, A. Kokalj, M. Lazzeri, L. Martin-Samos, N. Marzari, F. Mauri, R. Mazzarello, S. Paolini, A. Pasquarello, L. Paulatto, C. Sbraccia, S. Scandolo, G. Sclauzero, A. P. Seitsonen, A. Smogunov, P. Umari, and R. M. Wentzcovitch, J. Phys.: Condens. Matter **21**, 395502 (2009).

[37] J. P. Perdew, K. Burke, and M. Ernzerhof, Phys. Rev. Lett. **77**, 3865 (1996).

[38] H. J. Monkhorst and J. D. Pack, Phys. Rev. B **13**, 5188 (1976).

[39] S. Baroni, S. De Gironcoli, A. Dal Corso, and P. Giannozzi, Rev. Mod. Phys. **73**, 515 (2001).

[40] G. Leibfried and W. Ludwig, Solid State Phys. **12**, 275 (1961).

[41] S. Baroni, P. Giannozzi, and E. Isaev, Reviews in Mineralogy and Geochemistry **71**, 39 (2010).

[42] See Supplemental Material at http://link.aps.org/supplemental/10.1103/PhysRevB.98.094103 for the parameters of the third order Birch-Murnaghan equation of state.

[43] R. Nomura, K. Hirose, N. Sata, Y. Ohishi, D. Suetsugu, C. Bina, T. Inoue, D. Wiens, and M. Jellinek, Phys. Earth Planet. Inter. **183**, 104 (2010).

Ab initio Determination of the Phase Diagram of CO_2 at High Pressures and Temperatures

Beatriz H. Cogollo-Olivo[1,*] Sananda Biswas,[2] Sandro Scandolo,[3] and Javier A. Montoya[4]

[1]*Universidad de Cartagena, Doctorado en Ciencias Físicas, 130001 Cartagena de Indias, Colombia*
[2]*Institut für Theoretische Physik, Goethe-Universität Frankfurt, 60438 Frankfurt am Main, Germany*
[3]*The Abdus Salam International Centre for Theoretical Physics (ICTP), Strada Costiera 11, 34151 Trieste, Italy*
[4]*Universidad de Cartagena, Instituto de Matemáticas Aplicadas, 130001 Cartagena de Indias, Colombia*

The experimental study of the CO_2 phase diagram is hampered by strong kinetic effects leading to wide regions of metastability and to large uncertainties in the location of some phase boundaries. Here, we determine CO_2's thermodynamic phase boundaries by means of *ab initio* calculations of the Gibbs free energy of several solid phases of CO_2 up to 50 Gigapascals. Temperature effects are included in the quasiharmonic approximation. Contrary to previous suggestions, we find that the boundary between molecular forms and the nonmolecular phase V has, indeed, a positive slope and starts at 21.5 GPa at $T = 0$ K. A triple point between phase IV, V, and the liquid phase is found at 35 GPa and 1600 K, indicating a broader region of stability for the nonmolecular form than previously thought. The experimentally determined boundary line between CO_2-II and CO_2-IV phases is reproduced by our calculations, indicating that kinetic effects do not play a major role in that particular transition. Our results also show that CO_2-III is stabilized at high temperature and its stability region coincides with the P-T conditions where phase VII has been reported experimentally; instead, phase II is the most stable molecular phase at low temperatures, extending its region of stability to every P-T condition where phase III is reported experimentally.

DOI:

Widely studied during the past years, carbon dioxide (CO_2) is a fascinating system that, despite its simple molecular form at ambient conditions, exhibits a rich polymorphism at high pressures and temperatures, with up to seven crystalline structures reported experimentally so far, in addition to an amorphous form (see Fig. 1). At room temperature the molecular gas transforms into a liquid at 7.5 MPa which then solidifies at 0.5 GPa into CO_2-I, a molecular crystal with space group Pa$\bar{3}$ [1,2]. By further increasing pressure at ambient temperature, CO_2-I transforms to the orthorhombic phase III (*Cmca* space group) above 10 GPa, with a minimal volume change [3]. A recent theoretical study has provided insights into the microscopic mechanism of the Pa$\bar{3}$-to-*Cmca* transition [4]. Heating compressed CO_2-III above ~470 K [5,6] leads to the transformation into phase II. However, this transition is not reversible: CO_2-II can be recovered at ambient temperature while pressurized, suggesting that CO_2-III is a kinetic product of the compression of CO_2-I and not a stable phase [5,7]. With the exception of a recent theoretical study [8], all previous theoretical work confirms that CO_2-II is more stable than CO_2-III at ambient temperature and below. Initially described as a structure with carbon in an unconventional sixfold coordination, phase II was interpreted as an intermediate state between the molecular and the extended solid form of CO_2 [9], however, subsequent studies disproved the existence of such an intermediate bonding state and identified the structure of phase II as composed of undistorted molecules, with space group $P4_2/mnm$ [10]. CO_2-II transforms into CO_2-IV when it is heated in the 500–720 K range, depending on
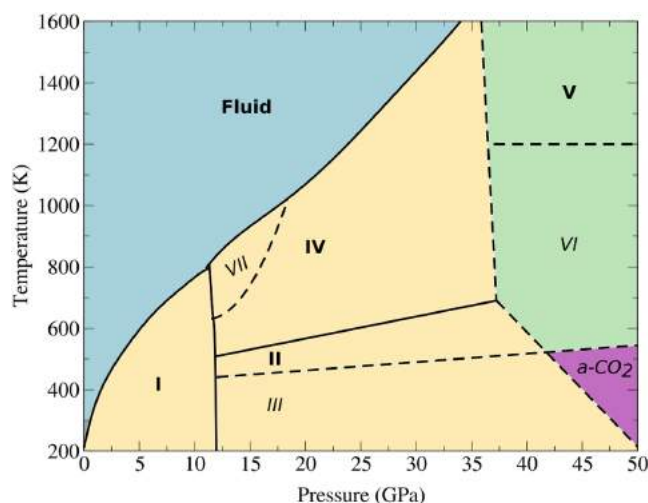

FIG. 1. CO_2 phase diagram adapted from Ref. [15]. Yellow, green, blue, and purple areas correspond to the molecular, nonmolecular, fluid, and amorphous forms of CO_2, respectively. Solid lines correspond to thermodynamic phase boundaries, while dashed lines are kinetic boundaries. Names in bold and italic indicate thermodynamic and metastable phases, respectively.

pressure [5,7]. Phase IV, similar to phase II, was also initially interpreted as an intermediate bonding state [11]; here again, this interpretation was disproved by showing experimentally that CO_2-IV is still composed of well defined linear molecules and that its crystalline structure is rhombohedral with space group $R\bar{3}c$ [12]. At higher temperatures, an intermediate phase between CO_2-I and CO_2-IV was observed by heating CO_2-I to ~950 K and compressing it up to 20 GPa. The crystal structure of this molecular high-temperature stable phase (CO_2-VII) belongs to space group *Cmca*. [13]. Despite the fact that CO_2-VII and CO_2-III have the same space group, some differences in their Raman spectra and in their lattice parameters suggested that their structures might be quantitatively and qualitatively different [13]. However, a recent theoretical study has shown that CO_2-III and CO_2-VII belong to the same configurational energy minimum and that CO_2-III is a low temperature metastable manifestation of CO_2-VII [14].

The nonmolecular CO_2-V phase was first synthesized by laser heating CO_2-III above 40 GPa and 1800 K [16], and its crystalline structure has now been determined as a fully tetrahedral partially collapsed cristobalitelike structure, with space group $I\bar{4}2d$ [17,18]. By compressing CO_2-II to 50 GPa at 530 and 650 K, another nonmolecular form of carbon dioxide (CO_2-VI) was obtained [11]. Its vibrational spectra is consistent with those of metastable layered tetrahedral structures, as shown in [19]. In addition to the molecular and nonmolecular phases, an amorphous form of carbon dioxide (a-CO_2) was observed upon compressing CO_2-III in the pressure range from 40 to 48 GPa at room temperature [7]. The microscopic structure of a-CO_2 has been explained as a frustrated mixture of threefold and fourfold coordinated carbon atoms, in an intermediate metastable form towards fully tetrahedral coordination [20]. Finally, CO_2-V has been reported to dissociate into elemental carbon (diamond) and oxygen ($\epsilon - O_2$) at pressures between 30 and 80 GPa, and temperatures above 1700 K, [21,22]. However, more recent theoretical [23] and experimental [24] works have not observed a transition from the nonmolecular CO_2-V phase into a dissociated state. Moreover, Dziubek *et al.* [24] confirmed that CO_2-V is the only stable phase among all known nonmolecular forms of carbon dioxide, as already proposed by a previous experimental work [25] as well as by theoretical structural searches in the previous decade. The fate of CO_2 at high pressures has important implications for the Earth's global carbon budget [26]. CO_2 degassing in the upper mantle affects melting beneath oceanic ridges [27] and carbonate decomposition [28] may have implications for plume formation in the lower mantle [29]. Therefore, a precise assessment of the transition lines between CO_2 phases, can offer a better understanding of the dynamics of CO_2 within the context of the deep carbon cycle. The goal of defining a complete thermodynamic

phase diagram for this basic molecular system has been elusive to experimentalists due to the unique and incredibly strong kinetic limitations and the metastability that are present in CO_2's molecular and extended forms, this, in addition to diverse interpretations of the experimental diffraction data coming from very small samples in diamond anvil cell (DAC) experiments. It is, then, problematic that, after many decades of research, there is no final thermodynamic phase diagram for CO_2 in a range of *P-T* conditions that have been accessible in the lab by diamond anvil cell experiments since the end of the previous century. In this sense, by avoiding uncertainties coming from kinetic limitations and metastability, our Letter presents a well motivated purely *ab initio* density functional theory (DFT)-based determination of the complete phase diagram of CO_2 in an ample pressure and temperature range.

The currently accepted phase diagram including all the mentioned forms of solid CO_2 along with the region where it becomes a fluid is shown in Fig. 1.

In this particular system, strong kinetic effects hinder the experimental determination of the phase boundaries, while the small size of the samples in high-pressure experiments makes structure determinations quite difficult. As a consequence, several questions remain open regarding the nature and location of the phase boundaries and the stability of the phases reported in Fig. 1. In the molecular portion of the phase diagram, open questions include the relative stability of CO_2-II and CO_2-III at low temperature, and the nature of CO_2-VII, in particular its structural relationship with CO_2-III. At higher pressures, one of the fundamental questions is the location of the phase boundary between molecular and nonmolecular phases. Santoro *et al.*, for example, proposed a phase diagram where the boundary between molecular and nonmolecular phases at room temperature is located at 20 GPa, roughly half-way between the lowest pressure of quenching and the pressure of synthesis for this phase [30,31]. Moreover, the kinetic boundary between CO_2-III and the a-CO_2 nonmolecular structure, i.e., the *P-T* region where the transformation occurs upon compression, has a negative slope [32], while basic thermodynamic considerations suggest that the slope of the true phase boundary should be positive [31]. Theoretical determinations of the molecular-nonmolecular boundary at zero temperature, based on *ab initio* electronic structure methods, predict transition pressures in the range between 18 and 21 GPa when going from both CO_2-II and CO_2-III to the nonmolecular forms [28,30,33].

In this Letter, we extend the theoretical determination of the phase diagram of CO_2 to finite temperatures for all stable phases except CO_2-I. Phase boundaries between the molecular phases II, III, and IV, and the nonmolecular phase V are calculated based on an *ab initio* approach; for the determination of free energies, the vibrational contributions are treated in the quasiharmonic approximation (QHA).

165   *Ab initio* electronic structure calculations were carried
166 out using DFT and the projector augmented wave method,
167 as implemented in the Quantum ESPRESSO suite [34,35] with
168 a kinetic energy cutoff of 200 Ry for the plane-wave basis
169 set. The generalized gradient approximation was employed
170 for the exchange-correlation energy and implemented using
171 the Perdew-Burke-Ernzerhof functional [36]. Our system is
172 well represented by this approach as shown by previously
173 calculated intramolecular $C = O$ bond lengths of CO_2-II at
174 different levels of theory, which are generally consistent
175 with our values [14,37,38]. The Monkhorst-Pack method
176 [39] was used to generate the k point grids for sampling the
177 Brillouin zone. Variable-cell optimization of all structural
178 parameters was performed for the four phases in the range
179 of pressures between 10 and 70 GPa. Density functional
180 perturbation theory within the linear response scheme [40]
181 was used to calculate phonon frequencies at zero temper-
182 ature. The zero-point energy and the finite-temperature
183 contributions to the Helmholtz free energy were computed
184 in the QHA [41,42], which is valid where harmonic effects
185 dominate the material's properties. It is commonly accepted
186 as a criterion that increasingly relevant contributions
187 coming from anharmonicities are expected to appear at
188 $T \sim 1.2\Theta_D$ and above [43,44]. Even more, the range of
189 temperatures in which QHA remains valid is significantly
190 expanded under high pressure [43–45]. For this particular
191 study, the calculated Θ_D takes values between 3485 K and
192 3500 K for the three molecular forms considered at the
193 lowest pressure in our work (10 GPa), which are clearly
194 higher than the highest temperature registered in this
195 study, i.e., 1600 K. Thus, the temperature region under
196 consideration in this work spans approximately from
197 0.05 to $0.45\Theta_D$, assuring us of the validity of the quasi-
198 harmonic approximation below the melting curve of CO_2
199 for all solid forms. For the construction of the pressure-
200 temperature phase diagram, the Helmholtz free energy at
201 different temperatures was fitted to a third order Birch-
202 Murnaghan equation of state (EOS). Finally, the Gibbs free
203 energy was calculated as

$$G(P,T) = F[V(P,T),T] + PV(P,T), \qquad (1)$$

206   Room-temperature equations of state obtained with the
207 above approximations are compared with experimental data
208 for phases CO_2-II, CO_2-III, CO_2-IV, and CO_2-V in Fig. 2.
209 The agreement is good and confirms the validity of the
210 approach. Phase boundaries constructed based on the
211 calculated Gibbs free energies are shown in Fig. 3. It is
212 worth mentioning that although most phases in this
213 study are molecular, the van der Waals approximation
214 was not used since, in simulations under very high
215 pressure, the dispersion function becomes constant at
216 distances much shorter than the standard van der Waals
217 radii, resulting in not affecting the valence geometries or
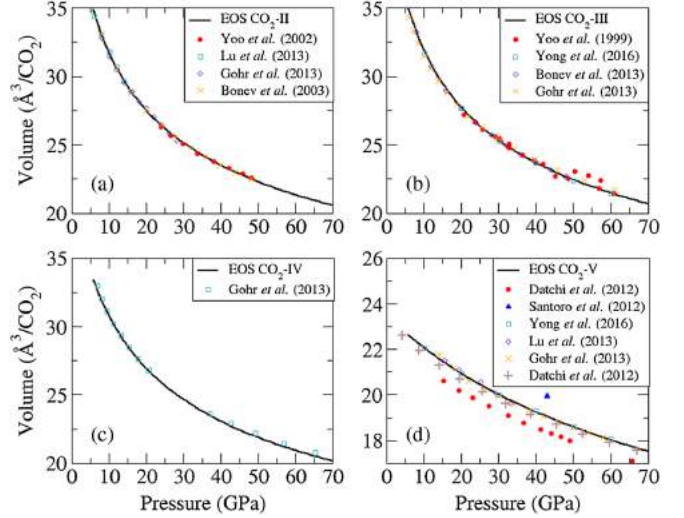218 energies [46,47].

FIG. 2.   Pressure-volume relation of phases (a) II, (b) III, (c) IV,
and (d) V of CO_2 at room temperature are shown in black solid
lines. For each case, reported values from experimental (red
circles) and theoretical (blue squares, purple diamonds, and yellow
crosses) studies for the different phases are displayed as well.

219   We begin our discussion with an analysis of the
220 molecular solid region of the phase diagram. This region
221 is indicated in yellow in Fig. 1; it contains the molecular
222 phases I, II, III, and IV, and its upper bound in pressure
223 coincides with the experimentally reported transitions to
224 the nonmolecular phases. Since phase I as well as its
225 boundaries with the other phases are well known and
226 constrained, we focus specifically on phases II, III, and IV,
227 at pressures higher than 12 GPa. According to the enthalpy-
228 pressure relations, with and without the zero-point energy
229 contribution, at $T = 0$ K CO_2-II is the most stable molecu-
230 lar phase in the pressure range considered, until the
231 transition to CO_2-V. This indicates that the orthorhombic
232 *Cmca* structure (phase III) obtained experimentally from
233 the compression of phase I is, indeed, only metastable at
234 low temperatures. Notice that this remains true even after
235 the inclusion of zero-point contributions, in agreement with
236 previous reports [5,48]. At variance with our results as well
237 as with previous theoretical work, a recent theoretical study
238 [8] proposes a transition boundary between phases II and
239 III in which CO_2-III is stable up to ~570 K at 19 GPa. This
240 is at odds with experimental observations where the kinetic
241 transition from CO_2-III to CO_2-II occurs at much lower
242 temperatures [5]. Instead, our calculations show that
243 CO_2-III becomes more stable than CO_2-II at higher temper-
244 atures [solid green line with stars in Fig. 3(a)]. The
245 transition temperature between CO_2-III and CO_2-II has a
246 strong pressure dependence and reaches values in excess of
247 1000 K close to the boundary with the nonmolecular phase
248 V, with respect to its value close to CO_2-I. Comparing the
249 free energies of CO_2-II and CO_2-IV, we find that the
250 boundary between phases II and IV [solid brown line
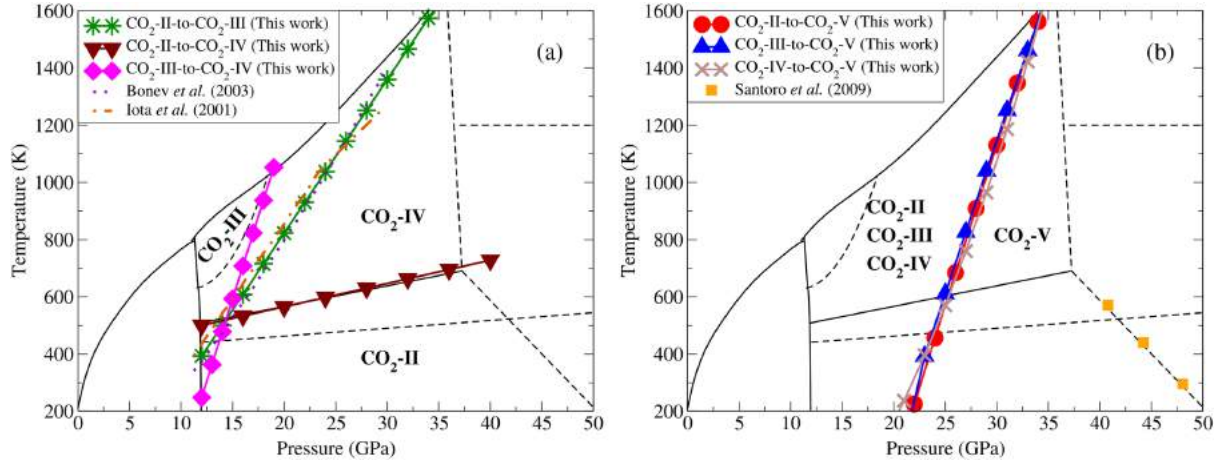251 with down triangles in Fig. 3(a)] agrees quite well with

F3:1 FIG. 3. (a) Phase boundaries between CO_2-II and CO_2-III (green, stars), CO_2-II and CO_2-IV (brown, down triangles), and CO_2-III and
F3:2 CO_2-IV (magenta, diamonds). Suggested boundaries reported by Iota *et al.* [5] (experimental) and Bonev *et al.* [48] (theoretical), are
F3:3 shown in orange dotted-dashed line and violet dotted line, respectively. (b) Phase boundaries between molecular phases CO_2-II (red,
F3:4 circles), CO_2-III (blue, up triangles), and CO_2-IV (gray, crosses), and the nonmolecular phase CO_2-V. Proposed limits of the kinetic
F3:5 region from experimental data from Ref. [32] (orange squares) are also included.

252 experimental data [12]. The weak pressure dependence of
253 the II-IV boundary reduces the region of stability of phase
254 II with respect to the starred green line in Fig. 3(a), by
255 confining it toward lower temperatures. Finally, we find
256 that the boundary between CO_2-III and CO_2-IV [solid
257 magenta line with diamonds in Fig. 3(a)] is almost vertical,
258 which restricts the domain of stability of phase III to a
259 narrow window of pressure and to temperatures above
260 400 K. We summarize the results of the free-energy
261 calculations for the three molecular phases II, III, and
262 IV in Fig. 4. Phases I and II emerge as the only stable
263 molecular phases of CO_2 from zero to ambient temperature.
264 Phases III and IV are both stabilized by temperature, and
265 phases II, III, and IV coexist at a triple point located at
266 15 GPa and 500 K.
267 Our findings are in agreement with simulations by Bonev
268 *et al.* [48] which suggested that the *Cmca* phase is a
269 temperature stabilized form [48]. Because the structure of
270 phase IV was not known at the time, Bonev *et al.* proposed
271 a wider region of stability for CO_2-III. Interestingly, as can
272 be seen in Fig. 3(a), the *P-T* region of stability of CO_2-III
273 obtained from our calculations has a large overlap with the
274 region of stability reported for the so-called phase VII of
275 CO_2 [13]. A recent theoretical work has shown that phases
276 III and VII have, in fact, the same crystal structure (space
277 group *Cmca*)[14]. Therefore, we confirm that phase III is
278 thermodynamically stable in the *P-T* region where phase
279 VII has been reported. Thus, the observation of phase III
280 outside this region (e.g., at ambient conditions, as a result of
281 the compression of phase I) must be attributed to kinetic
282 effects.
283 Now, we turn to the boundary between the molecular
284 phases and nonmolecular phase V [Fig. 3(b)]. We find that,
285 at zero temperature, the phase boundary between CO_2-II

286 and CO_2-V is located at 21.5 GPa. The transition between
287 (metastable) CO_2-III and CO_2-V would, instead, take place
288 at 20.8 GPa in the absence of kinetic effects. This is in good
289 agreement with previous theoretical works [28,30,33].
290 Phase boundaries between molecular phases and CO_2-V
291 are rather insensitive to the choice of the molecular
292 structure and they all have a positive slope, as already
293 suggested [31]. Considering that nonmolecular phases are
294 denser than molecular ones, a positive slope implies a
295 decrease of entropy in going from molecular to non-
296 molecular. This is not unexpected, given the stiffness of
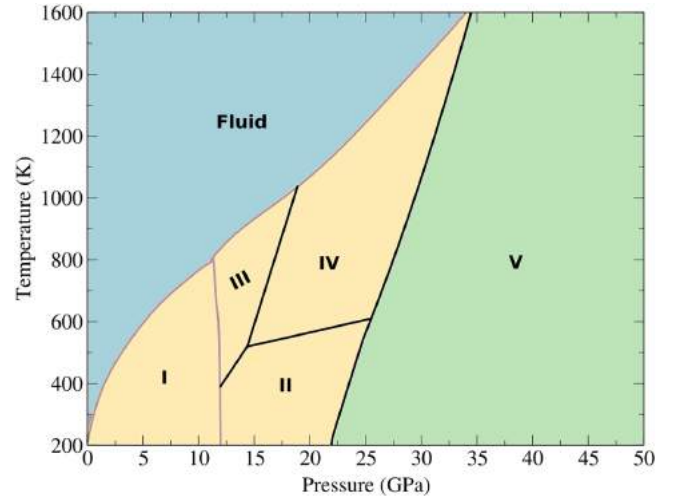

FIG. 4. Theoretical phase diagram for carbon dioxide at high   F4:1
pressure and temperature. Our calculated phase boundaries are   F4:2
shown with solid black lines, while previously reported thermo-   F4:3
dynamic boundaries are shown in gray. Yellow, green, and blue   F4:4
regions correspond to molecular, nonmolecular, and fluid forms   F4:5
of CO_2.   F4:6

the nonmolecular structure when compared with the molecular ones. Using the experimentally determined melting line, our calculations show a triple point between phases IV and V, and the liquid phase at 35 GPa and 1600 K. Therefore, the calculations suggest that molecular CO_2 could be stable up to pressures as high as 35 GPa, at high temperature.

In summary, we have presented finite-temperature theoretical calculations in the quasiharmonic approximation for various molecular and nonmolecular solid forms of CO_2. The calculations aimed at resolving experimental uncertainties and inconsistencies due to kinetic effects and metastability. We find that the boundary between the molecular phases and phase V has a positive slope, and starts at 21.5 GPa at $T = 0$ K. We also find that the phase diagram shows a triple point between phases IV, V, and the liquid phase at 35 GPa and 1600 K. This indicates that the nonmolecular phase V has a broader region of stability than previously reported. We were able to reproduce the known thermodynamic boundary line between CO_2-II and CO_2-IV, confirming that kinetic effects are not relevant in that transition. Finally, it was shown that phase II is the most stable molecular phase at low temperatures, extending its region of stability to every P-T condition where phase III has been reported experimentally. However, our results also show that CO_2-III is, instead, stabilized at high temperature and its stability region coincides with the P-T conditions where phase VII has been reported experimentally, implying that phase III and phase VII are, indeed, the same.

* bcogolloo@unicartagena.edu.co

[1] A. Simon and K. Peters, Acta Crystallogr. Sect. B **36**, 2750 (1980).
[2] R. T. Downs and M. S. Somayazulu, Acta Crystallogr. Sect. C **54**, 897 (1998).
[3] K. Aoki, H. Yamawaki, M. Sakashita, Y. Gotoh, and K. Takemura, Science **263**, 356 (1994).
[4] I. Gimondi and M. Salvalaglio, J. Chem. Phys. **147**, 114502 (2017).
[5] V. Iota and C. S. Yoo, Phys. Rev. Lett. **86**, 5922 (2001).
[6] F. A. Gorelli, V. M. Giordano, P. R. Salvi, and R. Bini, Phys. Rev. Lett. **93**, 205503 (2004).
[7] M. Santoro, F. A. Gorelli, R. Bini, G. Ruocco, S. Scandolo, and W. A. Crichton, Nature (London) **441**, 857 (2006).
[8] Y. Han, J. Liu, L. Huang, X. He, and J. Li, npj Quantum Mater. **4**, 10 (2019).
[9] C. S. Yoo, H. Kohlmann, H. Cynn, M. F. Nicol, V. Iota, and T. LeBihan, Phys. Rev. B **65**, 104103 (2002).
[10] F. Datchi, B. Mallick, A. Salamat, G. Rousse, S. Ninet, G. Garbarino, P. Bouvier, and M. Mezouar, Phys. Rev. B **89**, 144101 (2014).
[11] V. Iota, C. S. Yoo, J. H. Klepeis, Z. Jenei, W. Evans, and H. Cynn, Nat. Mater. **6**, 34 (2007).
[12] F. Datchi, V. M. Giordano, P. Munsch, and A. M. Saitta, Phys. Rev. Lett. **103**, 185701 (2009).
[13] V. M. Giordano and F. Datchi, Europhys. Lett. **77**, 46002 (2007).
[14] W. Sontising, Y. N. Heit, J. L. McKinley, and G. J. O. Beran, Chem. Sci. **8**, 7374 (2017).
[15] F. Datchi, G. Weck, A. M. Saitta, Z. Raza, G. Garbarino, S. Ninet, D. K. Spaulding, J. A. Queyroux, and M. Mezouar, Phys. Rev. B **94**, 014201 (2016).
[16] V. Iota, C. S. Yoo, and H. Cynn, Science **283**, 1510 (1999).
[17] M. Santoro, F. A. Gorelli, R. Bini, J. Haines, O. Cambon, C. Levelut, J. A. Montoya, and S. Scandolo, Proc. Natl. Acad. Sci. U.S.A. **109**, 5176 (2012).
[18] F. Datchi, B. Mallick, A. Salamat, and S. Ninet, Phys. Rev. Lett. **108**, 125701 (2012).
[19] M. S. Lee, J. A. Montoya, and S. Scandolo, Phys. Rev. B **79**, 144102 (2009).
[20] J. A. Montoya, R. Rousseau, M. Santoro, F. Gorelli, and S. Scandolo, Phys. Rev. Lett. **100**, 163002 (2008).
[21] O. Tschauner, H. K. Mao, and R. J. Hemley, Phys. Rev. Lett. **87**, 075701 (2001).
[22] K. D. Litasov, A. F. Goncharov, and R. J. Hemley, Earth Planet. Sci. Lett. **309**, 318 (2011).
[23] A. Teweldeberhan, B. Boates, and S. Bonev, Earth Planet. Sci. Lett. **373**, 228 (2013).
[24] M. Dziubek, Kamil F. Ende, D. Scelta, R. Bini, M. Mezouar, G. Garbarino, and R. Miletich, Nat. Commun. **9**, 3148 (2018).
[25] Y. Seto, D. Nishio-Hamane, T. Nagai, N. Sata, and K. Fujino, J. Phys. Conf. Ser. **215**, 012015 (2010).
[26] R. M. Hazen, A. P. Jones, and J. A. Baross, Rev. Mineral. Geochem. **75** (2013), http://www.minsocam.org/msa/rim/rim75.html.
[27] R. Dasgupta, A. Mallik, K. Tsuno, A. C. Withers, G. Hirth, and M. M. Hirschmann, Nature (London) **493**, 211 (2013).
[28] A. R. Oganov, S. Ono, Y. Ma, C. W. Glass, and A. Garcia, Earth Planet. Sci. Lett. **273**, 38 (2008).
[29] N. Takafuji, K. Fujino, T. Nagai, Y. Seto, and D. Hamane, Phys. Chem. Miner. **33**, 651 (2006).
[30] X. Yong, H. Liu, M. Wu, Y. Yao, J. S. Tse, R. Dias, and C. S. Yoo, Proc. Natl. Acad. Sci. U.S.A. **113**, 11110 (2016).
[31] M. Santoro, J. F. Lin, H. K. Mao, and R. J. Hemley, J. Chem. Phys. **121**, 2780 (2004).
[32] M. Santoro and F. A. Gorelli, Phys. Rev. B **80**, 184109 (2009).
[33] S. Gohr, S. Grimme, T. Shnel, B. Paulus, and P. Schwerdtfeger, J. Chem. Phys. **139**, 174501 (2013).
[34] P. Giannozzi et al., J. Phys. Condens. Matter **21**, 395502 (2009).

[35] P. Giannozzi *et al.*, J. Phys. Condens. Matter **29**, 465901 (2017).

[36] J. P. Perdew, K. Burke, and M. Ernzerhof, Phys. Rev. Lett. **77**, 3865 (1996).

[37] J.-H. Parq, S. K. Lee, S.-M. Lee, and J. Yu, J. Phys. Chem. C **120**, 23152 (2016).

[38] H. S. Yu, X. He, and D. G. Truhlar, J. Chem. Theory Comput. **12**, 1280 (2016).

[39] J. D. Pack and H. J. Monkhorst, Phys. Rev. B **16**, 1748 (1977).

[40] S. Baroni, S. de Gironcoli, A. Dal Corso, and P. Giannozzi, Rev. Mod. Phys. **73**, 515 (2001).

[41] G. Leibfried and W. Ludwig, Solid State Phys. **12**, 275 (1961).

[42] S. Baroni, P. Giannozzi, and E. Isaev, Rev. Mineral. Geochem. **71**, 39 (2010).

[43] R. J. Angel, F. Miozzi, and M. Alvaro, Minerals **9**, 562 (2019).

[44] O. Anderson, *Equations of State of Solids for Geophysics and Ceramic Science* (Oxford University Press, New York, 1995).

[45] R. J. Hardy, J. Geophys. Res. **85**, 7011 (1980).

[46] A. Hu, N. Chan, S. Wang, and F. Zhang, Phys. Lett. A **383**, 666 (2019).

[47] Y. Liu and W. A. Goddard, J. Phys. Chem. Lett. **1**, 2550 (2010).

[48] S. A. Bonev, F. Gygi, T. Ogitsu, and G. Galli, Phys. Rev. Lett. **91**, 065501 (2003).

Acknowledgements

Now, when this chapter of my life is about to conclude, it is time to thank all the people that made my path reach to this point. First of all, I would like to thank Prof. Javier Montoya, who bet on me several years ago and was my supervisor in both the Master and Ph.D. theses. Additionally, I am deeply grateful to the guidance provided by Prof. Sandro Scandolo, who I had the pleasure to meet seven years ago and has been a great model to follow, and an amazing academic grandfather. Finally, I would like to express my gratitude to Dr. Sananda Biswas, who had infinite patience, for guiding me through all the technical details that I needed for doing this thesis. I hope that you have learned with me at least a bit of all that I have learned from and with you during all this process.

I would like to acknowledge several institutions that made possible my doctoral studies in one way or the other: Colciencias, The Abdus Salam ICTP, the University of Cartagena, the Ph.D. in Physical Sciences program, and CINECA. Thanks to them I was able to be paid for studying while traveling to breathtaking places, to show my research advances, and using renowned computational facilities.

Finally, I would like to extend my endless gratitude to my family and friends. You are the reason why I am here, and this is for you.

References

[1] M. Born and R. Oppenheimer. Zur quantentheorie der molekeln. *Annalen der Physik*, 389(20):457–484, 1927.

[2] D. Pines. *Elementary Excitations in Solids*. Perseus Books, 1999.

[3] L. H. Thomas. The calculation of atomic fields. *Mathematical Proceedings of the Cambridge Philosophical Society*, 23(5):542–548, 1927.

[4] E. Fermi. Un metodo statistico per la determinazione di alcune priorietà dell'atome. *Accademia Nazionale dei Lincei*, 6:602–607, 1927.

[5] P Hohenberg and W. Kohn. Inhomogeneous electron gas. *Physical Review*, 136(3B):B864–B871, 1964.

[6] R. Martin. *Electronic Structure: Basic Theory and Practical Methods*. Cambridge University Press, 2004.

[7] W. Kohn and L. J. Sham. Self-consistent equations including exchange and correlation effects. *Physical Review*, 140(4A):A1133–A1138, 1965.

[8] M. C. Payne, M. P. Teter, D. C. Allan, T. A. Arias, and J. D. Joannopoulos. Iterative minimization techniques for ab initio total-energy calculations: molecular dynamics and conjugate gradients. *Review of Modern Physics*, 64:1045–1097, 1992.

[9] E. Wigner. Effects of the electron interaction on the energy levels of electrons in metals. *Transactions of the Faraday Society*, 34:678–685, 1938.

[10] M. Gell-Mann and K. A. Brueckner. Correlation energy of an electron gas at high density. *Physical Review*, 106:364–368, 1957.

[11] S. Misawa. Ferromagnetism of an electron gas. *Physical Review*, 140:A1645–A1648, 1965.

[12] L. Hedin and B. I. Lundqvist. Explicit local exchange-correlation potentials. *Journal of Physics C: Solid State Physics*, 4:2064, 1971.

[13] D. M. Ceperley and B. J. Alder. Ground state of the electron gas by a stochastic method. *Physical Review Letters*, 45:566–569, 1980.

[14] S. H. Vosko, L. Wilk, and M. Nusair. Accurate spin-dependent electron liquid correlation energies for local spin density calculations: a critical analysis. *Canadian Journal of Physics*, 58:1200–1211, 1980.

[15] J. P. Perdew and Alex Zunger. Self-interaction correction to density-functional approximations for many-electron systems. *Physical Review B*, 23:5048–5079, 1981.

[16] C. Lee, W. Yang, and R. G. Parr. Development of the colle-salvetti correlation-energy formula into a functional of the electron density. *Physical Review B*, 37:785–789, 1988.

[17] A. D. Becke. Density-functional exchange-energy approximation with correct asymptotic behavior. *Physical Review A*, 38:3098–3100, 1988.

[18] J. P. Perdew, K. Burke, and M. Ernzerhof. Generalized gradient approximation made simple. *Physical Review Letters*, 77:3865–3868, 1996.

[19] N. W. Ashcroft and N. D. Mermin. *Solid State Physics*. Harcourt College Publishers, 1976.

[20] P. Schwerdtfeger. The pseudopotential approximation in electronic structure theory. *ChemPhysChem*, 12:3143–3155, 2011.

[21] P. E. Blöchl. Projector augmented-wave method. *Physical Review B*, 50:17953–17979, 1994.

[22] P. Giannozzi, S. Baroni, N. Bonini, M. Calandra, R. Car, C. Cavazzoni, D. Ceresoli, G. L. Chiarotti, M. Cococcioni, I. Dabo, A. Dal Corso, S. De Gironcoli, S. Fabris, G. Fratesi, R. Gebauer, U. Gerstmann, C. Gougoussis, A. Kokalj, M. Lazzeri, L. Martin-Samos, N. Marzari, F. Mauri, R. Mazzarello, S. Paolini, A. Pasquarello, L. Paulatto, C. Sbraccia, S. Scandolo, G. Sclauzero, A. P. Seitsonen, A. Smogunov, P. Umari, and R. M. Wentzcovitch. Quantum espresso: A modular and open-source software project for quantum simulations of materials. *Journal of Physics: Condensed Matter*, 21:21832390, 2009.

[23] P. Giannozzi, O. Andreussi, T. Brumme, O. Bunau, M. Buongiorno Nardelli, M. Calandra, R. Car, C. Cavazzoni, D. Ceresoli, M. Cococcioni, N. Colonna, I. Carnimeo, A. Dal Corso, S. de Gironcoli, P. Delugas, R. A. DiStasio, A. Ferretti, A. Floris, G. Fratesi, G. Fugallo, R. Gebauer, U. Gerstmann, F. Giustino,

T. Gorni, J. Jia, M. Kawamura, H.-Y. Ko, A. Kokalj, E. Küçükbenli, M. Lazzeri, M Marsili, N. Marzari, F. Mauri, Nguyen; N. L., H.-V. Nguyen, A. Otero-de-la Roza, L. Paulatto, S. Poncé, D. Rocca, R. Sabatini, B. Santra, M. Schlipf, A. P. Seitsonen, A. Smogunov, I. Timrov, T. Thonhauser, P. Umari, N. Vast, X. Wu, and S. Baroni. Advanced capabilities for materials modelling with quantum espresso. *Journal of Physics: Condensed Matter*, 29:465901, 2017.

[24] J. D. Pack and H. J. Monkhorst. Special points for brillouin-zone integrations. *Physical Review B*, 16:1748–1749, 1977.

[25] G. P. Srivastava. *The Physics of Phonons*. Taylor & Francis Group, first edition, 1990.

[26] H. Wendel and R. M. Martin. Charge density and structural properties of covalent semiconductors. *Physical Review Letters*, 40:950, 1978.

[27] K. M. Ho, C. L. Fu, and B. N. Harmon. Vibrational frequencies via total-energy calculations. applications to transition metals. *Physical Review B*, 29:1575, 1984.

[28] K. Kunc and R. M. Martin. *Ab Initio* force constants of gaas: A new approach to calculation of phonons and dielectric properties. *Physical Review Letters*, 48:406, 1982.

[29] K. Parlinski, Z. Q. Li, and Y. Kawazoe. First-principles determination of the soft mode in cubic zro_2. *Physical Review Letters*, 78:4063, 1997.

[30] S. Baroni, S. de Gironcoli, A. Dal Corso, and P. Giannozzi. Phonons and related crystal properties from density-functional perturbation theory. *Reviews of Modern Physics*, 73:515, 2001.

[31] H. Hellmann. *Einführung in die Quantenchemie*. Deuticke, first edition, 1937.

[32] R. P. Feynman. Forces in molecules. *Physical Review*, 56:340–343, 1939.

[33] A. A. Quong, A. A. Maradudin, R. F. Wallis, J. A. Gaspar, A. G. Eguiluz, and G. P. Alldredge. First-principles screening calculation of the surface-phonon dispersion curves at the (001) surface of sodium. *Physical Review Letters*, 66:743–746, 1991.

[34] A. A. Quong and B. M. Klein. Self-consistent-screening calculation of interatomic force constants and phonon dispersion curves from first principles. *Physical Review B*, 46:10734–10737, 1992.

[35] R. F. Wallis, A. A. Maradudin, V. Bortolani, A. G. Eguiluz, A. A. Quong, A. Franchini, and G. Santoro. Comparison between phenomenological and pseudopotential force constants for the lattice dynamics of al. *Physical Review B*, 48:6043–6053, 1993.

[36] A. A. Quong. First-principles determination of the interatomic-force-constant tensor of au. *Physical Review B*, 49:3226–3229, 1994.

[37] R. M. Sternheimer. Electronic polarizabilities of ions from the hartree-fock wave functions. *Physical Review*, 96:951–968, 1954.

[38] S. Baroni, P. Giannozzi, and E. Isaev. Density-functional perturbation theory for quasi-harmonic calculations. *Solid State Physics - Advances in Research and Applications*, 71:39–57, 2010.

[39] G. Leibfried and W. Ludwig. Theory of anharmonic effects in crystals. *Reviews in Mineralogy and Geochemistry*, 12(C):275–444, 1961.

[40] R. Car and M. Parrinello. Unified approach for molecular dynamics and density-functional theory. *Physical Review Letters*, 55(22):2471, 1985.

[41] H. Dammak, Y. Chalopin, M. Laroche, M. Hayoun, and J.-J. Greffet. Quantum thermal bath for molecular dynamics simulation. *Physical Review Letters*, 103(19):0601, 2009.

[42] M. Ceriotti, G. Bussi, and M. Parrinello. Nuclear quantum effects in solids using a colored-noise thermostat. *Physical Review Letters*, 103(03):0603, 2009.

[43] A. H. Barrozo and M. de Koning. Comment on "quantum thermal bath for molecular dynamics simulation". *Physical Review Letters*, 107(19):8901, 2011.

[44] H. Dammak, M. Hayoun, Y. Chalopin, and J.-J. Greffet. Dammak et al. reply:. *Physical Review Letters*, 107(19):8902, 2011.

[45] D. M. Ceperley. Path integrals in the theory of condensed helium. *Reviews of Moder Physics*, 67(2):79, 1995.

[46] I. Errea, M. Calandra, and F. Mauri. Anharmonic free energies and phonon dispersions from the stochastic self-consistent harmonic approximation: Application to platinum and palladium hydrides. *Physical Review B*, 89(06):4302, 2014.

[47] K. Lejaeghere, V. Van Speybroeck, G. Van Oost, and S. Cottenier. Error estimates for solid-state density-functional theory predictions: An overview by means of the ground-state elemental crystals. *Critical Reviews in Solid State and Materials Sciences*, 39(1):1–24, 2014.

[48] Kurt Lejaeghere, Gustav Bihlmayer, Torbjörn Björkman, Peter Blaha, Stefan Blügel, Volker Blum, Damien Caliste, Ivano E. Castelli, Stewart J. Clark, Andrea Dal Corso, Stefano de Gironcoli, Thierry Deutsch, John Kay Dewhurst, Igor Di Marco, Claudia Draxl, Marcin Dułak, Olle Eriksson, José A. Flores-Livas, Kevin F. Garrity, Luigi Genovese, Paolo Giannozzi, Matteo Giantomassi, Stefan Goedecker, Xavier Gonze, Oscar Grånäs, E. K. U. Gross, Andris Gulans, François Gygi, D. R. Hamann, Phil J. Hasnip, N. A. W. Holzwarth, Diana Iuşan, Dominik B. Jochym, François Jollet, Daniel Jones, Georg Kresse, Klaus Koepernik, Emine Küçükbenli, Yaroslav O. Kvashnin, Inka L. M. Locht, Sven Lubeck, Martijn Marsman, Nicola Marzari, Ulrike Nitzsche, Lars Nordström, Taisuke Ozaki, Lorenzo Paulatto, Chris J. Pickard, Ward Poelmans, Matt I. J. Probert, Keith Refson, Manuel Richter, Gian-Marco Rignanese, Santanu Saha, Matthias Scheffler, Martin Schlipf, Karlheinz Schwarz, Sangeeta Sharma, Francesca Tavazza, Patrik Thunström, Alexandre Tkatchenko, Marc Torrent, David Vanderbilt, Michiel J. van Setten, Veronique Van Speybroeck, John M. Wills, Jonathan R. Yates, Guo-Xu Zhang, and Stefaan Cottenier. Reproducibility in density functional theory calculations of solids. *Science*, 351(6280):aad3000–1–aad3000–7, 2016.

[49] Gianluca Prandini, Antimo Marrazzo, Ivano E. Castelli, Nicolas Mounet, and Nicola Marzari. Precision and efficiency in solid-state pseudopotential calculations. *npj Computational Materials*, 4(1):72, 2018.

[50] E. Kucukbenli, M. Monni, B. I. Adetunji, X. Ge, G. A. Adebayo, N. Marzari, S. de Gironcoli, and A. Dal Corso. Projector augmented-wave and all-electron calculations across the periodic table: a comparison of structural and energetic properties. arXiv, 2014. 1404.3015.

[51] Andrea Dal Corso. Pseudopotentials periodic table: From h to pu. *Computational Materials Science*, 95:337–350, 2014.

[52] M. Topsakal and R.M. Wentzcovitch. Accurate projected augmented wave (paw) datasets for rare-earth elements (re=la–lu). *Computational Materials Science*, 95:263–270, 2014.

[53] Stefan Kurth, John P. Perdew, and Peter Blaha. Molecular and solid-state tests of density functional approximations: Lsd, ggas, and meta-ggas. *International Journal of Quantum Chemistry*, 75(4–5):889–909, 1999.

[54] Viktor N. Staroverov, Gustavo E. Scuseria, Jianmin Tao, and John P. Perdew. Tests of a ladder of density functionals for bulk solids and surfaces. *Physical Review B*, 69(7):075102, 2004.

[55] Philipp Haas, Fabien Tran, and Peter Blaha. Calculation of the lattice constant of solids with semilocal functionals. *Physical Review B*, 79(8):085104, 2009.

[56] Gábor I. Csonka, John P. Perdew, Adrienn Ruzsinszky, Pier H. T. Philipsen, Sébastien Lebègue, Joachim Paier, Oleg A. Vydrov, and János G. Ángyán. Assessing the performance of recent density functionals for bulk solids. *Physical Review B*, 79(15):155107, 2009.

[57] Pascal Pernot, Bartolomeo Civalleri, Davide Presti, and Andreas Savin. Prediction uncertainty of density functional approximations for properties of crystals with cubic symmetry. *The Journal of Physical Chemistry A*, 119(21):5288–5304, 2015.

[58] Larry A. Curtiss, Krishnan Raghavachari, Paul C. Redfern, and John A. Pople. Assessment of gaussian-2 and density functional theories for the computation of enthalpies of formation. *The Journal of Chemical Physics*, 106(3):1063–1079, 1997.

[59] Joachim Paier, Robin Hirschl, Martijn Marsman, and Georg Kresse. The perdew–burke–ernzerhof exchange-correlation functional applied to the g2-1 test set using a plane-wave basis set. *The Journal of Chemical Physics*, 122(23):234102, 2005.

[60] Yan Zhao and Donald G. Truhlar. Density functionals with broad applicability in chemistry. *Accounts of Chemical Research*, 41(2):157–167, 2008.

[61] Lars Goerigk and Stefan Grimme. A thorough benchmark of density functional methods for general main group thermochemistry, kinetics, and noncovalent interactions. *Physical Chemistry Chemical Physics*, 13(14):6670–6688, 2011.

[62] John P. Perdew and Karla Schmidt. Jacob's ladder of density functional approximations for the exchange-correlation energy. *AIP Conference Proceedings*, 577(1):1–20, 2001.

[63] John P. Perdew, Adrienn Ruzsinszky, Jianmin Tao, Viktor N. Staroverov, Gustavo E. Scuseria, and Gábor I. Csonka. Prescription for the design and selection of density functional approximations: More constraint satisfaction with fewer fits. *The Journal of Chemical Physics*, 123(6):062201, 2005.

[64] Fabien Tran, Julia Stelzl, and Peter Blaha. Rungs 1 to 4 of dft jacob's ladder: Extensive test on the lattice constant, bulk modulus, and cohesive energy of solids. *The Journal of Chemical Physics*, 144(20):204120, 2016.

[65] Mari Einaga, Masafumi Sakata, Takahiro Ishikawa, Katsuya Shimizu, Mikhail I. Eremets, Alexander P. Drozdov, Ivan A. Troyan, Naohisa Hirao, and Yasuo Ohishi. Crystal structure of the superconducting phase of sulfur hydride. *Nature Physics*, 12(9):835–838, 2016.

[66] Raffaello Bianco, Ion Errea, Matteo Calandra, and Francesco Mauri. High-pressure phase diagram of hydrogen and deuterium sulfides from first principles: Structural and vibrational properties including quantum and anharmonic effects. *Physical Review B*, 97(21):214101, 2018.

[67] Ion Errea, Matteo Calandra, Chris J. Pickard, Joseph R. Nelson, Richard J. Needs, Yinwei Li, Hanyu Liu, Yunwei Zhang, Yanming Ma, and Francesco Mauri. Quantum hydrogen-bond symmetrization in the superconducting hydrogen sulfide system. *Nature*, 532(7597):81–84, 2016.

[68] Elissaios Stavrou, Lin H. Yang, Per Söderlind, Daniel Aberg, Harry B. Radousky, Michael R. Armstrong, Jonathan L. Belof, Martin Kunz, Eran Greenberg, Vitali B. Prakapenka, and David A. Young. Anharmonicity-induced first-order isostructural phase transition of zirconium under pressure. *Physical Review B*, 98(22):220101, 2018.

[69] Joseph R. Nelson, Richard J. Needs, and Chris J. Pickard. High-pressure caf_2 revisited: A new high-temperature phase and the role of phonons in the search for superionic conductivity. *Physical Review B*, 98(22):224105, 2018.

[70] O.L. Anderson. *Equations of State of Solids for Geophysics and Ceramic Science.* Oxford University Press, 1995.

[71] Francis Birch. Elasticity and constitution of the earth's interior. *Journal of Geophysical Research (1896-1977)*, 57(2):227–286, 1952.

[72] Kuldeep Kholiya, Jeewan Chandra, and Swati Verma. Analysis of equation of states for the suitability at high pressure: Mgo as an example. *Physica B: Condensed Matter*, 2014:289353, 2014.

[73] J. Shanker, S.S. Kushwah, and P. Kumar. Theory of thermal expansivity and bulk modulus for mgo and other minerals at high temperatures. *Physica B: Condensed Matter*, 233(1):78–83, 1997.

[74] J. Ross MacDonald. Review of some experimental and analytical equations of state. *Reviews of Modern Physics*, 41(2):316–349, 1969.

[75] Kamal Devlal and B. R. K. Gupta. Equation of state for inert gas solids. *Pramana - Journal of Physics*, 69(2):307–312, 2007.

[76] P Vinet, J H Rose, J Ferrante, and J R Smith. Universal features of the equation of state of solids. *Journal of Physics: Condensed Matter*, 1(11):1941–1963, 1989.

[77] Frank D. Stacey. Theory of thermal and elastic properties of the lower mantle and core. *Physics of the Earth and Planetary Interiors*, 89(3):219–245, 1995.

[78] Frank D. Stacey. Finite strain, thermodynamics and the earth's core. *Physics of the Earth and Planetary Interiors*, 128(1):179–193, 2001.

[79] F.D. Stacey and P.M. Davis. High pressure equations of state with applications to the lower mantle and core. *Physics of the Earth and Planetary Interiors*, 142(3):137–184, 2004.

[80] F. P. Bundy. Pressure-temperature phase diagram of elemental carbon. *Physica A*, 156(1):169–178, 1989.

[81] D. A. Young. *Phase Diagrams of the Elements.* University of Carlifornia Press, first edition, 1991.

[82] K. S. Novoselov, A. K. Geim, S. V. Morozov, D. Jiang, Y. Zhang, S. V. Dubonos, I. V. Grigorieva, and A. A. Firsov. Electric field effect in atomically thin carbon films. *Science*, 306(5696):666–669, 2004.

[83] S. Iijima. Helical microtubules of graphitic carbon. *Nature*, 354(6348):56–58, 1991.

[84] H. W. Kroto, J. R. Heath, S. C. O'Brien, R. F. Curl, and R. E. Smalley. C_{60}: Buckminsterfullerene. *Nature*, 318(6042):162–163, 1985.

[85] A. G. Whittaker. Carbon: A new view of its high-temperature behavior. *Science*, 200(4343):763–764, 1978.

[86] P. P. K. Smith and P. R. Buseck. Carbyne forms of carbon: Do they exist? *Science*, 216(4549):984–986, 1982.

[87] M. P. Grumbach and R. M. Martin. Phase diagram of carbon at high pressures and temperatures. *Physical Review B*, 54:15730–15741, 1996.

[88] A. A. Correa, S. A. Bonev, and G. Galli. Carbon under extreme conditions: Phase boundaries and electronic properties from first-principles theory. *Proceedings of the National Academy of Sciences*, 103(5):1204–1208, 2006.

[89] A. A. Correa, L. X. Benedict, D. A. Young, E. Schwegler, and S. A. Bonev. First-principles multiphase equation of state of carbon under extreme conditions. *Physical Review B*, 78:024101, 2008.

[90] Miguel Martinez-Canales, Chris J. Pickard, and Richard J. Needs. Thermodynamically stable phases of carbon at multiterapascal pressures. *Physical Review Letters*, 108:045704, 2012.

[91] L. X. Benedict, K. P. Driver, S. Hamel, B. Militzer, T. Qi, A. A. Correa, A. Saul, and E. Schwegler. Multiphase equation of state for carbon addressing high pressures and temperatures. *Physical Review B*, 89:224109, 2014.

[92] Xiaofei Wang, Sandro Scandolo, and Roberto Car. Carbon phase diagram from ab initio molecular dynamics. *Physical Review Letters*, 95:185701, 2005.

[93] M. Schöttler, M. French, D. Cebulla, and R. Redmer. Free energy model for solid high-pressure phases of carbon. *Journal of Physics: Condensed Matter*, 28(14):145401, 2016.

[94] M. Ross. The ice layer in uranus and neptune—diamonds in the sky? *Nature*, 292(5822):435–436, 1981.

[95] W. B. Hubbard. Interiors of the giant planets. *Science*, 214(4517):145–149, 1981.

[96] Laura Robin Benedetti, Jeffrey H. Nguyen, Wendell A. Caldwell, Hongjian Liu, Michael Kruger, and Raymond Jeanloz. Dissociation of ch4 at high pressures and temperatures: Diamond formation in giant planet interiors? *Science*, 286(5437):100–102, 1999.

[97] L. M. Ghiringhelli, C. Valeriani, E. J. Meijer, and D. Frenkel. Local structure of liquid carbon controls diamond nucleation. *Physical Review Letters*, 99:055702, 2007.

[98] T. S. Metcalfe, M. H. Montgomery, and A. Kanaan. Extrasolar carbon planets. *ArXiv:astro-ph/0504214*, 2005.

[99] S. Seager, M. Kuchner, C. A. Hier-Majumder, and B Militzer. Mass-radius relationships for solid exoplanets. *The Astrophysical Journal*, 669(2):1279–1297, 2007.

[100] J. S. Albinson and A. Evans. Possible role of the white dwarf in grain formation in cataclysmic variable systems. *Astrophysics and Space Science*, 131:443–447, 1987.

[101] J. L. Barrat, J. P. Hansen, and R. Mochkovitch. Crystallization of carbon-oxygen mixtures in white dwarfs. *Astronomy and Astrophysics*, 199:L15–L18, 1988.

[102] P. Dufour, J. Liebert, G. Fontaine, and N. Behara. White dwarf stars with carbon atmospheres. *Nature*, 450:522–524, 1988.

[103] L. Segretain, G. Chabrier, M. Hernanz, E. Garcia-Berro, J. Isern, and R. Mochkovitch. Cooling theory of crystallized white dwarfs. *Astrophysical Journal*, 434:641–651, 1994.

[104] T. S. Metcalfe, M. H. Montgomery, and A. Kanaan. Testing white dwarf crystallization theory with asteroseismology of the massive pulsating DA star BPM 37093. *The Astrophysical Journal*, 605(2):L133–L136, 2004.

[105] B. J. Alder and R. H. Christian. Behavior of strongly shocked carbon. *Physical Review Letters*, 7:367–369, 1961.

[106] F. P. Bundy. The p, t phase and reaction diagram for elemental carbon, 1979. *Journal of Geophysical Research: Solid Earth*, 85(B12):6930–6936, 1980.

[107] J. R. Rygg, J. H. Eggert, A. E. Lazicki, F. Coppari, J. A. Hawreliak, D. G. Hicks, R. F. Smith, C. M. Sorce, T. M. Uphaus, B. Yaakobi, and G. W. Collins. Powder diffraction from solids in the terapascal regime. *Review of Scientific Instruments*, 83(11):113904, 2011.

[108] R. F. Smith, J. H. Eggert, R. Jeanloz, T. S. Duffy, D. G. Braun, J. R. Patterson, R. E. Rudd, J. Biener, A. E. Lazicki, A. V. Hamza, J. Wang, T. Braun, L. X. Benedict, P. M. Celliers, and G. W. Collins. Ramp compression of diamond to five terapascals. *Nature*, 511(7509):330–333, 2014.

[109] J. Wang, F. Coppari, R. F. Smith, J. H. Eggert, A. E. Lazicki, D. E. Fratanduono, J. R. Rygg, T. R. Boehly, G. W. Collins, and T. S. Duffy. X-ray diffraction of molybdenum under ramp compression to 1 tpa. *Physical Review B*, 94(10):104102, 2016.

[110] David R Robinson and Mark Wilson. The liquid⟷amorphous transition and the high pressure phase diagram of carbon. *Journal of Physics: Condensed Matter*, 25(15):155101, 2013.

[111] J. Sun, M. Martinez-Canales, D. D. Klug, C. J. Pickard, and R. J. Needs. Persistence and eventual demise of oxygen molecules at terapascal pressures. *Physical Review Letters*, 108(4):045503, 2012.

[112] Y. Crespo, M. Fabrizio, S. Scandolo, and E. Tosatti. Collective spin 1 singlet phase in high-pressure oxygen. *Proceedings of the National Academy of Sciences*, 111(29):10427–10432, 2014.

[113] Y. Akahama, H. Kawamura, D. Häusermann, M. Hanfland, and O. Shimomura. New high-pressure structural transition of oxygen at 96 gpa associated with metallization in a molecular solid. *Physical Review Letters*, 74(23):4690–4693, 1995.

[114] M. Nicol, K. R. Hirsch, and W. B. Holzapfel. Oxygen phase equilibria near 298 k. *Chemical Physics Letters*, 68(1):49–52, 1979.

[115] D. Schiferl, D. T. Cromer, L. A. Schwalbe, and R. L. Mills. Structure of 'orange' $^{18}O_2$ at 9.6 gpa and 297 k. *Acta Crystallographica Section B*, 39(39):153–157, 1983.

[116] F. Gorelli, M. Santoro, L. Ulivi, and M. Hanfland. Crystal structure of solid oxygen at high pressure and low temperature. *Physical Review B*, 65(17):172106, 2002.

[117] I. N. Goncharenko, O. L. Makarova, and L. Ulivi. Direct determination of the magnetic structure of the delta phase of oxygen. *Physical Review Letters*, 93(5):055502, 2004.

[118] Y. Ma, A. R. Oganov, and C. W. Glass. Structure of the metallic ζ -phase of oxygen and isosymmetric nature of the ϵ-ζ phase transition: Ab initio simulations. *Physical Review B*, 76(6):064101, 2007.

[119] G. Weck, S. Desgreniers, P. Loubeyre, and M. Mezouar. Single-crystal structural characterization of the metallic phase of oxygen. *Physical Review Letters*, 102(25):255503, 2009.

[120] H. Fujihisa, Y. Akahama, H. Kawamura, Y. Ohishi, O. Shimomura, H. Yamawaki, M. Sakashita, Y. Gotoh, S. Takeya, and K. Honda. O_8 cluster structure of the epsilon phase of solid oxygen. *Physical Review Letters*, 97(8):085503, 2006.

[121] L. F. Lundegaard, G. Weck, M. I. McMahon, S. Desgreniers, and P. Loubeyre. Observation of an o_8 molecular lattice in the ϵ phase of solid oxygen. *Nature*, 443(7108):201–204, 2006.

[122] O. Degtyareva, E. Gregoryanz, H. K. Mao, and R. J. Hemley. Crystal structure of sulfur and selenium at pressures up to 160 gpa. *High Pressure Research*, 25(1):17–33, 2005.

[123] Y. Akahama, M. Kobayashi, and H. Kawamura. Structural studies of pressure-induced phase transitions in selenium up to 150 gpa. *Physical Review B*, 47(1):20–26, 1993.

[124] J. C. Jamieson and D. B. McWhan. Crystal structure of tellurium at high pressures. *The Journal of Chemical Physics*, 43(4):1149–1152, 1965.

[125] R. J. DeSando and R. C. Lange. The structures of polonium and its compounds-i α and β polonium metal. *Journal of Inorganic and Nuclear Chemistry*, 28(9):1837–1846, 1966.

[126] F. El Haj Hassan, A. Hijazi, M. Zoaeter, and F. Bahsoun. Structural and electronic properties of bcc tellurium under high pressure. *Physica B: Condensed Matter*, 363(1-4):82–87, 2005.

[127] M. Otani and N. Suzuki. Structural and superconducting transition in selenium at high pressure. *Physical Review B*, 63(10):104516, 2001.

[128] T. Oda, K. Sugimori, H. Nagao, I. Hamada, S. Kagayama, M. Geshi, H. Nagara, K. Kusakabe, and N. Suzuki. Oxygen at high pressures: A theoretical approach to monoatomic phases. *Journal of Physics: Condensed Matter*, 19(36):365211, 2007.

[129] Q. Lv, X. Jin, T. Cui, Q. Zhuang, Y. Li, Y. Wang, K. Bao, and X. Meng. Crystal structures and electronic properties of solid fluorine under high pressure. *Chinese Physics B*, 26(7):076103, 2017.

[130] P. Li, G. Gao, and Y. Ma. Modulated structure and molecular dissociation of solid chlorine at high pressures. *Journal of Chemical Physics*, 137(6):064502, 2012.

[131] T. Kenichi, S. Kyoko, F. Hiroshi, and O. Mitsuko. Modulated structure of solid iodine during its molecular dissociation under high pressure. *Nature*, 423:971–974, 2003.

[132] T. Kume, T. Hiraoka, Y. Ohya, S. Sasaki, and H. Shimizu. High pressure raman study of bromine and iodine: Soft phonon in the incommensurate phase. *Physical Review Letters*, 94(6):065506, 2005.

[133] D. Duan, Y. Liu, Y. Ma, Z. Liu, T. Cui, B. Liu, and G. Zou. Ab initio studies of solid bromine under high pressure. *Physical Review B*, 76(10):104113, 2007.

[134] Y. Fujii, K. Hase, Y. Ohishi, H. Fujihisa, N. Hamaya, and A. Onodera. Pressure-induced monoatomic tetragonal phase of metallic iodine. *Solid State Communications*, 59(2):85–89, 1986.

[135] Y. Fujii, K. Hase, N. Hamaya, Y. Ohishi, A. Onodera, O. Shimomura, and K. Takemura. Pressure-induced face-centered-cubic phase of monatomic metallic iodine. *Physical Review Letters*, 58(8):796–799, 1987.

[136] R. Reichlin, A. K. McMahan, M. Ross, S. Martin, J. Hu, R. J. Hemley, H. K. Mao, and Y. Wu. Optical, x-ray, and band-structure studies of iodine at pressures of several megabars. *Physical Review B*, 49(6):3725–3733, 1994.

[137] Y. Fujii, K. Hase, Y. Ohishi, H. Fujihisa, N. Hamaya, K. Takemura, O. Shimomura, T. Kikegawa, Y. Amemiya, and T. Matsushita. Evidence for molecular dissociation in bromine near 80 gpa. *Physical Review Letters*, 63(5):536–539, 1989.

[138] H. Fujihisa, Y. Fujii, K. Takemura, and O. Shimomura. Optical, x-ray, and band-structure studies of iodine at pressures of several megabars. *Journal of Physics and Chemistry of Solids*, 56(10):1439–1444, 1995.

[139] M. Bastea, A. C. Mitchell, and W. J. Nellis. High pressure insulator-metal transition in molecular fluid oxygen. *Physical Review Letters*, 86(14):3108–3111, 2001.

[140] B. Militzer, F. Gygi, and G. Galli. Structure and bonding of dense liquid oxygen from first principles simulations. *Physical Review Letters*, 91(26):265503, 2003.

[141] G. Weck, P. Loubeyre, J. H. Eggert, M. Mezouar, and M. Hanfland. Melting line and fluid structure factor of oxygen up to 24 gpa. *Physical Review B*, 76(5):054121, 2007.

[142] A. F. Goncharov, N. Subramanian, T. R. Ravindran, M. Somayazulu, V. B. Prakapenka, and R. J. Hemley. Polymorphism of dense, hot oxygen. *Journal of Chemical Physics*, 135(8):84512, 2011.

[143] R. Nomura, K. Hirose, N. Sata, Y. Ohishi, D. Suetsugu, C. Bina, T. Inoue, D. Wiens, and M. Jellinek. Precise determination of post-stishovite phase transition boundary and implications for seismic heterogeneities in the mid-lower mantle. *Physics of the Earth and Planetary Interiors*, 183(1-2):104–109, 2010.

[144] I. L. Karle and J. Karle. Internal motion and molecular structure studies by electron diffraction. *The Journal of Chemical Physics*, 17(11):1052–1058, 1949.

[145] A. Simon and K. Peters. Single-crystal refinement of the structure of carbon dioxide. *Acta Crystallographica Section B*, 2:112750–112751, 1980.

[146] R. T. Downs and M. S. Somayazulu. Carbon dioxide at 1.0 gpa. *Acta Crystallographica Section C*, 54(7):897–898, 1998.

[147] K. Aoki, H. Yamawaki, M. Sakashita, Y. Gotoh, and K. Takemura. Crystal structure of the high-pressure phase of solid co2. *Science*, 263(5145):356–358, 1994.

[148] I. Gimondi and M. Salvalaglio. Co2 packing polymorphism under pressure: Mechanism and thermodynamics of the i-iii polymorphic transition. *The Journal of Chemical Physics*, 147(11):114502, 2017.

[149] V. Iota and C. S. Yoo. Phase diagram of carbon dioxide: Evidence for a new associated phase. *Physical Review Letters*, 86(26):5922–5925, 2001.

[150] F. A. Gorelli, V. M. Giordano, P. R. Salvi, and R. Bini. Linear carbon dioxide in the high-pressure high-temperature crystalline phase iv. *Physical Review Letters*, 93(20):3–6, 2004.

[151] M. Santoro, F. A. Gorelli, R. Bini, G. Ruocco, S. Scandolo, and W. A. Crichton. Linear carbon dioxide in the high-pressure high-temperature crystalline phase iv. *Nature*, 441(7045):857–860, 2006.

[152] C. S. Yoo, H. Kohlmann, H. Cynn, M. F. Nicol, V. Iota, and T. LeBihan. Crystal structure of pseudo-six-fold carbon dioxide phase ii at high pressures and temperatures. *Physical Review B*, 65(10):104103, 2002.

[153] F. Datchi, B. Mallick, A. Salamat, G. Rousse, S. Ninet, G. Garbarino, P. Bouvier, and M. Mezouar. Structure and compressibility of the high-pressure molecular phase ii of carbon dioxide. *Physical Review B*, 89(14):144101, 2014.

[154] V. Iota, C. S. Yoo, J. H. Klepeis, Z. Jenei, W. Evans, and H. Cynn. Six-fold coordinated carbon dioxide vi. *Nature Materials*, 6(1):34–38, 2007.

[155] F. Datchi, V. M. Giordano, P. Munsch, and A. M. Saitta. Structure of carbon dioxide phase iv: Breakdown of the intermediate bonding state scenario. *Physical Review Letters*, 103(18):1–4, 2009.

[156] V. M. Giordano and F. Datchi. Molecular carbon dioxide at high pressure and high temperature. *Europhysics Letters*, 77(4):46002, 2009.

[157] W. Sontising, Y. N. Heit, J. L. McKinley, and G. J. O. Beran. Theoretical predictions suggest carbon dioxide phases iii and vii are identical. *Chemical Science*, 8:7374, 2017.

[158] F. Datchi, G. Weck, A. M. Saitta, Z. Raza, S. Garbarino, G. Ninet, D. K. Spaulding, J. A. Queyroux, and M. Mezouar. Structure of liquid carbon dioxide at pressures up to 10 gpa. *Physical Review B*, 94(1):014201, 2016.

[159] V. Iota, C. S. Yoo, and H. Cynn. Quartzlike carbon dioxide: An optically nonlinear extended solid at high pressures and temperatures. *Science*, 283(5407):1510–1513, 1999.

[160] M. Santoro, F. A. Gorelli, R. Bini, J. Haines, O. Cambon, C. Levelut, J. A. Montoya, and S. Scandolo. Partially collapsed cristobalite structure in the non molecular phase v in co2. *Proceedings of the National Academy of Sciences*, 109(14):5176–5179, 2012.

[161] F. Datchi, B. Mallick, A. Salamat, and S. Ninet. Structure of polymeric carbon dioxide co2 - v. *Physical Review Letters*, 108(12):125701, 2012.

[162] M. S. Lee, J. A. Montoya, and S. Scandolo. Thermodynamic stability of layered structures in compressed co2. *Physical Review B*, 79(14):144102, 2009.

[163] O. Tschauner, H. K. Mao, and R. J. Hemley. New transformations of co2 at high pressures and temperatures. *Physical Review Letters*, 87(7):075701, 2001.

[164] K. D. Litasov, A. F. Goncharov, and R. J. Hemley. Crossover from melting to dissociation of co2under pressure: Implications for the lower mantle. *Earth and Planetary Science Letters*, 309(3–4):318–323, 2011.

[165] M. Santoro, J. F. Lin, H. K. Mao, and R. J. Hemley. In situ high p-t raman spectroscopy and laser heating of carbon dioxide. *The Journal of Chemical Physics*, 121(6):2780–2787, 2004.

[166] M. Santoro and F. A. Gorelli. Constraints on the phase diagram of nonmolecular co2 imposed by infrared spectroscopy. *Physical Review B*, 80(18):184109, 2009.

[167] A. R. Oganov, S. Ono, Y. Ma, C. W. Glass, and A. Garcia. Novel high-pressure structures of mgco3, caco3 and co2 and their role in earth's lower mantle. *Earth and Planetary Science Letters*, 273(1–2):38–47, 2008.

[168] S. Gohr, S. Grimme, T. Söhnel, B. Paulus, and P. Schwerdtfeger. Pressure dependent stability and structure of carbon dioxide—a density functional study including long-range corrections. *The Journal of Chemical Physics*, 139:174501, 2013.

[169] X. Yong, H. Liu, M. Wu, Y. Yao, J. S. Tse, R. Dias, and C. S. Yoo. Crystal structures and dynamical properties of dense co2. *Proceedings of the National Academy of Sciences*, 113(40):11110–11115, 2016.

[170] S. A. Bonev, F. Gygi, T. Ogitsu, and G. Galli. High-pressure molecular phases of solid carbon dioxide. *Physical Review Letters*, 91(6):065501, 2003.